Universidad Autónoma de Madrid

Light-matter interactions at the nanoscale

non-linearities, electrons and exciton polaritons

Author:
Jaime Abad Arredondo

Supervisors:
Antonio I. Fernández Domínguez
Francisco José García Vidal

A thesis submitted in fulfillment of the requirements for the degree of Doctor of Philosophy

in the

Departamento de Física Teórica de la Materia Condensada,
Programa de doctorado en Física de la Materia Condensada, Nanociencia y Biofísica.

Madrid, 2024

'*El mundo era tan reciente, que muchas cosas carecían de nombre, y para mencionarlas había que señalarlas con el dedo.*'

G. García Márquez, *Cien Años de Soledad*

'*And it is said that the naming of the world was the first act of dominion.*'

J.R.R. Tolkien, *The Silmarillion*

Agradecimientos

Hay mucha gente sin la cual esta tesis no habría podido existir. Por ello, quiero dedicar estas primeras páginas a expresar mi sincera gratitud hacia todos vosotros.

Primero quiero agradecer a mis directores de tesis, Antonio y FJ, vuestra inmensa labor durante estos años de doctorado. Vuestra tutela me ha permitido adentrarme en el mundo de la investigación y he tenido el placer de aprender de vosotros a hacer ciencia, que no deja de ser un arte en sí mismo. Gracias por la paciencia, apoyo incondicional y generosidad al compartir conmigo vuestro saber hacer. Me considero tremendamente afortunado de haber podido contar con vosotros en este viaje.

Después, por orden geográfico e histórico, gracias a Álvaro, Miguel e Iñaki, mis predecesores en el despacho 301, por vuestra guia y compañerismo. En qué momento soy yo el más senior de ese despacho, siempre lleno de cabezas privilegiadas! Gracias también a los actuales habitantes del 301: Alberto, compañero por estos caminos nanofotónicos, Nacho, a.k.a. la persona más amable del mundo, y Phillip, al que ya puedo dedicarle estas palabras en castellano dado su superlativo dominio del idioma.

Saliendo de nuestro despacho, quiero agradecer al frente biológico, particularmente a Filip y a Anita, por vuestra paciencia escuchándonos hablar de los temas más infectos durante las comidas, y por vuestra infinita sabiduría sobre la magia de la vida con la que nos iluminábais constantemente.

Ya fuera de nuestra guarida tras la puerta roja, quiero dar las gracias a mis fieles compañeros de descansillos y despotrique: Manu y Juanjo, que habéis hecho que estos años tan difíciles sean más llevaderos, y me habéis explicado con infinita paciencia (una y otra vez) la magia oscura de los Hamiltonianos con estados fraccionalizados y los efectos de estados excitados en many body systems. Estoy seguro de que os irá genial en lo que os propongáis y espero poder disfrutar de vuestra compañía durante mucho tiempo. Gracias también a César, siempre dispuesto para un *mistowebo* y un buen café mañanero, y a Yuri, Pablo, Alonso y Diego

por vuestra compañía durante estos años. También quiero dedicar unas palabras para Celia, Diego y Paula, mis compañeros en la andadura del outreach. Fue un verdadero placer trabajar con vosotros. Sois todos personas excepcionales. Sin salir de la facultad de ciencias, quiero también dar las gracias a todos los profesores que me habéis acompañado de alguna manera en mi paso por el doctorado (y alguno por la carrera!). Gracias a Diego Martín, Johannes Feist, Pablo García, (de los mejores profesores que he tenido, y que sin duda tiene el cielo ganado por perdonarme los retrasos en la entrega de documentación) y Carlos Antón. Finalmente, quiero dar las gracias al personal de la cafetería, y en particular a Pili, quien casi casi compensa el café torrefacto con su simpatía.

I also want to thank Vincenzo and Riccardo, who introduced me to the world of plasmonics and nanophotonics by supervising my BSc and MSc theses, respectively. Your unparalleled command of Spanish inspired me to learn Italian, which, sadly, has yet to result in me being able to say anything more complicated than: *grazie*!

The results in this thesis would not have been possible without the multiple collaborations carried out with experimental groups. I want to thank Professors Douglas Natelson and Vinod Menon, together with their respective students, for the very enriching collaborations and the opportunity of working alongside them. In the same way, I want to thank Professor Said Rodriguez at AMOLF, and the members of his group, Zhou, Giel, Vashist and Kevin. Muchísimas gracias por todo Said, no solo por tu paciencia y excelencia en el trabajo, sino también por el cariño brindado y la hospitalidad al recibirme en AMOLF de imprevisto. Por todo esto, y más, estaré siempre agradecido.

I would also like to wholeheartedly thank the members of the tribunal for accepting the request to evaluate my thesis, and the reserve members for their availability. I hope that you may enjoy the content of these pages as much as I have enjoyed writing them.

Saliendo del ámbito académico, quiero acordarme de quien me ha apoyado durante todos estos años. Particularmente la gente de Alhaurín: Alberto, Carlos, Víctor, Pablo, Virtudes, Iván, Inés, Dave, Ángel, Pedro y Desi, así como quien también es alhaurino aunque le pese: Paula y

Clara. En el frente Madrileño no puedo dejar de dar las gracias a Guille (perdón, frente complutense), y a quienes me acompañaron durante la carrera: María y Jesús. Que no os quepa ninguna duda, esta tesis también existe gracias a vosotros.

También quiero dar las gracias a toda mi familia. Tanto la sanguínea, como sobrevenida (que no es menos familia). Gracias Manuel, Pilar y Lalo por acogerme como uno más de vosotros. Gracias también a todos mis tíos: Pablo, Maruxa, Manuel, Carmiña (latita de sardinas) y José Enrique por vuestro apoyo, interés y cariño, así como a mi abuela, quien se encargó de mi durante los años de carrera y a la que debo haber podido centrarme plenamente en los estudios (así como aproximadamente el 80% de la biomasa que me compone). Muchas gracias abuela, esta tesis en gran medida existe gracias a tu trabajo y cuidados. Gracias también a mi abuelo, gran impulsor de las ciencias en mi adolescencia (y que se encuentra entre los que más ha sufrido por si no llegaba a tiempo con el depósito de esta tesis) y a Jane, por siempe intentar traer algo de literatura a una casa de ingenieros y científicos rarísimos.

A mi hermana, Julia, gracias por tu ejemplo de valentía y sensibilidad, así como por compartir la música conmigo. Mamá, gracias por ser un ejemplo de disciplina, humildad, determinación, y creatividad así como por tu apoyo y amor incondicionales. Papá, gracias por traernos la música. Seguiremos cantando por y para ti. Esta tesis, y lo que hoy soy al margen de ella os lo debo a vosotros, y por ello, gracias.

No podía terminar los agradecimientos sin dedicar unas palabras a la persona que más me ha acompañado durante el doctorado, y quien en los peores momentos me ha mantenido en pie. Muchas gracias, Alba, por la comprensión, paciencia y amor, así como por las risas y los planes. Gracias por formar parte de esto.

En definitiva, a todos los presentes en estos párrafos, y a los que probablemente haya olvidado, gracias. Estas páginas existen porque vosotros las habéis hecho posibles.

Madrid, ~~JunioJulioAgostoSeptiembreOctubreNoviembre~~ Diciembre de 2024.

Jaime

Abstract

English

This thesis is devoted to the theoretical study of light matter interactions in the context of nanophotonics, showcasing their multiple manifestations. In particular we show, that by modifying the structure of these interactions, and under certain conditions, either light or matter components of a coupled light-matter system can act as mediators, giving rise to effective interactions that can dramatically modify the dominant phenomenology of a given system.

The document begins with a broad introductory chapter, providing the necessary conceptual background, followed by three self-contained chapters. Each chapter employs complementary classical and quantum approaches to study light matter interactions in different settings.

In Chapter 2, we investigate matter-mediated photon-photon interactions arising from the non-linear optical response of an oil due to a thermo-optical effect. By embedding a diffractive system in this oil, we predict spontaneous symmetry-breaking, instantaneous momentum conservation violations, and dynamical phases in this driven-dissipative periodic system. These predictions are verified experimentally through collaboration, thus demonstrating the abrupt crossover between the realm of linear optics and conservation laws, and non-linear behaviour.

Chapter 3 focuses on light-matter interactions, with a focus on both weak and strong coupling regimes. We achieve fluorescence enhancement in hybrid metallo-dielectric cavities, which are modelled via semi-analytical approach, and obtain significant enhancement of the fluorescence signal by tuning the geometrical parameters of our cavities through numerical optimization techniques. Additionally, we demonstrate a novel method for electroluminescence-driven probing of strong coupling in plasmonic nanogaps, which we describe through a combination of numerical simulations and analytical modelling. Measurements obtained from the experimental implementation of this proof of concept, developed in

collaboration with our theoretical efforts, are well reproduced by our theoretical description.

Finally, in Chapter 4 we examine photon-mediated matter-matter interactions, specifically, free electron interactions with quantum targets. To this end, we develop a Hamiltonian framework based on macroscopic QED to describe how free electrons may be used to probe and manipulate quantum coherence. We first exploit our description to analyse the interaction of a free electron with an isolated quantum emitter, and demonstrate quantum state preparation and state tomography protocols which chiefly depend on the quantum coherence of the free electron. We also study the interaction of a free electron with a polaritonic target, composed of a strongly-coupled light-matter system. We find that due to quantum interference, modulated electrons are able to address target-specific energy transitions, in contrast to the broadband nature of traditional free electron excitation.

This work advances our understanding of light-matter interactions across a range of regimes, providing both theoretical insights and accompanying external experimental confirmations. A significant part of our research centres on developing new frameworks for describing and analysing these interactions, including a macroscopic QED-based approach for describing light-mediated matter-matter interactions, a novel application of linear stability analysis to spatially extended non-linear optical systems, and comprehensive numerical modelling applied across diverse scenarios. By bridging theoretical predictions with experimental validations, this thesis contributes to the advancement of methodologies for controlling and manipulating quantum and classical systems, with potential applications in quantum technologies and nanophotonics.

keywords: Nanophotonics, plasmonics, light-matter interaction, spontaneous symmetry breaking, fluorescence reshaping, strong coupling, polaritons, free-electrons, modulated electrons.

Castellano

Esta tesis está dedicada al estudio teórico de las interacciones luz-materia en el contexto de la nanofotónica, explorando sus múltiples manifestaciones. En particular, mostramos que al modificar la estructura de estas interacciones, y bajo ciertas condiciones, los componentes de luz o materia de un sistema acoplado luz-materia pueden actuar como mediadores, dando lugar a interacciones efectivas que pueden modificar drásticamente la fenomenología dominante de un sistema dado.

El documento comienza con un amplio capítulo introductorio, que sienta las bases conceptuales necesarias para el resto de la tesis, seguido de tres capítulos independientes y autocontenidos. En cada capítulo empleamos descripciones complementarias, tanto clásicas como cuánticas, para estudiar las interacciones luz-materia en los diferentes escenarios.

En el Capítulo 2, investigamos interacciones fotón-fotón mediadas por la materia que surgen de la respuesta óptica no lineal de un aceite debido a un efecto termoóptico. Al incorporar un sistema difractivo en este aceite, predecimos ruptura espontánea de simetría, violaciones instantáneas de la conservación del momento lateral y fases dinámicas en este sistema periódico disipativo bajo bombeo. Estas predicciones son verificadas experimentalmente con colaboración experimental. De este modo, demostramos la transición abrupta entre el ámbito de la óptica lineal y las leyes de conservación, y los comportamientos no lineales.

El Capítulo 3 se centra en las interacciones luz-materia, abarcando tanto los regímenes de acoplamiento débil como fuerte. Logramos una mejora en la fluorescencia en cavidades híbridas metalo-dieléctricas, que son modeladas mediante un enfoque semianalítico, y obtenemos una mejora significativa en la señal de fluorescencia ajustando los parámetros geométricos de nuestras cavidades mediante técnicas de optimización numérica. Además, demostramos un método novedoso para explorar el acoplamiento fuerte en huecos plasmónicos nanométricos utilizando electroluminiscencia, que describimos mediante una combinación de simulaciones numéricas y modelado analítico. Nuestra descripción teórica reproduce con precisión las medidas obtenidas en la implementación experimental de esta prueba de concepto, desarrollada en colaboración con

nuestros esfuerzos teóricos.

Finalmente, en el Capítulo 4 examinamos interacciones materia-materia mediadas por fotones, específicamente, interacciones de electrones libres con objetivos cuánticos. Para ello, desarrollamos un marco hamiltoniano basado en la electro-dinámica cuántica macroscópica para describir cómo los electrones libres pueden usarse para sondear y manipular la coherencia cuántica. Primero, aprovechamos nuestra descripción para analizar la interacción de un electrón libre con un emisor cuántico aislado, y demostramos protocolos de preparación de estados cuánticos y tomografía de estados que dependen fundamentalmente de la coherencia cuántica del electrón libre. También estudiamos la interacción de un electrón libre con un objetivo polaritónico, compuesto por un sistema de luz-materia fuertemente acoplado. Encontramos que, debido a la interferencia cuántica, los electrones modulados son capaces de bombear transiciones energéticas específicas del objetivo, en contraste con la naturaleza de la excitación de banda ancha tradicionalmente asociada a los electrones libres.

El presente trabajo amplía nuestra comprensión de las interacciones luz-materia en una variedad de regímenes, proporcionando tanto perspectivas teóricas como confirmaciones experimentales externas. Una parte significativa de nuestra investigación se centra en el desarrollo de nuevos marcos para describir y analizar estas interacciones, incluyendo un enfoque basado en la electrodinámica cuántica macroscópica para describir interacciones materia-materia mediadas por luz, una aplicación novedosa del análisis de estabilidad lineal a sistemas ópticos no lineales espacialmente extendidos, y amplio uso del modelado numérico aplicado a diversos escenarios. Al conectar predicciones teóricas con validaciones experimentales, esta tesis contribuye al avance de metodologías para controlar y manipular sistemas cuánticos y clásicos, con aplicaciones potenciales en tecnologías cuánticas y nanofotónica.

Palabras clave: Nanofotónica, plasmonica, interacción luz-materia, ruptura espontánea de simetría, modulación de fluorescencia, acoplo fuerte, polaritones, electrones libres, electrones modulados.

Contents

Abstract **ix**
English . . . ix
Castellano . . . xi

1 Introduction **1**
1.1 Light and matter in the classical regime . . . 3
1.1.1 Electromagnetic waves in vacuum . . . 3
1.1.2 Electromagnetic waves in presence of macroscopic media . . . 5
1.1.3 Classical description of the electromagnetic response 9
1.2 Light and matter in the quantum regime . . . 13
1.2.1 Quantum light . . . 14
1.2.2 Quantum emitters . . . 17
1.2.3 Light-Matter interaction in the quantum regime . 20
1.2.4 Interaction regimes . . . 23
1.3 Plasmonics and Nanophotonics . . . 27
1.4 Summary of contents . . . 32

2 Matter mediated photon-photon interaction: thermo-optical non-linearities and spontaneous symmetry breaking **37**
2.1 Introduction . . . 37
2.1.1 Primer on non-linear dynamical systems . . . 37
2.1.2 Thermo-optical non-linearities . . . 44
2.2 Symmetries in nanophotonics and system under study . 47
2.3 Spontaneous symmetry breaking . . . 50
2.3.1 Linear stability analysis and inversion-symmetry breaking . . . 51

2.3.2 Dynamical behaviour & discrete translational symmetry breaking 62
2.4 Conclussions & outlook 70

3 Excitons in nanophotonic structures 73
3.1 Introduction 73
3.1.1 Matter excitations 75
3.2 Fluorescence triggered by β-decay 77
3.2.1 Theoretical Approach 79
3.2.2 Periodic Nanocavities 83
3.2.3 Optimized Nanocavities 87
3.3 Electroluminescence to probe strong-coupling 93
3.3.1 Electrically driven light emission 96
3.3.2 Experimental setup and measurements 98
3.3.3 Theoretical modelling 103

4 Light-mediated matter-matter interactions 117
4.1 Free electrons in nanophotonics 118
4.2 mQED for Nanophotonics 119
4.2.1 Outline of the derivation for general electronic transitions 120
4.2.2 Particularization for free and bound electrons . . 123
4.2.3 Scattering matrix and Magnus expansion 127
4.3 Quantum state preparation and readout with free electrons 130
4.3.1 Model 131
4.3.2 Ideally modulated electrons 132
4.3.3 State preparation with non-ideally modulated electrons 135
4.3.4 Quantum state tomography 151
4.4 Modulated electrons to probe and manipulate polaritonic targets 158
4.4.1 Target-probe system and Hamiltonian 159
4.4.2 Electron-target interaction 164
4.4.3 CL, EELS and PINEM in polaritonic targets . . 168
4.4.4 Modulated electron beams and polaritons 174

4.5 Conclusions 181

5 Conclusions and outlook 185
English 185
Castellano 189

A Details of the linear stability analysis derivation 195

B Details about transfer matrix derivation and implementation 199
B.1 Transfer matrix and spherical vector harmonics expansion 199
B.2 Expressions for relevant magnitudes 201
B.2.1 Field Enhancement 201
B.2.2 Radiative Purcell 204
B.2.3 Total Purcell 205
B.3 Particle Swarm Optimization 206

C Evaluating the hyperbolic character of multilayer nanocavities 209

D Far-field model of EL from plasmonic structures 213

E MQED for nanophotonics 217
E.1 Outline of the hamiltonian derivation 217
E.2 General light matter interaction Hamiltonian for arbitrary electronic transitions 222
E.2.1 Matter-matter interaction through light 222
E.2.2 Light-matter interaction: Current centered modes 231
E.3 Electronic transitions of interest 234
E.3.1 Localized transitions: dipolar quantum emitters . 234
E.3.2 Free electrons 235
E.3.3 Bound electron - free electron interaction 238
E.4 Quasi-static Dyadic Green's Function of a Sphere 240
E.4.1 Evaluation of QE-cavity coupling 244
E.4.2 Evaluation of free electron - cavity coupling . . . 244
E.4.3 Validity of the quasi-static approximation 246

F Free electron probing of the hydrogen atom wavefunctions **251**

G Magnus expansion of electron-QE interaction **255**

G.1 Interaction Hamiltonian in the interaction Picture 255

G.2 Scattering matrix and Magnus expansion 257

G.2.1 First term in the expansion: Ω_1 258

G.2.2 Second term in the expansion: Ω_2 258

G.2.3 Third term in the expansion: Ω_3 261

G.3 Evaluation for free electron-QE interaction through free space 265

H Modulation integrals of relativistic PINEM electrons **269**

I Phase locking with non-ideal modulated electrons **273**

References **275**

Publications **311**

List of Figures

1.1 Coupling regimes and anticrossing behavior. 25

2.1 Example of bistable systems 41
2.2 Limit cycles 43
2.3 Characterization of linear response of the system. 48
2.4 Self interaction of waves in non-linear medium. 57
2.5 Prediction of spontaneous inversion symmetry breaking . 59
2.6 Experimental measurement of inversion symmetry breaking 61
2.7 Dynamical behaviour in diffractive systems 64
2.8 Dynamical regimes from full-wave numerical simulations 67
2.9 Limit cycles in diffractive system 69

3.1 Experimental demonstration of CR enhancement 78
3.2 Sketch of the spherical hyperbolic cavities. 80
3.3 Simple hyperbolic spherical cavities 84
3.4 Numerical validation of analytical approach. 86
3.5 Spectral response of PSO-optimized cavities of different number of metallo-dielectric layers. 88
3.6 Resonant fields in the PSO-designed cavities. 90
3.7 Structural properties of PSO-designed cavities 91
3.8 Schematic process of light generation from inelastic tunnelling 97
3.9 Experimental devices, EL, PL and characterization. . . . 99
3.10 Experimental EL and PL spectra, inferred plasmonic density of states and polarization behavior of emission. . . . 101
3.11 Schematics of simulation geometry and meshing. 105
3.12 Numerical near field modelling 108

3.13 Polarization selected far field spectra, experimental and theoretical 111
3.14 Detailed comparison between experimental data and two-plasmon model 114

4.1 Ground state probabilities and QE purity after single interaction event. 139
4.2 Attainable QE steady states through continuous modulated electron driving. 143
4.3 Eigenvalues and dynamical behaviour of QE under continuous electron driving. 145
4.4 QE dynamics under continuous driving with modulated electrons. 148
4.5 Rabi oscillations under coherent electron driving. 151
4.6 Maximum electron-QE entanglement. 155
4.7 Quantum state tomography with free electrons. 156
4.8 Sketch of free electron interaction with polaritonic target and energy landscape. 160
4.9 Matrix elements connecting the ground state of target with states of the first excitation manifold. 165
4.10 CL signal from polaritonic target 169
4.11 EELS and PINEM results from the perspective of electron energy change and CL far-field intensity. 171
4.12 Effect of modulation on polariton populations and emission. 177
4.13 Tuning total electron energy gain and loss by electron modulation. 180

B.1 Numerical validation of analytical, field enhancement calculations. 203

C.1 Demonstration of hyperbolic character of periodic nanocavities 210
C.2 Demonstration of hyperbolic character of PSO-designed nanocavities 211

E.1 Sketch of the spherical nanoparticle. 241

E.2 Effect of electrodynamical and non-locality on the nanoparticle response. 248

F.1 Mapping transitions between hydrogen eigenfunctions with EELS 253

G.1 Integration contours 259
G.2 Integrated coupling strengths of higher orders of the Magnus expansion 267

List of Abbreviations

1D	One dimention
2D	Two dimentions
3D	Three dimentions
CL	Cathodoluminescence
CR	Cherenkov Radiation
cQED	cavity Quantum Electro-Dynamics
EELS	Electron-energy-loss spectroscopy
EL	Electroluminescence
EM	Electromagnetic
LSP	Localized Surface Plasmon
mQED	macroscopic Quantum Electro-Dynamics
NP	Nano-particle
PSO	Particle swarm optimization
QE	Quantum emitter
QED	Quantum Electro-Dynamics
STM	Scanning Tunneling Microscope
SPP	Surface Plasmon Polariton
TMD	Transition-metal dichalcogenide

Chapter 1

Introduction

The present thesis is devoted to the study of interactions in the context of nanophotonics, and, in particular, we show that light-matter interactions can lead to radically different phenomenology depending on the structure of the coupling between the different entities. Specifically, we will explore the situation in which light and matter interact resonantly, and off-resonance. The former case leads to light and matter excitations being dressed by each other in the weak coupling regime, and to the formation of hybrid light-matter states known as polaritons in the strong coupling limit. In the latter case of non-resonant interaction, one finds that either light or matter components may play the role of a mediator in an effective interaction, leading to effects of matter-mediated photon-photon interactions, or photon-mediated matter-matter interaction.

Throughout this thesis, we will study these different interactions through both classical and quantum formalisms. In order to cover this breadth of topics, in this chapter we provide a general didactic introduction to the relevant theoretical aspects of classical electromagnetism and quantum theory needed to understand the content of the different chapters, and point towards more advanced references when necessary. While introducing these concepts, we also provide a brief summary of the historical landmarks of how the different ideas under consideration came to be. We remark that the introduction given here is of general character, and that each of the following chapters of this thesis is preceded by an introduction specific to the topic under consideration. Therefore, although we invite the reader to go through the complete introductory chapter, we now indicate the key concepts treated in the

following sections so that readers familiar with them may skip them:

Section 1.1: concepts in classical electromagnetism

⇒ Sec.1.1.1. Electromagnetic waves in vacuum, Dyadic Green's Function, and linearity of Maxwell's equations in vacuum.

⇒ Sec.1.1.2. Macroscopic Maxwell's equations, constitutive relations and nonlinear expansion of the polarization vector. Power radiated by classical dipole in presence of macroscopic media.

⇒ Sec.1.1.3. Classical description of the electromagnetic response: Drude-Lorentz oscillator model, causality and Kramers-Krönig relations.

Section 1.2: light and matter in the quantum regime

⇒ Sec.1.2.1. Light quantization in nanophotonics. Photons as eigenmodes of a harmonic oscillator.

⇒ Sec.1.2.2. Matter quantization: Hamiltonian of idealized two-level quantum emitters, and associated ladder operators.

⇒ Sec.1.2.3. Light-matter interaction in the quantum regime: Quantum electrodynamics formulation of spontaneous decay of a dipolar quantum emittter, Purcell effect and its connection with classical formulation. Jaynes-Cummings Hamiltonian, and parametrization of the coupling strength through Fermi's Golden Rule.

⇒ Sec.1.2.4. Interaction regimes in light-matter coupled systems: Jaynes Cummings Hamiltonian in the single optical mode approximation, master equation formalism for open quantum systems, and equivalent non-hermitian Hamiltonian in the weak excitation regime. Polariton formation, associated eigenenergies and Hopfield coefficients. Purcell effect from the weak coupling limit of polariton energies. Polariton dispersion in the strong-coupling regime.

Section 1.3: plasmonics and nanophotonics

⇒ Diffraction limit and the problem of confining light at the nanoscale. Charge oscillations in metals and sub-wavelength confinement. Some current directions in the field of nanophotonics.

Section 1.4: summary of contents

⇒ Brief description of the main topics treated in the different chapters

of this thesis, together with the main results achieved, and references to the corresponding publications.

1.1 Light and matter in the classical regime

1.1.1 Electromagnetic waves in vacuum

Much of the understanding of the behaviour of light stems from its classical description in terms of fields. The equations that govern how these fields evolve in space-time and are created by sources are the Maxwell's Equations (ME) [1, 2], which in vacuum are given by

$$\nabla \cdot \mathbf{E}(\boldsymbol{r}, t) = \frac{\rho(\boldsymbol{r}, t)}{\epsilon_0}, \tag{1.1a}$$

$$\nabla \cdot \boldsymbol{B}(\boldsymbol{r}, t) = 0, \tag{1.1b}$$

$$\nabla \times \mathbf{E}(\boldsymbol{r}, t) = -\frac{\partial \boldsymbol{B}(\boldsymbol{r}, t)}{\partial t}, \tag{1.1c}$$

$$\nabla \times \boldsymbol{B}(\boldsymbol{r}, t) = \mu_0 \boldsymbol{J}(\boldsymbol{r}, t) + \mu_0 \epsilon_0 \frac{\partial \mathbf{E}(\boldsymbol{r}, t)}{\partial t}. \tag{1.1d}$$

These equations describe the spatio-temporal evolution of the vector fields $\mathbf{E}(\boldsymbol{r}, t)$ and $\boldsymbol{B}(\boldsymbol{r}, t)$ (respectively the electric field and magnetic induction), and how these are created by the matter sources $\boldsymbol{J}(\boldsymbol{r}, t)$ and $\rho(\boldsymbol{r}, t)$, which represent the current density and charge density respectively, and the parameters μ_0 and ϵ_0 denote the vacuum susceptibility and permittivity, respectively. These vectorial equations implicitly contain the continuity equation for charge conservation $\nabla \cdot \boldsymbol{J}(\boldsymbol{r}, t) + \partial_t \rho(\boldsymbol{r}, t) = 0$. This set of equations is linear and as such, general solutions can be constructed as linear combinations of other solutions. This linearity reflects the fact that photons are in general non-interacting in vacuum[1]. In the

[1] This is the case for field intensities below the Schwinger limit at $E_c \approx 10^{18}$ V/m [3], above which electron-positron pair production is possible, which in turn gives rise to a non-zero photon-photon coupling. This is an active area of research and to this date no direct evidence of strong field vacuum polarization has been found. So for our purposes we are clearly fine by assuming linearity of fields in vacuum. However, as we will show later on, including matter into the picture lowers the requirement for the appearance of non-linear behaviour in the fields.

absence of free charges and currents, the above equations can be manipulated to show that the electric field (and magnetic induction) propagates through free space in the form of waves. Such wave equation, for harmonic fields ($\mathbf{E}(\boldsymbol{r},t) = \mathbf{E}(\boldsymbol{r},\omega)e^{-i\omega t}$), is simply given by

$$\nabla^2\mathbf{E}(\boldsymbol{r},\omega) + \left(\frac{\omega}{c}\right)^2 \mathbf{E}(\boldsymbol{r},\omega) = 0, \tag{1.2}$$

where the solution is waves that propagate through space at the speed of light, $c \equiv 1/\sqrt{\epsilon_0\mu_0}$, which naturally emerges from Maxwell's equations. More generally, the wave equation for the electric and magnetic fields with sources, assuming harmonic time dependence read

$$\nabla \times \nabla \times \mathbf{E}(\boldsymbol{r},\omega) - \left(\frac{\omega}{c}\right)^2 \mathbf{E}(\boldsymbol{r},\omega) = i\omega\mu_0 \boldsymbol{J}(\boldsymbol{r},\omega), \tag{1.3}$$

$$\nabla \times \nabla \times \boldsymbol{B}(\boldsymbol{r},\omega) - \left(\frac{\omega}{c}\right)^2 \boldsymbol{B}(\boldsymbol{r},\omega) = \mu_0 \nabla \times \boldsymbol{J}(\boldsymbol{r},\omega). \tag{1.4}$$

These inhomogeneous equations are notably harder to solve for general current distributions. However, one can make use of the Green's Function formalism and solve a simpler accessory problem. The current inhomogeneous wave equation can be understood as a linear differential operator acting on the electric field as $\mathcal{L}\mathbf{E}(\boldsymbol{r},\omega) = \boldsymbol{J}(\boldsymbol{r},\omega)$. Instead of tackling the problem generally, we can seek the solution to the simpler differential problem: $\mathcal{L}\mathbf{G}_i(\boldsymbol{r},\boldsymbol{r}',\omega) = \delta(\boldsymbol{r}-\boldsymbol{r}')\hat{u}_i$, where $\mathbf{G}_i$ is then the electric field solution for a punctual current inhomogeneity located at $\boldsymbol{r}'$, and directed in the $\hat{u}_i$ direction. By obtaining this solution for $\hat{u}_i$ in all three Cartesian components, the electric field and magnetic induction can be obtained from these solutions for an arbitrary current density as

$$\mathbf{E}(\boldsymbol{r},\omega) = \mathbf{E}_0(\boldsymbol{r},\omega) + i\omega\mu_0 \int_V d\boldsymbol{r}\, \mathbf{G}(\boldsymbol{r},\boldsymbol{r}',\omega)\cdot \boldsymbol{J}(\boldsymbol{r}',\omega), \tag{1.5}$$

$$\boldsymbol{B}(\boldsymbol{r},\omega) = \boldsymbol{B}_0(\boldsymbol{r},\omega) + \mu_0 \int_V d\boldsymbol{r}\, \mathbf{G}(\boldsymbol{r},\boldsymbol{r}',\omega)\cdot \Big(\nabla \times \boldsymbol{J}(\boldsymbol{r}',\omega)\Big). \tag{1.6}$$

Where the zero subscript denotes the homogeneous solution in the absence of sources, $\mathbf{G}$ is the electromagnetic *Dyadic Green's Function* constructed from the $\mathbf{G}_i$ vectors, and the volume integration is performed over the spatial extent of the field sources. Note again that linearity

of Maxwell's equations is what enables the use of the Green's Function formalism.

1.1.2 Electromagnetic waves in presence of macroscopic media

If field sources are placed near (or inside) macroscopic media, Maxwell's equations need to be supplemented. Particularly, the presence of *external* sources, such as an external charge or current density, will result in the media accumulating its own *induced* charges and currents as a response to the external fields. As such, the total current and charge densities in the system can be split into two contributions as $\rho(\boldsymbol{r},t) = \rho_{ext}(\boldsymbol{r},t) + \rho_{ind}(\boldsymbol{r},t)$ and $\boldsymbol{J}(\boldsymbol{r},t) = \boldsymbol{J}_{ext}(\boldsymbol{r},t) + \boldsymbol{J}_{ind}(\boldsymbol{r},t)$. This material response can be described by defining the polarization $\boldsymbol{P}(\boldsymbol{r},t)$ and magnetization $\boldsymbol{M}(\boldsymbol{r},t)$ density vectors. Then, the induced charge and currents can be written in terms of these as $\rho_{ind}(\boldsymbol{r},t) = -\nabla\cdot\boldsymbol{P}(\boldsymbol{r},t)$ and $\boldsymbol{J}_{ind}(\boldsymbol{r},t) = \partial_t\boldsymbol{P}(\boldsymbol{r},t) + \nabla\times\boldsymbol{M}(\boldsymbol{r},t)$ [4, 5]. Introducing these definitions into the vacuum Maxwell's equations in Eqs. (1.1) and rearranging produces the macroscopic Maxwell's equations:

$$\nabla\cdot\boldsymbol{D}(\boldsymbol{r},t) = \rho_{ext}(\boldsymbol{r},t), \tag{1.7a}$$

$$\nabla\cdot\boldsymbol{B}(\boldsymbol{r},t) = 0, \tag{1.7b}$$

$$\nabla\times\mathbf{E}(\boldsymbol{r},t) = -\frac{\partial\boldsymbol{B}(\boldsymbol{r},t)}{\partial t}, \tag{1.7c}$$

$$\nabla\times\boldsymbol{H}(\boldsymbol{r},t) = \boldsymbol{J}_{ext}(\boldsymbol{r},t) + \frac{\partial\boldsymbol{D}(\boldsymbol{r},t)}{\partial t}, \tag{1.7d}$$

where the newly introduced displacement field $\boldsymbol{D}(\boldsymbol{r},t) = \epsilon_0\mathbf{E}(\boldsymbol{r},t) + \boldsymbol{P}(\boldsymbol{r},t)$, and magnetic field $\boldsymbol{H}(\boldsymbol{r},t) = \frac{1}{\mu_0}\boldsymbol{B}(\boldsymbol{r},t) - \boldsymbol{M}(\boldsymbol{r},t)$ absorb the material response. To complete the material description, one still needs to link the polarization and magnetization currents to field intensities. Throughout this thesis, we will focus on non-magnetic media, meaning $\boldsymbol{M}(\boldsymbol{r},t) = 0$. On the other hand, the polarization can be expressed as a power series in terms of the incident electric field. In a medium with

zero-response time[2] this expansion is given by [6]

$$\boldsymbol{P}(\boldsymbol{r},t) = \epsilon_0 \left[\chi^{(1)}\mathbf{E}(\boldsymbol{r},t) + \chi^{(2)}\mathbf{E}(\boldsymbol{r},t)^2 + \chi^{(3)}\mathbf{E}(\boldsymbol{r},t)^3 + \dots\right], \quad (1.8)$$

where the coefficients $\chi^{(i)}$ are the material's susceptibilities at different orders. The first term in the expansion, $\chi^{(1)}$, is known as the linear susceptibility and it describes the material response independent of field intensities, preserving the linearity of Maxwell's equations in vacuum. On the other hand, the inclusion of higher order terms introduces a dependence of the material properties on field amplitudes, which in time acts back on the fields, therefore, this non-linear response leads light to interact with itself through the material's response. Note that the expansion in Eq. (1.8) is independent of the origin of the non-linear mechanism, and therefore the field intensities at which such non-linearities become relevant depend very much on the mechanism involved. For instance, when looking at non-linear response stemming from bound electrons in atoms, one would expect that that these will become dominant when the external fields are of the order of the characteristic atomic field strength, given by $E_{at} = e/(4\pi\epsilon_0 a_0^2)$, with $-e$ being the electron's charge and $a_0 = 4\pi\epsilon_0\hbar^2/me^2$ is the Bohr radius. In this expression we also find the normalized Planck's constant $(h/2\pi)$ and the electron's mass (m). At these applied field strengths, the electrons will wander off the parabolic minima of the effective atomic potential, giving rise to an anharmonic response. One can evaluate this field amplitude to be of the order of $E_{at} \approx 5 \times 10^{11}$ V/m [3]. These field intensities have been attainable with lasers since the advent of chirped pulse amplification techniques developed in 1980s [7], which opened the door to the development of the very rich field of non-linear optics. Of course this is by no means the only source of non-linear behaviour. For instance, this phenomenology can also arise from hot electron formation in epsilon-near zero materials [8,

[2] From arguments of causality, such medium would have to be lossless and dispersion-less.

[3] Note how, from this back of the envelope calculation, one can see that by inclusion of matter into the system, the field intensities required to observe photon-photon interactions are reduced by 7 orders of magnitude compared to the required intensities given by the Schwinger limit mentioned in footnote 1.

9], or from thermo-optical effects [10, 11], which can become relevant at even lower input power densities, as we shall show on Chapter 2 .

For the majority of the present thesis, however, restricting ourselves to the linear response regime will suffice to accurately describe the different setups under study. In this situation, the most general form of the displacement field, assuming local behaviour and isotropic media, is given by

$$\boldsymbol{D}(\boldsymbol{r},t) = \epsilon_0 \int dt' \epsilon(\boldsymbol{r}, t-t')\mathbf{E}(\boldsymbol{r},t'). \tag{1.9}$$

This expression indicates that the displacement field at a given time is influenced by the electric field at all previous times, as required by causality[4], and weighted by the convolution with the relative permittivity of the material, $\epsilon(\boldsymbol{r},t)$. From the linearity of these equations, one can perform a spectral decomposition of the different fields by performing a Fourier transform as

$$\boldsymbol{F}(\boldsymbol{r},t) = \int d\omega \boldsymbol{F}(\boldsymbol{r},\omega)e^{-i\omega t}, \tag{1.10}$$

which in time allows to greatly simplify the constitutive relationships through the use of the convolution theorem. In the case of non-magnetic media, this yields

$$\boldsymbol{D}(\boldsymbol{r},\omega) = \epsilon_0\epsilon(\boldsymbol{r},\omega)\mathbf{E}(\boldsymbol{r},\omega), \tag{1.11a}$$

$$\boldsymbol{H}(\boldsymbol{r},\omega) = \frac{1}{\mu_0}\boldsymbol{B}(\boldsymbol{r},\omega). \tag{1.11b}$$

These constituent relations then lead to a modified wave equation for the electric field in presence of macroscopic, isotropic, electric, media as

$$\nabla \times \nabla \times \mathbf{E}(\boldsymbol{r},\omega) - \left(\frac{\omega}{c}\right)^2 \epsilon(\boldsymbol{r},\omega)\mathbf{E}(\boldsymbol{r},\omega) = i\omega\mu_0 \boldsymbol{J}_{ext}(\boldsymbol{r},\omega). \tag{1.12}$$

This wave equation is similar to the one in vacuum, shown in Eq. (1.3), with the crucial difference that the response of the macroscopic media is encoded through the presence of the relative permittivity $\epsilon(\boldsymbol{r},\omega)$.

[4] We will explore the consequences of causality when studying the theoretical description of the optical properties of materials, in section 1.1.3.

Note that the permittivity is space-dependent to account for different homogeneous materials or even systems in which the refractive index smoothly changes in space. In absence of sources, and for a homogeneous medium, the above wave equation accepts plane waves as solutions $\mathbf{E}(\boldsymbol{r},\omega) \propto e^{i\boldsymbol{k}\cdot\boldsymbol{r}}$, where the wavevector, $\boldsymbol{k}$, encodes the propagation direction of the wave and the associated wavelength. In particular $k \equiv |\boldsymbol{k}| = \sqrt{\epsilon}k_0$, with $k_0 = \omega/c$ being the vacuum wavevector. This expression motivates the definition of the refractive index $n = \sqrt{\epsilon}$, which can be related to the propagation speed of light in a homogeneous medium as $v = c/n$.

In the same spirit as before, we can seek a solution to this inhomogeneous equation by obtaining the Dyadic Green's Function. The total solution to the inhomogeneous wave equation is given by

$$\mathbf{E}(\boldsymbol{r},\omega) = \mathbf{E}_0(\boldsymbol{r},\omega) + i\omega\mu_0 \int_V d\boldsymbol{r}\, \mathbf{G}(\boldsymbol{r},\boldsymbol{r}',\omega)\cdot\boldsymbol{J}_{ext}(\boldsymbol{r}',\omega), \tag{1.13}$$

which looks virtually identical to Eq. (1.5) with the current density substituted by the external current. However, now the Dyadic Green's Function is the solution to the modified differential problem: $\mathcal{L}\mathbf{G}_i(\boldsymbol{r},\boldsymbol{r}',\omega) = \delta(\boldsymbol{r}-\boldsymbol{r}')\hat{u}_i$ with $\mathcal{L} = \left[\nabla\times\nabla\times - \left(\frac{\omega}{c}\right)^2\epsilon(\boldsymbol{r},\omega)\right]$. By solving for the different components of the dyadic, one is capable of calculating how arbitrary currents produce fields in presence of macroscopic media.

One of the most relevant application of the Green's Function formalism is finding the fields produced by an electric point dipole. It can be shown that an ideal point dipole has an associated current density given by $\boldsymbol{J}(\boldsymbol{r},\omega) = -i\omega\boldsymbol{\mu}\delta(\boldsymbol{r}-\boldsymbol{r}_0)$, with $\boldsymbol{\mu}$ being the dipole moment. Using the expression above for the field created by an arbitrary current one sees that the field created by an ideal point dipole is given by [12]

$$\mathbf{E}(\boldsymbol{r},\omega) = \mu_0\omega^2\mathbf{G}(\boldsymbol{r},\boldsymbol{r}_0,\omega)\cdot\boldsymbol{\mu}. \tag{1.14}$$

From Poynting's theorem, in a lossless medium, the total power radiated by a given current distribution is equal to the power it dissipates [12],

which in the case of the point-like dipole under discussion is given by

$$P = -\frac{1}{2}\int_V d\boldsymbol{r}' \,\mathrm{Re}\left[\boldsymbol{J}^*(\boldsymbol{r}',\omega)\cdot\mathbf{E}(\boldsymbol{r},\omega)\right]$$
$$= \frac{\mu_0\omega^3}{2}\mathrm{Im}\left[\boldsymbol{\mu}^*\cdot\mathbf{G}(\boldsymbol{r}_0,\boldsymbol{r}_0,\omega)\cdot\boldsymbol{\mu}\right]. \tag{1.15}$$

This is one of the most important results in this section as we shall see later. To gain some insight into why this might be the case, consider the following situation. For an electric dipole in vacuum, we denote the associated Dyadic Green's Function by $\mathbf{G}_0$, and the total power radiated by the dipole will be $P_0 = \mu_0|\boldsymbol{\mu}|^2\omega^4/(12\pi c)$ [12]. If we now consider the situation in which the dipole is in presence of some material structure, one can choose to split the total Green's Dyadic into two parts: one corresponding to the case in absence of macroscopic media, i.e., in vacuum, $\mathbf{G}_0$, and other that contains the fields that the different material structures scatter, $\mathbf{G}_s$, as $\mathbf{G} = \mathbf{G}_0 + \mathbf{G}_s$, which allows to write the total radiated power by the dipole as

$$\frac{P}{P_0} = \frac{6\pi c}{\omega}\mathrm{Im}\left[\hat{u}^*_{\boldsymbol{\mu}}\cdot\mathbf{G}(\boldsymbol{r}_0,\boldsymbol{r}_0,\omega)\cdot\hat{u}_{\boldsymbol{\mu}}\right] \tag{1.16}$$
$$= 1 + \frac{6\pi c}{\omega}\mathrm{Im}\left[\hat{u}^*_{\boldsymbol{\mu}}\cdot\mathbf{G}_s(\boldsymbol{r}_0,\boldsymbol{r}_0,\omega)\cdot\hat{u}_{\boldsymbol{\mu}}\right]. \tag{1.17}$$

Thus, the total power radiated by a point dipole depends on how the fields are scattered back from the surrounding material structures, and consequently, the radiative properties of the point dipole can be engineered through appropriate material patterning.

1.1.3 Classical description of the electromagnetic response

Until now, we have shown that Maxwell's equations allow to study how the fields respond to the presence of matter characterized by some permittivity $\epsilon(\boldsymbol{r},\omega)$. In this way, matter is treated as a continuum over which the fields propagate. By experimentally measuring the optical properties of materials, one can make accurate theoretical predictions about the behaviour of fields. However, we still have not provided a microscopic view of the processes that lead materials to have different

optical responses. Throughout this section, we take a brief look at the most common descriptions of optical matter response in classical electromagnetism, which we will employ throughout this thesis and can be used as a basis to understand how different material families inherit their properties.

Note that the framework introduced in this section describes how fields are created and respond to the properties of macroscopic media. However, it does not describe how these fields act back on matter. The necessary theory to supplement Maxwell's equations would come from Hendrik A. Lorentz in 1895 [13], when he described the force that a given charge and current distribution experience under the influence of an electric and magnetic field, i.e., the *Lorentz force*. This theory came nearly 30 years[5] after the original Maxwell publication in 1865 [1]. After Thomson's discovery of the electron in 1987 [15], in 1909, Lorentz [16] provided one of the first efforts at linking a microscopic view of a material to its macroscopic optical response. He proposed a simple oscillator model with a characteristic resonant frequency, suggesting that, under the influence of a harmonic electric field, an electron bound by some potential will have an equation of motion given by

$$\ddot{x}(t) + \gamma\dot{x}(t) + \omega_0^2 x(t) = \frac{eEe^{-i\omega t}}{m}, \tag{1.18}$$

where ω_0 represents the resonant frequency of the bound electron,γ represents an effective damping (which may come from a wide variety of microscopic processes), E is the incident electric field amplitude[6], and e and m are respectively the electron charge and mass. Assuming that the movement of the electron is also harmonic $x(t) = x(\omega)\exp\{-i\omega t\}$,

[5] A very interesting perspective of why Maxwell's equations took so long to gain traction in the scientific community is given by Dyson in Ref. [14].

[6] Note that when deriving optical response of materials from microscopic models, one usually differentiates the externally applied electric field, and the local field that is felt by the microscopic sub-system. These two are in general not the same due to the influence of matter surrounding the microscopic region of interest, thus modifying the externally applied field. See [5] for instance.

then the displacement can be obtained to be

$$x(\omega) = \frac{\frac{eE}{m}}{\omega_0^2 - \omega^2 - i\omega\gamma}. \tag{1.19}$$

For a material containing N of such bound electrons per unit volume, then the total polarization will be given by $P(\omega) = Nex(\omega)$, which allows to extract the relative permittivity of such material to be

$$\epsilon(\omega) = 1 + \frac{\omega_p^2}{\omega_0^2 - \omega^2 - i\omega\gamma}, \tag{1.20}$$

where we have defined the plasma frequency as $\omega_p = \sqrt{\frac{Ne^2}{m\epsilon_0}}$. This is known as the Lorentz oscillator model and it is very successful at modelling the optical response of materials in which interband transitions are relevant. This simple model also serves to illustrate a general property that material description must fulfil: causality [17]. Particularly, by looking at Eq. (1.9), causality requires that the displacement vector at a given time is only influenced by the electric field at previous times. This is equivalent to requiring that if the electric field impinges on the material at $t = 0$, then $\epsilon(t)$ is 0 for $t < 0$. From the expression above, we have

$$\epsilon(t) = \int_{-\infty}^{\infty} d\omega \left[1 - \frac{\omega_p^2}{\omega^2 - \omega_0^2 + i\gamma\omega}\right] e^{-i\omega t} \tag{1.21}$$

$$= 2\pi\delta(t) - \int_{-\infty}^{\infty} d\omega \, \frac{\omega_p^2}{(\omega - \omega_+)(\omega - \omega_-)} e^{-i\omega t}. \tag{1.22}$$

The delta above stems from the zero response time of vacuum, and the poles in the denominator are given by $\omega_\pm = -i\frac{\gamma}{2} \pm \sqrt{\omega_0^2 - \left(\frac{\gamma}{2}\right)^2}$. The second integral can be evaluated by using the residue theorem. In order to obtain regularized behaviour at $|\omega| \to \infty$ the factor $e^{-i\omega t}$ must vanish. Therefore for $t < 0$ the integral has to be performed in the upper complex half plane ($\mathrm{Im}(\omega) > 0$), while for $t > 0$ the integral is performed in the lower half plane ($\mathrm{Im}(\omega) < 0$). Since the poles of the integrand always lie in the lower half plane (for $\omega_0 \neq 0$ and $\gamma > 0$), then one has that $\epsilon(t) = 0$ for $t < 0$, granting causality. More generally, the causality

argument allows to extract general features of material responses. Over the next few lines we follow Ref. [18]. Suppose that now we focus on the polarization vector, which we write in terms of a response function, χ, as $\boldsymbol{P}(t) = \epsilon_0 \int dt' \chi(t-t')\mathbf{E}(t')$. From causality arguments, we have shown that $\chi(t<0) = 0$, which means we can express this response function as the product of a Heaviside function, $\theta(t)$, and some other arbitrary function, $Y(t)$. Since the Heaviside function imposes causality, we are free to choose the function $Y(t)$ for $t < 0$. By using the Fourier transform of the Heaviside function [19], and the convolution theorem, one finds that

$$\chi(\omega) = \frac{i}{2\pi}\mathcal{P}\int d\omega' \frac{Y(\omega')}{\omega - \omega'} + \frac{Y(\omega)}{2}. \tag{1.23}$$

Where $\mathcal{P}$ stands for the Cauchy principal value. Now we can exploit the freedom to choose $Y(t)$ for $t < 0$. If we assume that Y is even, then its Fourier transform is a purely real function, which from above then implies: $Y(\omega) = 2\mathrm{Re}(\chi(\omega))$. On the other hand, if Y is odd, then its Fourier transform is purely imaginary function, and therefore we have $Y(\omega) = 2i\mathrm{Im}(\chi(\omega))$. Putting these expressions back into the equation above we obtain

$$\mathrm{Re}[\chi(\omega)] = \frac{1}{\pi}\mathcal{P}\int d\omega' \frac{\mathrm{Im}[\chi(\omega')]}{\omega' - \omega}, \tag{1.24}$$

$$\mathrm{Im}[\chi(\omega)] = -\frac{1}{\pi}\mathcal{P}\int d\omega' \frac{\mathrm{Re}[\chi(\omega')]}{\omega' - \omega}. \tag{1.25}$$

These are known as the Kramers-Krönig relations, and they establish the relationship between the real and the imaginary part of a material's optical response. Note that since $\epsilon(\omega) = 1 + \chi(\omega)$, and the imaginary part of the permittivity is associated with optical absorption, these relationships establish that dispersion, i.e., the fact that a material's response is frequency-dependent, is inextricably linked to optical absorption.

Besides the aforementioned Lorentz model, which is useful for describing the response of materials presenting inter-band transitions, other widely used model is known as the Drude model. This model is useful for describing materials whose response is characterized by intraband transitions, such as conduction electrons in metals. As such, metals are

widely described with this model. One can actually obtain the Drude result from the Lorentz expression in Eq. (1.20) by simply setting $\omega_0 = 0$, i.e., by considering a non-bound electron. The Drude permittivity reads:

$$\epsilon(\omega) = 1 - \frac{\omega_p^2}{\omega(\omega + i\gamma)}. \tag{1.26}$$

Generally speaking, materials will have several interband transitions and also some remanent response in the limit of $\omega \to \infty$, therefore, it is common to write a generalized Lorentz-Drude model as a sum of these different contributions as [5]

$$\epsilon(\omega) = \epsilon_\infty + \sum_i \frac{\omega_{pi}^2}{\omega_{0i}^2 - \omega^2 - i\omega\gamma_i}, \tag{1.27}$$

which then can be fitted to experimental measurements of the material's optical properties. Note that these two schemes presented here are but the tip of the iceberg, and that the unification of microscopic and macroscopic electromagnetism is an immense and rich topic on its own. We refer the reader to [17, 20] for a more complete read on the different models of the optical properties of different families of materials. It is also interesting to note that all these material descriptions hinge on a coarse-graining procedure, in which some internal degrees of freedom at the microscopic level are replaced by some macroscopic collective response. These strategies also become relevant in the so-called *effective medium approximations*, in which the properties of composite materials are modelled through the mixture of the macroscopic constituents' properties. These ideas and conceptual understanding of an effective medium as something that can be internally structured is what led to the birth of the fascinating field of metamaterials [21–23], which introduced unprecedented flexibility in the effective properties of material.

1.2 Light and matter in the quantum regime

Once the classical description of light and matter has been introduced, in this section, we will focus on how light and matter are described

within a quantum-mechanical framework, and also give a brief historical rendition of the birth of these ideas.

1.2.1 Quantum light

It is a widespread belief that scientist at the end of the 19^{th} century were certain about their understanding of the natural world, and that the physical sciences were therefore considered an almost closed topic. In fact, there is a famous quote, attributed to Lord Kelvin that reads:

> There is nothing new to be discovered in physics now. All that remains is more and more precise measurement.

However, there is no actual record of him ever saying this[7]. Furthermore, Lord Kelvin was well aware that there were some problems that simply could not be explained from the existing theories at the time. This can be seen from one lecture he delivered in 1900, later published in 1901 [24] in which he talks about two problems in particular. The first one was the results of the Michelson-Morley experiment, which attempted to measure the relative motion of earth to ether by measuring the speed of light. The second problem was that the predictions for heat capacities of materials obtained from the kinetic theories of gases were significantly larger than the experimental measurements made at low temperature. These, together with the puzzling results of the photo-electric effect and black-body radiation shows that 19^{th} century physicists were all but content with the state of physics at the time. Lord Kelvin in particular proved to have tremendous foresight, since these problems would only be solved after the advent of special relativity, and quantum mechanics respectively. The first hint of the need of quantizing light comes at the beginning of the 20^{th} century from Planck's success at reproducing the experimentally measured black-body radiation spectrum. Planck's ansatz was that optical modes of frequency ν had an associated energy $h\nu$ (from then on, h is the Planck's constant), and that only whole numbers of excitations of this energy could be accommodated in the system. This allowed him to circumvent the equipartition theorem of the

[7] Apparently, this quote is suspected to be a paraphrase of something that Albert Michelson said.

kinetic theory of gases and use the machinery from statistical physics to successfully reproduce the blackbody spectrum. These quanta of light could also be used to explain the photo-electric effect, and thus the evidences of the quantum nature of light sparked the birth of quantum physics.

Nowadays, we employ the term *photon* to refer to the quantum units of light, i.e., to the quantum excitations of the electromagnetic field. Usually, photons are associated with the corpuscular picture of light and therefore thought about as the "particles" of light, which has led some authors to develop strong feelings about the use of the term [25][8]. This is so because although it can be conceptually useful to think about photons as light particles, formally, quantization procedures of the electromagnetic field lead to the conclusion that photons should be understood as excitations of the electromagnetic modes sustained by each particular system. For instance, canonical quantization procedures (see Ref. [26], among others), usually write the quantized fields in terms of plane-wave modes, while quantization in the field of cavity quantum electrodynamics (cQED) favours the quantization in terms of localized modes. For now, we will restrict ourselves to the situation in which proper optical modes are present, and therefore light can be described through a hamiltonian formalism as [26]

$$\hat{H} = \sum_i \hbar\omega_i \left(\hat{a}_i^\dagger \hat{a}_i + \frac{1}{2} \right), \tag{1.28}$$

where the summation runs over all optical modes of the system, each with frequency ω_i, and the operators $\hat{a}_i$ ($\hat{a}_i^\dagger$) act on the quantum EM state by annihilating (creating) a photon in the corresponding mode. These satisfy the bosonic commutation relations $[\hat{a}_i, \hat{a}_{i'}^\dagger] = \delta_{i,i'}$, with $\delta_{i,i'}$ being the Kronecker delta. More explicitly, these operators act on the Fock number basis (denoting the number of photons in a given mode)

[8] In the mentioned work, besides providing a very interesting historical introduction to the development of the field of quantum electrodynamics, the author recalls: "I suggested that a license be required for use of the word "photon", and offered to give such a license to properly qualified people".

as

$$\hat{a}_i^\dagger |n_i\rangle = \sqrt{n_i + 1}\, |(n+1)_i\rangle\,, \tag{1.29a}$$

$$\hat{a}_i |n_i\rangle = \sqrt{n_i}\, |(n-1)_i\rangle\,. \tag{1.29b}$$

Therefore, a Fock state $|n_j\rangle$ has the associated energy $H|n_j\rangle = \hbar\omega_j(n_j + 1/2)|n_j\rangle$, where the $\hbar\omega_j/2$ represents the zero-point energy of the fields, and indicating that the energy difference between every two adjacent number states is always given by $\hbar\omega_j$, i.e., the photon energy. We note in passing, that the Hamiltonian in Eq. (1.28) is exactly equivalent to the quantum Hamiltonian for a set of harmonic oscillators. This again reinforces the conceptual picture outlined above, since photons are then just the minimal oscillation amplitude that these oscillators (the optical modes) can exchange.

In fact, the existence of these optical modes (understood as eigenfunctions of the wave equation) is so vital for the application of the quantum machinery, that devising a general strategy to quantize EM fields in presence of arbitrary material structure remains an area of intense theoretical research to this day. This is the case for instance when dealing with lossy materials or open systems. In this direction, several strategies have led to successful results. One of such strategies is for instance macroscopic quantum electrodynamics (mQED) [27, 28], in which one abandons the description in terms of discrete optical modes and instead employs modes that live in a frequency continuum, while keeping an overall Hamiltonian description. The response of these modes is described through the use of the previously introduced Dyadic Green's Function of the system. We will demonstrate the power of this approach to parametrize light-matter interactions in Chapter 4. On the other hand, approaches based on a quasi-normal mode (QNM) decomposition [29, 30] of the response of the system try to extend the more traditional strategies to open systems in which normal modes do not exist, and phenomenological approaches, that decompose the optical continuum into several modes and background, have also advanced significantly, providing accurate solutions of complex systems [31–33].

1.2.2 Quantum emitters

In the same way that the previously introduced experiments indicated the quantum nature of light, other experimental results from the end of the 19^{th} century hinted at the quantum nature of matter. The most famous example is probably the discrete emission lines from atoms. Rydberg [34] had already successfully identified that the frequencies of the different emission lines could be well predicted as being proportional to the difference of inverses of squares of integers numbers in 1890. However, the origin of these discrete energy steps remained a mystery. Just for perspective, Rutherford's experiments, that would introduce the idea of the atom as a very small positive nucleus surrounded by a large electronic cloud weren't performed until 1911. Shortly after the introduction of this solar-system-like model of an atom, Bohr (1913) proposed a model for the hydrogen atom in which electrons could only occupy certain stable orbits around the nucleus. These orbits where characterized by having an angular momentum that was a multiple of the reduced Planck's constant, $\hbar = h/2\pi$. This ansatz reproduced the Rydberg results for the hydrogen atom and could express the phenomenological constants introduced by Rydberg in terms of fundamental constants. This explanation however, clashed with the classical understanding that accelerated charges (like an electron orbiting the nucleus) radiate energy, and therefore, these atoms should not be stable.

The main hurdle in the understanding of the quantum phenomena at the time was the lack of a formal framework to treat these problems. This would change in 1925, when Schrödinger postulated his famous wave equation [35]. This work begins by crystallizing the oscillatory nature of matter, proposed by De Broglie [36], into a wave equation. Schrödinger was well aware that this was an outlandish idea, as he states in the opening paragraph of the paper:

> The point of view taken here [...] is rather that material points consist of, or are nothing but, wave-systems. This extreme conception may be wrong, indeed it does not offer as yet the slightest explanation of why only such wave-systems

> seem to be realized in nature as correspond to mass-points of definite mass and charge.

However, through the rest of the paper, he establishes the wave equation that describes the evolution of the wave-nature of matter and draws its link to classical Hamiltonian mechanics. He then proceeds to solve the hydrogen atom problem, providing the same energy levels that Bohr found, reproducing known results for the stark effect in the hydrogen atom. Among other things, he also shows that his theory is non-compatible with special relativity, and thus incomplete. This last issue would be fixed by Dirac in 1928 [37], when he presented a wave equation compatible with relativity. Just like this, 30 years after the initial quantization from Planck, modern quantum mechanics was born.

Throughout this thesis, we will deal with the interaction of light with matter. Particularly our focus will be on light in the visible spectrum. This is relevant since photons in this frequency range have associated energies in the order of 1 eV, which happens to be the characteristic order of magnitude of many electronic phenomena. This includes bandgaps in semi-conductors, or excitons in materials[9]. Furthermore, by solving for the allowed energies of an electron within an infinite potential well, one can see that when the electron is confined within length-scales of the order of the nm, then the corresponding electronic excitations have energies in the range of the eV. This indicates that electronic excitations present in confined systems, like atoms, molecules, or quantum dots, will also have energy differences commensurate with optical photons, showing that there exists a huge variety of matter excitations available to study the phenomenology of light-matter interaction.

In general, we will describe the electronic states by the annihilation (creation) operators: $\hat{c}_i$ ($\hat{c}_i^\dagger$). These operators remove (create) an electron in the corresponding electronic eigenstate and fulfil fermionic anticommutaion relations $\{\hat{c}_i, \hat{c}_j^\dagger\} = \delta_{i,j}$. Since the energy ranges under consideration do not allow for actual creation or destruction of matter,

[9] Excitons are a particular kind of electronic excitation formed by a bound electron-hole pair. These can be optically bright, since they can recombine to emit single photons. We will show some work done with materials that present an excitonic response on Chapter 3

usually these operators will appear in pairs as $\hat{c}_i^\dagger \hat{c}_j$, which signifies the transition of an electron from the eigenstate $j \to i$. For localized transitions, like the ones happening in atoms, molecules or quantum dots, it is usual to focus on only two energy levels of interest with a well defined energy gap, E_a. This is valid so long as the rest of the energy levels have energy spacing much larger than E_a. Then the two eigenstates of interest can be labelled as the ground, and excited states, in which case we can define

$$\hat{\sigma}^\dagger = |e\rangle\langle g| = \hat{c}_e^\dagger \hat{c}_g, \tag{1.30a}$$

$$\hat{\sigma} = |g\rangle\langle e| = \hat{c}_g^\dagger \hat{c}_e, \tag{1.30b}$$

as the usual ladder operators of the quantum emitter (QE). These also fulfil fermionic anticommutation relations $\{\hat{\sigma}, \hat{\sigma}^\dagger\} = 1$. Then the Hamiltonian of this QE can be written simply as $\hat{H}_{QE} = \hbar\omega_e |e\rangle\langle e| + \hbar\omega_g |g\rangle\langle g|$. Since it is usual to define the origin of energies at the ground state energy of the emitter, we can simply subtract $\mathbb{1}\hbar\omega_g$ from the Hamiltonian above, which then yields the free Hamiltonian for an ideal two level system as

$$\hat{H}_{QE} = \hbar\omega_{eg}\hat{\sigma}^\dagger\hat{\sigma}, \tag{1.31}$$

with $\omega_{eg} = \omega_e - \omega_g$, which explicitly shows that the relevant energy scale in the internal dynamics of the QE is given by the energy difference between the two available energy levels. However, bear in mind that this is by far not the only relevant parameter of the QE, particularly when interacting with light. In the following section we will hint at how the actual spatial structure of these electronic eigenstates has an effect in the characteristics of the light-matter interaction. This will be shown more explicitly in later sections of this thesis, where we will introduce free electrons in the picture (whose wavefunction have markedly different spatial structure to that of bound electrons in QEs) which will serve to exemplify how different electronic eigenstates can interact very differently with light.

1.2.3 Light-Matter interaction in the quantum regime

From the previous section, we have seen that by using the Schrödinger equation, the correct energy levels of quantum systems can be predicted. These energy levels can be used to understand how matter absorbs photons, however, it cannot explain the lifetimes associated with spontaneous emission. In order to properly describe the interaction between light and matter, it is necessary to describe both components in a quantum picture in the framework of quantum electrodynamics (QED). We begin this section by explicitly showing the effect of the electromagnetic environment on the emission processes.

We consider now states of a combined light and matter system. We will study the transition from an initial ($|i\rangle$) to final ($|f\rangle$) states. The energies associated with these states are E_i and E_f respectively, which have to be identical from energy conservation arguments. The total decay rate of the $i \to f$ transition can be calculated in the limit of weak interaction strength from Fermi's golden rule

$$\gamma = \frac{2\pi}{\hbar^2} \sum_f \left| \langle f | \hat{H}_I | i \rangle \right|^2 \delta(\omega_i - \omega_f), \tag{1.32}$$

where the sum runs over all the possible joint final states. We will be considering electronic transitions taking place between bound states in atoms or molecules, to which we refer as QEs in general. Since these transitions are localized in length-scales much smaller than the free-space wavelength of light, the interaction Hamiltonian can be taken in the dipole approximation: $\hat{H}_I = -\hat{\boldsymbol{\mu}} \cdot \hat{\mathbf{E}}$. In this Hamiltonian, the dipole operator can be expressed by using the spatial displacement quadrature, $\hat{x} \propto \left[\hat{\sigma}^\dagger + \hat{\sigma}\right]$, as $\hat{\boldsymbol{\mu}} = \boldsymbol{\mu}\left[\hat{\sigma}^\dagger + \hat{\sigma}\right]$, with $\hat{\sigma}_= |g\rangle\langle e|$ and $\boldsymbol{\mu} = \langle g | \hat{\boldsymbol{\mu}} | e \rangle$ is the transition dipole moment[10]. On the other hand, the fields at the

[10] Note that in writing the dipole operator in this fashion, we have assumed that it is a real quantity. It is also important to note that this parameter encapsulates the spatial distribution of the wavefunctions associated in the electronic transition. Later on in the thesis we will rework these ideas with arbitrary electronic transitions so that these dependencies will become more apparent.

emitter's position can be expanded as [26]

$$\hat{\mathbf{E}} = \sum_n \left[\mathbf{E}_n^+ \hat{a}_n(t) + \mathbf{E}_n^- \hat{a}_n^\dagger(t) \right], \tag{1.33}$$

where the summation is over the complete set of eigenmodes. We now look for transitions that happen between an initial state given by the QE being in an excited state $|i\rangle = \hat{\sigma}^\dagger |g\rangle \otimes |0\rangle$, and final states in which the excitation has been put into one of the modes of the electromagnetic fields as $|f\rangle = \hat{a}_n^\dagger |g\rangle \otimes |0\rangle$. Then the total decay rate can be written as

$$\gamma = \frac{2\pi}{\hbar^2} \sum_n \left[\boldsymbol{\mu} \cdot (\mathbf{E}_n^+ \mathbf{E}_n^-) \cdot \boldsymbol{\mu} \right] \delta(\omega_n - \omega_0), \tag{1.34}$$

where ω_0 is the energy difference between the ground and excited state. From this expression alone, one can see that the decay rate of the emitter is directly linked to the amplitude of the field profiles at the emitter position. This leads to the idea that by modifying the available optical modes for the emitter to decay into, then the decay rate can be modified. This intuition is formalized in the concept of density of states. Furthermore, by writing the field profiles in terms of normal modes, and linking it to the bi-linear expansion of the Dyadic Green's Function, it can be shown [12] that the expression above can be equivalently written as

$$\gamma = \frac{2\mu_0 \omega_0^2}{\hbar} \left[\boldsymbol{\mu} \cdot \mathrm{Im} \left\{ \mathbf{G}(\boldsymbol{r}_0, \boldsymbol{r}_0, \omega_0) \right\} \cdot \boldsymbol{\mu} \right]. \tag{1.35}$$

The decay rate of such QE in vacuum turns out to be $\gamma_0 = \mu_0 \omega_0^3 |\boldsymbol{\mu}|^2 / (3\pi\hbar c)$. Therefore we arrive at the result that the normalized decay rate of the emitter to that of vacuum is given by

$$\frac{\gamma}{\gamma_0} = \frac{6\pi c}{\omega_0} \left[\hat{u}_\mu \cdot \mathrm{Im} \left\{ \mathbf{G}(\boldsymbol{r}_0, \boldsymbol{r}_0, \omega_0) \right\} \cdot \hat{u}_\mu \right]. \tag{1.36}$$

This expression states that the radiative properties of quantum emitters can be modified by appropriately structuring the emitter's surrounding. This is known as the Purcell effect [38], and it has the deep conceptual implication that the radiative properties of an emitter are in no way

intrinsic, which was the prevalent thought at the time of Purcell's discovery, but are instead a reflection of how the internal degrees of freedom of a given electronic transition interact with the electromagnetic environment. Furthermore, note that the normalized decay-rate in Eq. (1.36) has exactly the same expression as the normalized radiated power by a classical dipole given in Eq. (1.16), so that

$$\left[\frac{\gamma}{\gamma_0}\right]_{\text{QED}} = \left[\frac{P}{P_0}\right]_{\text{Classical}}. \tag{1.37}$$

This important connection establishes that one can make predictions of how a given macroscopic environment modifies the quantum radiative properties of an emitter through the use of simple classical electromagnetic calculations. We will extensively use this connection throughout this thesis.

The total decay rate calculated above can be decomposed in several parts, such as the vacuum decay rate of the emitter, γ_0, and the rate at which the emitter decays into the optical modes of the system, g. We call g the light-matter coupling strength. One of the simplest ways to model the dynamics of a QE coupled to an electromagnetic environment is through the hamiltonian

$$\hat{H} = \int \mathrm{d}\omega\ \hbar\omega\, \hat{a}^\dagger(\omega)\hat{a}(\omega) + \hbar\omega_0 \hat{\sigma}^\dagger\hat{\sigma} + \int \mathrm{d}\omega\, \hbar \left[g(\omega)\hat{a}^\dagger(\omega)\hat{\sigma} + \text{h.c.}\right]. \tag{1.38}$$

This Hamiltonian is composed of a continuum of bosonic modes and a QE, interacting with coupling strength, $g(\omega)$. To parametrize the coupling strength, we can plug the interaction Hamiltonian above into Fermi's golden rule given in Eq. (1.32), and equate the total decay rate to the decay rate given in Eq. (1.35). This allows to direcly parametrize the light-matter coupling strength in the case of a dipolar quantum emitter interacting with an electromagnetic continuum as

$$g(\omega_0) = \frac{\omega_0}{\hbar}\sqrt{\frac{\hbar\mu_0}{\pi}\boldsymbol{\mu}\cdot \text{Im}\left\{\mathbf{G}(\boldsymbol{r}_0,\boldsymbol{r}_0,\omega_0)\right\}\cdot\boldsymbol{\mu}}, \tag{1.39}$$

which agrees with expressions obtained from more sophisticated derivations [39]. Note that in the equation above, the Green's Dyadic contains the response of the localized optical modes. In the next section we allow the system to radiatively decay and investigate the possible dynamics than can arise in this simple setup.

1.2.4 Interaction regimes

In this section we pay attention to the characterization of the different interaction strength regimes between light and matter. In today's literature, the terms weak and strong coupling are part of common terminology used to describe the associated phenomenology that arises in any given system. In particular, these terms contain useful information about the dynamics of photons and matter excitations in these light-matter coupled systems. In order to illustrate the difference between these two regimes, we will make use of a toy quantum system, from which we will be able to draw connections to previous results postulated in this chapter. Consider the system described by the so-called Jaynes-Cummings Hamiltonian:

$$\hat{H} = \hbar\omega_b \hat{a}^\dagger \hat{a} + \hbar\omega_f \hat{\sigma}^\dagger \hat{\sigma} + \hbar g \left(\hat{a}^\dagger \hat{\sigma} + \hat{a} \hat{\sigma}^\dagger \right), \tag{1.40}$$

which is composed of a single bosonic mode ($\hat{a}$), and a matter resonance ($\hat{\sigma}$), with eigenfrequencies ω_b and ω_f respectively. These interact with a coupling strength, g, which is chosen to be real. This Hamiltonian preserves the number of excitations in the system, which is a valid description of quantum systems for coupling strengths below the ultrastrong coupling regime, where coupling strength becomes comparable to the energy difference between ground and excited states[11]. Now we consider that these two modes experience spontaneous decay through their coupling to vacuum, and therefore we consider the problem of an *open quantum system*. This situation can be treated formally through the use of a master equation formalism [40], in which case, the time evolution

[11] In this thesis we will not encounter any such system, and therefore, in general this excitation-exchanging Hamiltonian will suffice for the light-mater interaction characterization.

of the density matrix of the joint light-matter system is given by:

$$\frac{d}{dt}\hat{\rho} = -\frac{i}{\hbar}\left[\hat{H}, \hat{\rho}\right] + \frac{\gamma_b}{2}\hat{\mathcal{L}}_b(\hat{\rho}) + \frac{\gamma_f}{2}\hat{\mathcal{L}}_f(\hat{\rho}), \tag{1.41}$$

where the last two terms are Lindblad super-operators, describing the Markovian[12] coupling between the bosonic and fermionic modes with the vacuum by the use of the different decay rates, γ_f and γ_b. These super-operators have expressions given by $\hat{\mathcal{L}}_f(\hat{\rho}) = 2\hat{\sigma}\hat{\rho}\hat{\sigma}^\dagger - \left\{\hat{\sigma}^\dagger\hat{\sigma}, \hat{\rho}\right\}$, and its counterpart, changing the electronic ladder operators by the bosonic annihilation operator.

For our current purposes, we note that the dynamics described by Eq. (1.41) in the case of spontaneous decay for states in the single excitation manifold are completely equivalent [41, 42] to those given by the time-evolution in the Schrödinger equation under a non-hermitian Hamiltonian equivalent to that in Eq. (1.40), with the eigenfrequencies promoted to complex quantities given by $\omega_b \to \tilde{\omega}_b = \omega_b - i\gamma_b/2$ and $\omega_f \to \tilde{\omega}_f = \omega_f - i\gamma_f/2$. The corresponding eigenfrequencies of the joint system are then given by

$$\Omega_\pm = \frac{\tilde{\omega}_f + \tilde{\omega}_b}{2} \pm \sqrt{|g|^2 + \left(\frac{\tilde{\omega}_f - \tilde{\omega}_b}{2}\right)^2}. \tag{1.42}$$

These eigen-energies, together with the corresponding eigenvectors, $|\psi_\pm\rangle$, are all that is needed to illustrate the different coupling regimes. From the eigenvectors, we are particularly interested on evaluating the degree of mixing between light and matter components in the system. To do this, we evaluate the light (or matter) component of the different eigenvectors through what are commonly known as the Hopfield coefficients, given by $C_l^{(\pm)} \equiv |\langle\psi_\pm|\hat{a}^\dagger|0,g\rangle|^2$ ($C_m^{(\pm)} \equiv |\langle\psi_\pm|\hat{\sigma}^\dagger|0,g\rangle|^2$). Fig. 1.1(a,b) contain the real and imaginary part of the eigenenergies of the above Hamiltonian as a function of coupling strength for zero detuning ($\omega_b = \omega_f$), while Fig. 1.1(c) illustrates the anticrossing behaviour of the eigenstates with light-matter detuning and fixed coupling strength.

[12] Here Markovian can be understood to mean that the interaction of the system with the vacuum does not modify the vacuum's properties.

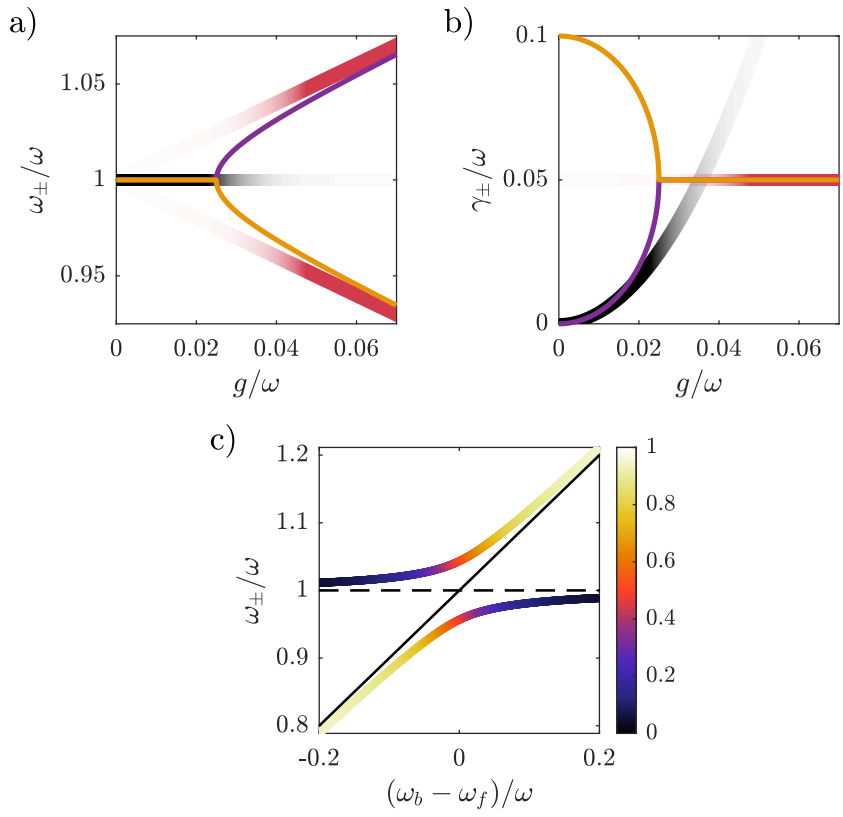

FIGURE 1.1: Eigenvalues of the non-hermitian Jaynes-Cummings Hamiltonian describing the coupling between a bosonic mode and a matter resonance, which has eigenfrequencies $\Omega_\pm = \omega_\pm - i\gamma_\pm/2$. a) Real and b) imaginary part of the two eigenfrequencies of the coupled system in the case of no detuning. In (a,b) the yellow and purple line correspond to the two eigenfrequencies, while the black and red lines indicate the prediction of the weak, and strong coupling regime respectively. c) Anti-crossing behaviour of the two eigenfrequencies when scanning the bosonic mode frequency across the matter resonance. The colour-scale indicates the light fraction of the two eigenmodes, demonstrating maximum mixing of light and matter component when the two modes are in resonance.

In colour we show the light fraction of the different eigenstates. Focusing on Fig. 1.1(a,b), at zero coupling strength, the two eigenvalues are given by the bare eigenfrequencies of the two constituents, and the light-matter mixing is exactly 0 ($C_l^{(+)} = 0$, $C_l^{(-)} = 1$). For non-zero

coupling, we can taylor-expand the eigenfrequencies and find

$$\Omega_{\pm}^{wc} = \frac{\tilde{\omega}_f + \tilde{\omega}_b}{2} \pm \left(\frac{\tilde{\omega}_f - \tilde{\omega}_b}{2} + \frac{|g|^2}{\tilde{\omega}_f - \tilde{\omega}_b} + O(|g|^4) \right), \tag{1.43}$$

which shows that the eigenfrequencies remain close to the bare frequencies of the constituents, while the coupling among them induces changes in the complex resonance frequencies. Of particular importance is the case of resonant modes ($\omega_f = \omega_b$), in which case the modified eigenenergy of the upper, matter-like transition[13] is given by

$$\Omega_{+}^{wc} = \tilde{\omega}_f - 2i\frac{|g|^2}{\gamma_b - \gamma_f}. \tag{1.44}$$

This expression encapsulates the spirit of the weak coupling regime, and contains the most relevant effect within this regime: the Purcell effect. In the weak coupling regime, matter transitions are dressed by the optical modes, and their properties are modified by this interaction. However, the degree of mixing remains low, and there is no coherent transfer of excitations between the light and matter components of the system: i.e., excitations remain mostly light or matter-like. In the particular case of the Purcell effect, the coupling leads to the modification of the decay rate of a given transition. The Purcell effect can be quantified by the Purcell factor, as done in Eq. (1.37), as the ratio of the modified decay rate Γ_f, to the bare one, γ_f, which in the present case reads

$$P_f = \frac{\Gamma_f}{\gamma_f} = 1 + 4\frac{|g|^2}{(\gamma_b - \gamma_f)\gamma_f}. \tag{1.45}$$

Note that this result is completely equivalent to that obtained through a simple rate equation in which a slowly decaying oscillator is weakly coupled to a rapidly decaying oscillator, and as such, one can understand the weak coupling regime as dominated by assisted decay (or excitation). In Fig. 1.1(a,b) one sees that the resonant frequency stays the same, while the radiative decay is enhanced (and suppressed!) quadratically.

[13] Note that at zero coupling the upper hybrid state tends to become identical to the matter resonance as $\Omega_+ \overset{g\to 0}{=} \tilde{\omega}_f$, and therefore, in the weak coupling limit, this eigenstate retains highly matter-like characteristics.

In the opposite limit, assuming that the coupling strength is much larger than the complex detuning, we Taylor-expand around zero detuning, so that the eigenenergies are

$$\Omega_{\pm}^{sc} = \frac{\tilde{\omega}_f + \tilde{\omega}_b}{2} \pm \left(|g| + \frac{\left(\frac{\tilde{\omega}_f - \tilde{\omega}_b}{2}\right)^2}{2|g|} \right). \tag{1.46}$$

In the case of resonant interaction ($\omega_f = \omega_b$), one sees that the energy difference between the eigenenergies of the system only depends on the coupling strength as: $\Omega = \Omega_+^{sc} - \Omega_-^{sc} = 2|g|$ (Fig. 1.1(a)), while the decay rate is saturated to the average value of the two constituents (see Fig. 1.1(b)). This energy difference between the interacting modes is called the Rabi-splitting, and it is the hallmark of the strong coupling regime. In this regime, the coupling strength, g, is larger than the rates of the decay mechanisms, and therefore, photons can be exchanged multiple times between the constituents of the system before decaying. This coherent photon exchange results in the formation of new eigenmodes called *polaritons* [43], composed by a high proportion of both light and matter constituents, with their properties being a mixture of both of them. This coherent exchange is reflected on the system's decay dynamics as oscillations at the characteristic Rabi frequency. In Fig. 1.1(c) we present the typical anticrossing behaviour of the eigenvalues of a strongly-coupled light matter system. One can see that as the detuning between the light and matter resonances diminishes, the eigenvalues deviate from the bare resonances (indicated by the dashed and dotted lines). In the same plot, the colour of the line indicates the proportion of light in the eigenstates, which approaches 1/2 as the detuning between the entities becomes smaller than the coupling strength, and polaritons form in the system. Note also how the two eigenmodes exchange their light and matter character after the crossing.

1.3 Plasmonics and Nanophotonics

In what follows, we provide a brief review of the field of nanophotonics, with special emphasis on the role of plasmonics in its development. The

intention is to give the reader a general understanding of the properties of all the different nanophotonic implementations that we will treat throughout this thesis; These range from localized to collective plasmonic resonances, as well as metallo-dielectric hybrid structures, which will provide the nanophotonic component of the different studies present in this thesis.

In section 1.2.2, we introduced that the material excitations with energies in the visible range are predominantly of electronic nature, and that their associated localization length-scale is of the order of the nanometer. Therefore, the relevant field for the study of these matter components is that of nano-photonics, i.e., the study of the behaviour of light at the nanoscale. When considering the interaction of these electronic transitions confined at the nanoscale with free-space radiation with wavelengths on the order of hundreds of nm, one finds that this scale mismatch causes their coupling to be very weak. As a consequence, these electronic transitions are usually weak emitters (with small decay rates). However, from our discussion in section 1.2.3, we indicated that by providing optical modes with large density of states at the emitter's location, one can greatly enhance the decay rate of these emitters.

However, it turns out that confining visible light into the nano-scale is not trivial. On the one hand, the diffraction limit establishes a bound on how much light can be focused through optical elements, which rules out the use of free-space optics as a platform for the study of light-matter interactions. On the other hand, dielectric structures below a certain size limit will not sustain optical resonances. The typical rule of thumb is that dielectric resonators must have a characteristic size of the order of light's wavelength in the medium, and therefore their size is tightly linked to the desired operation frequency. One may think of these resonant modes in dielectric structures as standing wave patterns in which there is a coherent exchange of energy between the electric and magnetic part of the fields. For resonators much smaller than the wavelength, this energy balance cannot be achieved, and therefore these particles have weak optical response.

Nonetheless, by including some other mechanism to restore this energy balance, it becomes possible to achieve optical response for deeply

sub-wavelength particles. This is exactly what makes metals special: due to the presence of the quasi-free electron gas in metals' conduction band, the coherent energy exchange can be established between the fields and the charge oscillations in the plasma. These collective charge oscillations in metals receive the name of plasmons[14], and the field that studies their properties and manipulation is consequently termed *plasmonics* [44]. Plasma oscillations can be roughly categorized into the two main groups of surface and volume plasmons. Volume plasmons appear in the bulk of metals at frequencies of the order of the plasma frequency of the material, generally on the order of several eVs [45, 46], which is higher than optical photons. On the other hand, surface plasmons appear at the interface between metals and dielectrics, being exponentially localized to the boundary. These appear at lower photon energies, generally at a fraction of the material's plasma frequency, making them specially suitable for their nanophotonic application.

Due to the presence of these charge oscillations, metallic nanoparticles (NPs) can have very strong optical responses, and allow for deeply sub-wavelength localization of optical fields. This makes plasmonic platforms tremendously attractive for the study of light-matter interactions, and therefore the development of the understanding of the behaviour of metals is tightly linked to the developments in the field of nanophotonics. In this way, abundant phenomenology has been demonstrated through the use of plasmonic structures, like radiative decay enhancement [47] and suppression [48], general tailoring of emission properties of quantum emitters [49, 50], polariton formation in strong coupling regime with single molecules [51] and with collective excitations [42, 51, 52], polariton lasing [53], modification of exciton transport properties [54, 55] and chemical reaction rates due to vacuum engineering [56], or handling of vacuum Casimir forces [57], among other fascinating phenomena.

A classical example of plasmonic response that allows to showcase some of its properties is that of a small metallic NP. In the quasi-static limit ($\lambda \gg R$), only the dipolar response of the NP is relevant, since higher order multipolar resonances are weakly excited. In this situation,

[14] Although in many cases they also receive the name of plasmon-polaritons owing to their mixed light-matter nature.

the NP's response upon plane wave excitation is uniquely determined by the dipolar polarizability, which can be written as

$$\alpha_s(\omega) = 4\pi\epsilon_0\epsilon_b R^3 \frac{\epsilon(\omega) - \epsilon_b}{\epsilon(\omega) + 2\epsilon_b}, \tag{1.47}$$

where R is the NP's radius, $\epsilon(\omega)$ its corresponding permittivity, and ϵ_b the host medium permittivity. From the above expression, one sees that whenever $\epsilon(\omega) = -2\epsilon_b$, the polarizability will behave resonantly. In the case of a Drude metal NP, the polarizability will resonate at $\omega \approx \omega_{sp} \equiv \omega_p/\sqrt{\epsilon_\infty + 2\epsilon_b}$, where we have introduced the surface plasmon frequency, ω_{sp}. We remark that this corresponds only to the dipolar surface plasmon, and that when one performs a generalized treatment, many such resonances appear, even in the case of the simple spherical NP[15]. These resonances appear as a consequence of the finite extent of the metallic domain, and therefore belong to the family of surface plasmons. This is indicated both by the resonant frequency being lower than the plasma frequency of the metal, and through the sensitivity of the resonance to the permittivity of the NP's local environment, ϵ_b, which stems from the evanescent fields spilling out into the local NP's environment. One can characterize the interaction strength of such NP with light through the scattering and absorption cross-sections, which are respectively given by

$$\sigma_{abs}(\omega) = \frac{\omega}{\epsilon_0\sqrt{\epsilon_b}c}\mathrm{Im}\left(\alpha_s(\omega)\right), \tag{1.48}$$

$$\sigma_{scatt}(\omega) = \frac{\omega^4}{6\pi\epsilon_0^2\epsilon_b^{3/2}c^4}\mathrm{Im}\left(\alpha_s(\omega)\right). \tag{1.49}$$

By taking their ratio one sees that $\sigma_{abs}/\sigma_{scatt} \propto (\lambda/R)^3$, which indicates that for smaller particles absorption will be the dominant phenomena, while for larger particles scattering will dominate. Taking again the example of the Drude metal, and assuming the good resonator limit ($\gamma \ll \omega_{sp}$), one can see that the absorption cross section normalized to

[15] Later in this thesis, we use the Dyadic Green's Function for a metallic NP in the quasi-static approximation in which these resonances beyond the dipolar response can be seen. We provide its derivation in Appendix E.4.

geometric area can be written as:

$$\frac{\sigma_{abs}(\omega_{sp})}{\pi R^2} = \frac{\omega_p^2}{\gamma}\frac{R}{c}\frac{12\epsilon_b}{(\epsilon_\infty + 2\epsilon_b)^3}, \tag{1.50}$$

which in the case of noble metals can be orders of magnitude larger than 1. For example, considering a very small, $R = 30$ nm silver sphere in vacuum, we can use the Drude parameters for silver as $\omega_p \approx 9$ eV, $\gamma \approx 20$ meV and $\epsilon_\infty \approx 1$. Then, the absorption cross section in this case would be around 300 times larger than its geometrical size. The fact that these nanometric metallic structures can have cross-sections orders of magnitude larger than their geometrical size illustrates how strongly they interact with optical fields, and also their potential to convert free propagating light into highly localized fields (or vice versa by reciprocity). From our expression of the surface plasmon frequency, we note that the resonance frequency is size independent. This shows that in the quasi-static description of small NPs only material properties determine the resonant frequency and associated lineshape of resonances. As soon as one considers larger NPs, retardation effects come into play and the optical resonances become size-dependent. In order to describe the optical response in this regime one has to employ the full electrodynamical description given by Maxwell's equations. For isolated spheres one can use the analytical Mie solution for optical scattering [58]. We will make use of an extension of this formalism in Chapter 3 to describe the interaction of light with a hyperbolic spherical system.

One of the main properties of plasmons is that since free electrons are fundamental in the resonant mechanism then electron-electron scattering and other processes are unavoidable, introducing absorption into the mix. This absorption causes plasmons to have small lifetimes (on the order of tens of femtoseconds [59]), and therefore a spectrally broad optical response. As we showed on our calculations of section 1.2.4, this is very desirable to enhance the radiative decay of not-very bright emitters, however for other applications it would be desirable to have access to longer lifetimes. This need has spurred the study of alternative setups in which these longer lifetimes are available, from which many different research lines have emerged. One option is to create metallodielectric

hybrids with the intention of combining the sub-wavelength localization of plasmons and the longer lifetimes of dielectric microcavities or photonic crystals [29, 31, 60–63]. However, one can also see that by shifting the attention from localized plasmonic resonances to the collective response of periodic arrays, the lifetimes of these collective modes can be greatly enhanced [64–66]. This idea is taken to the extreme in the case of resonances known as *bound states in the continuum*, which can be understood as symmetry-protected, collective resonances which in the ideal case have infinite lifetimes [67, 68]. Other strategies involved the addition of gain media into the system [69], which also branched into the fascinating topic of Parity-Time symmetric systems (and their photonic implementation) [70–72]. Finally, one may also embrace these losses and harness them as drivers of, for instance, the thermo-optical nonlinearity of a medium [10, 11], or more generally, as heat sources at the nanoscale. This field of study is known as *thermoplasmonics* [73–75]. A whole different route taken by the community is to abandon the use of metals and exploit the lossless nature of dielectics [76]. This line of research has been particularly driven by the study of high refractive index materials, and in particular by the family of the transition metal dichalcogenides [77, 78], which we will briefly describe in the next section.

1.4 Summary of contents

As mentioned at the beginning of this chapter, throughout this thesis we will study how light-matter interactions lead to markedly different phenomenology depending on the entities under consideration. Particularly, the three main chapters of this thesis are dedicated to the study of photon-photon interactions mediated by matter, light-matter interactions, and photon-mediated matter-matter interactions. Each of the chapters is self contained and presents the use of complimentary techniques to treat these interactions from both classical and quantum perspectives. In the same way, each chapter is preceded by a specific introductory section where we provide a contextualization of our work, which serves to outline our contributions to the field. The appendices at

the end of this thesis are reserved for lengthy mathematical derivations and other accessory explanations. In more detail, the structure of each chapter are as follows:

Chapter 2: matter-mediated photon-photon interaction

In Chapter 2 we will study matter-mediated photon-photon interactions, in the form of non-linear optical response. The content of this chapter is based on the results of a collaboration with the experimental group of Prof. Said Rodriguez, at AMOLF in the Netherlands. First, we provide a brief introduction to the key concepts of dynamical systems that are not usually encountered in the field of nanophotonics. We theoretically predict spontaneous symmetry breaking, instantaneous violation of lateral momentum conservation, and the appearance of dynamical phases in a driven-dissipative diffractive system, composed by a periodic diffraction grating embedded in a medium with a thermo-optical non-linearity. From calculations at the level of Maxwell's equations we develop two complementary approaches to tackle the problem: a numerical implementation that captures the dynamical behaviour of the system and predicts breaking of the discrete translational symmetry, and a semi-analytical approach to perform a linear stability analysis based on the Born scattering series, which predicts which momentum components lead the system to become unstable. These predictions meet experimental confirmation in the measurements performed by the group of Prof. Said Rodriguez. Thus, we demonstrate how photon-photon interactions can lead to the breaking of symmetries and conservation laws employed in linear electromagnetism to classify and predict physical behaviour. The results of this chapter have been published in Physical Review Letters [P1].

Chapter 3: excitons in nanophotonic structures

In Chapter 3 we focus on light-matter interaction itself, and exploit its properties to showcase two different sets of phenomena. On the one hand, in Section 3.2 we take advantage of the weak-coupling physics

to enhance the fluorescence of emitters embedded in hybrid metallo-dielectric structures. In particular, we consider a spherical multilayer configuration, which we semi-analytically model through the use of a scattering matrix formalism, for which we provide compact expressions for the magnitudes of interest. Taking advantage of this semi-analytical character, we employ numerical optimization to greatly enhance the performance of these cavities, yielding enhancements of the fluorescence signal of around 4 orders of magnitude for several multilayer configuration. This work was carried in collaboration with the experimental group of Vinod Menon in City University College, USA. On the other hand, in Section 3.3, in collaboration with the group of Prof. Douglas Natelson, from Rice University, USA, we showcase strong coupling phenomenology between few layers of a transition metal dichalcogenide and a plasmonic nanogap. Taking advantage of the high confinement of the plasmonic nanogap, we demonstrate the introduction of highly local driving through electroluminescence by biasing the nanocavity. This is modelled through full numerical simulations and the development of an analytical approach to complement the numerical near field simulations to reproduce the far-field emission signatures of the strongly coupled light-matter nanojunction. The results of this chapter have been published in Physical Review Applied [P2] and Nano-letters [P3] respectively.

Chapter 4: light-mediated matter matter interactions

In Chapter 4 we will study how light can mediate the interaction between matter components in a given system. In particular, we will focus on the interaction between free electrons and targets composed of both light and matter components. To describe this interaction, we first develop a model hamiltonian from the framework of mQED which serves to model the interaction between general electronic transitions and optical modes. In this picture, the interactions between different electronic transitions appear as second order processes mediated by light-matter interactions. We then parametrize this Hamiltonian for the particular cases of highly localized transitions, as in atoms or molecules, and free electrons. In

Section 4.3 we apply this model to the study of the interaction of a free electron with an isolated quantum emitter, paying special attention to how the quantum degrees of freedom of the free electron can yield measurable changes in the emitter's state and induce dynamics of special interest for quantum state preparation. We find that engineering of the free electron wavefunction leads the electron to inherit coherent properties which it generally lacks. We further exploit this coherence to develop a protocol to perform complete state determination by free electron interaction. In Section 4.4, we increase the complexity of the target by coupling the quantum emitter to an optical mode such that these enter the strong coupling regime. We find that the free electron is able of characterizing the target energy landscape, and that by appropriate preparation of the free electron wavefunction, one is able of selectively targetting specific transitions within the anharmonic polariton energy ladder with an effectively enhanced coupling strength. The results present in the mentioned sections of this chapter are respectively under review for publication [P4] and published in Nanophotonics [P5].

1

Chapter 2

Matter mediated photon-photon interaction: thermo-optical non-linearities and spontaneous symmetry breaking

2.1 Introduction

In this chapter we study how photon-photon interactions (in the form of optical non-linearities) can rapidly lead to the breaking of the symmetries that describe the optical behaviour of a given system in the linear regime, and to the appearance of dynamical behaviour. This phenomenology is of special importance since symmetries are a vital tool in the understanding and categorizing the physical properties of a system. This chapter is heavily based on [P1] and the experimental measurements we show were performed by Zhoumuyan Geng and Giel Keijsers, at the group of Said R. Rodriguez at AMOLF, Netherlands.

2.1.1 Primer on non-linear dynamical systems

We begin this chapter by giving a brief introduction to several concepts found in the realm of nonlinear systems. We will illustrate these concepts

by giving simple examples, most of them extracted[1] from Ref. [79]. The aim of these examples is to give some footing to readers that might not have previous experience in the world of non-linear dynamics, and even though the phenomenology we will later show takes place on a much more complex system, we believe having these general brushstrokes will prove helpful.

Linearization

Consider one has a one variable differential equation that we may write as $\dot{x} = f(x)$, where the dot notation indicates time derivative, and $f(x)$ can be any function. One can understand a great deal about the dynamics that this equation describes by looking at the *fixed points*, i.e., points x_f at which $f(x_f) = 0$, and therefore are stationary points. Suppose we define a new variable $x = u + x_f$, where u is assumed to be small. Then the differential equation can be Taylor expanded around x_f as

$$\dot{u} = \cancelto{0}{f(x_f)} + uf'(x_f) + O(u^2), \tag{2.1}$$

where we have used the prime notation of spatial derivative. This expression indicates that depending on the sign of the derivative, two different behaviours arise: for $f'(x_f) > 0$, any finite deviation from x_f will be exponentially amplified, while for $f'(x_f) < 0$ this difference will be attenuated. This allows to classify the fixed point either as an unstable (repulsive) or stable (attractive) fixed point. For higher dimensional systems, or with higher order time derivatives[2] the idea is pretty much the same: one now has a set of coupled differential equations, that we can write in vector notation as $\dot{\mathbf{x}} = \mathbf{f}(\mathbf{x})$, where $\mathbf{f}(\mathbf{x}) \cdot \hat{e}_i = f_i(\mathbf{x})$. Fixed points are such that make $\mathbf{f}(\mathbf{x_f}) = 0$, and again, writing $\mathbf{x} = \mathbf{x_f} + \mathbf{u}$, we can Taylor expand around these points as

$$\dot{\mathbf{u}} = \mathbf{J}(\mathbf{x_f})\mathbf{u} + O(u^2), \tag{2.2}$$

[1] We strongly recommend this textbook as an introduction to the world of non-linear dynamics, with special emphasis on low-dimensional dynamical systems.

[2] One can always write a n^{th} order differential equation as n first order coupled differential equations by defining auxiliary variables.

where we have introduced the Jacobian matrix with expression $J_{i,j} = (\partial f_i/\partial x_j)$. One can see that the types of dynamics that will arise now depend on the particular eigenvalues of the Jacobian matrix around the fixed point. This procedure is called linear stability analysis, and allows to predict and classify the different behaviours that a given system can demonstrate. Furthermore, this procedure shows that the same kind of dynamics can emerge in very different systems as long as they behave similarly around fixed points. This seemingly innocent statement leads to the powerful concept of universality, where the scaling laws of observables are the same across a wide range of systems[3].

Bistability

A bistable system is one in which two stable fixed points coexist. A very simple example of a bi-stable system is given by one that follows the differential equation $\dot{x} = rx + x^3 - x^5$, where r is a parameter. In this system (and restricting ourselves to $x \geq 0$), $x = 0$ is a stable fixed point for $r < 0$, and $x = x_t(r) = \sqrt{1/2 + \sqrt{r + 1/4}}$ is a stable fixed point for $r > -1/4$. This shows that for $r \in [-1/4, 0]$ two stable fixed points coexist. We show this in Figure 2.1(a), where we show in solid black lines the stable fixed points for every given value of r, and in dashed black lines the unstable fixed points. This plot serves to illustrate the concept of a *bifurcation*. A bifurcation is the process by which, as a parameter is varied, the number or type of fixed points available in the system changes, and therefore the qualitative dynamics present also change. The parameter value at which this bifurcation takes place is called a *bifurcation point*. For example, in the particular case presented, at $r = -1/4$ the system goes from having a single stable fixed point to possessing two of them for $r > -1/4$, therefore $r = -1/4$ is a bifurcation point (and also $r = 0$).

From Fig. 2.1(a), one may also understand how bistability can lead to hysteretic behaviour (non-reversible dynamics). The colour map in this panel indicates the value of $\dot{x}$ at each point, which we reinforce by plotting the gradient direction as a vector field. Suppose we were

[3]For a very interesting compilation of universal behaviour in chaotic systems see [80].

to perform an experiment in which we start at $r = -0.5$, and slowly increase r until $r = 0.1$ and then take it back to $r = -0.5$. Looking at Fig. 2.1(a), one sees that when initially increasing r, the system would follow the lower stable fixed point (x=0) until it became unstable at $r = 0$ and then switched to the upper, stable fixed point until reaching $r = 0.1$. On the way back, the system would remain in this upper stable fixed point until $r < -0.25$, when the system would revert to the $x = 0$ stable fixed point. We display this trajectory in Fig. 2.1(b) for clarity, where we have added arrowheads indicating the direction of the parameter scan. This example illustrates how bistability may lead the system to take different paths for $r \in [-1/4, 0]$ depending on the direction of the scan, demonstrating the non-reversible character of the dynamics.

This type of behaviour is prevalent in non-linear systems, and although not as transparent as our last example, one can also easily find this behaviour in the photon number inside a driven non-linear cavity. The equation of motion for the light field amplitude, α, inside a single mode cavity with a Kerr-nonlinearity, U, under a driving amplitude, F, is given by

$$i\dot{\alpha} = (-\Delta - i\frac{\Gamma}{2} + U|\alpha|^2)\alpha + i\sqrt{\kappa_1}F. \tag{2.3}$$

Where $\Gamma = \gamma + \kappa$ is the total loss rate, κ is the mirror loss rate, Δ is the detuning between the driving and the resonant frequency of the cavity, and F is the amplitude of the driving laser. It can be shown that the fixed points of the photon number $N = |\alpha|^2$ obtained from this equation are given by the condition

$$\mathcal{N}^3 - 2\frac{\Delta}{\Gamma}\mathcal{N}^2 + \left(\left(\frac{\Delta}{\Gamma}\right)^2 + \frac{1}{4}\right)\mathcal{N} = \mathcal{F}, \tag{2.4}$$

where for compactness we have introduced $\mathcal{N} \equiv UN/\Gamma$, and $\mathcal{F} \equiv \kappa U F^2/\Gamma^3$ as the renormalized photon-number and driving. In Fig. 2.1(c) we show how many physically meaningful solutions this equation has as a function of the renormalized driving and detuning. We observe a region with a unique stable fixed point, and a region with 3 fixed points,

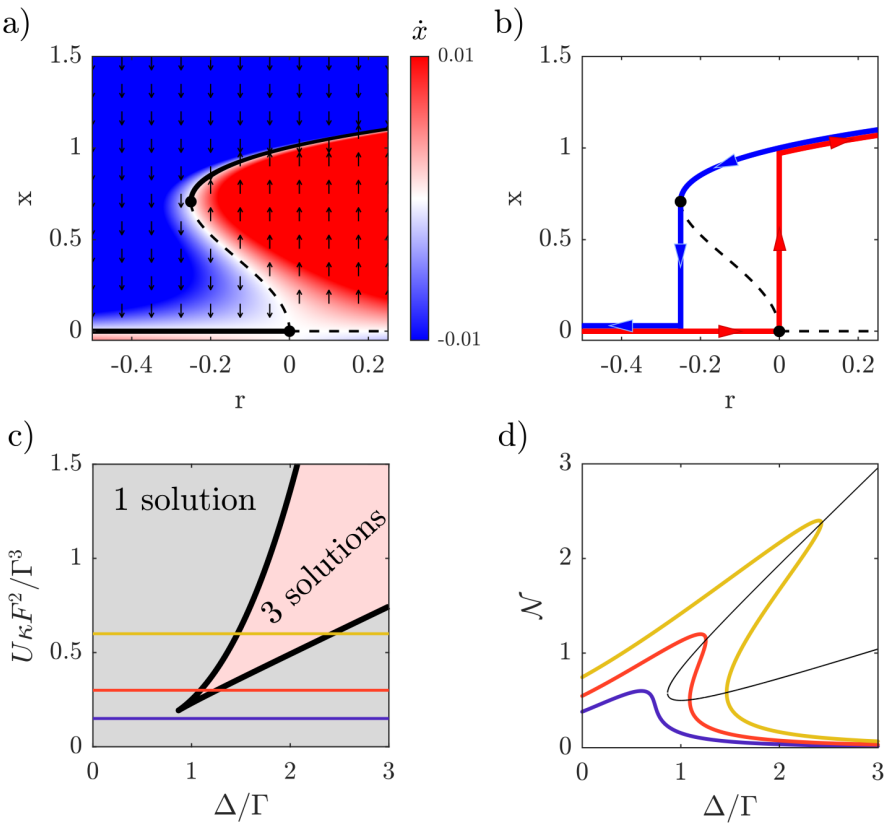

FIGURE 2.1: Figure illustrating the concepts of bifurcation and hysteresis. a) Example of a system that displays bifurcations at $r = -1/4$ and $r = 0$. Between these two points the system displays two stable fixed points while outside of this interval only one stable fixed point exists. b) Schematic representation of the hysteresis cycle that arises from continuously sweeping r in the same system depicted in (a). c) Number of steady state fixed points in a driven Kerr optical cavity as a function of cavity-laser detuning and driving amplitude. Horizontal coloured lines indicate the driving amplitude used for the different curves in panel (d). d) Normalized cavity photons as a function of detuning for the normalized amplitudes shown in (c). The thin back line indicates the condition $\partial\mathcal{F}/\partial\mathcal{N} = 0$, which the different curves intersect giving rise to the bistable region.

two stable and one unstable, just like the case in Fig. 2.1(a). The thick black line indicates the boundary between these two regions. To find this boundary, one may note that at the frontier between these two regions, the photon number goes through an inflection point and its derivative becomes infinite $\partial\mathcal{N}/\partial\mathcal{F} = \infty$. By using the inverse function

rule [81], one may equivalently cast this condition as $\partial\mathcal{F}/\partial\mathcal{N} = 0$. In Figure 2.1(d) we show the normalized photon number in the cavity as a function of detuning for different driving amplitudes, indicated by the horizontal lines of corresponding colours in Fig. 2.1(c). We also show as a thin black line the $\mathcal{N}$ values at which $\partial\mathcal{F}/\partial\mathcal{N} = 0$. Note that the photon number solutions intersect this curve at an inflection point, and therefore the black line in Figure 2.1(c) encloses the region in which more than one physically-meaningful solution exists. From our discussion of Fig. 2.1(a,b), these results show that such non-linear cavity is also expected to be bistable and display non-reciprocal dynamics.

Limit cycles

As our last item we will introduce the concept of a *limit-cycle*. Limit cycles are closed orbits in phase space to which nearby points approach either as $t \to \infty$ or $t \to -\infty$, that is, either orbits coalesce into the limit cycles or they are repelled away from them. Maybe the simplest example of such dynamics is given by the Van der Pol oscillator, which evolves in time according to

$$\ddot{x} + \mu(x^2 - 1)\dot{x} + x = 0. \tag{2.5}$$

Where we assume $\mu \geq 0$. This oscillator has its origins in the first non-linear circuits used in the earliest radios. It is usual to recast this equation in terms of a set o first order differential equations. To do so, it is enough to define $y \equiv \dot{x}$. With this substitution, the Van der Pol oscillator equation now reads

$$\dot{x} = y, \tag{2.6a}$$

$$\dot{y} = -\mu(x^2 - 1)y - x. \tag{2.6b}$$

Eqs. (2.6) illustrate that in order to completely characterize the state of the oscillator, it is enough to know x and y (or equivalently $\dot{x}$). This pair of variables then define what is known as the *phase space* of the oscillator, since every point encodes a unique state of the oscillator. With $\mu = 0$ the equations above are those of a simple harmonic oscillator,

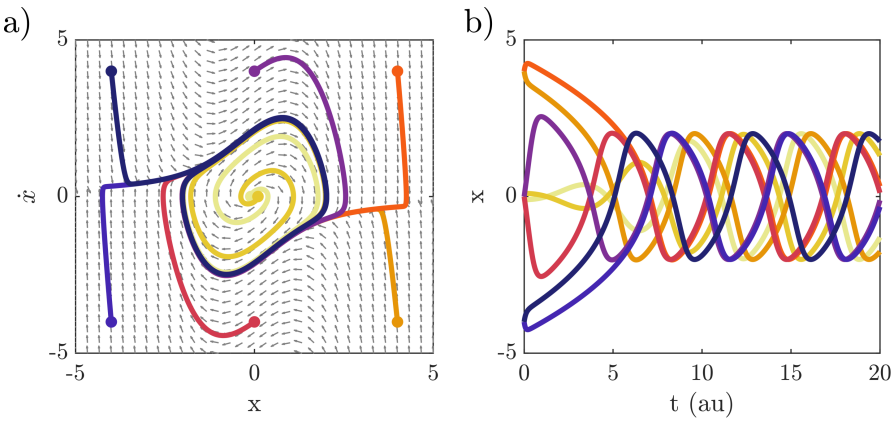

FIGURE 2.2: Limit cycles in the Van der Pol oscillator. a) Trajectories in phase space for $\mu = 0.8$ for several different starting conditions. Vector field in the background illustrates the local gradient in phase space. b) Oscillator amplitude against time for all the different trajectories shown in (a), showing that all oscillations are identical with the exception of a time offset.

with sinusoidal solutions that trace closed circular trajectories in phase space. Note that despite the dynamics being characterized by closed periodic curves in phase space, these don't affect nearby trajectories, and therefore for $\mu = 0$ no limit cycle exists. When the non-linear term is introduced the dynamics change. This contribution has the form of a damping term, with the peculiarity that only when $|x| > 1$ it behaves like an actual damping, while when $|x| < 1$ it introduces gain. Therefore one would expect that the equation above predicts that the oscillator will be kept running at some stable amplitude. In fact, it can be shown that the dynamics of this equation $\forall \mu > 0$ are characterized by a limit cycle.

In Fig. 2.2(a) we show the trajectories in the phase space for several different starting conditions, shown as circular points, for the particular value of $\mu = 0.8$. Note how all trajectories coalesce into the same periodic orbit. From our discussion about the amplifying or suppressing role of the non-linearity, we see that for starting conditions outside of the limit cycle, the damping quickly brings them into the stable oscillations, while for initial conditions near the unstable fixed point $\dot{x} = x = 0$, the oscillations are amplified and the system also reaches the same stable

oscillations in the limit cycle. We show the oscillator amplitude as a function of time in Fig. 2.2(b), where one can see that despite all the different initial conditions, the system always oscillates in the same way (albeit with a different phase offset).

In this particular system, and within the discussed parameter range ($\mu > 0$), the origin is an unstable fixed point and the limit cycle is stable (attracting from both sides). Therefore, for every initial condition different from exactly $\dot{x} = x = 0$, the system will reach the limit cycle. However, if we relax the conditions on μ, one can see that for $\mu < 0$, the origin is a *stable* fixed point. Thus, initializing the system with $\mu < 0$, the oscillator will be drawn to the origin of phase space, and as a consequence, the steady state dynamics will be characterized by a stationary state. If μ is increased beyond 0, the fixed point will become unstable and the oscillator will depart the origin, spiralling into the limit cycle as previously discussed, and therefore, its steady state will be characterized by periodic oscillatory motion. This discussion indicates that at $\mu = 0$ the system experiences a *Hopf bifurcation*, which is characterized precisely by this behaviour, i.e., by the system going from possessing a stationary steady state solution, to displaying self-sustained oscillatory behaviour.

2.1.2 Thermo-optical non-linearities

As we showed at the beginning of this thesis, the material's response to an externally applied field can be expanded as a power series (Eq. (1.8)), as $\boldsymbol{P} = \epsilon_0 \sum_n \chi^{(n)} \mathbf{E}^n$, where $\chi^{(n)}$ is the n-th order susceptibility. It can be shown that $\chi^{(2)}$ is only non-zero in non-centrosymmetric systems (i.e., without inversion symmetry) [6], while the $\chi^{(3)}$ non-linearity is not limited by this constraint. Since many material families are characterized by having inversion symmetry (gases, liquids, amorphous solids or abundant crystal families), then the most common kind of non-linear response in bulk-matter is given by the third-order non-linearity. A particular case of this is the well-known Kerr non-linearity, in which the refractive index of a material can be described as being intensity dependent as $n = n_0 + n_2 I$.

In this thesis, we focus on the thermo-optical non-linearity present in cinnamon oil which, as we outline now, can be mapped onto this kind of third order non-linear behaviour. The thermo-optical effect reflects a material's refractive index dependence on temperature as: $n = n_0 + \frac{dn}{dT}\Delta T$. In our particular case, this temperature change is due to the non-zero absorption in the oil, which dissipates power in the medium proportionally to $|\mathbf{E}|^2$ and introduces a temperature change linear to the dissipated power. By neglecting diffusion and formally solving the heat equation, one finds that the refractive index of the oil can be written as

$$n(\mathbf{r},t) = n_0 - \gamma \int_{-\infty}^{t} ds K(t-s)|\mathbf{E}(\mathbf{r},s)|^2, \tag{2.7}$$

where n_0 is the linear refractive index, γ is the nonlinearity strength, $\mathbf{E}(\mathbf{r},t)$ is the electric field, and $K(t) = e^{-t/\tau}/\tau$ is the memory kernel. This kernel has been previously used to describe the behaviour of oil-filled cavities, with good agreement between theoretical and experimental results [82, 83]. The functional form of the memory kernel stems from the thermal nature of the phenomenology, however, any process characterized by exponential relaxation dynamics can be described in a similar manner. Note that for field amplitudes that vary in a timescale much longer than τ, this non-linear behaviour is exactly the same as a Kerr-type non-linearity, therefore, τ represents the thermal relaxation time of the oil, which we refer to as the system's memory time. In this section, we deal with response times that are much larger than the optical cycle, and therefore fields change almost-instantaneously in the thermal-timescale, which will significantly simplify the theoretical treatment. All the material parameters used in this chapter are extracted from experimental measurements.

Although we have only spoken of the thermo-optical non-linearity in the context of oils, this effect is also prevalent in the context of solid state materials [84–86], in which phenomenology such as cavity resonance spectral tunability [87] or all-optical switching [88] have been demonstrated. However, oils have several advantages over these, such

as increased ease of integration in a nanophotonic system, larger damage threshold, and large thermo-optical coefficients [89]. It is important to note that since this non-linearity is of thermal origin, the associated timescales are generally considered to be intrinsically slow (tens of microseconds). In our work we actively take advantage of this, which in turn allows to extract particularly clear insights of the origin of the phenomenology that we will discuss over this chapter. Nevertheless, it has already been noted [10] that the limiting factor in the speed of these processes is the dissipation rate, which can be enhanced by orders of magnitude if these non-linear materials are integrated with plasmonic nano-structures. This strategy would allow to push the phenomenology that we present in this chapter to timescales of the order of the few picoseconds, and therefore to frequencies in the Tera-hertz regime.

Introducing this non-linear response into an optical cavity can lead to a plethora of fascinating behaviour, such as dynamical hysteresis [82], stochastic resonances [83], limit cycles and chaos [90], or neuron-like excitable response [91]. Even in situations in which memory does not play a major role, one also finds exciting results, such as light becoming superfluid [92], or enhanced sensing capabilities through noise [93, 94]. Furthermore, by studying the statistical laws that govern measurements in fluctuating systems [95], one can also exploit these laws to obtain increased measurement precision [96]. The phenomenology that arises from the interplay of the laser-driven optical cavity and the non-linear medium falls under the umbrella of the field of *driven-dissipative systems*. The breadth of this topic falls out of the scope of the present thesis, however we point out that, just like the examples of dynamical behaviour shown in Section 2.1.1, most modelling done in this topic relies on parametrizing the system in terms of few relevant variables, like photon number in the cavity, making theoretical predictions simple. In contrast, by including the diffraction grating within the non-linear cavity, the fields inside the cavity become spatially structured, which as we will show, has large implications for the dynamical behaviour of the system. This means that one has to describe the spatial dependence of the fields within the model to accurately capture the non-linear response, which makes the problem rather challenging.

2.2 Symmetries in nanophotonics and system under study

Symmetries have been one of the most fruitful and influential concepts in 20$^{\text{th}}$ century physics, and they lay at the foundations of the most successful theories of our time: from Noether's theorem that links continuous symmetries to conserved quantities [97], gauge symmetries in electromagnetism and quantum field theories or unitary symmetries in quantum mechanics. Symmetries allow to classify systems and provide predictive power over their properties without the need of performing calculations. In fact, precisely because these properties emerge from the symmetries alone, one can think about them as being "protected" by these symmetries. This is exactly the reason why the field of topological physics has exploded in popularity, starting from condensed matter physics [98, 99], and branching into many different domains. Of course, photonics is not an exception and demonstrations of topological phenomena in photonics have also been abundant and varied [100–103]. Part of the reason of the success of topological photonics is that at the time of its inception, the optics community had interests that were a fertile ground for these new ideas, particularly in the fields of metamaterials [21–23] and *photonic crystals* [104–106]. The aim of both of these disciplines is to design artificial materials with on-demand optical properties by spatially structuring them. Usually, these structures are periodic, and therefore they can be considered as the optical analogues of atomic crystals.

In this chapter, we study how the response of these periodic systems, which is deeply linked to their internal symmetries, can be modified by non-linear effects. The particular test-bed we will use for this purpose is the system schematically shown in Figure 2.3(a): a one-dimensional metallic grating coated with cinnamon oil and deposited o top of a glass substrate. The oil will be the element responsible for the introduction of non-linearities in the system, as we have shown in the previous section. The grating elements are aluminium [107] wires 90 nm wide and 70 nm tall, with a lattice constant of 366 nm. The fabrication and experimental measurements we show in this chapter were carried out

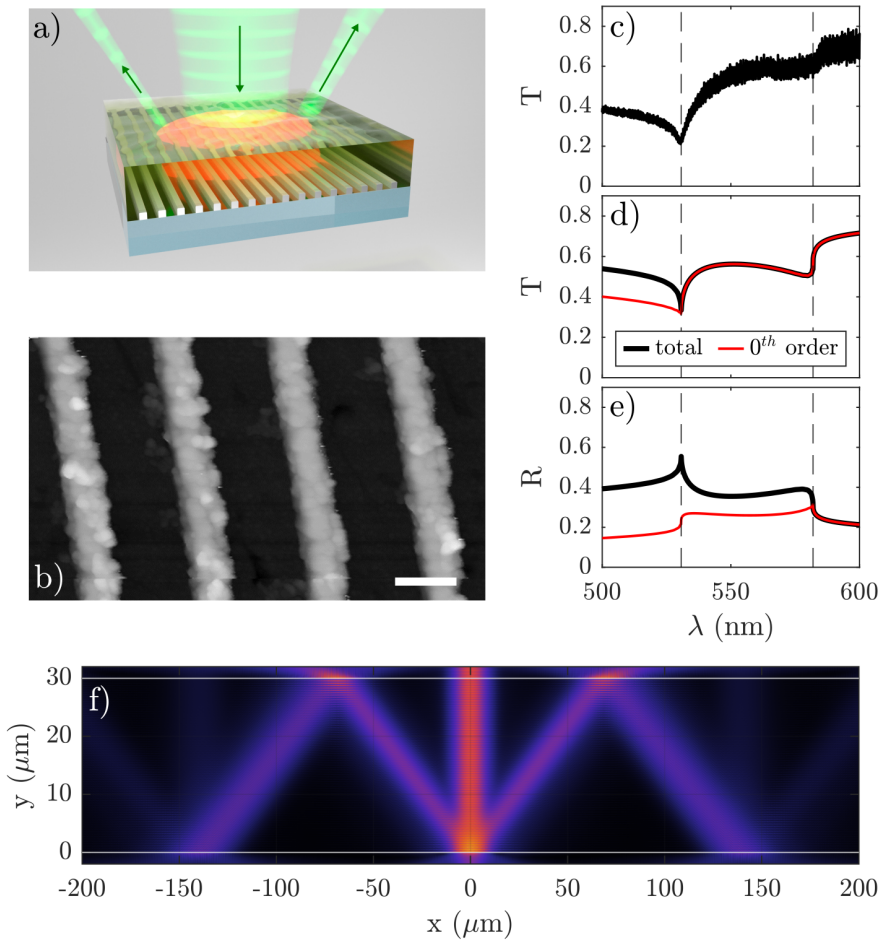

FIGURE 2.3: System in which we will explore the effect of photon-photon interaction. a) Schematic illustration of the system under study: an inversion symmetric oil coated metallic grating deposited on a glass substrate. b) SEM image of the grating. Scale bar 200 nm c) Experimentally measured transmittance of the grating d,e) Numerically calculated transmittance and reflectance spectra. Vertical lines in (c-e) represent the onset of the first diffraction order in the oil and glass. f) Electric field amplitude profile upon exciting the system with a 10 μm wide Gaussian beam. The colour scale goes from black (minimum) to yellow (maximum).

by the group of Prof. Said R. K. Rodriguez at AMOLF. We show a SEM micrograph image of the grating in Figure 2.3(b). As we stated above, much of the grating's linear response can be understood from

symmetries alone. Particularly, one may think about Bloch's theorem, by which the waves scattered by a periodic potential must share the same periodicity [108]. Essentially, Bloch's theorem relies on the conservation of the momentum parallel to the lattice vector, and it establishes that light can only exchange momentum with the grating in integer multiples of $\Delta k_{\parallel} = 2\pi/a$. Furthermore, one can use the dispersion relation of plane waves in an homogeneous medium to figure out when these momentum components become propagating. For normal incidence of the excitation, a plane wave that has exchanged N $\Delta k_{\parallel}$ momenta with the grating will be propagating if $\lambda_0 \leq na/N$, where n is the refractive index of the homogeneous medium. These propagating momentum components that appear through the interaction with the periodic structure are nothing more than the diffraction orders of the grating. The emergence of these diffraction orders can be directly observed in the transmission spectra. In Figure 2.3(c) we show the experimentally measured transmittance spectra of the grating, in which we can observe two regions of rapid derivative change around wavelengths of 530 and 580 nm respectively. These two wavelengths, marked by vertical dashed lines in the figure, correspond to the wavelength at which the first diffraction order ($N = 1$) becomes propagating in the glass ($n_g \approx 1.45$, $\lambda_0 \approx 530$ nm), and in the oil ($n_o \approx 1.59$, $\lambda_0 \approx 580$ nm). We can corroborate this through numerical simulations. In Figure 2.3(d,e) we show the numerically simulated[4] transmittance and reflectance spectra in which we have shown both the total magnitude, and the contribution of the zero order ($N = 0$) transmittance and reflectance. For the transmittance in Fig. 2.3(d), the 0^{th} order and total magnitudes only differ for $\lambda < 530$ nm, indicating that the first diffraction order only carries power below this wavelength, while for the reflectance into the oil region in Fig. 2.3(e) the two magnitudes differ for $\lambda < 580$ nm, demonstrating the onset of the first diffraction order in the oil region. We further demonstrate the presence of this diffraction order in Fig. 2.3(f), where we plot the electric field amplitude obtained from a finite size simulation in which the

[4] Throughout this thesis, we will make extensive use of the software COMSOL Multiphysics. Unless otherwise stated, most of the times we refer to numerical simulations we will be employing such tool.

grating is excited by a 10 μm Gaussian beam at $\lambda = 532$ nm. As the beam impacts on the grating, two beam replicas are formed along the first diffraction order, which later on reach the end of the oil layer and experience total internal reflection back into the oil[5]. Also, note that since the diffraction grating is inversion symmetric, the amplitudes of both of these replica beams are identical.

2.3 Spontaneous symmetry breaking

In section 2.1.1, we showed that the behaviour of a non-linear system could be understood by the classification of its fixed points, and that as the parameters of the system change, it might experience bifurcations events in which the number, or class of fixed points changes. For higher dimensional systems, these bifurcations might be accompanied by events of spontaneous symmetry breaking (SSB), in which one or several of the symmetries of the model are spontaneously broken. Studies of SSB have shaped physics for decades [109]. For instance, phenomena like the laser, Bose-Einstein condensation and the associated superfluidity and superconductivity, the Josephson effect, or the Higgs mechanism all appear when a rotational U(1) symmetry is broken [110–112]. In the context of atomic [113] and optical [114–121] systems, several examples of mirror symmetry SSB, have been reported, which lead to phenomenology such as the creation of localized states or quantum entanglement generation [122, 123]. In periodic systems, symmetry broken states are known in the context of solid state physics. For example, the charge density wave state is characterized by a redefinition of the periodicity of the atomic lattice through interactions [124]. More generally, these symmetry broken states in periodic systems governed by oscillatory physics have been theoretically analysed [125], but have found scarce demonstration in the field of optics, with the exception of a very recent demonstration in the context of lasing from periodic plasmon metasurfaces with gain [126].

[5] Later on we will show images of the system taken at the top glass-oil interface. In these images, one expects to observe bright dots corresponding to these diffraction orders.

In this chapter, we demonstrate SSB in the nanophotonic domain by the use of a thermo-optical non-linearity (presented in Sec. 2.1.2) in conjunction with the periodic system introduced in Sec. 2.2, i.e., a plasmonic diffraction grating. We emphasize that the response of this system upon normal plane wave illumination is chiefly characterized by momentum conservation. This is encoded in the two main symmetries of the system: inversion symmetry, and the discrete translational symmetry afforded by Bloch's theorem. We will tackle this problem by two complimentary approaches. First, we perform a linear stability analysis of the system. This allows to understand how the system behaves as it leaves the linear regime, and how it is expected to depart from it, while retaining some analytical insight of the problem. Secondly, we will perform full-wave simulations to capture the complete dynamics as we completely depart from the linear regime.

2.3.1 Linear stability analysis and inversion-symmetry breaking

The starting point of our discussion is about the different timescales in the present problem. On the one hand, the response time of the optical fields is of the order of the optical dissipation rate, Γ, and on the other, the response of the non-linear medium will be on the order of the memory time of the oil, τ. In our setup, these two timescales are orders of magnitude apart ($\tau/\Gamma^{-1} \sim 10^9$), which allows to assume that the optical response to a change in refractive index is basically instantaneous. This in turn means that we can obtain the response of the optical fields in frequency domain for the particular refractive index profile at a given time t, which allows to write the electric field as $\mathbf{E}(\boldsymbol{r}, \omega, t)$. It will also be convenient to cast Eq. (2.7) in differential form. By deriving $n(\boldsymbol{r}, t)$ with respect to time, and applying the Leibniz integral rule for differentiation under the integral sign, one finds that Eq. (2.7) can be equivalently written as

$$\tau\, \dot{n}(\boldsymbol{r}, t) + n(\boldsymbol{r}, t) = n_0 - \gamma |\mathbf{E}(\boldsymbol{r}, \omega, t)|^2, \tag{2.8}$$

where the dot notation is used to indicate a time derivative. In the absence of external drive ($|\mathbf{E}| = 0$) this equation predicts that the refractive index profile, $n(\boldsymbol{r}, t)$, exponentially relaxes to n_0, which shows that the homogeneous background field is a stable fixed point in absence of driving. By including non-zero driving, the system may experience a bifurcation above a certain incident field amplitude, therefore, it is important to understand the effect of the small refractive index modulations introduced by the non-linearity.

As introduced in Section 1.1, the electric field in presence of macroscopic media obeys a Helmholtz equation given by Eq. (1.12) as

$$\nabla \times \nabla \times \mathbf{E}(\boldsymbol{r}, \omega) - k_\omega^2 \epsilon(\boldsymbol{r}, \omega)\mathbf{E}(\boldsymbol{r}, \omega) = i\omega\mu_0 \boldsymbol{J}_{ext}(\boldsymbol{r}, \omega),$$
$$\mathbf{E}(\boldsymbol{r}, \omega) = i\omega\mu_0 \int_V d\boldsymbol{r}\, \overline{\overline{G}}(\boldsymbol{r} - \boldsymbol{r}', \omega) \cdot \boldsymbol{J}_{ext}(\boldsymbol{r}', \omega).$$

Where in the second line above we have solved for the electric field by use of the Green's Function formalism as given in Eq. (1.13), with $\overline{\overline{G}}$ being the Dyadic Green's Function. Throughout this whole section, we use $k_\omega = \omega/c$ to denote the light's wavevector in vacuum, and $k_0 = n_0 k_\omega$ to denote the wavevector in the homogeneous medium. In absence of external current sources, if a small refractive index perturbation, $\Delta n(\boldsymbol{r})$, is introduced in a medium of background refractive index n_0, so that the refractive index is given by $n(\boldsymbol{r}) = n_0 - \Delta n(\boldsymbol{r})$, the above Helmholtz equation may be written as

$$\nabla \times \nabla \times \mathbf{E}(\boldsymbol{r}, \omega) - k_\omega^2 \epsilon(\boldsymbol{r}, \omega)\mathbf{E}(\boldsymbol{r}, \omega) = -\frac{2k_0^2}{n_0} \Delta n(\boldsymbol{r})\mathbf{E}(\boldsymbol{r}, \omega).$$

Therefore, upon the introduction of a small refractive index perturbation, $\Delta n(\boldsymbol{r}, t)$, in a medium of refractive index n_0, then the total electric field obeys the self-consistent expression [12]:

$$\mathbf{E}\left(\boldsymbol{r}, \omega, t\right) = -\frac{2k_0^2}{n_0} \int d\, \boldsymbol{r}'\, \overline{\overline{G}}\left(\boldsymbol{r} - \boldsymbol{r}', \omega\right) \cdot \Delta n(\boldsymbol{r}', t)\mathbf{E}\left(\boldsymbol{r}', \omega, t\right). \quad (2.9)$$

Where the integral is performed over the region where the index is modified. Note that, in anticipation of the treatment that follows, we have introduced a slow time dependence on the refractive index perturbation

and electric field, t. This timescale will be of the order of the thermal relaxation time of the nonlinear medium, which as we will later show is orders of magnitude larger than the optical cycle, allowing us to safely introduce this new time dependence. For compactness, and since we only consider monochromatic illumination, we omit the frequency dependence from now on. For small enough refractive index changes, Born's approximation allows to perturbatively expand the electric field, writing it in powers of the refractive index change. Therefore, the total field reads

$$\mathbf{E}\left(\boldsymbol{r},t\right)=\sum_{n=0}^{\infty}\mathbf{E}_{n}\left(\boldsymbol{r},t\right) \tag{2.10}$$

$$\mathbf{E}_{n+1}\left(\boldsymbol{r},t\right)=-\frac{2k_{0}^{2}}{n_{0}}\int d\ \boldsymbol{r}'\ \overline{\overline{G}}\left(\boldsymbol{r}-\boldsymbol{r}'\right)\cdot\Delta n(\boldsymbol{r}',t)\mathbf{E}_{n}\left(\boldsymbol{r}',t\right). \tag{2.11}$$

We will take the first term in the series to be the linear system's solution $\mathbf{E}_{0}\left(\boldsymbol{r},\omega\right)$, and the rest correspond to corrections introduced by the non-linearity in the oil. Note that this expression will only be valid if the electric fields remains close to their linear values. Assuming that the maximum modulation will be small, we restrict this treatment to the first order correction, which allows to write the total electric field in the oil as

$$\mathbf{E}\left(\boldsymbol{r},t\right)=\mathbf{E}_{0}\left(\boldsymbol{r}\right)-\frac{2k_{0}^{2}}{n_{0}}\int d\ \boldsymbol{r}'\ \overline{\overline{G}}\left(\boldsymbol{r}-\boldsymbol{r}'\right)\cdot\Delta n(\boldsymbol{r}',t)\mathbf{E}_{0}\left(\boldsymbol{r}'\right). \tag{2.12}$$

This first expression is at the heart of the linearization procedure, since only linear terms in the refractive index perturbation are kept. Writing $n(\boldsymbol{r},t)=n_{0}-\Delta n(\boldsymbol{r},t)$, inserting our perturbative expansion of the electric field into Eq. (2.8), and neglecting quadratic terms in $\Delta n(\boldsymbol{r},t)$ one sees that the refractive index perturbation evolves according to

$$\begin{aligned}\tau\ \dot{\Delta}n(\boldsymbol{r},t)+\Delta n\left(\boldsymbol{r},t\right)&=-\gamma\left|\mathbf{E}_{0}\left(\boldsymbol{r}\right)\right|^{2}\\&\quad+2k_{\omega}^{2}\gamma\int d\boldsymbol{r}'\left[F(\boldsymbol{r},\boldsymbol{r}')+F^{*}(\boldsymbol{r},\boldsymbol{r}')\right]\Delta n(\boldsymbol{r}',t).\end{aligned} \tag{2.13}$$

Where we have introduced the quantities $F(\boldsymbol{r},\boldsymbol{r}')=n_{0}\mathbf{E}_{0}^{*}\left(\boldsymbol{r}\right)\cdot\overline{\overline{G}}\left(\boldsymbol{r}-\boldsymbol{r}'\right)\cdot\mathbf{E}_{0}\left(\boldsymbol{r}'\right)$, which capture the scattering of the linear fields with the index

perturbations that these fields create. In other words, these expressions quantify the self interaction of the linear fields due to the presence of the non-linearity and, as such, describe the matter-mediated photon-photon interaction that gives rise to the phenomenology we describe in this section. By this procedure, we have obtained a differential equation describing the evolution of the refractive index profile in which the fields only appear as their values in the linear regime, and that only depends linearly on the refractive index change. However, in its current form is not exactly transparent.

To gain some insight into the dynamics predicted by Eq. (2.13) we split the refractive index change of the semi-infinite medium into a static, $\Delta n_s(\boldsymbol{r})$, and dynamic part $\delta n(\boldsymbol{r}, t)$. Furthermore, the linear field solution in the oil can be written as a sum of plane waves as $\mathbf{E}_0(\boldsymbol{r}) = \sum_\alpha \boldsymbol{\mathcal{E}}_\alpha e^{i\boldsymbol{k}_\alpha \cdot \boldsymbol{r}}$, with the different momentum components present being

$$\boldsymbol{k}_0 = -\, k_0 \mathbf{u}_y, \tag{2.14a}$$

$$\boldsymbol{k}_1 = +\, k_0 \mathbf{u}_y, \tag{2.14b}$$

$$\boldsymbol{k}_2 = \Delta k_\parallel \mathbf{u}_x + \sqrt{k_0^2 - \Delta k_\parallel^2}\, \mathbf{u}_y, \tag{2.14c}$$

$$\boldsymbol{k}_3 = -\, \Delta k_\parallel \mathbf{u}_x + \sqrt{k_0^2 - \Delta k_\parallel^2}\, \mathbf{u}_y, \tag{2.14d}$$

which correspond respectively to the incident and 0^{th}-order reflection, together with the ± 1 diffraction order ($\Delta k_\parallel = 2\pi/a$), which are the propagating diffraction orders at the considered excitation wavelength of $\lambda_0 = 532$ nm. It can then be shown[6] that the momentum components of the time-dependent refractive index change evolves according to

$$\tau\, \dot{\delta n}\left(\boldsymbol{k}, t\right) + \delta n\left(\boldsymbol{k}, t\right) = \frac{2}{|n_0|} \frac{\gamma\, |\boldsymbol{\mathcal{E}}_0|^2}{\chi} \sum_{\alpha,\beta} \mathcal{M}_{\alpha\beta}(\boldsymbol{k}) \delta n\left(\boldsymbol{k} + \boldsymbol{k}_\alpha - \boldsymbol{k}_\beta, t\right) . \tag{2.15}$$

This expression has several interesting properties. First of all, the competition between drive and dissipation in this driven-dissipative system explicitly appears in the factor $\gamma |\boldsymbol{\mathcal{E}}_0|^2/\chi$, in which $|\boldsymbol{\mathcal{E}}_0|$ is the amplitude

[6] For the complete derivation, see Appendix A.

of the electric field incident on the grating and χ is the loss tangent of the oil (the ratio of the imaginary to real part of the oil's linear refractive index). Secondly, Eq. (2.15) is non-local in momentum space, since it couples each momentum component, $\boldsymbol{k}$, with all those that lay at the difference of two wavevectors present in the linear solution. This allows the high momentum components present in the evanescent fields of the grating to feed momentum components of propagating character. The coefficient that characterizes how strongly these momentum components couple to each other is given by

$$\mathcal{M}_{\alpha\beta}(\boldsymbol{k}) = \frac{\chi F_{\beta\alpha}\left(\boldsymbol{k}_\beta - \boldsymbol{k}\right)}{\frac{\left|\boldsymbol{k}-\boldsymbol{k}_\beta\right|^2}{k_0^2} - 1 - 2i\chi} + \frac{\chi F^*_{\alpha\beta}\left(\boldsymbol{k} + \boldsymbol{k}_\alpha\right)}{\frac{\left|\boldsymbol{k}+\boldsymbol{k}_\alpha\right|^2}{k_0^2} - 1 + 2i\chi}, \tag{2.16}$$

and the expression for $F_{\alpha\beta}$ is given by

$$F_{\alpha\beta}\left(\boldsymbol{k}\right) = \frac{\boldsymbol{\mathcal{E}}^*_\alpha}{|\boldsymbol{\mathcal{E}}_0|} \cdot \left[\mathbb{I} - \frac{\mathbf{kk}}{k_0^2}\right] \cdot \frac{\boldsymbol{\mathcal{E}}_\beta}{|\boldsymbol{\mathcal{E}}_0|}. \tag{2.17}$$

The derivation of both of these magnitudes can be found in Appendix A. Note that the coefficients in Eq. (2.16) diverge for momentum components that are found k_0 away from the momentum components present in the linear solution, and therefore these momentum components are expected to dominate the non-linear dynamics of the system. On the other hand, $F_{\alpha\beta}$ can be understood as a consequence of the vectorial nature of electromagnetic fields, since the form of Eq. (2.17) largely follows from the form of the Green's Dyadic.

To study the dynamics predicted by Eq. (2.15), instead of direct numerical integration, one can solve an equivalent eigenvalue problem. That is, one can look for the eigenfunctions $\delta\tilde{n}_\lambda(\mathbf{k}, t)$ that satisfy

$$\sum_{\alpha,\beta} \mathcal{M}_{\alpha\beta}(\boldsymbol{k})\delta\tilde{n}_\lambda(\boldsymbol{k} + \boldsymbol{k}_\alpha - \boldsymbol{k}_\beta, t) = \lambda\delta\tilde{n}_\lambda(\boldsymbol{k}, t), \tag{2.18}$$

which upon insertion in Eq. (2.15) evolve in time according to

$$\delta\tilde{n}_\lambda(\boldsymbol{k}, t) = \delta\tilde{n}_\lambda(\boldsymbol{k}, 0) \exp\left[\left(-1 + \frac{2}{|n_0|}\frac{\gamma\left|\boldsymbol{\mathcal{E}}_0\right|^2}{\chi}\lambda\right)\frac{t}{\tau}\right]. \tag{2.19}$$

Eq. (2.19) shows that the eigenvalues completely determine the dynamics of the different eigenfunctions in Eq. (2.18). For instance, for eigenvalues with a positive real part, the term in parenthesis in the exponent of Eq. (2.19) can become positive for large enough input fields, which shows that these eigenfunctions will experience exponential amplification beyond a certain critical field. This critical field is then given by $\gamma \left|\boldsymbol{\mathcal{E}}_{0,\mathrm{c}}\right|^2 = |n_0|\chi/2\mathrm{Re}\left(\lambda\right)$. Conversely, eigenvalues with negative real part will never experience exponential amplification. The eigenfunction with the largest $\mathrm{Re}(\lambda)$ will have the lowest associated critical field, and therefore it will be the dominant perturbation as the system is driven into the non-linear regime. If the eigenvalues are complex, then these eigenvalues will oscillate in time with a characteristic frequency $\omega_\lambda = 2\gamma \left|\boldsymbol{\mathcal{E}}_0\right|^2 \mathrm{Im}\left(\lambda\right) / \left|n_0\right| \chi\tau$. In this case, as the drive exceeds the non-linear threshold, the non-linear perturbation will exponentially grow while oscillating in time, in a similar fashion to the Hopf bifurcation shown in Figure 2.2 of Section 2.1.1. Note that throughout this discussion the memory time of the non-linear medium establishes an order of magnitude for the timescales of the dynamics. However, one can see that the dynamics will also be influenced by how far above the critical field the system is driven.

Solving Eq. (2.18) is a complicated task. As a first attempt and to set some intuition of the results that will follow, one might neglect all the terms in the sum in which $\alpha \neq \beta$. This is equivalent to only retaining the self-interaction of the different plane waves due to the non-linear medium. In this situation, the equation becomes local in momentum space and can be readily solved to show that the corresponding eigenvalue for each momentum component is just $\lambda(\boldsymbol{k}) = \sum_\alpha \mathcal{M}_{\alpha\alpha}(\boldsymbol{k})$. As an example, we illustrate these eigenvalues in Fig. 2.4(a,b) where the real and imaginary parts of $\sum_\alpha \mathcal{M}_{\alpha\alpha}(\boldsymbol{k})$ are respectively shown. These were obtained for the case in which a plane wave with $\lambda = 532$ nm hits our grating at normal incidence, and assuming $\chi = 10^{-3}$. At this incident wavelength, the linear solution is composed by the 4 momentum components given in Eq. (2.14). From the expression of the couplings in Eq. (2.18), each of these momentum components, $\boldsymbol{k}_\alpha$, gives rise to two circular regions of resonant $\mathcal{M}_{\alpha\alpha}(\boldsymbol{k})$ of radius k_0 centered respectively at

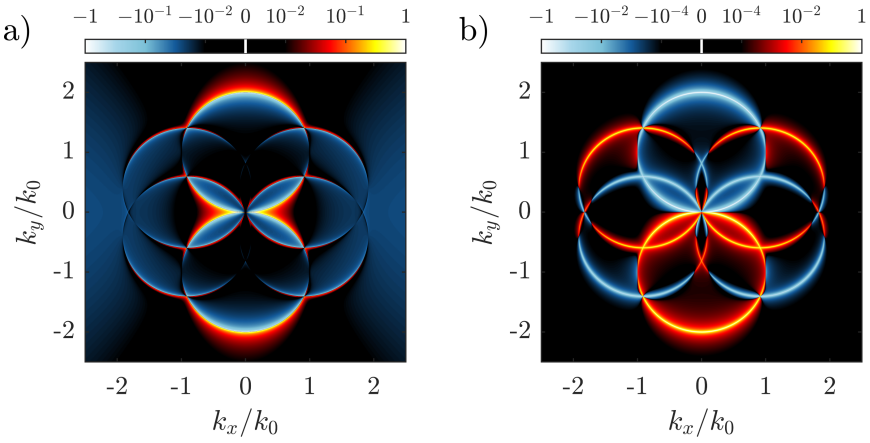

FIGURE 2.4: a) Real and b) imaginary part of the quantity $2\sum_\alpha \mathcal{M}_{\alpha\alpha}(\boldsymbol{k})$ for $\chi = 10^{-3}$ and a plane wave with $\lambda = 532$ nm impacting the grating described in Section 2.2 at normal incidence. We remark that the value of χ used for the plot is merely for illustration reasons. The experimental measurements of χ indicate a significantly lower value than used here, and therefore, much more sharply peaked distributions around $\boldsymbol{k} = k_0 \pm \boldsymbol{k}_\alpha$.

$\pm\boldsymbol{k}_\alpha$. Since the circular regions corresponding to the incident and 0^{th}-order reflection overlap[7], the quantity $\sum_\alpha \mathcal{M}_{\alpha\alpha}(\boldsymbol{k})$ will be characterized by the presence of 6 of such circular resonant regions that mark the relevant momentum components for the non-linear processes. These circular regions can be clearly identified in Fig. 2.4(a,b). The positive values of $\mathrm{Re}(\sum_\alpha \mathcal{M}_{\alpha\alpha}(\boldsymbol{k}))$ in Fig. 2.4(a) indicate that, within this approximation, some momentum components will be exponentially amplified when the system is driven beyond its critical point. Furthermore, given the non-zero imaginary part $\mathrm{Im}(\sum_\alpha \mathcal{M}_{\alpha\alpha}(\boldsymbol{k}))$ in Fig. 2.4(b), these momentum components will simultaneously oscillate while exponentially growing.

In order to tackle the complete eigenvalue problem in Eq. (2.18) we discretize momentum space, numerically determine the eigenvalues and eigenfunctions. In order to perform the discretization, two key properties of the problem can be exploited: first, since we know which momentum components will be the most relevant (those for which $\mathcal{M}_{\alpha\beta}$ diverges), we generate a discretization that is much finer around these

[7] See in Eq. (2.14) that $\boldsymbol{k}_1 = -\boldsymbol{k}_0$.

points. Secondly, since in our linear solution all wavevectors are diffraction orders of the grating, the lateral momentum for all of these is just $N2\pi/a$, and therefore, only wavevectors that differ by a whole number of reciprocal lattice vectors will be coupled in the eigenvalue problem. This allows to discretize k_x values by setting the spacing to be a fraction of the reciprocal lattice vector: $\Delta k_x = 2\pi/Na$. This is equivalent to forcing the system to be periodic over N grating periods.

In Fig. 2.5(a), we show the discretization points generated according to these principles for equivalent systems which are periodic over 1, 4, 16, and 64 grating periods. Note that the generated momentum discretization is symmetric with respect to both the k_x and k_y axes. The eigenvalue spectrum obtained for each of these discretizations is shown in Fig. 2.5(b). We can see that as the k-space sampling is made denser, the eigenvalues coalesce into the same continuous lines, indicating convergence with respect to momentum discretization, and therefore, that these results are representative of the continuum case without any imposed periodicity. As discussed before, the eigenvalues with the largest positive real part will dominate the non-linear dynamics, since these will have the lowest non-linear threshold. For each discretization, we highlight the four eigenvalues with the largest real part with a white outline. We observe that these eigenvalues also have a non-zero imaginary part, which demonstrates that the system is indeed expected to enter a dynamical phase after crossing the non-linear threshold. The final relevant information contained in this panel is that the dominant eigenvalues come in degenerate pairs[8]. In Fig. 2.5(c) we show the momentum components of the eigenfunctions associated to these degenerate eigenvalues. The two eigenfunctions are plotted in red and green respectively. Since these eigenfunctions are extremely peaked around particular momentum values, we have represented the most relevant momentum components as dots, with their respective size indicating the weight of the momentum contribution. In this panel, the dashed, large circle encloses all the momentum components that may come from propagating plane waves, while the black circles show the momenta for which $\mathcal{M}_{\alpha\beta}$ is resonant.

[8] This is the case for all imposed periodicities except when the system is forced to have the same periodicity as the grating.

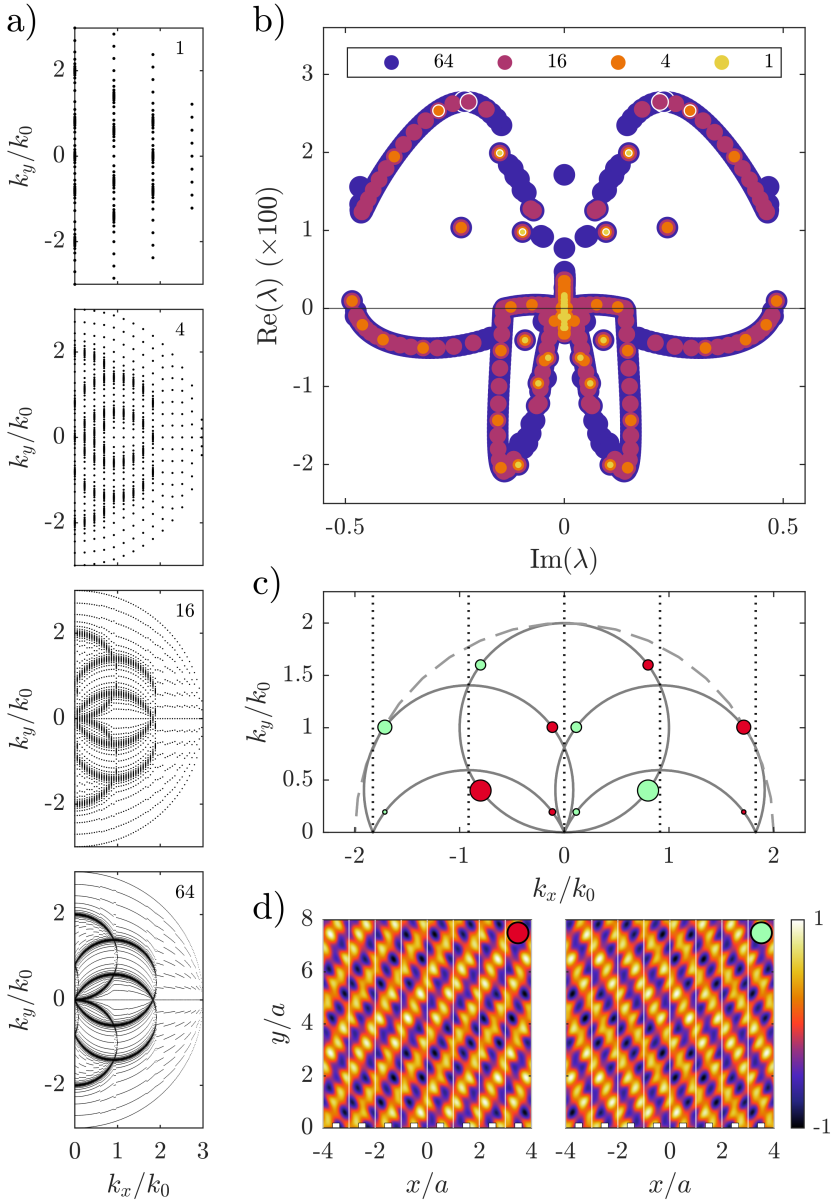

FIGURE 2.5: a) momentum discretizations used to numerically solve the eigenvalue problem. b) Corresponding eigenvalue spectrum. c) Momentum components of the two dominant eigenfunctions. d) Real space representation of the eigenfunctions.

As it was expected, the momentum components that characterize the dominating eigenfunctions all lie along these momentum values. The dotted vertical lines represent the momentum components allowed by Bloch's theorem ($k_x = N2\pi/a$), showing that the momentum components present in the dominant eigenfunctions do not comply with the grating's periodicity, leading to the breaking of Bloch's theorem and of the discrete translational symmetry of the grating. Finally, one can see that the two eigenfunctions shown in Fig. 2.5(c), and which we render in real space in Fig. 2.5(d) are specular images of each other. Since these eigenfunctions are degenerate, as the system is driven over the non-linear threshold, small fluctuations may lead any of these two (or any linear combination of them) to start exponentially growing. This allows to make the striking prediction that not only momentum components alien to the grating's periodicity will be generated, but also that the system can spontaneously break the inversion symmetry[9], showing that through the non-linearity the optical response can become loose of the constraints imposed by momentum conservation in the linear regime.

This prediction can be tested experimentally. Our colleagues from the group of Prof. Said Rodriguez at AMOLF performed experiments in which a 532 nm laser would be used to excite the oil-embedded grating. They performed sinusoidal sweeps in input power, and recorded the transmittance for the different driving conditions. The result of one of such experiments is shown in Fig. 2.6(a). One can see that the transmittance shows irreversible dynamics, that is, that for the same drive conditions two different transmittance states are available. This hysteresis may by itself be taken as an indication of bistability, however, the very rapid dynamics shown in transmittance at around 2.39 s indicates that the system is indeed transitioning between different states, signalling that a bifurcation has taken place at those driving conditions. We will also explain this bistability with the results present in the next section. After the very fast transition, the transmittance displays an exponential relaxation, shown as an inset in the panel. The half-width

[9] Again, we remark that this is the case for all imposed periodicities larger than one grating period, since the dominant eigenfunction is unique and does not have a degenerate partner.

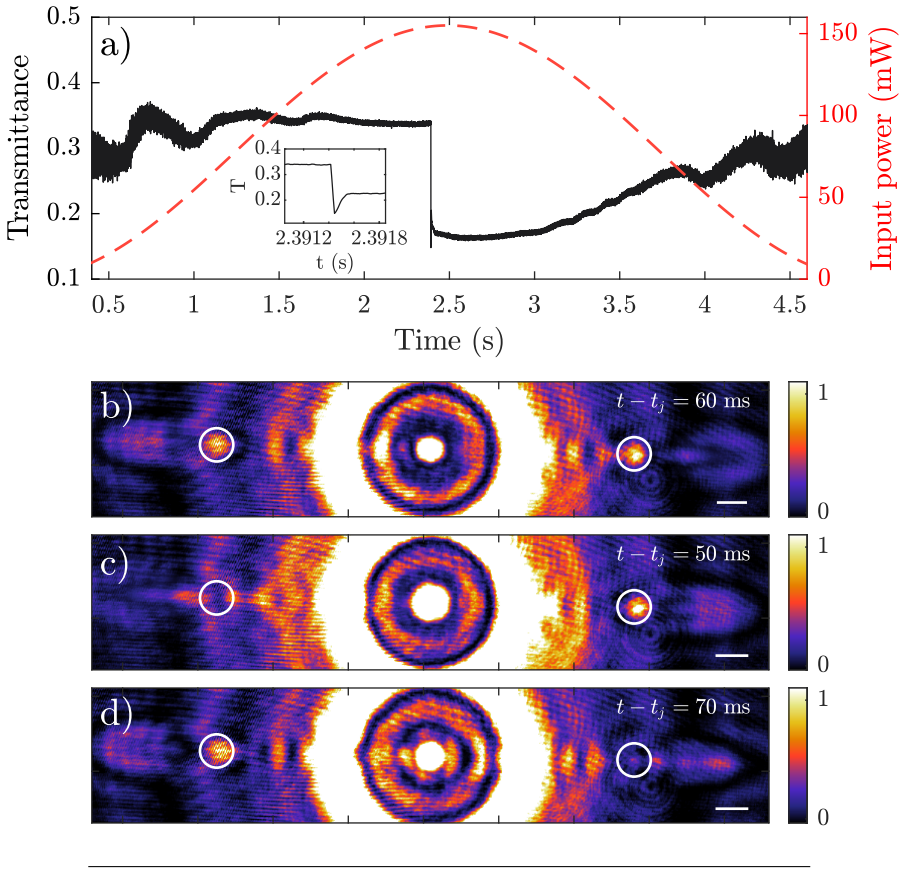

FIGURE 2.6: Experimental measurement hinting at the inversion symmetry breaking. a) Experimentally measured transmittance as a function of input power, displaying a very abrupt change in the transmittance around $t_j = 2.39145$ s. This abrupt change is accompanied by an overshoot and an exponential relaxation (inset). b-d) CCD images taken in reflection at the top oil-glass interface recorded after t_j. White circles have been included to highlight the presence of the ± 1 diffraction orders.

of this overshoot is of the order of 60 μs, which is indicative of the thermal relaxation time of the oil, τ [82, 83]. As we anticipated, this memory time is orders of magnitude larger than the timescales of the electromagnetic problem, validating our previous assumptions.

In order to investigate whether this bifurcation is accompanied by the aforementioned inversion symmetry breaking, our colleagues collected real space reflection images using a CCD camera. The excitation beam has a waist of around 10 μm, and the camera's focal plane is set at

the top oil-glass interface. Therefore, from our discussion in section 2.2 (and particularly around Fig. 2.3(f)) the reflection image is expected to be composed of three main signals: a central disk corresponding to direct specular reflection from the grating, and two beam-replicas due to the excitation of the ± 1 diffraction orders, which in the linear regime have the same amplitude. Three snapshots from the camera taken after the rapid jump at $t_j \approx 2.39$ s are shown in Fig. 2.6(b-d). We have drawn white circles to highlight the location of the diffraction orders. Notice that while in Fig. 2.6(b) the diffraction orders have symmetrical amplitude, in Fig. 2.6(c,d) these are asymmetrically populated, which indicates that indeed inversion symmetry breaks upon crossing the NL threshold in the experimental system. Interestingly, the time between these snapshots is of the order of 10 ms, which hints at the presence of rich dynamics in this system that cannot be accessed through the CCD due to the limited acquisition frame-rate.

2.3.2 Dynamical behaviour & discrete translational symmetry breaking

In order to capture the dynamical behaviour of the system, our colleagues modified the experimental setup to isolate the signal from the marked circles in Fig. 2.6 (corresponding to the ± 1 diffraction orders) and measure it with photodetectors (PD). These photodetectors have a much higher acquisition rate, which allows to resolve the fast dynamics that the system experiences after the bistability jump. In Fig. 2.7(a) we show the measurements of the signal from the PDs for the same input power modulation as in Fig. 2.6. The signals from both PDs have been offset for clarity. One can see that at the bistability jump (vertical dashed black line) the signal starts oscillating. Since the PD measurements have high temporal resolution, we can zoom in these oscillations and find that there is a wide range of dynamics present in these time traces. In Fig. 2.7(b-d) we focus on three windows representative of the different oscillatory behaviours that arise. Each of the time windows is 15 ms long. The power rise during these 15 ms is much smaller than the standard deviation in laser noise, which allows to assume that

the input power is constant over these time windows. The dynamics shown in these windows range from anti-correlated oscillations indicative of the inversion symmetry breaking (Fig. 2.7(b)), to completely chaotic in Fig. 2.7(c) or heavily correlated in Fig. 2.7(d). These self sustained oscillations are indicative of the presence of limit cycles [79], which is congruent with the SSB mechanism derived in the previous section. We argue that, as the driving conditions are slowly changed, the system goes through a cascade of bifurcations which lead to the appearance of all these different dynamics. In all of these, the continuous time translation symmetry is broken, since the system self oscillates spontaneously[10], however, depending on the driving conditions one may have that inversion symmetry may or may not be broken.

As we indicated before, the breaking of inversion symmetry implies that lateral momentum is not being conserved. However, we can show that this breaking only happens locally in time, and that momentum is still conserved when looking at the whole dynamics. To do so, we analyse the statistics of the normalized contrast of the diffraction orders $(I_- - I_+)/(I_- + I_+)$. In the analysis, we include data from right after the bi-stability jump to the end of the dynamical regime at around 4 s, and from several power scans. In Fig. 2.7(e) we show the cumulative distribution function (CDF) for both the data from the PDs (grey bars) and the CCD (Orange dots). The fact that those two distributions pass through $1/2$ at 0 contrast indicates that contrast imbalance favouring the I_+ or I_- diffraction orders are equally likely. Therefore, a time integrated measurement over long enough time would yield a signal of the same amplitude for the I_+ and I_- diffraction orders, demonstrating that although momentum conservation is violated locally in time, it still holds on average.

[10] Note that although the optical driving has a characteristic timescale, the oscillations in Fig. 2.7 happen at much lower frequencies. As discussed when deriving the analytical model in the previous section, this comes from the characteristic timescale of the light transients being orders of magnitude smaller than the oil's response time τ. This allows to assume that the fields are stationary with respect to the non-linear index timescales. In this sense, since what matters for the refractive index change is electric field intensities, these are static and the timescale of the optical frequencies disappears from the problem completely, showing that the emergent timescales of the dynamical phenomena are not due to the frequency of the optical cycle.

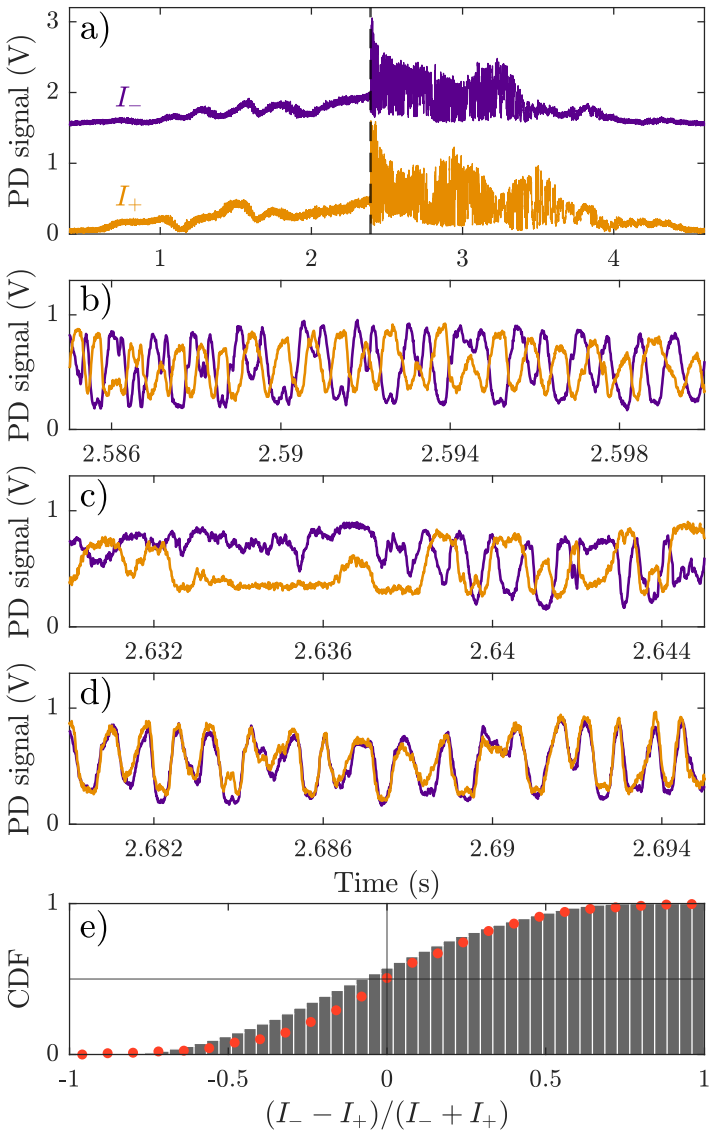

FIGURE 2.7: a) PD signal from the ±1 diffraction order ($I_\pm$) through a input power scan like in Fig. 2.6. I_- has been offset for clarity. b-d) 15 ms windows taken after the bistability jump displaying anticorrelated (b), chaotic (c) and correlated (d) oscillations. e) CDF of the diffraction order contrast for the PD (grey) and CCD (orange).

From the theoretical derivation in the previous section, we provided analytical insight into the onset of the non-linear regime and how it can

lead to the appearance spontaneous symmetry breaking. However this treatment lacks the predictive power to characterize the limit cycles that emerge and is also limited by being an inherently perturbative treatment, expected to fail for large drive intensities. Therefore, to complement the theoretical understanding we implemented a second strategy. The second approach is based on performing full-wave simulations of non-linear electromagnetic scattering under plane wave illumination. One criticism of this approach is that the experimental system does not extend infinitely due to the finite lateral extent of the excitation beam, and therefore, plane wave excitation might not be an accurate representation of what takes place in the experiments. However, we know that the beam is wide enough so that its response can be characterized by the discrete translational symmetry of the grating. This comes out in the clear presence of the diffraction orders as beam replicas in Fig. 2.3. Furthermore, in the derivation of the results in the previous section, in Appendix A, we briefly discuss that reducing the size of the nonlinear region has the effect of raising the threshold for non-linear phenomena. Therefore, we can expect that the same kind of phenomenology that appears in the experiments will also appear in our simulations, albeit at lower critical input powers.

To implement the simulations, we take advantage again of the large difference in the timescales of optical and non-linear processes, and solved the electromagnetic scattering in the frequency domain and the evolution of the refractive index in time domain. This way, the total electric field for a driving of frequency ω is written as $\mathbf{E}(\boldsymbol{r}, \omega, t)$, where $t \sim \tau \gg 2\pi/\omega$. The refractive index of the oil medium is described by Eq. (2.8). Unless otherwise stated, the simulations consists of aluminium wires deposited on top of a glass substrate, and embedded in a layer of nonlinear oil which is then capped by another layer of glass, in agreement with the experimental setup. In the lateral direction, the simulation domain is chosen to contain a certain number of grating periods, which then becomes a *supercell* of the grating. At the lateral boundaries, mirror conditions were applied so that the finite simulation domain

represents an infinitely extended, periodic structure[11]. Note that these lateral boundaries impose a general inversion symmetry over the infinite system.

We show the result of several of these simulations in Fig. 2.8. For all of these, the input power over the grating is first increased, and then kept at a certain value (in this case, 1.9 GW/m^2). The profile of the input power is shown as a dotted line in Fig. 2.8(a_1). Figures. 2.8(a_1-a_5) show the reflected power dynamics when the simulation domain is composed of 1, 2, 4, 8 and 16 grating periods respectively. This is the same as the imposed periodicity over the grating. In all of these cases, as the input power is first increased, the reflected power goes through a phase of rapid oscillations ($t < 40\tau$). These oscillations correspond to the excitation of guided modes in the oil layer. We note that these dynamics are identical for all cases and take place when the system is still behaving quasi-linearly. After this, different dynamical regimes emerge depending on the imposed periodicity. When the solution is forced to keep the periodicity of the grating, the reflected power reaches a steady state, while, when the simulation supercell contains 2, 4 or 8 grating periods (Fig. 2.8(a_2-a_4)), the reflected power shows self sustained oscillations, and finally, the largest supercell of 16 grating periods shows chaotic dynamics. Note that from our results in section 2.3.1, the non-linear thresholds of larger supercells are expected to be lower[12], and therefore, for the same input power, the larger supercells are found deeper into the non-linear regime. This is congruent with the dynamics shown in Fig. 2.8(a_1-a_5), where the smaller supercell still hasn't reached the bifurcation, and the oscillations displayed by successively larger supercells are more complex, ending in the chaotic dynamics from Fig. 2.8(a_5).

From the numerical simulations we also have access to the spatial structure of the non-linear refractive index. In Fig. 2.8(b_1-b_5) we show the refractive index change $\Delta n(\boldsymbol{r}) = n_0 - n(\boldsymbol{r})$ at the time marked by a

[11] The infinite extent only applies in the lateral direction, i.e., the axis of periodicity. This simulation domain is finite in the vertical direction and terminated with perfectly matched layers to absorb the incoming radiation.

[12] This is true until the supercell size is large enough and the critical threshold converges to a particular value. We can see this in Fig. 2.5 where the critical thresholds of a 16 and 64 period supercell are practically identical.

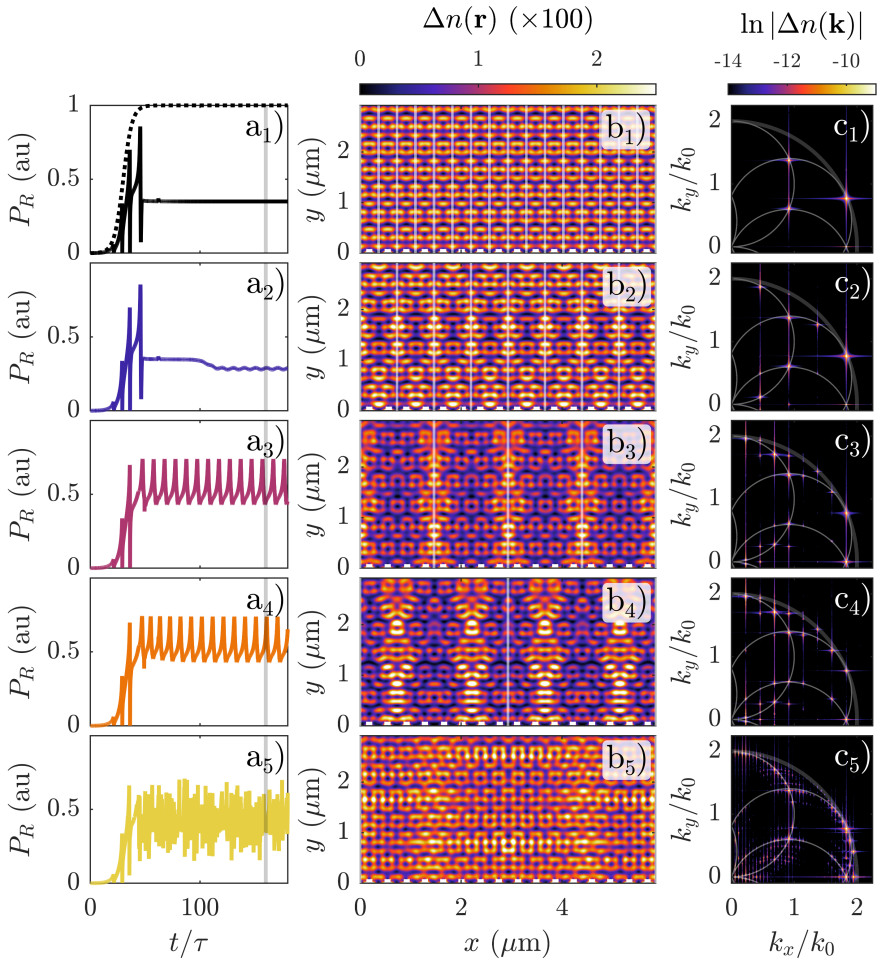

FIGURE 2.8: Subindexes are used to indicate the size of the supercell used in the simulation, where 1 to 5 corresponds to 1, 2, 4, 8, and 16 grating periods per supercell respectively. a) Reflected power as a function of time. Input power profile shown as a dotted line in panel (a_1). All panels experience the same peak input power. b) Refractive index change at $t = 160\tau$, time marked by vertical grey line in panel (a). Vertical white lines indicate the edges of the simulation domain. c) Fourier transform of the refractive index profile in (b).

vertical line in Fig. 2.8(a). The vertical white lines showcase the edges of the simulation supercell in each case, and small rectangles at the bottom of the plot indicate the grating's wires. Note that in all of these plots, the maximum change of the refractive index is of $2.5 \cdot 10^{-2}$, validating

the use of the perturbative approach in the previous section. We see that in all of these cases the refractive index profile breaks the grating's periodicity, the exception being Fig. 2.8(b_1), where the boundaries impose this periodicity. In light of these results, the bistabiliy of Fig. 2.6 can be understood as the nonlinear grating making the fast transition from the symmetric to a symmetry-broken state, with an accompanying change in reflectance values. Furthermore, this result connects the apparition of the self-sustained oscillations with the emergence of momentum components in the refractive index (and in the fields) that do not comply with Bloch's theorem. To explore deeper into this, we present in Fig. 2.8(c) the Fourier transform of the refractive index maps. In all these plots, we have included in a thin white line the momentum components that are predicted to be dominant by the treatment in section 2.3.1, and in a faint, thick white line a circle of radius $2k_0$ that engulfs all the momentum components in the refractive index that can come from propagating plane waves. Reassuringly, most of the momentum contributions of the numerically calculated refractive index maps fall along the thin lines, with larger systems presenting a higher density of momentum components and Fig. 2.8(c_5) displaying almost homogeneous momentum population along these circles, as expected from the chaotic dynamics. This result indicates that the spontaneous symmetry breaking mechanism observed here is the same as derived semi-analytically in the previous section, and that the momentum components that appear when the driving crosses the non-linear threshold are the same ones that remain when the system enters the self-sustained oscillations.

The oscillations in Fig. 2.8, and the ones displayed in the experimental measurements indicate that as the system goes through the bifurcation, it enters into a limit-cycle regime. This would then qualify the bifurcation as a Hopf bifurcation. As introduced before, limit cycles are closed orbits in phase space that attract or repel nearby trajectories. In our case, as the SSB takes place the system approaches the limit cycle. We illustrate this in Fig. 2.9. Again the numerical subindexes in these panels is used to indicate the number of grating periods in the simulation supercell, where 1 to 3 correspond to 1, 2 and 4 grating periods respectively. The panels (a_1-a_3) contain the same data as in Figure 2.8,

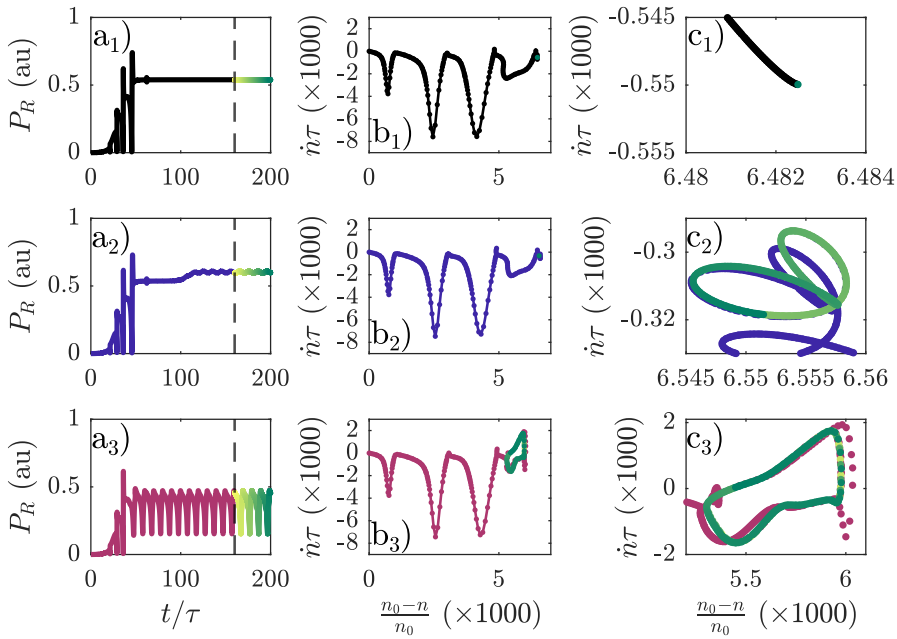

FIGURE 2.9: Subindexes are used to indicate the size of the supercell used in the simulation, where 1 to 3 corresponds to 1, 2, and 4 grating periods per supercell respectively. a) Reflected power as a function of time. Colour coding after $t = 169\tau$ used to indicate time values b) Phase space trajectory of the complete time evolution c) Zoom-in of the final part of the trajectory, evidencing the presence of limit cycles.

however, the reflected power data after $t = 160\tau$ has been colour-coded to indicate time. To represent the limit cycle, one usually displays the dynamics in phase space. This can be easily done for systems with few variables, but can be more challenging for systems in which the dynamical phenomena depends on a lot of variables. In our case, for instance, the dynamics depend on the value of the electric field at every position in space. In order to create the phase portrait, two general approaches are available: either one is somehow able of identifying the most relevant degrees of freedom, or one can follow a coarse-graining approach like it is usually done in statistical physics. Here we opt for the latter and represent the system's dynamics in terms of the average refractive index in the non-linear domain, and its average time derivative. This is shown in Fig. 2.9(b). One can see that the initial trajectory is identical

for all simulations since at the initial part of the time evolution the system behaves quasilinearly, and then the different dynamics set in. A zoom-in of the final part of these dynamics is shown in Fig. 2.9(c). While in Fig. 2.9(c_1) the system just arrives at a steady state, in both Fig. 2.9(c_2,c_3) the system dynamics settles into periodic closed orbits in phase space, illustrating the limit cycle.

2.4 Conclussions & outlook

In this chapter, we have studied the effects of non-linearities on the properties of light. Using a simple one-dimensional diffraction grating embedded in an oil with a thermo-optical nonlinearity as a basis, we have theoretically predicted inversion and discrete translational spontaneous symmetry breaking, together with the apparition of limit cycles and chaotic dynamics. Together with the group of Said Rodriguez, at AMOLF, we have found experimental verification of these predictions in the direct observation of the inversion symmetry breaking and the dynamical phases.

In this process, one realizes that most of our basic understanding of the properties of light and its behaviour in presence of macroscopic media is due to the fact that photons do not interact among themselves. As a consequence, the equations that describe the behaviour of light are linear. This linearity allows to apply powerful results like Bloch's theorem to understand light's interaction with periodic systems, or even more crucially, to study different spectral components of light independently. The fact that one can separate the different frequency components of light and perform independent studies means that in a linear-electromagnetic setup, under constant driving conditions, the system will always reach a steady state. Of course the different frequency components oscillate in time, but their corresponding amplitude will be constant, and therefore, a linear electromagnetic problem is characterized by a continuous time translation symmetry.

Throughout this chapter we have shown that the dynamical response of the driven nonlinear grating is characterized by a limit cycle behaviour, which is backed by experimental realization. The phase of the

limit cycle oscillation is chosen spontaneously, similarly to the choice of phase of a scalar field in a U(1) symmetry breaking transition [110–112]. This is why limit cycles have become very interesting as physical realizations of *time crystals*. The concept of a time crystal was proposed in the context of condensed matter physics as a state of matter in which, in spite of having a time-independent hamiltonian, the ground state of a system would be characterized by a periodic oscillatory motion [127]. Shortly after the proposal, a series of no-go theorems proved that this state of matter was not possible [128–130], and therefore the community shifted to driven systems in order to look for it. Several implementations of time crystals can be found on the literature, with these being classified as discrete [131], or continuous[13] time crystals [132–135]. In the context of photonics, discrete time crystals have been demonstrated with Kerr microresonators [136], while continuous time translation symmetry breaking has only recently been demonstrated in an optomechanical setup [137], with our diffractive system constituting the newest addition to the list.

Our particular demonstration of a continuous time crystal has further implications for the blooming field of time-varying media [138], particularly in the domain of space-time metamaterials. In this research domain, material properties are modulated in timescales similar to the optical frequency and in spatial length-scales commensurate with the wavelength of light. These ideas enabled the demonstration of phenomenology like photon pair generation [139], optical drag [140], photon localization [141] or amplification [142], together with beautiful demonstrations such as the space-time analogue of the double slit experiment [143]. In order to realize these experiments, a precise control over the spatio-temporal modulation is required, which at speeds commensurate with the speed of light becomes a non-trivial task. Therefore, the prospect of a self-modulating spatio-temporal medium, together with

[13] The distinction between continuous and discrete time crystals is similar to the breaking of a continuous or discrete symmetry. In discrete time crystals there is a periodic drive and the system breaks this discrete temporal translational symmetry by developing a subharmonic response. In continuous time crystals, the drive is constant, and the continuous time translation symmetry is broken by the system spontaneously self-oscillating at frequencies determined by internal parameters.

the ultrafast response time of epsilon near zero materials [144, 145], or plasmonically enhanced thermo-optical media [10, 146] provides a very compelling platform for the realization of such phenomena.

Chapter 3

Interaction regimes of excitons in nanophotonic structures

3.1 Introduction

In this chapter we focus on how the light-matter interaction can modify both the optical properties of nano-scale emitters and their coupling to external excitations, and pay special attention to the phenomenology that arises in the weak and strong-coupling interaction regimes. As we mentioned in the introductory chapter to this thesis, due to the scale mismatch between the electronic excitations with energies in the optical range, and of the free-space wavelength of light, the excitation of quantum emitters with far field illumination is very inefficient. To remedy this, nanophotonic structures (particularly plasmonic) are employed to allow efficient energy injection and extraction from these emitters. Furthermore, since the processes of far-field excitation and spontaneous emission are connected by Lorentz reciprocity, designing a nanostructure that enhances the rate of excitation will directly lead to an enhancement of the radiative rates of quantum emitters in such setups. This symmetry in excitation-emission is what is behind of, among other things, the advantageous dependence of the surface-enhanced Raman Scattering signal on the field enhancement of $(\mathbf{E}/\mathbf{E}_0)^4$, with $\mathbf{E}$ ($\mathbf{E}_0$) being the field at the molecule's location in presence (absence) of the nanostructure [147, 148], which leads to the possibility of performing single-molecule Raman spectroscopy [149, 150].

However, under some circumstances far field excitation may not be a particularly good option (as we will later show) and one may instead make use of local probes to pump excitations into the system. Notably, charged particles are widely used for this matter since they can be introduced in the system in several different ways and have some properties that make them very attractive. For instance, in vacuum, uniformly moving charges have an associated evanescent electric field. This vanishing character gives rise to a very short-range interaction with matter, which is routinely exploited in traditional electron-microscope based optical characterization techniques, such as cathodoluminescence (CL), or electron-energy-loss spectroscopy (EELS) [151, 152], which can provide subnanometric spatial resolutions [153, 154], surpassing by far the resolutions available for the diffraction-limited, far field illumination schemes. On the other hand, tunnelling currents can also be used to introduce photons to nanoscale environments, as demonstrated in the contexts of vertical tunnel junction in the solid state community [155], light emission from scanning tunnelling microscopes (STMs) [156], or the efforts within the nanophotonics community to realize electrically-driven optical antennas [157–159]. In this chapter, we will employ moving charges to provide the excitations to our nanoscale systems. Specifically, in Section 3.2 we study the use of positrons emitted from the β-decay of radionuclides, customarily used in positron-emission tomography (PET) [160, 161], to trigger fluorescence, while in Section 3.3 we demonstrate the potential of tunnelling currents across plasmonic nanogaps [157, 162] to probe strong coupling in highly confined systems. We will introduce each of these sources over the next sections of the chapter, but for now, it will suffice to say that these will be considered as classical currents, and therefore, their modelling can be done through Maxwell's equations. In Chapter 4 we will tackle the description of similar electronic excitations when the quantum degrees of freedom of the electrons become important. We proceed by introducing the matter excitations that will be the matter component in following studies about light-matter interaction.

3.1.1 Matter excitations

In this chapter we will make use of two different families of electronic transitions: those present in confined structures, like atoms, molecules or quantum dots, and those present in semiconductors. In both of these families exists a wide variety of systems supporting electronic eigenstates with energy gaps in the visible spectra. The choice of matter component then chiefly answers to the desired application and the nanostructure to which the matter-component is to be interfaced with. For instance, if quantum light generation is the intended purpose, then one would preferably choose an emitter with as simple as possible energy landscape and in which the principal decay mechanism would be radiative. This is so because as the complexity of an emitter increases, so do the available decay mechanisms, leading the overall quantum yield (the ratio of radiated and absorbed photons) of the emitter to diminish. If on the other hand, one wishes to maximize light-matter coupling strength, then an emitter with high transition dipole moment is preferable. Of course experimental integration also plays a vital role in the choice of quantum emitters, and each emitter choice has associated limitations.

Due to the simplicity of the energy landscape, it then seems natural to think about atoms as the appropriate choice for quantum-optical applications[1]. However their utilization requires the use of cryogenics, and atoms are difficult to implement in solid-state cavities. For these reasons, molecules and quantum dots, despite their lower quantum yield, higher decoherence rates and bandwidths, present a compelling platform for their exploitation in nanophotonic cavities, since they can be individually isolated and manipulated and allow room-temperature operation. In the first part of this chapter, we will demonstrate a setup in which one would use one of such molecules: a nanometric cavity whose intended operation happens at room temperature. Note that while these molecules have been used to demonstrate strong light-matter coupling [51], we will focus on the modification of their radiative properties [49], and as such we will be operating in the weak coupling regime.

[1] And indeed, they have been extensively used in the microwave (Rubidium [163]) and optical regime (Cesium [164]) since the early days of cQED to demonstrate quantum-optical phenomena in mirror-mirror cavities.

On the other hand, semiconductor materials also host electronic excitations that can be used for the study of light matter interactions. Among these, *excitons* are of particular interest to us. Excitons are electron-hole pairs bound by coulomb interaction [43, 165], which appear as very sharp resonances in absorption and photoluminescence measurements, with exciton lifetimes that can be found in the order of a few picoseconds [166, 167]. In bulk semiconductors, excitons have binding energies of the order of the few hundred meVs, which already hints at the possibility of exploiting these excitonic resonances as light sources for light matter interaction at room temperature. It is important to note that in general[2], higher exciton binding energy is also accompanied by larger excitonic transition dipole moments. Thus finding materials which present excitons with increased binding energies is desirable not only to operate at room temperature, but also to reach ever stronger regimes of light-matter interaction. Since charge screening is weaker in lower dimensional systems, higher exciton binding energies appear in 2D semiconductors like the family of transition metal dichalcogenides (TMDs) [77, 168]. Materials in this family are ideal for coupling to optical resonators since they interact strongly with light through sharp excitonic modes, and have been previously used to demonstrate strong-coupling phenomenology [169–171]. Furthermore, these excitons have high binding energies of a few hundred meV, making them stable even at room temperature [172], particularly in the monolayer limit [166, 173–175]. Moreover, in these materials, 2D monolayers only interact weakly among each other, and mainly by Van der Waal's forces, which allows them to retain the large excitonic binding energies and bright transition dipole moments of the isolated monolayers even when multiple layers are stacked[3]. Of course this anisotropy in the electronic structure leads to an anisotropic optical response as we will later show. In the second part of this chapter we will show how strong light-matter coupling can be reached between few layers of a TMD, and a nanophotonic nanostructure with deeply subwavelength optical confinement.

[2] At least for typical direct parabolic valence and conduction bands.

[3] An extreme case of this is CrSBr, which besides behaving as a Van Der Waal's 2D material, due to extreme in-plane anisotropy, it effectively behaves as a 1D material [176], displaying very bright excitons, even in the bulk limit.

3.2 Fluorescence triggered by β-decay

As anticipated, in this section we will study how the fast charged particles generated in β-decay can be used to trigger fluorescence, and how one can use nanophotonic techniques to greatly enhance this signal. The results on this section are based on [P2] and they were carried out in collaboration with the group of Prof. Vinod Menon at City University College, New York. Note that although free electrons are routinely employed in the context of nanophotonics [151, 152, 154, 171, 177], the use of radionuclides to generate them has not been explored so far within the community. However, in the field of medical diagnosis these radiotracers are customarily used in PET scanners, and therefore the present work intends to extend and enhance the diagnosis and imaging capabilities of already existing techniques. In what follows, we introduce previous efforts in the medical field to exploit the light generated by moving charges to motivate the setup under study.

Previously, we introduced that free charges moving at constant speed, due to the evanescent nature of their electric field in vacuum, can only exchange energy when they come across some optical modes in their close vicinity. However, it is also possible for moving charges to radiate in an homogeneous medium if their speed is larger than the phase speed of light in such medium, i.e., if they are superluminal. This phenomenon is known as Cherenkov radiation (CR) [178], and although it was discovered in the context of radioactive solutions in water, it has also been found to happen from the radionuclides (such as ^{18}F or ^{124}I) used in PET imaging [160, 161]. Therefore, the prospect of exploiting these complementary light emission mechanisms led to the development of 2-channel imaging techniques [179, 180] by imaging the γ-rays (in the $\sim$ 100 keV range) generated by electron-positron annihilation (as in the traditional PET scans), and the CR that β-particles create as they travel through tissue. Combining these two channels would lead to shorter acquisition times and higher spatial resolution [181], while also allowing to use ideas from nanotechnology to modulate the CR [182, 183]. For instance, in Fig. 3.1 we show some preliminary experimental results from the group of Prof. Vinod Menon, where they demonstrate

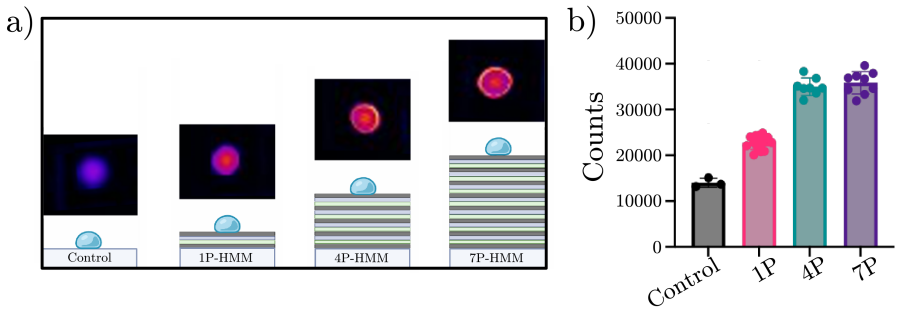

FIGURE 3.1: Experimental proof-of-principle of the enhancement of CR signal through a hyperbolic metamaterial. a) Yttrium-90 nanoparticles deposited on top of a hyperbolic medium composed of stacks of aluminium oxide, silver, and germanium. b) CR signal recorded with a filter at 620 nm, demonstrating the signal enhancement.

enhanced CR signal stemming from nanoparticles made of Yttrium-90 isotope deposited on top of a planar hyperbolic medium.

Nonetheless, imaging through with CR has two main shortcomings that make this strategy non-viable: first, β-particles only meet the superluminality condition for a few mm away from the radioisotopes. Secondly, the CR spectra[4] in an homogeneous, non-dispersive medium yields a power spectra $P(\omega) \propto \omega$, which is peaked at the ultraviolet, outside the transparency window of biological tissue found in the near infrared [186], leading most of the emitted CR to be absorbed. These two factors lead the CR signal to be orders of magnitude smaller than ambient light [187]. This low brightness is the main hurdle to overcome in order to make CR-based imaging techniques viable.

One of the most promising avenues to overcome the limitations of CR is to combine the radiotracers with fluorescent agents, which present promising properties for their use in room temperature applications. This scheme is known as Secondary Cerenkov-induced Fluorescence Imaging (SCIFI) [188, 189], and it usually utilizes quantum dots or molecules with large Stokes Shift attached to the radiotracers. These molecules get excited by the CR emitted in the β-decay of the radionuclides and are

[4] Described by the Frank-Tamm formula [184, 185].

chosen so that their emission is in the visible or infrared, within the biological transparency window [187]. Furthermore, this scheme allows to minimize the impact of the two main constraints of fluorescence imaging: the limited penetration depth and the tissue autofluorescence under external illumination [181, 182]. Moreover, recent developments in nanophotonics have led to an unprecedented degree of control over the spectral [190] and spatial [191] characteristics of CR. With demonstrations in the theoretical and experimental domains using metamaterial [183, 192–194] and plasmonic [195–197] ideas. However, the proposed structures are unsuitable for their medical use due to their extended character.

In this section, we apply plasmonic metamaterial ideas to SCIFI and design spherical hyperbolic nanocavities [198] to enhance the fluorescence triggered by the travelling β-particles. The structures under study are depicted in Fig. 3.2(a), where a dielectric core, in which a fluorescent emitter is embedded, is surrounded by alternating, nm-thick, metal-dielectric layers. This configuration is the spherical equivalent of indefinite bulk metamaterials [190, 199]. Radiotracers are attached to the surface of the nanocavity, which after experimenting decay will trigger fluorescence.

3.2.1 Theoretical Approach

In order to evaluate the performance of the hyperbolic cavities, we first introduce the fluorescence enhancement factor, f_E. In steady state conditions, it is defined as the fluorescence count rate per emitter normalized to some reference configuration [200]. In the weak excitation limit (below fluorophore saturation) it can be written as

$$f_E = \left(\frac{|\mathbf{E}|}{|\mathbf{E}_0|}\right)^2 \times \frac{\phi}{\phi_0}. \tag{3.1}$$

In this expression, the processes of excitation and emission are factored in independently. The first term captures the enhancement in the excitation rate of the fluorophore (assuming random orientation), i.e., how many more photons make it to the fluorophore when it is in the cavity, $|\mathbf{E}|^2$, as compared to the reference configuration, $|\mathbf{E}_0|^2$. In the present

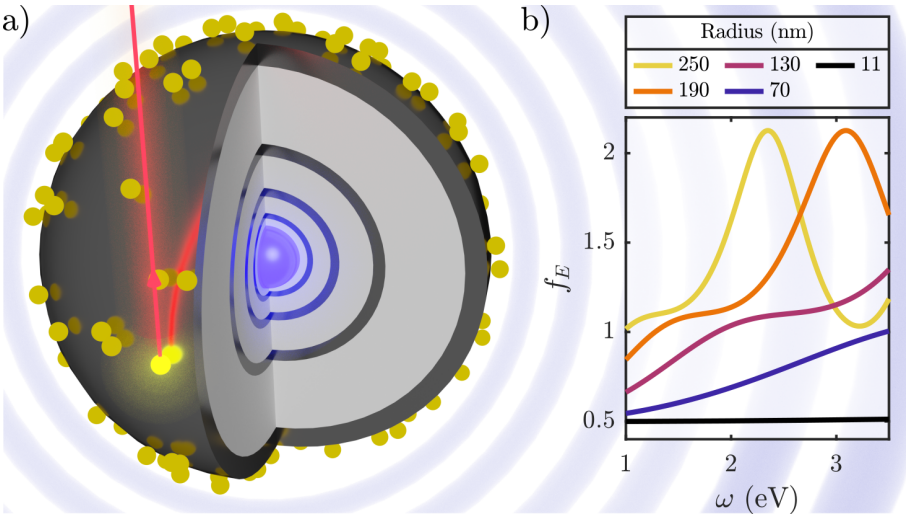

FIGURE 3.2: a) Render of the hyperbolic nanocavities under study. The cavities are composed by a silica core, surrounded by silver (black) and silica (grey) layers. Radioisotopes attached to the surface (yellow) emit positrons (red) by β-decay that then trigger the fluorescence (violet) of an emitter placed at its center. b) Fluorescence enhancement spectra for bare SiO_2 spheres of various sizes normalized to free space. These will serve as the benchmark against what we will compare the performance of our nanocavities.

case, the source that triggers fluorescence are β particles generated from radioactive decay, and we take lossless dielectric spheres of the same total size of the cavity as reference. In particular these will be made of silica, which is widely used in medical imaging research [180]. The second term in Eq. (3.1), on the other hand, represents the change in the fluorescence quantum yield of the composite system, ϕ, as compared to the reference, ϕ_0. We assume that the fluorophores have a perfect intrinsic quantum yield ($\phi_0 = 1$), thus, $\phi/\phi_0 = \phi < 1$. Therefore, this term captures the quantum yield loss due to the introduction of absorption in the system. The problem can be simplified by neglecting the Stokes shift of the molecule, which allows to evaluate the excitation enhancement and quantum yield loss at the same frequency[5]. It is worth noting that although simple, Eq. (3.1) has allowed to accurately describe

[5]Despite this, note that the formalism that follows would be perfectly applicable for the case in which the Stokes shift is accounted for.

the modification of the radiative properties of fluorescent agents [49] in the presence of various plasmonic nanostructures [201, 202].

The nanocavities (shown schematically in Fig. 3.2(a)) for which we solve Maxwell's equations in order to obtain the f_E in Eq. (3.1) are composed by a spherical core of radius $R_{\text{in}} = 11$ nm made from silica ($n = 1.5$) that is covered by alternating spherical shells made from silver (modelled through the refractive index given in Ref. [203]) and silica. The fluorescent molecule will be modelled as a point dipole and will be placed in the centre of the cavity. The radiotracers are attached to the outside of the nanocavity, with radius R_{tot} and the β-decay and subsequent CR generation is modelled by a current line, equivalent to the current generated by a single positron [204, 205], that runs parallel to the nanostructure's surface at a distance of 3 nm, corresponding to the size of the radionuclide. The positron's energy is assumed to be of 50 keV, which guarantees that no CR emission would take place in an homogeneous aqueous medium.

Since the cavity has spherical symmetry, one can expand the fields in terms of vector spherical harmonics [185], and then apply a transfer-matrix [206, 207] formalism to (semi)analytically evaluate the f_E. In what follows, we outline the derivation, but more details can be found in the Appendix B. First, by the use of the vector spherical harmonics, the electric field in the n^{th} layer of the cavity can be written as

$$\mathbf{E}_{\alpha,n}(\mathbf{r}) = \sum_{l,m} \left[A_{\alpha,l,m}(n)\mathbf{J}_{\alpha,l,m}(k_n, \mathbf{r}) + B_{\alpha,l,m}(n)\mathbf{H}_{\alpha,l,m}(k_n, \mathbf{r}) \right]. \quad (3.2)$$

Where α labels the polarization of the mode (TE or TM), l and m are the usual angular momentum indices in the spherical harmonics, and $\mathbf{J}_{\alpha,l,m}$ and $\mathbf{H}_{\alpha,l,m}$ are the spherical vector harmonics, whose radial dependence is given by spherical Bessel and Hankel functions of the first kind respectively. Next, one needs to construct the transfer matrices that satisfy the electromagnetic continuity conditions between two media, and thus relate the amplitudes of the electric field in two consecutive

layers:

$$\begin{pmatrix} A_{\alpha,l,m}(n+1) \\ B_{\alpha,l,m}(n+1)) \end{pmatrix} = T^{+}_{\alpha,l}(n) \begin{pmatrix} A_{\alpha,l,m}(n) \\ B_{\alpha,l,m}(n)) \end{pmatrix}. \tag{3.3}$$

For a nanocavity of N metallo-dielectric layers, the fields at the centre (n=0) and outside of the cavity ($n = N+1$), are then connected by the ordered product of these matrices. We define this ordered product as

$$\mathcal{M}_{\alpha,l} = T^{+}_{\alpha,l}(N)T^{+}_{\alpha,l}(N-1)\ldots T^{+}_{\alpha,l}(1)T^{+}_{\alpha,l}(0). \tag{3.4}$$

Once this matrix is known, the expressions for the field enhancement, and the total (T) and radiative (R) Purcell factors of the fluorophore in the nanostructure are given by

$$\mathbf{E} = \frac{\mathbf{E}^{\text{in}}}{\langle \mathcal{M}_{E1} \rangle_{11}}, \tag{3.5}$$

$$\mathcal{P}_T = n_{\text{core}}\,\text{Re}\left[1 - \frac{\langle \mathcal{M}_{E1} \rangle_{12}}{\langle \mathcal{M}_{E1} \rangle_{11}}\right], \tag{3.6}$$

$$\mathcal{P}_R = n^2_{\text{core}} \left| \frac{\det(\mathcal{M}_{E1})}{\langle \mathcal{M}_{E1} \rangle_{11}} \right|^2. \tag{3.7}$$

In these expressions, $\mathbf{E}^{\text{in}}$ is the field incident on the system evaluated at the fluorophore's location, n_{core} is the refractive index of the central region of the nanocavity, and the $\langle \mathcal{M} \rangle_{ij}$ notation is used to denote the i-th column and j-th row of the matrix. These expressions attain this simple form since only the TE modes with $l = 1$ have non-zero value at the centre of the sphere (See Appendix B). In order to evaluate f_E, one needs to evaluate the field enhancement normalized to the reference case (a SiO_2 nanoparticle of equivalent size), which from Eq. (3.5) gives $|\mathbf{E}/\mathbf{E}_0| = \langle \mathcal{M}^0_{E1} \rangle_{11} / \langle \mathcal{M}_{E1} \rangle_{11}$, where the zero superscript is used to indicate the reference quantity. To evaluate the quantum yield, one just has $\phi = \mathcal{P}_R/\mathcal{P}_T$ obtained from above. In Fig. 3.2(b) we show the fluorescence enhancement factor (normalized to vacuum) for the reference silica nanoparticles, demonstrating small fluorescence attenuation

($0.5 \leq f_E \leq 1$) for subwavelength nanoparticles, and a moderate enhancement ($f_E \approx 2$) for larger radii due to the presence of Mie resonances [208]. The small deviations from the free-standing configuration make these lossless particles a good reference to compare our cavities against.

3.2.2 Periodic Nanocavities

Once the framework has been introduced, we begin by investigating the simplest configuration in which all metallo-dielectric layers have the same width, d. This gives a characteristic spatial period to the structure of $2d = R_{n+2} - R_n$. These cavities have been explored in the context of low-threshold lasing [209] and second harmonic generation [210]. If the periodicity is much smaller than the free-space wavelength of light, one can use a metamaterial description [198]. The corresponding expressions for the permittivity tensor, borrowed from the bulk planar counterpart [199, 211, 212], are given by

$$\epsilon_r = \frac{\epsilon_{\mathrm{Ag}}\epsilon_{\mathrm{SiO_2}}}{(1-\eta)\epsilon_{\mathrm{Ag}} + \eta\epsilon_{\mathrm{SiO_2}}}, \tag{3.8a}$$

$$\epsilon_t = \eta\epsilon_{\mathrm{Ag}} + (1-\eta)\epsilon_{\mathrm{SiO_2}}, \tag{3.8b}$$

for the radial and tangential components respectively, with η being the filling fraction. At $\eta = 0.5$, one has that $\mathrm{Re}(\epsilon_t\epsilon_r) = \mathrm{Re}(\epsilon_{\mathrm{Ag}})\epsilon_{\mathrm{SiO_2}}$, which is negative if $\omega < 3.8$ eV (the silver plasma frequency [203]), demonstrating the hyperbolic character of these cavities[6].

Fig. 3.3 contains a comprehensive study of the properties of the hyperbolic cavities with $\eta = 0.5$ and different geometrical sizes. This is parametrized by the total radius: $R_{\mathrm{tot}} = R_{\mathrm{in}} + Nd$, where $R_{\mathrm{in}} = 11$ nm is the silica core radius and N the number of layers forming the shell. Columns indicate N from 1 (left) to 7 (right), while each row contains a different magnitude (top to bottom): field enhancement, $|\mathbf{E}/\mathbf{E}_0|$, radiative Purcell, $\mathcal{P}_R$, quantum yield, ϕ, and fluorescence enhancement, f_E. We observe that the core-shell nanoparticle's [213] ($N = 1$) behaviour is

[6] In Appendix C, we show that this assertion also holds for a more sophisticated homogeneization scheme, derived specifically for spherical multilayers.

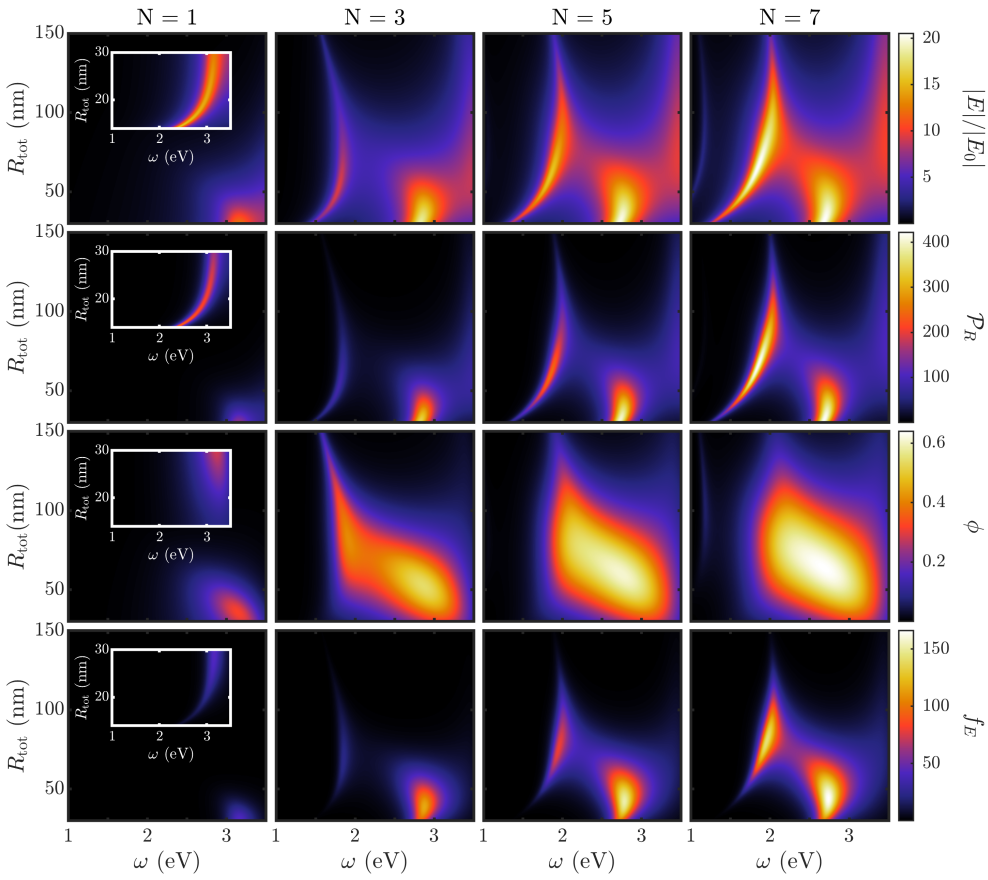

FIGURE 3.3: Spectral characteristics of hyperbolic spherical cavities. Different figures of merit for the hyperbolic cavities are shown as a function of frequency, ω, and total cavity size, R_{tot}. Rows from top to bottom represent the different magnitudes: field enhancement, radiative Purcell, quantum yield and fluorescence enhancement, while the columns (from left to right) correspond to a different number of metallodielectric layers of the cavity: core-shell ($N = 1$) and hyperbolic cavities with $N = 3$, 5 and 7.

markedly different from the rest of the cases, with its optical response being the weakest. Only for $R_{\text{tot}} < 30$ nm (see insets in the left column), the silver thickness becomes comparable to the skin depth and localized plasmons modes appear above 3 eV. For ever-smaller cavities, these localized plasmons red-shift due to hybridization effects [214]. Regardless, due to the strong optical absorption in this spectral range, the quantum

yield is strongly reduced, leading to weak fluorescence enhancements ($f_E < 50$).

On the other hand, the panels in the three right columns of Fig. 3.3 show that the hyperbolic cavities behave markedly different than the core-shell case. Remarkably, these panels reveal that the behaviour is very similar for all N, indicating that these are indeed behaving as metamaterial-cavities. The optical response of these hyperbolic cavities is dominated by two maxima in the field enhancement and radiative Purcell, which become stronger for larger N. The high frequency resonance ($\omega \approx 2.7$ eV) vanishes for $R_{\text{tot}} > 50$ nm, while the lower frequency mode ($\omega \approx 1.8$ eV) remains relevant for much larger structures. As we will show later, this different dependence with the cavity size of the two modes stems from their different natures. Due to the reduced impact of optical absorption, the quantum yield maps develop a broad maximum between the two optical resonances, reaching quantum yields superior to 60%. These magnitudes combine to produce a fluorescence enhancement that is dominated by the higher-frequency mode for $R_{\text{tot}} \leq 50$ nm, and by the lower frequency mode for $50\,\text{nm} \leq R_{\text{tot}} \leq 120\,\text{nm}$, while for larger cavity size, optical losses lead to a much smaller f_E.

To gain further insight into the nature of these modes, numerical simulations are performed with COMSOL. In Fig 3.4(a,b), we show the numerical electric field intensities for the case of $R_{\text{tot}} = 60\,\text{nm}$ and $N = 7$ for $\omega = 1.8$ eV and $\omega = 2.7$ eV. The spatial structure of the resonances gives information about their nature: fields in the lower frequency resonance ($\omega = 1.8$ eV) are strongly localised in the first (and second) silica layers indicating that this is a whispering-gallery mode, while the fields in the higher frequency resonance are evanescent away from the innermost metallic layer, indicating that it is a localized surface plasmon [214]. Furthermore, this interpretation is validated by the dependence of the modes on the total cavity size in Fig. 3.3. This numerical tool also allows to validate the semi-analytical calculations. In Fig 3.4(c), we compare the analytically calculated f_E (black line) and the numerically obtained counterpart (purple circles), demonstrating excellent agreement. For both of these results, it was assumed that the fluorophore was located exactly at the centre of the cavity, however, one can test the robustness

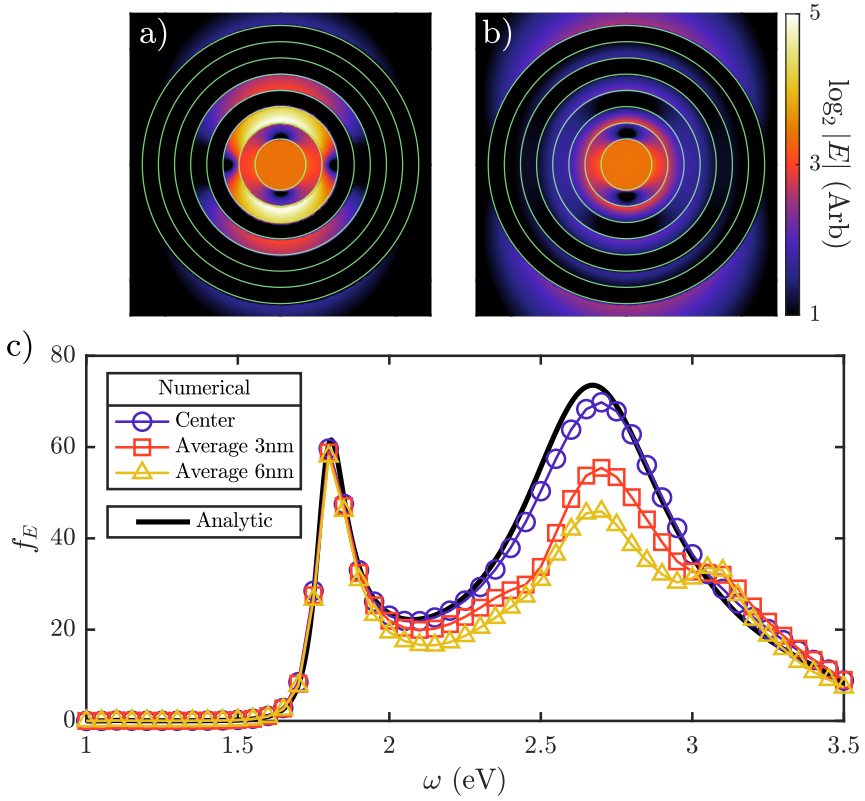

FIGURE 3.4: Electric field intensities for a $N = 7$ hyperbolic nanocavity with $R_{\text{tot}} = 60$ nm obtained at a) $\omega = 1.8$ eV and b) $\omega = 2.7$ eV. Green lines are used to indicate the boundaries between adjacent regions. c) Fluorescence enhancement spectra for the same cavity above obtained by the semi-analytical (black) and numerical (purple circles) methods. Orange squares and yellow triangles display the effect on the f_E of displacing the molecule within the cavity's core. For each of these datasets the molecule was displaced 3 and 6 nm respectively.

of these results through numerical simulations by modifying the position of the molecule. In Fig 3.4(c) we show the f_E spectra obtained by the spatial and orientational averaging of molecules located 3 nm (orange squares) and 6 nm (yellow triangles) away from the center. As expected, the whispering gallery mode at 1.8 eV is insensitive to this averaging, while the evanescent nature of the plasmon modes at higher frequencies leads to a strong alteration of the f_E. This behaviour of the f_E in the

plasmon resonance can be understood from the presence of higher order plasmonic dark modes [215, 216]. As the molecule is placed closer to the silica-silver interface, these higher angular momentum modes (that are more tightly bound to the interface) become excited, which leads the f_E spectra to develop the new features.

3.2.3 Optimized Nanocavities

Since the transfer matrix formalism provides a quasi-analytical solution that can be evaluated orders of magnitude faster than any numerical implementation, it is then compelling to use it to optimize these hyperbolic nanocavities. Particularly, in this section we will see how one can significantly enhance the f_E (up to a 10^4 factor) at a given operation frequency, ω_{opt}, through the tuning of the thickness of the different nanocavity layers. Therefore, for a N-layer nanocavity, we set up an N-dimensional optimization problem by applying a particle-swarm optimization (PSO) method [217–219]. In this family of algorithms, a set of candidate solutions (particles) are initially randomly generated to span the search space, and then iteratively evolved according to a simple set of dynamical equations. These dynamical equations contain forcing terms that relate to the best solution found by each particle, and more crucially, to the best overall solution found by the swarm. This sharing of information among individuals is what creates the flocking behaviour of the particles in the swarm, and allow to efficiently explore the design space, overcoming local minima. This method of optimization has gathered much attention lately due to its versatility and ease of implementation [220]. In Appendix B we give technical details about the implementation we use.

Fig. 3.5(a-d) presents the outcome of the geometry optimization for cavities of 1, 3, 5 and 7 layers respectively. For all these designs, the radius of the core is fixed at $R_{\text{in}} = 11$ nm, and the thickness of the different layers is free to change. The maps show the f_E spectra as a function of the optimization frequency. The dotted black line represents the condition $\omega = \omega_{\text{opt}}$, along which the f_E spectra develops its maxima and the white solid lines correspond to the different resonances of

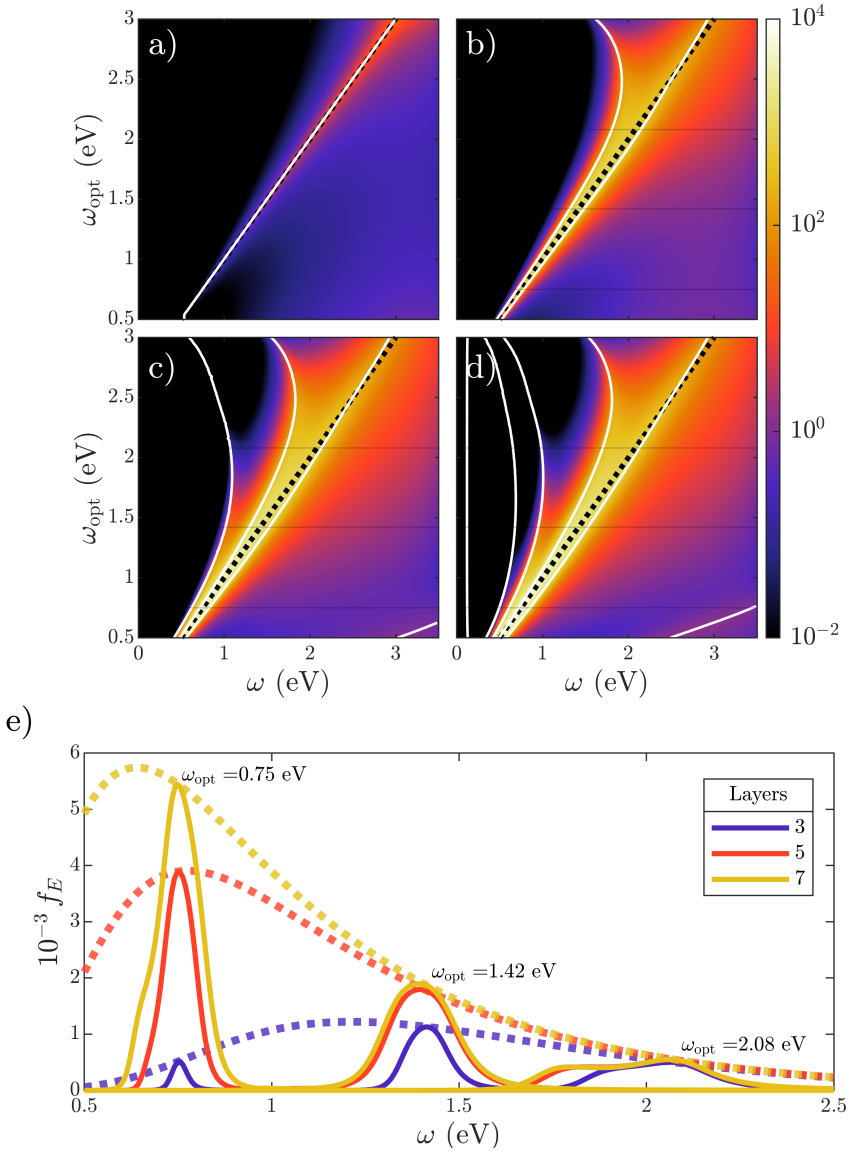

FIGURE 3.5: (a-d) f_E spectra of PSO-optimized cavities for nanoshells of 1, 3, 5, and 7 (a to d respectively) metallo-dielectric layers as a function of optimization frequency, $\omega_{\rm opt}$. For all these designs $R_{\rm in} = 11$ nm. The black dotted line marks the condition $\omega = \omega_{\rm opt}$, and the solid white lines indicate the resonances of the structures obtained by the condition $\langle \mathcal{M}_{E1} \rangle_{11} = 0$. (e) f_E spectra of PSO-designed cavities of 3, 5 and 7 layers for different $\omega_{\rm opt}$: 0.75, 1.42, and 2.08 eV, indicated by the faint horizontal lines in panels (b-d). Dotted lines show the maximum f_E obtained along the condition $\omega = \omega_{\rm opt}$ for the cavities of different layer number.

the optimized nanocavities, obtained from the condition $\langle \mathcal{M}_{E1} \rangle_{11} = 0$. This is equivalent to the scattering resonant condition in Mie formalism [208], see Appendix B for more details. Fig. 3.5(a-d) shows that the f_E maxima in the PSO-cavities is obtained by the spectral overlapping of different resonances. At high ω_{opt} this mechanism is not very effective, and only the localized surface plasmon (already present in the core-shell case in Fig. 3.5(a)) is effectively matched to the resonance condition. For lower optimization frequencies, the PSO algorithm is able to efficiently shift the resonance frequency of other modes present in the multilayered cavities through geometrical tuning and making them coalesce onto the optimization frequency. As a consequence, for optimization frequencies nearing the infrared, the PSO algorithm is able of producing very large f_E factors, that get larger as the number of available modes is increased i.e. as the number of layers of the cavity grows.

In order to more clearly compare the outcome of the optimization for the different cavities, we show in solid lines in Fig. 3.5(e) the f_E spectra for the optimized cavities of 3 (purple), 5 (orange) and 7 (yellow) layers for three different optimization frequencies, indicated as horizontal black lines in Fig. 3.5(b-d). One observes that the spectra obtained for each ω_{opt} do not overlap with each other, due to their single-peaked nature. However, the resulting maxima get stronger and narrower for decreasing optimization frequency. In dotted lines, we show the f_E value along the condition $\omega = \omega_{\text{opt}}$, demonstrating how the maximum f_E attainable through optimization grows and redshifts as the number of layers, N is increased. As we have shown in Fig. 3.5(a-d), this behaviour comes from having more available modes for larger number of metallodielectric layers that are frequency matched much more efficiently at near-infrared frequencies. In contrast, the f_E enhancement achieved at higher frequencies is virtually the same for cavities of all different layer number. This shows that indeed, the hyperbolic cavities can only achieve significant fluorescence enhancement through a localized plasmon resonance.

Next, we take a look at the geometric characteristics of the PSO-designed cavities. The panels of Fig. 3.6 show the electric field amplitude evaluated at $\omega = \omega_{\text{opt}}$ for the $N = 7$ cavities obtained for the optimization frequencies in Fig 3.5(e): 0.75 eV (a), 1.42 eV (b) and

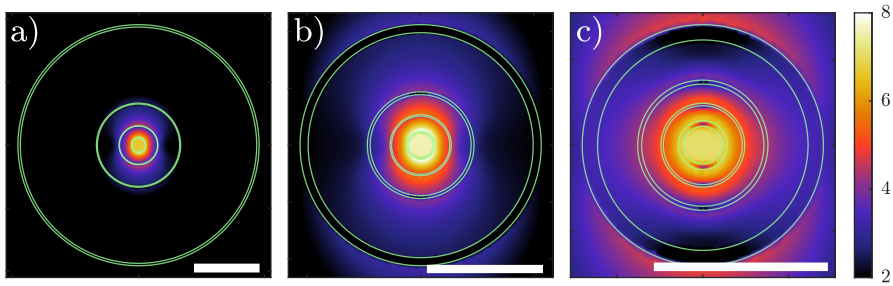

FIGURE 3.6: Resonant electric field amplitude in log scale for $N = 7$ cavities at ω_{opt}: a) 0.75, b) 1.42, and c) 2.08 eV. The amplitude of the electric field at the center of the cavity has been set to the same value in all cases and the fields are plotted in a base 2 logarithmic scale. The boundaries between layers is shown in green solid lines and the white scale bar is 100 nm long in the three panels.

2.08 eV (c). The boundary between different layers is shown in solid green line, and the white scale-bar is 100 nm in all panels. This figure demonstrates that the optimized cavities are characterized by a highly anisotropic thickness distribution of the layers, far from the periodic case studied in Sec. 3.2.2. As ω_{opt} is increased, the geometrical properties of the cavities are modified. Particularly, the silver layers become thicker and cavity size is reduced as the optimization frequency increases. This change in geometry is accompanied by a smooth change of the optical resonance behind the f_E optimization: at low frequency, in Fig. 3.6(a) the fields are tightly contained within the innermost dielectric layers. At $\omega_{\text{opt}} = 1.42$ eV, in Fig. 3.6(b), fields still mainly exist within the dielectric layer, but with significantly larger spreading. On the other hand, in Fig. 3.6(c), at $\omega_{\text{opt}} = 2.08$ eV the fields penetrate considerably within the silver layers, with an intense evanescent tail spilling out of the cavity. This transition demonstrates the transition from whispering gallery-modes at 0.75 eV to localized surface plasmons at 2.08 eV.

In Fig. 3.7 we give a more complete view of the geometrical properties of the PSO-designed cavities. Fig. 3.7(a) shows the radial structure of the optimized cavities of 3, 5 and 7 layers as a function of ω_{opt}. The solid lines indicate the dielectric-metal boundaries, and the shaded regions indicate the metallic layers. In this figure, one can clearly observe

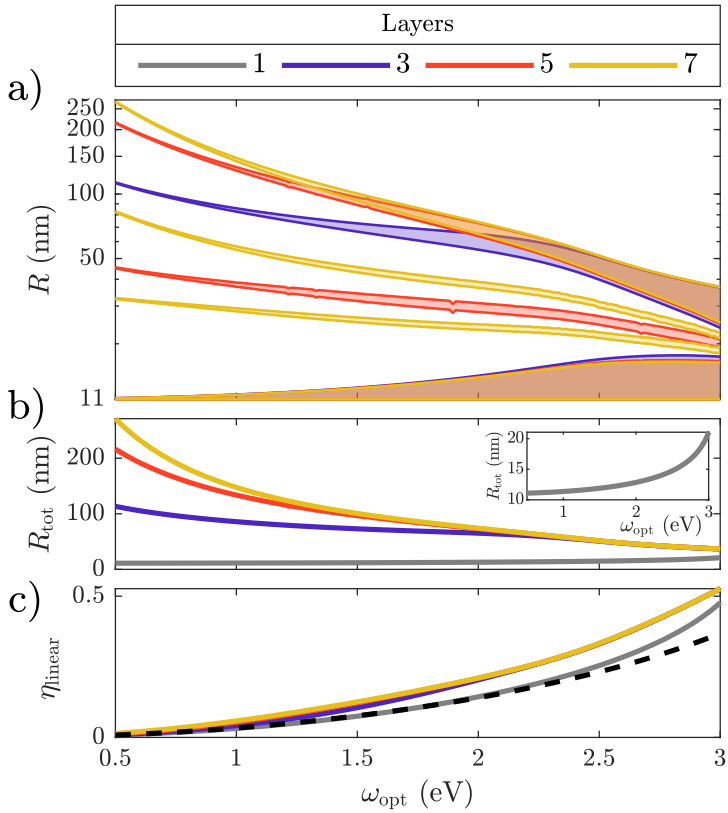

FIGURE 3.7: Legend shared by all panels. a) Radial distribution of PSO-designed cavities of 3, 5 and 7 metallo-dielectric layers. Solid lines indicate the boundaries between the regions. Colour-shaded areas correspond to the silver layers, while the un-coloured regions are made of silica. b) Total external radius of the optimized designs, with inset showing how the core-shell nanocavity ($N = 1$) is the only one that monotonically increases in size with increasing ω_{opt}. c) Metal filling fraction of metal in the PSO-designed cavities. Dashed line shows the condition for which $\epsilon_t(\omega_{\text{opt}}) = 0$.

that the trend outlined before applies to all the designs: at low ω_{opt} the cavities are composed of thin metallic shells separating large dielectric regions. As the desired operation frequency is increased, the design yields thicker metallic shells, and when $\omega_{\text{opt}} \approx 2$ eV, only the localized surface plasmon mode is available and the innermost and outermost metallic shells of all designs become almost identical, with intermediate metallic shells remaining thin. Regarding the size of the designs, Fig. 3.7(b) shows that all designs at high frequencies tend to have the

same size, again due to the role of the localized plasmon as the main mechanism available for enhancing the fluorescence. When diminishing the optimization frequency, all cavities except the core shell ($N = 1$, shown more clearly in the inset) increase in size, with the design getting larger the more layers it contains.

One can see however, that this happens in a very particular way. In Fig. 3.7(c) we show the metal filling fraction in the optimized designs and remarkably, all designs follow the same trend going from negligible filling fraction at infrared frequencies to around 0.5 filling near 3 eV. In particular, the multilayer nanocavities all have perfectly overlapping filling fraction. We remark that this filling fraction is not given by the usual definition of the fraction of volume occupied by a given material, but it is instead defined as the fraction of the radial distribution occupied by it, hence the linear subtext in η_{linear}. The motivation behind this choice is that for spherical multilayer systems, the effective tangential permittivity (Given in Appendix C) depends on this quantity, and not on the volumetric counterpart. Interestingly, all filling fraction curves in Fig. 3.7(c), lay very close to the condition that gives $\text{Re}(\epsilon_t(\omega_{\text{opt}})) = 0$, shown as a black, dashed line. From the expression for ϵ_t in Eqs. (3.8), the filling fraction that satisfies this condition is given by

$$\eta_{\epsilon_t=0} = \frac{\epsilon_{\text{SiO}_2}}{\epsilon_{\text{SiO}_2} - \text{Re}(\epsilon_{\text{Ag}}(\omega_{\text{opt}}))}. \tag{3.9}$$

Upon insertion of this filling fraction into the expressions for ϵ_r and ϵ_t in Eqs. (3.8), one finds that $\text{Re}\left(\epsilon_r(\omega_{\text{opt}})\epsilon_t(\omega_{\text{opt}})\right) < 0$ for $\omega_{\text{opt}} < 3.8$ eV, which allows to argue that in spite of their structural inhomogeneity, the PSO designs perform as hyperbolic cavities within the visible and infrared regimes. This conclusion is again backed by the less transparent effective permittivity derived for spherically layered systems given in Appendix C.

Conclusions

In this section we have seen how the main theoretical concepts of nanophotonics may be applied for technological applications, in particular, in the field of fluorescence imaging. Through the use of light-matter

interactions, we modify the radiative properties of quantum emitters and show that very significant enhancement of the fluorescence signal triggered by radioactive β-decay can be obtained through the use of hyperbolic nanocavities. Furthermore, thanks to our semi-analytical framework, we are able of very quickly determining the response of any given design, which we leverage to perform efficient numerical optimization of the nanocavity designs. The optimized designs boast an enhancement of the fluorescence signal close to 4 orders of magnitude, almost a 100-fold increase with respect to the previously studied periodic spherical case.

The hyperbolic nanostructures under study, alternating silver and silica spherical shells, form part of a larger effort in the scientific community of designing hybrid metal-dielectric nanostructures for nanophotonics [60–63, 221–223]. Bringing these two material families together can lead to designs that boast both the long lifetimes of dielectric resonators, together with the high field confinement of plasmonic nanocavities. In the present case, the higher weight of the field enhancement in f_E leads the optimized cavities to display very high field confinement, and in general, plasmonic behaviour, as can be seen from the moderate quality factors of the resonances in Fig. 3.7(e). However, through the tuning of the geometrical degrees of freedom these hybrid nanocavities allow for extreme tunability of the cavity resonance from the near UV to almost the frontier between the near and mid-infrared.

3.3 Electroluminescence to probe strong-coupling

As shown in the beginning of this thesis (Section 1.2), light-matter interaction leads to different phenomenology depending on the magnitude of the interaction strength. When these entities interact weakly, the dominant phenomenology is characterized by the modification of radiative rates [224, 225], as we have seen in the previous section. However, when the interaction strength is large enough, the light and matter components of the system hybridize, forming part light-part matter states known as *polaritons* [41, 226]. The transition between these two regimes as the interaction strength is progressively increased is signalled

by first, the appearance of a dip in the cavity scattering spectra due to the absorption of the matter component [227, 228], and then through the development of the so-called Rabi doublet, which marks the transition into the strong-coupling regime [41, 226, 229]. The optical response of the strongly coupled system can be highly sensitive to the quantum state of the matter excitations [226], which provides a means of manipulating quantum states of light and can enable high-fidelity quantum operations [230–232] and nonclassical photon generation [233, 234].

To reach the strong coupling regime, a coherent excitation exchange must be established between the light and matter components, and therefore it is required that the interaction strength is larger than the multiple decay mechanisms present. In what follows we present a simplified picture of the paradigmatic case of an atom inside a single-mode optical cavity and discuss the relevant figures of merit for reaching the strong coupling regime. In this situation, the atom-cavity coupling strength, g, can be estimated to be [12]

$$g = \frac{\mu}{\hbar}\sqrt{\frac{\hbar\omega_0}{2\epsilon_0 V}}, \tag{3.10}$$

where μ is the transition dipole moment of the atom, ω_0 is the resonant frequency of cavity and V is the mode volume of the optical cavity. For an optical mode with a Lorentzian profile, one has that the linewidth of the resonance is directly related to the decay rate as $\Delta\omega = \gamma/2$, and therefore the quality factor of such cavity may be written as $Q = 2\omega_0/\gamma$. Thus, in order to be in the strong coupling regime ($g > \gamma$), the atom-cavity system must fulfil:

$$\mu\frac{Q}{\sqrt{V}} > 2\sqrt{2\epsilon_0\hbar\omega_0}. \tag{3.11}$$

The usefulness of this inequality resides in that it very neatly connects to the two main strategies that have been employed to reach the strong coupling regime. On the one hand, dielectric cavities and traditional setups employed in cQED rely on maximizing the quality factor to increase the confinement time [163, 164], whereas on the other hand, plasmonic structures can host modes characterized by very small mode

volumes [235], providing very large coupling strengths. In this section, we will go the plasmonic route, and exploit the large field confinement in nanometric metallic gaps. We note that the use of the mode volume to characterize the coupling strength is inherited from the pioneering works on the perturbation theory of radiofrequency cavities [236] and the control of spontaneous emission in them [237] and, while its use in high-Q cavities is valid, this concept does not provide an accurate description of the modification of radiative properties of emitters coupled to plasmonic cavities [238], in which various optical modes with linewidths comparable to their spectral separation are usually present [216]. Nevertheless, this limitation can be overcome by tackling the problem through a Quasi-Normal Mode approach and with an appropriate redefinition of the mode volume [239], or through alternative mQED-based quantization procedures [31]. Furthermore, Eq. (3.11) indicates that in order to boost the interaction strength, emitters with large dipole moments are desirable. In our particular case, we will be coupling a nanoscale resonator with the excitons present in a transition metal dichalcogenide (TMD).

Generally speaking, the probing of individual, strongly-coupled quantum emitters is done through diffraction-limited far field probes [240]. This strategy becomes problematic when dealing with excitonic materials coupled to plasmonic nanocavities, since these excitations are present over the whole sample and the extent of the plasmonic cavities is usually much smaller than the size of the diffraction-limited excitation spot. This then leads to the direct excitation of a very high proportion of excitons uncoupled to the cavity, obscuring the signal scattered from the strongly coupled ones. This can be remedied to some extent by employing techniques such as dark-field spectroscopy [170] or differential reflectance spectroscopy [241]. Nevertheless, near field probes such as EELS [171] provide a much more compelling candidate for the study of these interactions since one may directly target the region of interest.

In this section, we will explore the use of plasmonic nanostructures to realize nanoscale strong coupling when coupled to a TMD, and to simultaneously provide a local probing mechanism of the strong-coupling when electrically driven [P3]. The results shown in this section originate from the collaboration with the experimental group of Prof. Douglas

Natelson at Rice University. First, we will give a brief introduction to how electrically driven sources can produce light. Then, by coupling a plasmonic nano-junction to a few-layer TMD, we demonstrate polariton formation between localized surface plasmons and the TMD's excitons, and present this novel approach, which uses electrical driving to locally probe strong light-matter interaction at the nanoscale.

3.3.1 Electrically driven light emission

Electroluminescence (EL) is the process of light emission upon the passage of an electrical current. It can be understood as a consequence of the radiative recombination of electron and holes in a material, with its most widespread technological application being light-emitting diodes (LEDs). In this section however, we focus on light emission from tunnelling currents. The process by which these currents emit light is schematically depicted in Fig. 3.8, which shows the energy landscape of a biased metallic junction (bias voltage V_b) that has a dielectric potential barrier between the electrodes. Electrons tunnelling through the gap may do so without losing energy, before relaxing to the Fermi level through processes such as electron-phonon scattering. This is known as elastic tunnelling (dashed, horizontal arrow). However, in the presence of some optical density of states in the junction, electrons may emit a photon into any of the available optical modes before reaching the destination electrode as shown by the solid arrow in Fig. 3.8(a). This process is known as inelastic electron tunnelling (IET). In plasmonic junctions these IET events can excite surface plasmons, which can be detected when they radiatively decay into the far field. From energy conservation arguments, there will be a cut-off for the energy of the optical radiation produced given by $h\nu \leq eV_b$ [242–245]. Nevertheless, if the electron gas in the electrodes is at some finite temperature or in a non-equilibrium distribution, photons can be produced at energies above the applied bias by the tunnelling of hot carriers [162, 243, 245–249]. This results in what is known as over-bias emission.

Experimental demonstrations of light emission from IET now span almost half a century, with the first experiment by Lambe & McCarthy

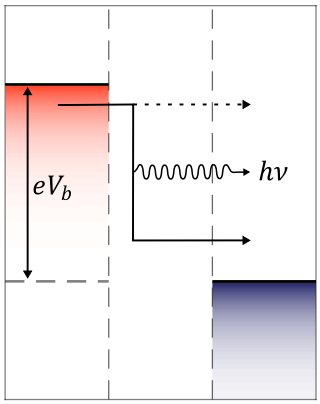

FIGURE 3.8: Schematic representation of the processes of elastic (dashed line) and inelastic (solid line) electron tunnelling through a metallic junction in which a photon emission process takes place.

taking place in 1976 [242]. Subsequent demonstrations of IET processes can be broadly framed within three different research communities: earlier works were produced within the solid state community investigating vertical tunnel junction [155], while later on IET was discovered in scanning tunnelling microscopes (STMs) [156], and even more recently, within the nanophotonics community there have been efforts to use this mechanism to realize electrically-driven optical antennas [157–159]. The theoretical modelling of light emission from the IET process in subnanometric metallic junctions is uniquely challenging due to the convergence of different orders of magnitude [250]. On the one hand, the metallic structures that host the optical density of states required for the IET mechanism are usually much larger than the nm scale, which directly forbids the use of ab-initio tools and favours a classical description of the EM fields. However, due to the subnanometric nature of the tunnelling gap and the high localization of the optical fields in the junction, non-local effects in the electrode's permittivity can play a relevant role [251], which in principle calls for the use of quantum-corrected or hydrodynamic models of metals [252, 253]. Furthermore, the quantum nature of the tunnelling process and electronic density of states of the

electrodes needs to be somehow interfaced with the results of classical electromagnetic calculations, with all of these factors being relevant for the proper description of the light emission process. Luckily, over the last 50 years of research several alternative modelling approaches for the problem have been explored, from which we will draw inspiration [254–257]. See [258] for a comparison of the different strategies employed in the past.

In what follows, we access the strong coupling regime in the interaction between the localized surface plasmons (LSP) [259] of a plasmonic junction and the excitons present in a TMD. The sub-nm sized gap between two metallic electrodes serves as an ultra-confined plasmonic nanocavity where incoherent photons are generated by hot carrier EL [162, 246, 247]. When a TMD is coupled in the near field to the nanogaps LSPs, the resulting exciton polaritons strongly modify the radiative local density of states that governs the IET process, resulting in the observation of the polaritonic resonances in the far-field spectra. The EL emission thus acts as an extremely local, near-field probe of plasmon-exciton polariton physics and a new means of controlling the flow of energy at the nanoscale through changing the dielectric environment.

3.3.2 Experimental setup and measurements

We begin by first showcasing the experimental devices fabricated by the group of Prof. Douglas Natelson at Rice University. In Fig. 3.9(a) we show a scanning electron microscope image of a nanoscale junction. The nanogap is created by the use of an electromigration technique [162], which results in the creation of a sub-nanometric tunnelling junction. Due to the stochastic nature of the electromigration process, atomic-scale irregularities are found over the nanogap region. The geometric dimensions of the junction were chosen so as to have a resonant mode at around 1.7 eV [162]. In Fig. 3.9(b) we show the EL spectra obtained from such junction. Note that the measured photon energies are well above the bias voltage, indicating that photon emission is dominated by over-bias emission due to the plasmon-enhanced radiative recombination of hot carriers [162, 243, 245–249]. The broad peak that appears in the bare

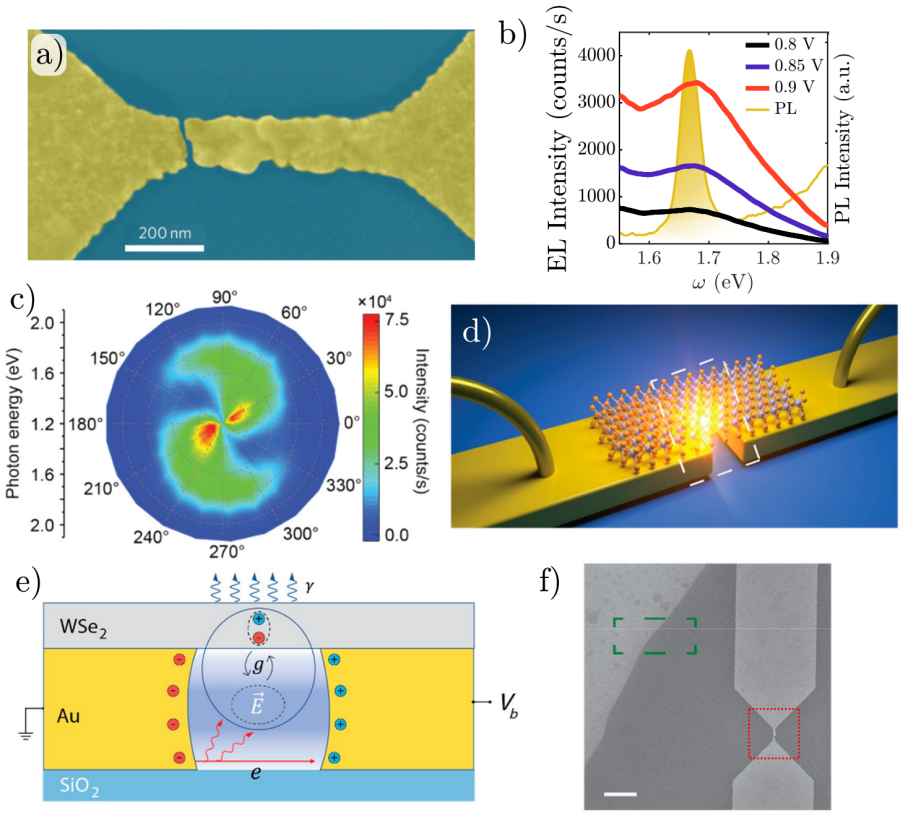

FIGURE 3.9: Schematics of experimental setup and various characterization for the TMD and EL spectrum. a) Scanning electron microscope image of the tunnelling junction formed after the electromigration process. b) EL spectra (no polarization selection) for a *bare* gold junction at different biases with a zero-bias conductance of $0.11G_0$ ($G_0 \equiv 2e^2/h$, with e the electron charge and h, Plancks constant), plotted together with the PL spectrum (no polarization selection) for a plain bilayer of WSe_2 highlighting the presence of the A-exciton peak. c) Polarization selected EL spectra for bare gold junctions extracted from Ref. [162]. d) schematic of a fabricated hybrid TMD-on-gap structure and e) the diagram of plasmon-exciton coupling coupled to electrically driven tunnelling within the gap. f) Electron microscopy image of an electro-migrated junction with TMD on top. The scale bar in the figure is 2 μm. >Red rectangle indicates the junction location and the green rectangle the TMD flake edge.

junction at around 1.69 eV is assigned to a LSP resonance associated with transverse dipolar optically bright mode of the metal nanowire

with well-defined width ($\sim$ 120 nm) [162, 260]. While there is device-to-device variation in the overall plasmonic mode structure, this dipolar LSP appears consistently in this energy range (set by nanowire width) in these nanogap structures [260]. Note that the dipolar nature of the different resonances of the junction is carried into the far field encoded in the polarization of radiation. In Fig. 3.9(c) we show the polarization content of fields coming from a similar nanojunction in Ref. [162] (0° axis oriented along gold strip), demonstrating the rich polarization structure.

The photoluminescence (unpolarized detection) from a bare trilayer WSe_2, excited by a 532 nm laser, is also plotted in Fig. 3.9(b). The sharp peak appearing at 1.68 eV corresponds to the direct A exciton transition energy, consistent with previous studies [261–263]. The spectral overlap between the EL peak in the bare plasmonic junction and the PL exciton in the plain TMD indicates good spectral matching between the gap plasmon and the TMD excitons, opening the door to the possibility of strong light-matter coupling phenomena in the hybrid system. In Fig. 3.9(d) we show a 3D sketch of the setup we will study in this section: few layers of WSe_2 on top of a nanogap formed between two gold electrodes. Fig. 3.9(e) illustrates the coupling mechanics between the gap mode and the WSe_2 excitons and how the tunnelling current populates the exciton-polaritons that result from the coupling. An image of the TMD-coupled plasmonic junction structure is shown in Fig. 3.9(f). The junction shown in Fig. 3.9(a) is indicated by a red rectangle. We also indicate the edge of the TMD flake with a green rectangle. AFM measurements of the WSe_2 flake in this region indicate a thickness of 3.9 nm, consistent with trilayer WSe_2 [263].

When the coupled TMD-nanogap structure is biased to the EL regime, instead of the single broad and bright plasmonic resonance in this energy range routinely seen in bare metal junctions, two peaks in the emission (no polarization selection) are observed for this device, reproducing the Rabi splitting phenomenology of strongly coupled systems (Fig. 3.10(a)). These two peaks emerge around 1.69 eV, associated with two polariton-like states that result from the coupling between the LSP mode of the junction and the excitons in the WSe_2 flake. The spectral separation between polaritons of 50 meV allows us to estimate a

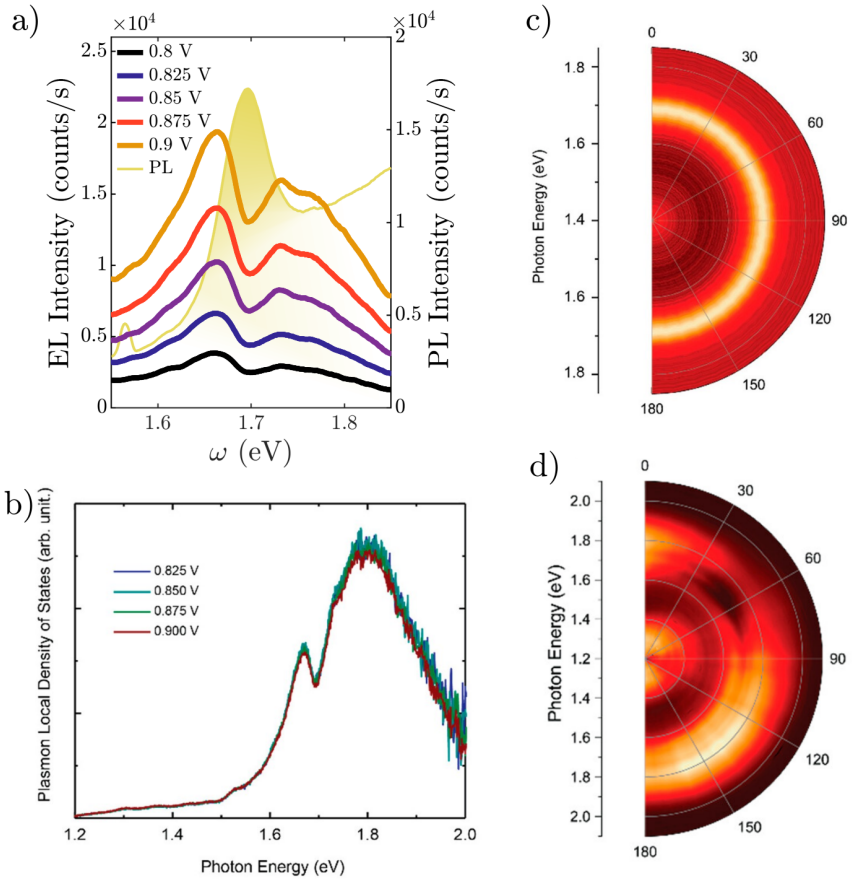

FIGURE 3.10: (a) Measured EL spectra (no polarization selection) at different biases with a zero-bias junction conductance of 0.20 G_0, plotted together with the PL spectrum measured for the WSe_2 on top. (b) Extracted optical radiative local density of states obtained by removing the Boltzmann-like hot carrier energy distribution for different biases [P3, 162]. (c,d) Polarization content of emission from the system obtained from c) PL and d) EL measurements, demonstrating that the PL emission is completely dominated by bright and decoupled excitons with no appreciable polarization dependence nor signal of plasmon presence, while the EL spectra is shaped by the junction properties since it inherits a rich polarization dependence of the emission, and displays a dip around 1.7 eV.

collective plasmon-exciton coupling strength of around 25 meV [235]. Doublet spectra for different bias voltages are shown together with the PL spectrum for the A exciton of this flake of WSe_2, highlighting the

correspondence between the exciton peak and the position of the dip in the EL spectra of the TMD-gap hybrid system. Again, note that the EL spectrum is dominated by over-bias emission. To extract the photonic density of states we apply a phenomenological normalization procedure developed in previous works [162, 245]. The scheme relies on the assumption that for photon energies above the bias, the EL intensity can be decomposed into a product of the radiative density of states, $\rho(\omega)$, and a Boltzmann factor with effective temperature as

$$I(\omega) \approx \mathcal{I}^{\alpha}\, \hbar\omega\, \rho(\omega)\, e^{-\hbar\omega/k_{\mathrm{B}}T_{\mathrm{eff}}}, \tag{3.12}$$

where $\mathcal{I}$ is the experimentally measured current running through the junction, and α is an experimentally determined parameter [162]. From the normalization procedure we obtain that effective temperatures in these measurements are of the order of 1400 K. It is important to remark that this effective temperature should not be interpreted as the temperature of the junction. If anything, it may be an indication of an out of equilibrium distribution of the electron gas in the metal. After obtaining the effective temperature for each bias voltage, we extract the radiative density of states, that we plot in Fig. 3.10(b). As can be seen, the extracted $\rho(\omega)$ in the polariton energy range all collapse perfectly for different biases, just as in the spectral range that is unaffected by the exciton. This consistency validates that the emission spectrum scales as the product of a polariton-modified $\rho(\omega)$ and a voltage-dependent hot carrier Boltzmann distribution in the metal.

The results in Fig. 3.10 show that the introduction of the TMD in close proximity to the cavity leads to a modification of the photonic density of states, analogously to effects seen in other examples of plasmon-exciton coupling [264–266]. Crucially, this modification in the density of states can be used to manipulate the radiative decay channels of the electrically generated hot carriers in the metal, which in turn converts their inelastic scattering processes in a direct probe for the strong coupling dynamics. To put into value the relevance of the method, in Fig. 3.10(c) we show the polarization resolved PL signal obtained under far-field excitation of the TMD-junction system. The isotropic exciton

peak intensity demonstrates that the far-field-excited PL contains no clear signs of the nanoscale plasmon-exciton coupling and therefore, this far-field PL is fully governed by emission from uncoupled TMD excitons, far from the nanogap but within the incident beam spot. On the contrary, in Fig. 3.10(d) we show the polarization dependence of the EL spectra being radiated from the device, which besides the several dipolar resonances reminiscent from the bare case, also show a splitting around 1.7 eV. This highlights that due to the small mode volume of the hybrid TMD-nanogap system, EL gives access to extremely local information that is inaccessible via far-field methods such as ordinary PL.

3.3.3 Theoretical modelling

In this section, we delve into the theoretical methods used to model this system and to investigate the exciton-plasmon interaction regime. Due to the structural complexity of the TMD-coupled nanojunction, we tackle the problem majorly through the use of numerical simulations in COMSOL. However, the presence of very different lengthscales in the different components makes the simulation of the complete geometry unfeasible. For instance, both the bowtie-like structure that extends for several microns, and the gold junction are made from the same 18 nm thick gold layer, and the gap distances in the nano junction are of the order of a few nanometers. Furthermore, the whole gold structure is topped by a TMD layer less than 5 nm thick. In order to properly resolve the extremely large field confinement in the nano gap, and the rapid variation of the fields in these nm-thick layers, the required discretization mesh is orders of magnitude denser than what would suffice in the corresponding homogeneous bulk media, severely limiting the size of the domain that one can simulate. Of course, this would not be a problem if all light emission from the system happened extremely locally from the gap region, however, the inelastic tunnelling processes will also launch surface plasmons polaritons (SPPs) from the gap, which in

the optical may propagate for tens of microns [267]. Therefore, the complete far-field signal will be composed by the EL from the hybrid TMD-nanojunction system at the gap, and the surface plasmons launched from the gap scattered by imperfections along the bowtie edges.

Since our interest mainly resides in capturing the strong coupling dynamics and how the EL carries away the radiative density of states from the gap, we model the system by two complementary approaches: on the one hand, we perform near-field simulations and extract the interaction parameters by a fitting to a simplified model [41]. Since the SPPs launched from the gap will only weakly interact with the TMD, we make negligible error by truncating the structure. Then, we postulate a two plasmon model to capture the influence of these SPPs launched from the nanogap in the far field.

Near field model and interaction regimes

To gain insight into the electromagnetic resonances supported by the junction and how these couple to the TMD excitons, we perform numerical simulations using the Maxwell's Equation solver in COMSOL Multiphysics and model the device by closely mimicking the geometrical dimensions of the experimental samples. Panels in Fig. 3.11 showcase the geometry of the junction and simulation domain. In Fig. 3.11(a) we show the top view of the gold nanojunction (yellow), deposited on a SiO_2 substrate (blue). The gold and SiO_2 are described respectively by the refractive index in Ref. [203] and a refractive index of 1.5. The nanojunction is composed by a 600 nm long and 120 nm wide gold strip that is connected at the edges to electronic contacts that branch out at 45 degrees. To create the nanogap, we cut the strip at an angle of 14° and create a gap of 14 nm. The gap is created at a lateral offset of 190 nm from the center of the strip to break the symmetries, as in the experimental samples. A close-up of the gap region enclosed by the dashed square in Fig. 3.11(a) is shown in Fig. 3.11(b). To simulate the atomic-scale imperfections that are naturally result from the electromigration process, we add two half cylinders of 5 nm radius to each of the faces of the nanogap cut to create a pico-cavity with a minimum gap distance

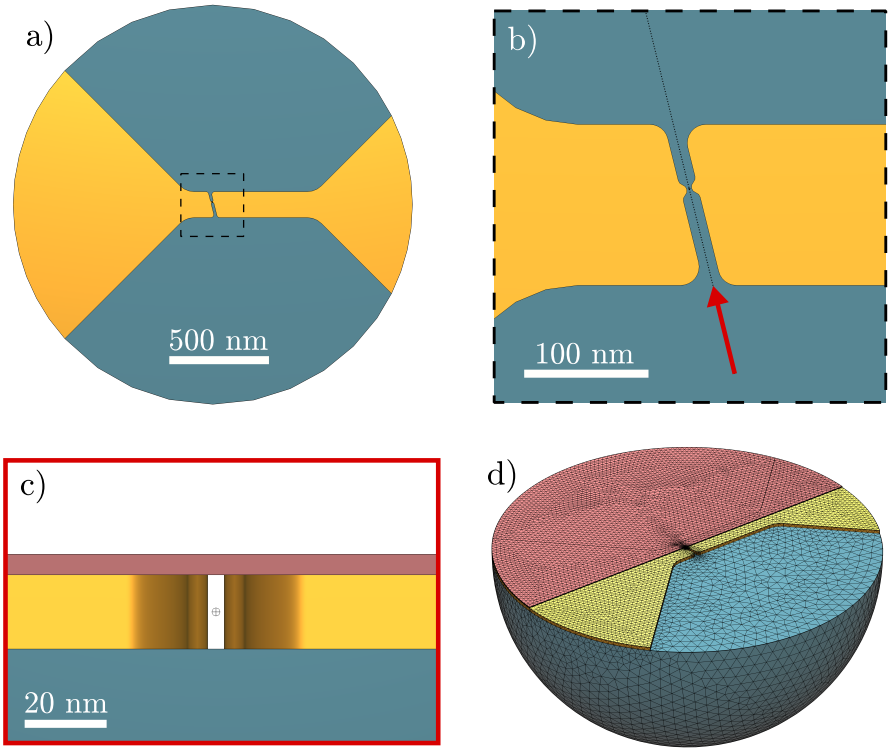

FIGURE 3.11: Schematics of simulation geometry and meshing. a) Top view of the gold strip (yellow) on top of a SiO_2 substrate (blue). Nanogap location indicated by dashed square. b) Close-up of nanogap in (a), showcasing the atomic-scale imperfections that serve as the tunnelling current hotspot. c) Side view of the junction along the line of sight indicated by the red arrow in (b). A 5 nm WSe_2 layer (red) is added on top of the gold junction, and white indicates air on top. The small sphere at the center of the gap indicates the source-dipole location. d) Meshing of the simulation domain containing the SiO_2 substrate, gold junction and TMD layer. The TMD has been cut in half to reveal the junction underneath. The simulation domain is composed of a 1 micron radius sphere centered around the source dipole position.

between the cylinders of 4 nm. Due to the exponential decay of the tunnelling probability with barrier width, most of the current in these devices will tunnel through the small gaps between such atomic-scale imperfections. As such, to simulate the tunnelling current, we place a dipolar source at the center of the 4 nm gap and set the dipole moment

pointing from one face of the gap to the other. The choice of these geometric parameters for the minimum gap distance and general gap separation is informed both from images of the experimental devices (See Fig. 3.9(a), for instance) and from estimations of the tunnelling distances based on the zero-bias conductance [268]. In Fig. 3.11(c) we show a view of the nanogap taken from the line of sight indicated by the red arrow in Fig. 3.11(b). In this panel we include the 5 nm layer of WSe_2 layer (red) on top of the 18 nm thick junction that covers the complete simulation domain. On top of the TMD layer we have air ($n = 1$). In Fig. 3.11(d) we display the meshing generated for this structure (colours are the same as previous panels), where we have omitted the top air half-space and cut the TMD layer by the middle to show the gold nanostructure underneath. Fig. 3.11 clearly illustrates the different length-scales at play in the problem, and how due to the presence of the small nanogap and thin extended layers it becomes necessary to truncate the simulation domain in order to avoid excessive computational cost. In the present case, the simulation domain is chosen to be a sphere of 1 μm radius, centered around the source dipole position and terminated with a scattering boundary condition.

To model the optical properties of the WSe_2 layer we employ a Clausius–Mossotti anisotropic dielectric function [269] that assumes that the exciton dipolar moments are oriented in-plane of the TMD layer. Thus, we have in- and out-of-plane permittivity components of the form

$$\epsilon_{\parallel}(\omega) = \epsilon_b \frac{1 + 2\beta(\omega)}{1 - \beta(\omega)} \tag{3.13a}$$

$$\epsilon_{\perp}(\omega) = \epsilon_b \tag{3.13b}$$

$$\beta(\omega) = \frac{\mu_{\mathrm{tmd}}^2}{3\epsilon_0 \hbar} \rho_{\mathrm{tmd}} \frac{2\omega_{\mathrm{tmd}}^2}{\omega_{\mathrm{tmd}}^2 - (\omega + i\gamma_{\mathrm{tmd}}/2)^2} \tag{3.13c}$$

where the different constants were obtained from the fitting to the experimental data in Ref. [173]. Thus, $\epsilon_b = 18$ is the background permittivity, and the exciton transition frequency, ω_{tmd}, and linewidth, γ_{tmd}, were set to 1.7 eV and 20 meV, respectively, in agreement with the bare PL spectrum in Fig. 3.10(a). We display this anisotropic material permittivity

in Fig. 3.12(a). Notice that the strong dispersion of the in-plane permittivity reflects that the dipole moment of the excitons in WSe_2 are in plane of the material [270]. Since the dipolar gap modes excited by the tunnelling current are characterized by strong in-plane fields within the gap, the (mostly in-plane) fields that leak out of the nanogap and into the TMD will strongly interact with the excitons, opening the door for the realization of strong coupling in the present devices. Real and imaginary parts of the in- and out-of-plane WSe_2 permittivity are shown in Fig. 3.12(a). Notice that such a small value for γ_{tmd} implies that the excitonic contribution to the real and imaginary parts of $\epsilon_{\parallel}(\omega)$ is relevant only within a spectral band of 20 meV. The weight of the exciton dipole moment and exciton density is given by $\mu_{\mathrm{tmd}}^2 \rho_{\mathrm{tmd}} = 10^{-4}$ e^2/nm. These values are in agreement with recent studies [271].

To obtain the detected intensity we calculate the radiative Purcell, $\mathcal{P}_R(\omega)$, or the local density of radiative states, obtained by integrating the time-averaged Poynting vector along the vertical (top) direction, and then, by adapting the phenomenological expression in Eq. (3.12), we define the numerical far-field emission intensity as

$$I_{\mathrm{ff}}(\omega) = \rho(\omega)\omega^4 e^{-\hbar\omega/k_B T_{\mathrm{eff}}} \tag{3.14}$$

where $\rho(\omega)$ is the local density of radiative photonic states at the electron tunnelling light source obtained from our numerical calculations of the radiative Purcell factor, and $T_{\mathrm{eff}} = 1400$ K [162], in agreement with the experimental estimates.

The emission spectra obtained from this model is shown in Fig. 3.12(b), where we plot the emission spectrum obtained from the numerical simulations, both in the case where the exciton is present (solid line) and when it is not (dashed line). In order to remove the exciton from the WSe_2 dispersion, we exploit the analytical expressions for the material properties in Eq. (3.13) and simply set $\mu_{\mathrm{tmd}} = 0$, therefore, without the exciton the TMD behaves as a non-dispersive dielectric with $\epsilon_{\parallel} = \epsilon_{\perp} = \epsilon_b$. This strategy allows to isolate the effects of the exciton presence from confounding factors related to resonance-shifts due to the modification of the strong background permittivity of the TMD. We observe that the

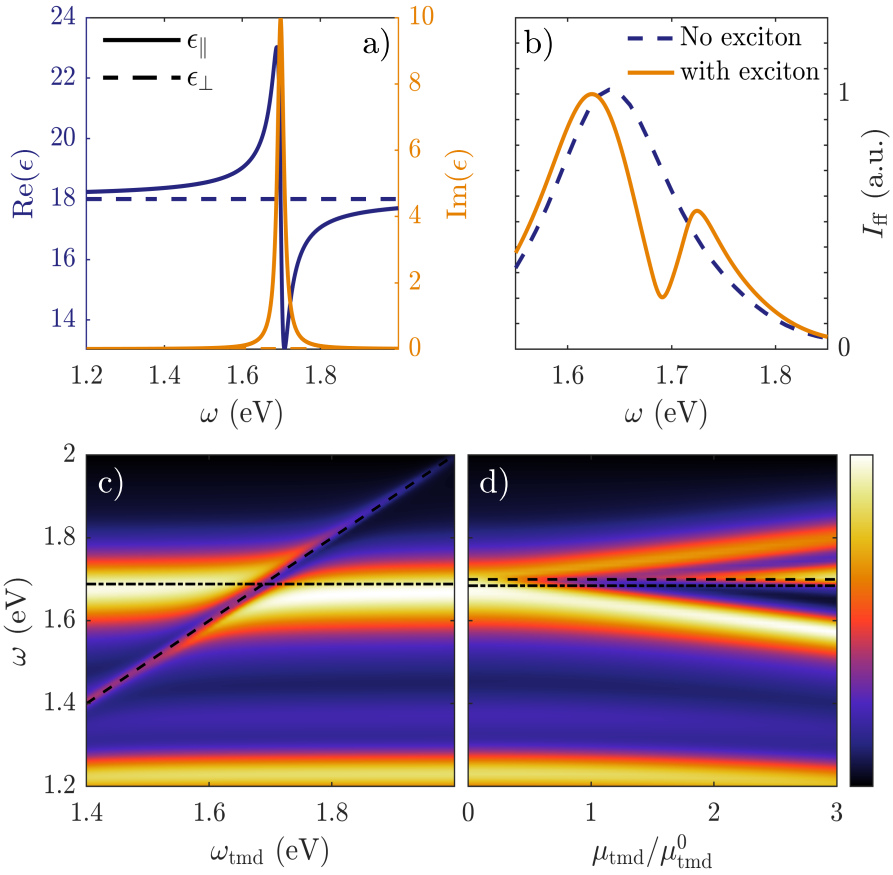

FIGURE 3.12: Numerical models of emission spectra for the hybrid TMD-on-gap structure. a) WSe_2 permittivity (real and imaginary parts) as utilized in our EM model. b) Numerical emission spectrum, $I_{\rm ff}(\omega)$, for the model TMD-plasmonic system. Solid (dashed) line corresponds to calculations including (excluding) the excitonic contribution to the WSe_2 permittivity. c-d) Numerical results for the emission $I_{\rm ff}$ maps by sweeping the model exciton frequency (c), and dipole moment (d). dashed lines indicate the exciton resonant frequency, and dot-dashed lines indicates the plasmon resonance. The colorbar, shared between panels (c) and (d), represents the far-field intensity values in linear scale between the minimum (black) and maximum (white) values.

numerical results reproduce the asymmetric doublet-like feature, with an emission dip at 1.7 eV observed in the experimental measurements in Fig. 3.10(a), and that this feature is clearly linked to the presence of the exciton as evidenced by the single resonance observed in absence of

the exciton.

We further employ our EM model to perform a systematic analysis of the plasmon-exciton coupling strength to identify in which light-matter coupling regime (weak or strong) our device is operating. Fig. 3.12(c,d) present two different studies that investigate whether the strong-coupling regime is reached and well-developed polariton states are formed in the experimental samples. Figure 3.12(c) presents the usual anti-crossing map broadly employed in the literature to identify the onset of strong coupling. In our calculations, we swept the WSe_2 exciton frequency from 1.4 to 2 eV, keeping the rest of the model parameters, and therefore the plasmon frequency, fixed. Black dotted lines plot both frequencies. We fitted the numerical emission map to the expression of the intensity spectrum obtained for a simplified model consisting of a single excitonic emitter interacting with a single plasmonic resonance [41]. Note that this depends only on 5 variables, the plasmon and exciton frequencies and linewidths, as well as their interaction strength. As a result of the fitting, we extracted a plasmon-exciton coupling strength g=31 meV, consistent with the experimental values.

Fig. 3.12(d) presents a similar study, but now sweeping the exciton dipole moment. The value taken in the TMD permittivity in Fig. 3.12(a) is labelled as μ^0_{tmd}. For $\mu_{\mathrm{tmd}} \ll \mu^0_{\mathrm{tmd}}$, the spectrum presents a single peak at 1.7 eV. A dip emerges with increasing dipole moment, initially due to exciton absorption and subsequently, because of polariton formation. For $\mu_{\mathrm{tmd}} \gg \mu^0_{\mathrm{tmd}}$, two polariton branches are clearly apparent, and another emission peak emerges in between the Rabi doublet. This feature can be attributed to the light scattered by WSe_2 excitons that remain uncoupled to the plasmon resonance, described through a strong variation in the real part of $\epsilon_{\parallel}(\omega)$ in our model. Such a small peak feature at the exciton energy can also be seen in experimentally measured polarized spectra [P3]. The fitting of this numerical map yields the same plasmon-exciton coupling strength as the previous one at $\mu_{\mathrm{tmd}} = \mu^0_{\mathrm{tmd}}$. The surface plasmon linewidth extracted from both maps is γ_{sp}=90 meV, which allows us to conclude that the experimental samples are in the plasmon-exciton strong coupling regime, based on the strong coupling criterion $4g > \gamma_{\mathrm{sp}} + \gamma_{\mathrm{tmd}}$ [230, 272].

Far-field model and Polarization measurements

As introduced, the far field signal obtained from EL contains information both about the near field coupling dynamics, and the SPPs scattered away from the junction. The electromigration process yields atomic scale variations (protrusions and bumps) within the nanogap, causing device-to-device variations in the relevant plasmon mode's linewidth in EL spectra and rich spectral mode features at different detected polarizations [162, 260]. However, due to the well-defined direction of current flow during the electromigration process, gap formation is strongly favoured in the perpendicular direction to the current flow. Therefore, the polarization characteristics of the far field radiation originating from the LSPs at the nanojunction will be somewhat stable among different devices. On the other hand, radiation originating from the SPPs will be highly influenced by factors such as where along the strip the gap is formed, the initial phase profile acquired in the junction region, structural inhomogeneities along the device's surface, or how the gold strip fans out into the larger contacts. All these will give rise to different beating patterns that radiate differently into the far field. In Fig. 3.13(a,b) we show polarization-selected EL spectra of two representative TMD-coupled devices. Note how the polarization of the dipolar mode at 1.25 eV is stable for the two devices, while the broader feature one can see for photon energies around 1.8 eV shifts its polarization characteristics, in agreement with the previous interpretation of how structural variability affects the the localized and delocalized resonances of the system. Note also the signatures of polaritonic splitting around 1.7 eV.

In the previous section, we showed that the EM simulations successfully reproduce the low-energy (around 1.25 eV) LSP mode and the TMD-coupled LSP resonance at 1.63 eV (see Fig. 3.12). In order to capture the effect of the SPP radiation and reproduce the complete polarization dependence of the EL spectra we develop an illustrative two-plasmon model based on a master equation formalism that accounts for all radiative losses (details given in Appendix. D). This model is composed of a LSP mode coupled to a TMD exciton and a weakly confined surface plasmon polariton mode. Notice that only the LSPs can

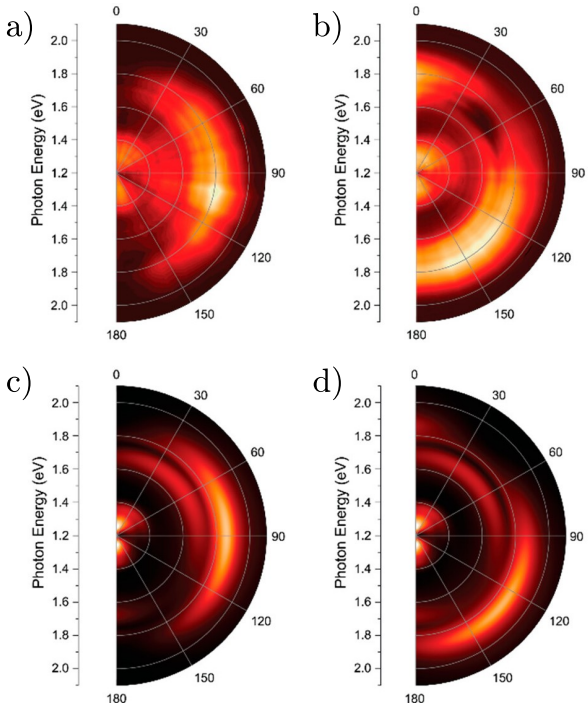

FIGURE 3.13: Unnormalized full contour plot of the experimental results and the numerical calculated polarization-resolved far field intensity. a-b) The upper panel shows the polar plot for the experimental measured spectra, while the lower panel shows the numerical results obtained from the theoretical formalism. The strong coupling feature is polarization dependent and is most visible at different polarization angles for three devices (∼70° in panel a, 45° in panel b, which can be explained by the variance of the guided surface plasmon mode's dominant polarization (90° in panel a and 130° in panel b.

be treated accurately in our EM calculations as the simulation volume ranged only up to 2 microns, much smaller than the propagation lengths of the SPPs in gold stripes of dimensions comparable to our samples, which are of the order of 10 microns [267]. From numerical simulations, it is possible to see that guided surface plasmon modes exist in our current geometry at energies above the TMD exciton, and that due to their delocalized nature, will remain largely decoupled from the TMD excitons [P3]. Assuming that EL pumping is small, and in order to account for optical and excitonic radiative decay [41], we can build an

effective non-hermitian Hamiltonian of the form

$$\hat{H}_{\text{eff}} = \hat{H}_{\text{pump}} + \hbar\Omega_1\,\hat{a}_1^\dagger\hat{a}_1 + \hbar\Omega_\sigma\,\hat{\sigma}^\dagger\hat{\sigma} + \hbar g(\hat{a}_1^\dagger\hat{\sigma} + \hat{a}_1\hat{\sigma}^\dagger) + \hbar\Omega_2\,\hat{a}_2^\dagger\hat{a}_2, \tag{3.15}$$

where $\hat{a}_1$ is the bosonic annihilation operator for the optical mode around 1.8 eV that our COMSOL simulations reproduce and which is coupled to the exciton, represented here by $\hat{\sigma}$, the excitonic annihilation operator. Both are coupled through a Jaynes-Cummings term with strength g. On the other hand, $\hat{a}_2$ is the annihilation operator for the exciton-decoupled, blue-detuned mode observed in the experiments. The pump term $\hat{H}_{\text{pump}} = \hbar\nu_1\ (\hat{a}_1^\dagger + \hat{a}_1) + \hbar\nu_2\ (\hat{a}_2^\dagger + \hat{a}_2)$, is created by the electron static-like current and it couples to both optical modes, and not the TMD excitons, with relative strengths given by ν_i. Note that in Eq. (3.15), $\Omega_i = \omega_i - i\gamma_i/2$ and, in the same fashion, $\Omega_\sigma = \omega_\sigma - i\gamma_\sigma/2$. These complex eigenenergies of the bare components of the system contain both the resonance frequency and γ's, the radiative decay rates. Ignoring the pumping term, the eigenfunctions of Eq. (3.15) are given by the polaritons formed by $\hat{a}_1$ and $\hat{\sigma}$, and the bare photons in mode $\hat{a}_2$. After treating the pump term of the hamiltonian using first-order perturbation theory [273], and finding the perturbed ground state of the system, one can then compute the power spectrum (under weak-pumping), given by [274]

$$I(\omega) = \text{Re}\left(\lim_{T\to\infty}\int_{-T/2}^{T/2}\frac{\mathrm{d}t}{T}\int_{-\infty}^{\infty}\mathrm{d}\tau\ \langle 0'|\hat{\xi}^\dagger(t)\hat{\xi}(t-\tau)|0'\rangle\,\frac{e^{-i\omega\tau}}{2\pi}\right), \tag{3.16}$$

where $\hat{\xi}_i = \vec{\mu_i}\hat{a}_i$, with $\vec{\mu_i}$ being the effective dipole moment of the optical modes. Assuming that detected emission mainly comes from the optical modes, and since the tunnelling electron current populates the optical modes incoherently, we can consider separately the intensity emitted by the polaritons, $I_1(\omega)$, and the bare $\hat{a}_2$ photons, $I_2(\omega)$ (analytical expressions given in Appendix. D). Finally, the measured intensity will be given by the projection of the far field amplitude over the polarizer,

which can be calculated as

$$I_T(\omega) = I_1(\omega)\cos^2(\phi - \phi_1) + I_2(\omega)\cos^2(\phi - \phi_2), \tag{3.17}$$

where ϕ is the polarizer angle and ϕ_i is the orientation of the dipole moment of mode $\hat{a}_i$. To evaluate this expression, the parameters of the TMD exciton and first cavity mode are set to the values obtained from our numerical simulations, while for the second cavity mode, the linewidth and resonant frequency are set according to estimations from the experimental measurements and the polarization of emission, ϕ_2, is set free to change to capture the response demonstrated by different devices.

Figures 3.13(c,d) show the far field intensity obtained from the two-plasmon model, mimicking the features of Fig. 3.13(a,b). For these results, the non-coupled guided plasmon mode is assumed to be at 1.79 eV with a linewidth $\gamma_{gp} = 140$ meV, and the dominant polarization dependence of its emission is allowed to vary from device to device (90 degrees in panel a, 130 degrees in panel b), while the near field radiation characteristics are extracted directly from the near field simulations. Note how these successfully capture the polarization characteristics of the dipolar mode at 1.25 eV. For ease of comparison, Fig. 3.14 shows a detailed comparison of the EL spectrum at different detected emission polarizations with the two-plasmon model for the device in Fig. 3.13(a). In Fig. 3.14(a,b) we show polarization-selected far field spectra obtained from the experiments (a), and the two-plasmon model (b), demonstrating how the relative peak heights of the upper and lower polariton contributions appears to change as polarization angle evolves. Polarization selection in detection can therefore reveal the onset of strong coupling in the system by filtering out far-field contributions from the SPPs that are not interacting with the TMD excitons. Fig. 3.14(c,d) compare the far field intensity without polarization selection from the experimental measurements (c), and the two-plasmon model (d), in which the contributions from the near field model features (dotted and dashed line) and the extra mode (dashed line) reproduce well the experimentally measured features.

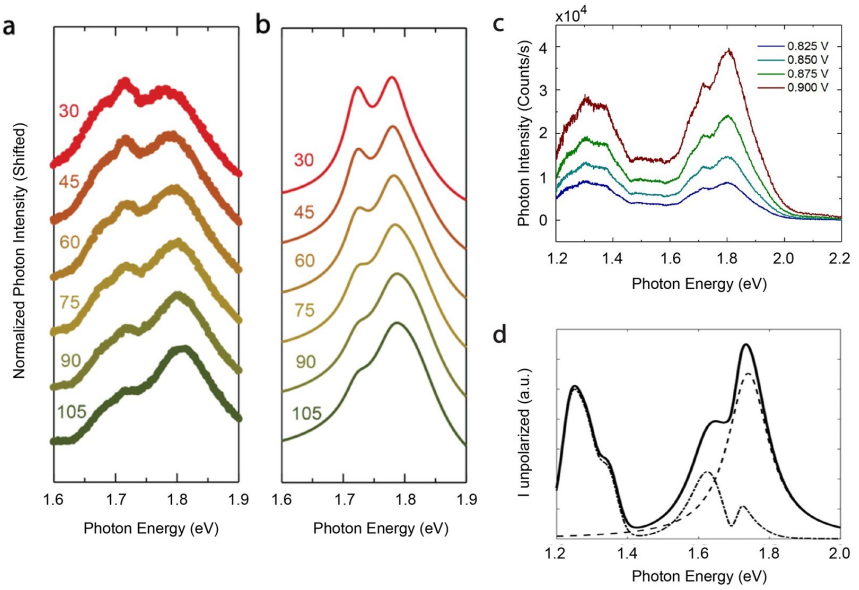

FIGURE 3.14: The two-plasmon model and polarization dependence. a) Polarization-selected EL spectra at fixed bias 0.8V with a zero-bias junction conductance of 0.09 G_0 at different detection polarizations. These are fixed-angle cuts of the data shown in the full polarization plot in Fig. 3.13(a). b) Calculated polarized spectra based on the simplified model involving coupling between the exciton and one of two plasmon modes. c) Non-polarization-selected spectra for the same device from biases of 0.825 V to 0.900 V. d) Numerical results for the single plasmon-exciton coupling calculation (dot dash line) and the decoupled guided surface plasmon mode (dashed line), plotted together with their incoherent sum, the total unpolarized spectra (solid line).

Conclusions

In this section we have demonstrated, both experimentally and theoretically, that when light and matter components of a system interact at a rate beyond the present decay channels, new hybrid states emerge. In particular, we have shown how the optical interaction between a nanogap and an adjacent TMD layer can reach the strong coupling regime, and that the EL acts as a new near-field probe to access such extreme local information, with polariton formation tuning the inelastic scattering of hot electrons tunnelling through the gap. By contrast, far-field PL measurements on these devices are not sensitive to the coupling of the extremely

localized nanogap modes to the TMD excitons.

The presented geometry exploits the in-plane nature of the excitons present in WSe_2 to couple them to the evanescent fields leaking from the extremely localized nanocavity formed between atomic-scale irregularities at the junction. The tunnelling current flowing across the junction excites modes with predominant in-plane field components, which strongly interacts with the TMD. Furthermore, since the TMD is suspended on top of the gap, no hybridization takes place between the electrodes and the material, circumventing difficulties present in previous efforts done in STMs to demonstrate the strong-coupling phenomenology [275, 276]. The results shown in this section open avenues for fabricating novel on-chip electroluminescent heterostructure devices that leverage and control plasmon-exciton coupling through proper nanoscale geometric engineering, and demonstrate that polaritonic effects, by determining the local photonic density of states, can be designed to manipulate the energetic relaxation of hot carriers in the metals supporting surface plasmons.

3

Chapter 4

Light-mediated matter-matter interactions

In the previous chapter we highlighted the potential of near field probes as compared to more traditional, diffraction-limited far-field probes to extract information from any nanophotonic setup, putting particular emphasis on the use of moving charged particles, such as positrons or electrons, for this purpose. Nevertheless, all the description made of these was done in terms of classical currents. In this chapter we go one step further and take into consideration the quantum degrees of freedom of these charged particles. In particular, we will focus on the use of free electron beams and investigate what new avenues the exploitation of the quantum coherence of their wavefunction may open with regard to quantum state manipulation and readout. The material in this chapter is closely related to two published works [P4, P5].

The chapter is structured as follows: first, we introduce some context on the use of free electrons in nanophotonics and the notion of *modulated electrons*. We then briefly introduce a framework developed to parametrize the interaction between matter transitions and light through the use of mQED. We use this framework to study the simpler case of modulated electrons interacting with a single QE and then with a more complicated plasmon-exciton polariton target.

4.1 Free electrons in nanophotonics

Traditional electron-beam-based optical characterization methods [151, 152], such as electron-energy-loss spectroscopy (EELS) or cathodoluminiscence (CL) microscopy employed in state-of-the-art electronic microscopes, present extraordinary spatial and spectral resolutions, approaching the subnanometric and milielectronvolt ranges, respectively [153, 154, 277–279]. These techniques use the evanescent character of free electron fields [185] to explore photonic and material excitations with a spatial selectivity that is innately larger than that attainable in optical spectroscopy. This has been exploited to probe features in different targets [151, 171, 177, 280] and makes free-electron probes ideal for the exploration of light-matter SC and polaritonic states in nanophotonic samples involving only a few excitons [P3, 171, 281, 282].

Moreover, in the last years, advances in ultrafast optical control of free-electron wavepackets reached the femtosecond scale, matching the optical period of visible light [177]. These are behind the emergence of techniques such as photon induced near-field electron microscopy (PINEM), that exploits the synchronous interaction between free-electrons and spatially-confined pulsed laser fields [283]. PINEM experiments have demonstrated that when free electrons interact with a driven optical resonator, their wavevector distribution can become discrete due to the exchange of individual photons with the target. Throughout this chapter, we will refer to electrons with a structured wavefunction as *modulated electrons*. In electron microscopy, modulated electrons, such as those prepared in PINEM setups, have become particularly relevant since, when allowed to drift through free space after the PINEM interaction, their spatial wavefunction is reshaped into trains of tightly focused sub-bunches. This strategy has allowed the coherent control of the free electron wavefunction [283–285], as well as the preparation of ultrashort electron pulses, which makes the nanometric probing of ultrafast dynamics in matter possible [283, 286–290]. This has led to striking results, such as the recording of the charge dynamics in out-of-equilibrium material systems [291], or of the sub-optical cycle dynamics of electromagnetic fields [292], and their associated phase distribution [293, 294].

Developments in PINEM theory [284, 295] and, generally, in the description of electron-photon interactions [296–298], together with the extraordinary degree of optical modulation (in time and momentum space) of electron beams attainable today [287, 290, 299], have made possible their use to imprint, exchange and manipulate quantum coherence in optical and material excitations, sustained by micro- and nano-cavities [280, 300–309], QEs [P4, 310–317] and hybdrid excitonic-photonic systems in the SC regime [P5, 318, 319], respectively. Therefore, these advances have opened the way towards the realization of quantum optics with electron beams [284, 296, 297, 299, 301, 320]. Crucially, theoretical investigations modelling realistic systems [311, 313, 314, 316] indicate that electronic bunching is key for the wavefunction engineering, as it leads to measurable changes in the excitation probability of quantum targets, such as QEs, and the possibility of inducing Rabi dynamics in them [310, 313]. Thus, a quantum treatment that considers the coherence properties of the modulated electron wavefunction is needed. In the next section, we introduce a mQED-based formalism we derived in order to parametrize the interaction of a modulated free electron with optical and matter resonances.

4.2 mQED for Nanophotonics

To begin this section, we remark that the interaction between a free electron, optical cavity and QE have been studied before (mostly as separate processes, but recently also in conjunction [318]). However, in this section we provide a unified description of the interaction between arbitrary electronic transitions and optical fields in terms of the common starting framework of mQED, which naturally particularizes for the cases of free electrons and QEs. Being based on mQED, and treating all interactions on equal footing, ensures the proper normalization of optical modes in arbitrary EM environments in our calculations. Thus,we obtain physically meaningful coupling strengths, even in situations in which the EM fields only serves as a non-resonant background. Therefore, these results pave the way for exploring quantum phenomena in field-mediated interactions between arbitrary electronic transitions, and

in general light matter interaction phenomena beyond the dipolar approximation of QEs.

4.2.1 Outline of the derivation for general electronic transitions

In this section we present an overview of the derivation of the Hamiltonian describing the interaction between electronic transitions and optical fields, in which a direct, field-mediated, interaction between electronic transitions is obtained. For a detailed derivation, see Appendix E. The starting point is a macroscopic QED Hamiltonian [28, 321] describing EM fields in a minimal coupling scheme and a term that describes a collection of electronic eigenstates:

$$\hat{H} = \iint d\boldsymbol{r}\, d\omega\, \hbar\omega \hat{\boldsymbol{f}}^\dagger(\boldsymbol{r},\omega)\hat{\boldsymbol{f}}(\boldsymbol{r},\omega) + \sum_i E_i \hat{c}_i^\dagger \hat{c}_i + \frac{e}{m}\hat{\mathbf{p}}\cdot\hat{\boldsymbol{A}}, \tag{4.1}$$

where $\hat{\boldsymbol{f}}(\boldsymbol{r},\omega)$ are the usual bosonic operators representing the fields created by an infinitesimal dipole moment, $\hat{c}_i$ is the annihilation operator of an electron in an eigenstate described by the wavefunction $\phi_i(r)$, $\hat{\mathbf{p}}$ is the momentum operator of the charged particles and $\hat{\boldsymbol{A}}$ is the vector potential operator, which can be written in terms of the $\hat{\boldsymbol{f}}(\boldsymbol{r},\omega)$ operators as

$$\hat{\boldsymbol{A}}(\boldsymbol{r}) = -i\int \frac{\mathrm{d}\omega}{\omega}\int \mathrm{d}\boldsymbol{r}' \left[\mathbf{G}(\boldsymbol{r},\boldsymbol{r}',\omega)\cdot\hat{\boldsymbol{f}}(\boldsymbol{r}',\omega) - \hat{\boldsymbol{f}}^\dagger(\boldsymbol{r}',\omega)\cdot\mathbf{G}^\dagger(\boldsymbol{r},\boldsymbol{r}',\omega)\right], \tag{4.2}$$

where $\mathbf{G}$ is the Dyadic Green's Function. We can also write the momentum operator in terms of the basis of electronic eigenfunctions, $\{\phi_i\}$ as

$$\hat{\mathbf{p}}(\boldsymbol{r}) = -i\hbar\sum_{i,j}\hat{c}_i^\dagger\hat{c}_j\phi_i^*(\boldsymbol{r})\nabla\phi_j(\boldsymbol{r}), \tag{4.3}$$

which motivates defining a dipole moment density $\boldsymbol{d}_{ij}(\boldsymbol{r}) \equiv \phi_i^*(\boldsymbol{r})\nabla\phi_j(\boldsymbol{r})$, and an operator describing the electronic jump between eigenstates $\phi_j \to \phi_i$ as $\hat{\sigma}_{ij} = \hat{c}_i^\dagger\hat{c}_j$. The Hamiltonian in Eq. (4.1), only contains terms

describing the direct interaction between the different electronic transitions and EM fields and, therefore, the interactions between different electronic transitions among themselves appears as a second order process. In order to capture this interaction explicitly, we will follow a procedure similar to that in Ref. [39] (described in Section E.2.1). The core idea of the derivation is that one may split the total EM response, codified in the Dyadic Green's Function, $\mathbf{G}$, into the part that is resonant with the electronic transitions, $\mathbf{G}^{(\mathrm{R})}$, and the non-resonant part to which electronic transitions are only weakly coupled and thus acts as a background, $\mathbf{G}^{(\mathrm{NR})}$. Therefore we write $\mathbf{G} = \mathbf{G}^{(\mathrm{R})} + \mathbf{G}^{(\mathrm{NR})}$, and consequently, the vector potential will also be written in this manner as $\hat{\boldsymbol{A}} = \hat{\boldsymbol{A}}^{(\mathrm{R})} + \hat{\boldsymbol{A}}^{(\mathrm{NR})}$. In Appendix E we find that under resonant condition of the electronic transitions involved, the dynamics of the system can be described by an effective Hamiltonian

$$\begin{aligned}\hat{H}_{\mathrm{eff}} = &\iint \mathrm{d}\boldsymbol{r}\,\mathrm{d}\omega\,\hbar\omega\,\hat{\boldsymbol{f}}^{\dagger}(\boldsymbol{r},\omega)\hat{\boldsymbol{f}}(\boldsymbol{r},\omega) + \sum_i (E_i - \hbar\delta_i)\,\hat{c}_i^{\dagger}\hat{c}_i \\ &+ \frac{e}{m}\hat{\mathbf{p}}\cdot\hat{\boldsymbol{A}}^{(\mathrm{R})} - \hbar \sum_{\substack{i,j \\ k,l\neq i,j}} g_{ij,kl}^{m-m}\hat{\sigma}_{ij}\hat{\sigma}_{kl}^{\dagger},\end{aligned} \tag{4.4}$$

where only the resonant part of the EM fields remains in the interaction term, and the off-resonant part gives rise to an effective, light-mediated, direct matter-matter interaction between electronic transitions and to a Lamb-shift, whose expressions are given by

$$g_{ij,kl}^{m-m} = \frac{e^2\hbar\mu_0}{2m^2}\iint d\boldsymbol{r}\,d\boldsymbol{r}'\,\boldsymbol{d}_{ij}(\boldsymbol{r})\cdot\mathrm{Re}\left\{\mathbf{G}^{(\mathrm{NR})}(\boldsymbol{r},\boldsymbol{r}',\Omega)\right\}\cdot\boldsymbol{d}_{kl}^{*}(\boldsymbol{r}'), \tag{4.5}$$

$$\delta_i = \sum_j g_{ij,ij}^{m-m}. \tag{4.6}$$

As stated above, to reach these expressions we have assumed that the energy difference associated with transitions $i \to j$ and $k \to l$ are similar so that $\Omega = \omega_{ij} \approx \omega_{kl}$. This effective Hamiltonian would also hold in the case that $\omega_{ij} \neq \omega kl$, but the Green's Function varies sufficiently smoothly over the frequency range of interest. Additionally, we also assumed $\boldsymbol{d}_{ij}^{*} = -\boldsymbol{d}_{ji}$, which is fulfilled by all the electronic transitions

that we will consider in this chapter. Using this condition, and the symmetry of the Dyadic Green's Function, it can be shown that this coupling satisfies: $g^{m-m}_{ij,kl} = (g^{m-m}_{kl,ij})^*$ and $g^{m-m}_{ij,kl} = g^{m-m}_{lk,ji}$. Once that a direct field-mediated coupling between electronic transitions has been introduced, we proceed to define new bosonic operators describing the EM fields in the spirit of the emitter-centered modes [321]. This is done in Section E.2.2, and the final Hamiltonian reads

$$\begin{aligned}\hat{H}_{\text{eff}} = &\sum_{ij}\int \mathrm{d}\omega\ \hbar\omega\, \hat{a}^\dagger_{ij}(\omega)\hat{a}_{ij}(\omega) + \sum_i (E_i - \hbar\delta_i)\, \hat{c}^\dagger_i \hat{c}_i \\ &+\hbar\sum_{ij}\int \mathrm{d}\omega\ g^{l-m}_{ij}(\omega)\left[\hat{a}_{ij}(\omega) + \hat{a}_{ji}(\omega)^\dagger\right]\hat{\sigma}_{ij} \\ &-\hbar \sum_{\substack{i,j\\ k,l\neq i,j}} g^{m-m}_{ij,kl}\hat{\sigma}_{ij}\hat{\sigma}^\dagger_{kl}. \end{aligned} \tag{4.7}$$

Note that the light-matter interaction term has the familiar Rabi-form that particularizes to the Jaynes-Cummings Hamiltonian under the rotating wave approximation. We remark that the indices in the summations over electronic eigenstates run through the whole set of eigenstates, and thus, noting that $\hat{\sigma}_{ji} = \hat{\sigma}^\dagger_{ij}$ one sees that the above Hamiltonian is Hermitian. The new set of bosonic operators $\hat{a}_{ij}$ are defined as

$$\hat{a}_{ij}(\omega) = \frac{-e}{m\omega g^{l-m}_{ij}(\omega)} \iint \mathrm{d}\boldsymbol{r}\ \mathrm{d}\boldsymbol{r}''\ \boldsymbol{d}_{ij}(\boldsymbol{r})\cdot\mathbf{G}^{(\mathrm{R})}(\boldsymbol{r},\boldsymbol{r}',\omega)\cdot\hat{\boldsymbol{f}}(\boldsymbol{r}',\omega), \tag{4.8}$$

and satisfy the canonical commutation relation of bosonic operators by construction: $[\hat{a}_{ij}(\omega), \hat{a}^\dagger_{ij}(\omega)] = 1$, which leads to the following expression for the couplings

$$g^{l-m}_{ij}(\omega) = \frac{e}{m}\sqrt{\frac{\hbar\mu_0}{\pi}}\sqrt{\iint \mathrm{d}\boldsymbol{r}\,\mathrm{d}\boldsymbol{r}'\,\boldsymbol{d}_{ij}(\boldsymbol{r})\cdot\mathrm{Im}\Big\{\mathbf{G}^{(\mathrm{R})}(\boldsymbol{r},\boldsymbol{r}',\omega)\Big\}\cdot\boldsymbol{d}^*_{ij}(\boldsymbol{r}')}. \tag{4.9}$$

Thus, in order to apply this formalism to any given system, one only has to determine the electronic transitions involved in the interaction,

and determine the classical Dyadic Green's Function for the EM fields to parametrize the Hamiltonian.

4.2.2 Particularization for free and bound electrons

In this chapter, we are interested in the interaction between free electrons, localized transitions in QEs, and optical modes. In Appendix E.3, we find that the current densities, $\boldsymbol{d}_{ij}(r)$, associated to transitions in dipolar QEs and free electrons propagating along the $\hat{z}$ axis are given by:

$$\boldsymbol{d}_{ij}^{QE}(\boldsymbol{r}) = -\frac{m\omega_{ij}}{e\hbar}\boldsymbol{\mu}_{ij}\delta^3(\boldsymbol{r}-\boldsymbol{r}_0), \tag{4.10a}$$

$$\boldsymbol{d}_{ij}^{e}(\boldsymbol{r}) = ik_0\frac{\delta^2(\boldsymbol{r}-\boldsymbol{r}_\perp)}{L}e^{i(k_j-k_i)z}\hat{z}, \tag{4.10b}$$

where $\boldsymbol{\mu}_{ij} = -e\langle j|\hat{r}|i\rangle$ is the usual transition dipole moment, $\omega_{ij} = \omega_j - \omega_i$ is the energy difference between the eigenenergies of eigenstates ϕ_j and ϕ_i of the QE[1], $k_0 = mv_0/\hbar$ is the momentum of the incoming electron and L is the length of a fictitious box used to quantise the momentum values. We have also introduced $\boldsymbol{r}_0$ as the location of the dipolar QE and $\boldsymbol{r}_{\perp,0}$ for the location of the free electron within the $x-y$ plane.

Free electron-bound electron interaction

The interaction between the free electron and dipolar transition inside a QE can be described through the matter-matter interaction term in the mQED Hamiltonian. Introducing the particular definition of the current densities associated to both transitions in Eq. (4.5) and interaction term in the Hamiltonian in Eq. (4.4), the free electron-bound electron interaction Hamiltonian is given by

$$\hat{H}_I^{e-QE} = -\hbar\sum_q g_q^{e-QE}\left[\hat{\sigma}-\hat{\sigma}^\dagger\right]\hat{b}_q, \tag{4.11}$$

[1]Note that the sign of ω_{ij} depends on the particular initial and final states under consideration. Through this chapter we will see terms that depend on this energy difference as $|\omega_{ij}|$ which indicate that they are independent of the transition direction, i.e. whether $i \to j$ or vice versa.

$$g_q^{e-QE} = ik_0 \frac{e\mu_0\omega_{QE}}{mL} \int \mathrm{d}z' \, \boldsymbol{\mu} \cdot \mathrm{Re}\left\{ \mathbf{G}^{(\mathrm{NR})}\left(\boldsymbol{r}_0, \boldsymbol{r}', |\omega_{QE}|\right)\right\} \cdot \hat{z} e^{iqz'}. \tag{4.12}$$

Where $\hat{\sigma} \equiv |g\rangle\langle e|$ is the QE's usual ladder operator, $\boldsymbol{\mu}$ the transition dipole moment, and $\hat{b}_q \equiv \sum_k |k-q\rangle\langle k|$ is the free electron's ladder operator whose action is to shift the whole electronic wavefunction in momentum space by an amount q. Importantly, from their definition, these ladder operators act such that $\hat{b}_{q_1}\hat{b}_{q_2} = \hat{b}_{q_1+q_2}$, and $\hat{b}_q^\dagger = \hat{b}_{-q}$, so that in general: $[\hat{b}_{q_1}, \hat{b}_{q_2}] = 0$. Note that to derive the Hamiltonian above we have used the non-recoil approximation, by which the momentum exchanged by the electron with the target, q, is much smaller than the momentum of the incoming electron, k_0. By using the free electron energy dispersion, the non-recoil approximation then allows to write the energy change of the electron as a function of the momentum exchange as

$$E_k - E_{k-q} \approx \frac{\hbar^2 kq}{m} \approx \hbar\, v_0\, q, \tag{4.13}$$

where we have assumed that $k_0 \gg q$ and $\hbar k \approx \hbar k_0 = m v_0$, where v_0 is the velocity of the incoming free electrons. We note that the use of this approximation is widespread in the literature, since the energies of free-electrons generated in conventional electron-microscope setups are on the order of 10^3 times larger than optical photons, and we will make extensive use of it throughout this thesis. Nevertheless, some works have focused on recoil engineering and other phenomena associated with slow electrons in which results beyond this approximation have been provided [317, 322]. Finally, assuming that the free-electron and QE interact through the non-resonant vacuum, we integrate Eq. (4.12) by using the near-field vacuum's Dyadic Green's Function in the quasi-static approximation [12]. The coupling strength for arbitrary dipole orientation in cartesian coordinates is then given by

$$g_q^{e-QE} = -\frac{e\, k_0\, |q|^2\, e^{iqz_{QE}}}{2\pi m L \epsilon_0 \omega_{QE}} \boldsymbol{\mu} \cdot \begin{pmatrix} \mathrm{sign}(qb_{e-QE}) K_1(|qb_{e-QE}|) \\ 0 \\ iK_0(|qb_{e-QE}|) \end{pmatrix}, \tag{4.14}$$

where $K_{0,1}$ are modified Bessel functions of the first kind, z_{QE} is the location of the QE along the z-coordinate, b_{e-QE} is the electron-QE impact parameter, and ω_{QE} is the resonant frequency of the QE. This expression is in agreement with previous calculations for the free-bound electron interaction strength [310].

As a passing remark, we highlight that since the coupling strength in Eq. (4.5) is parametrized in terms of the classical EM Green's Function, it can be used in conjunction with numerical solvers of Maxwell's equations to obtain coupling strengths in more complex situations. For instance, in Appendix F we illustrate how to calculate the coupling strength between a free electron and a transition in the hydrogen atom.

Single optical mode and electronic transition interaction

Assuming that the electronic transitions are interacting with a single mode optical cavity, then one may approximate the resonant cavity's Dyadic Green's Function as $\mathbf{G}^{(\mathrm{R})}(\boldsymbol{r},\boldsymbol{r}',\omega) \approx \boldsymbol{\mathcal{G}}(\boldsymbol{r},\boldsymbol{r}',\omega_c)\delta(\omega-\omega_c)$, where ω_c is the resonance frequency of the cavity. Under this assumption the light-matter interaction Hamiltonian and interaction strength read

$$\hat{H}_I^{l-m} = \hbar \sum_{ij} g_{ij}^{l-m} \left[\hat{a}_{ij} + \hat{a}_{ji}^\dagger\right] \hat{\sigma}_{ij}, \tag{4.15}$$

$$g_{ij}^{l-m} = \frac{e}{m}\sqrt{\frac{\hbar\mu_0}{\pi}}\sqrt{\iint \mathrm{d}\boldsymbol{r}\,\mathrm{d}\boldsymbol{r}'\,\boldsymbol{d}_{ij}(r)\cdot \mathrm{Im}\Big\{\boldsymbol{\mathcal{G}}(r,r',\omega_c)\Big\}\cdot \boldsymbol{d}_{ij}^*(r')}, \tag{4.16}$$

which can be particularized by introducing the transition dipole moments in Eq. (4.10). The interaction Hamiltonian for the QE-cavity interaction in the rotating wave approximation reads

$$\hat{H}_I^{c-QE} = \hbar g^{c-QE}\left[\hat{\sigma}\hat{a}^\dagger + \hat{\sigma}^\dagger\hat{a}\right], \tag{4.17a}$$

$$g^{c-QE} = \frac{\omega_{QE}}{\hbar}\sqrt{\frac{\hbar\mu_0}{\pi}\boldsymbol{\mu}\cdot \mathrm{Im}\left\{\boldsymbol{\mathcal{G}}(\boldsymbol{r}_0,\boldsymbol{r}_0,\omega_c)\right\}\cdot\boldsymbol{\mu}^*}. \tag{4.17b}$$

While for the free electron-cavity interaction one has

$$\hat{H}_I^{e-c} = \hbar \sum_q g_q^{e-c}\hat{b}_q\left(\hat{a}^\dagger - \hat{a}\right)\mathrm{sign}(q), \tag{4.18a}$$

$$g_q^{e-c} = \frac{ek_0}{mL}\sqrt{\frac{\hbar\mu_0}{\pi}\iint \mathrm{d}z\,\mathrm{d}z'\,\mathrm{Im}\left\{\hat{z}\cdot\boldsymbol{\mathcal{G}}(\boldsymbol{r},\boldsymbol{r}',\omega_c)\cdot\hat{z}\right\}e^{iq(z-z')}}, \quad (4.18b)$$

where for compactness we have defined $\boldsymbol{r} = [\boldsymbol{r}_{\perp,0}, z]$ and $\boldsymbol{r}' = [\boldsymbol{r}_{\perp,0}, z']$. A more detailed procedure for the particularization of these quantities is given in Section E.3 of Appendix E. Note that the cavity-QE Hamiltonian has been simplified from the previous Rabi Hamiltonian to the usual Jaynes-Cummings form by application of the rotating wave approximation [323], and the coupling strength simply reduces to the commonly used in the case of a dipolar emitter interacting with a single mode cavity [31].

In Section 4.4, we will deal with the interaction between these two electronic transitions and the three degenerate dipolar modes of a spherical nanoparticle. These three modes will be labelled as x, y and z. To evaluate the couplings, we derive the Dyadic Green's Function for the spherical nanoparticle in the quasi-static approximation in Appendix. E.4. Upon writing it as $\mathbf{G}(\boldsymbol{r},\boldsymbol{r}',\omega) \approx \boldsymbol{\mathcal{G}}(\boldsymbol{r},\boldsymbol{r}',\omega_c)\delta(\omega-\omega_c)$, and assuming that the QE is placed at $b_{c-QE}\hat{x}$ from the nanoparticle's center and that the free electron passes at $b_{e-c}\hat{x}$ from the cavity (as shown in Fig. 4.8), the expressions for these couplings turn out to be (see Sections E.4.1 and E.4.2)

$$\begin{pmatrix} g_x^{c-QE} \\ g_y^{c-QE} \\ g_z^{c-QE} \end{pmatrix} = \frac{\omega_{QE}}{6}\sqrt{\frac{\pi}{2}\left(\frac{R}{b_{c-QE}}\right)^3 \frac{1}{\hbar\omega_c}\frac{1}{\epsilon_0\, b_{c-QE}^3}} \begin{pmatrix} 2\,|\boldsymbol{\mu}\cdot\hat{x}| \\ 1\,|\boldsymbol{\mu}\cdot\hat{y}| \\ 1\,|\boldsymbol{\mu}\cdot\hat{z}| \end{pmatrix}, \quad (4.19)$$

$$\begin{pmatrix} g_{q,x}^{e-c} \\ g_{q,y}^{e-c} \\ g_{q,z}^{e-c} \end{pmatrix} = \frac{e\hbar k_0}{3mL}\,|q|^2 \sqrt{\frac{1}{\epsilon_0\hbar\omega_c}\frac{\pi R^3}{2}} \begin{pmatrix} K_1(|qb_{e-c}|) \\ 0 \\ K_0(|qb_{e-c}|) \end{pmatrix}. \quad (4.20)$$

Note that the functional dependence of the couplings in Eq. (4.20) is very similar to those in Eq. (4.14) due to treating the nanoparticle in the dipolar approximation. This allows to estimate an effective dipole moment for the spherical nanoparticle as

$$|\boldsymbol{\mu}_c| = \frac{2\pi}{3}\sqrt{\pi R^3\,\hbar\omega_c\epsilon_0}, \quad (4.21)$$

which agrees well with the one derived from comparing the polarizability of a sphere with that of a quantum two-level system [324]. Once we have shown how we parametrize our Hamiltonian in terms of mQED-based coupling strengths, we proceed to introduce the scattering matrix we will employ throughout this section to describe the free electron-target interaction.

4.2.3 Scattering matrix and Magnus expansion

In this chapter we are interested in the effects of a single electron[2] interacting with a variety of quantum targets and for that matter we will employ the scattering matrix formalism [304, 310, 312] by means of the Magnus expansion. In this section we give a general treatment considering the interaction of a free electron with an arbitrary quantum target formed (possibly) by a collection of optical modes and QEs. To begin with, we consider a free electron, with Hamiltonian, $\hat{H}_e = \sum_k E_k \hat{c}_k^\dagger \hat{c}_k$, whose eigenstates are momentum eigenstates, $|k\rangle$, with associated energies of $E_k = (\hbar k)^2/2m$. This electron is to interact with some target that is characterised by some Hamiltonian $\hat{H}_t$ with an associated set of eigenstates $|\phi\rangle$ with corresponding energies $\hbar\omega_\phi$. Then we choose the bare Hamiltonian of the system to be $\hat{H}_0 = \hat{H}_e + \hat{H}_t$. Furthermore, according to Hamiltonians in Eqs. (4.18) and (4.12), the interaction Hamiltonian between the free electron and the arbitrary target will have the general form: $\hat{H}_I = \sum_q \hat{H}_{I,q}\,\hat{b}_q$.

To study such interaction, we now apply the Magnus expansion. Generally speaking, the solution for an initial value problem of a first order differential equation such as $d\,|\psi(t)\rangle\,/dt = \hat{U}(t)\,|\psi(t)\rangle$ is given by the time ordered product

$$|\psi(t)\rangle = \mathcal{T}\exp\left[\int_{-t_0}^{t} dt'\,\hat{U}(t')\right]|\psi(t_0)\rangle \equiv \hat{S}(t,t_0)\,|\psi(t_0)\rangle\,. \tag{4.22}$$

[2] Throughout this chapter we will assume that only a single electron is interacting at any given time with the nanophotonic target under consideration, similar to the dilute electron beams studied in Ref. [310], and therefore we neglect exchange and correlation effects that appear when multiple electrons are considered [325].

Where we assume that the interaction starts at $t = -t_0$, and we will later take that $t_0 = t \to \infty$. By use of the Magnus expansion, one may construct a propagator, $\hat{S}$, as the true exponential of a matrix as

$$|\psi(t)\rangle = e^{\hat{\Omega}(t,-t_0)} |\psi(t_0)\rangle ,$$

where $\hat{\Omega}$ accepts a series decomposition $\hat{\Omega}(t) = \sum_n \hat{\Omega}_n(t)$, such that the first term in the expansion reads [326]

$$\hat{\Omega}_1(t, -t_0) = \int_{-t_0}^{t} \hat{U}(t_1) dt_1. \tag{4.23}$$

Note that this expansion is perturbative in nature, and therefore its validity rests on the coupling strength between the free electron and the target being small. In order to solve the Schrödinger equation, the $\hat{U}$ operator corresponds to the interaction Hamiltonian in the interaction picture as $\hat{U}(t) \equiv -i\hat{H}_{I,\text{int}}(t)/\hbar$, with $\hat{H}_{I,int}(\tau) = e^{i\hat{H}_0\tau/\hbar}\hat{H}_I e^{-i\hat{H}_0\tau/\hbar}$. Considering the Hamiltonians introduced above, and using the closure relation of the non-interacting eigenstates, the first term of the Magnus expansion may be written as

$$\hat{\Omega}_1(t, -t_0) = -\frac{i}{\hbar} \sum_{\phi,\phi',q} \langle\phi|\hat{H}_{I,q}|\phi'\rangle \, |\phi\rangle\langle\phi'| \, \hat{b}_q \int_{-t_0}^{t} \mathrm{d}t_1 \, e^{-i\left(v_0 q - (\omega_\phi - \omega_{\phi'})\right)t_1}, \tag{4.24}$$

where $\{|\phi\rangle\}$ is the set of non-interacting eigenstates of the quantum target, and we have assumed that the incoming electron has a well defined central momentum, k_0, and that the non-recoil approximation holds (i.e. $q \ll k \approx k_0$) such that $E_k - E_{k-q} \approx \hbar v_0 q$. Taking $t_0 = t \to \infty$, and turning the summation over momentum shifts into an integral by dividing by the momentum density $\Delta q = 2\pi/L$ [P5], one then has

$$\begin{aligned}\hat{\Omega}_1(t) &= -\frac{iL}{\hbar\pi v_0} \sum_{\phi,\phi'} |\phi\rangle\langle\phi'| \int \mathrm{d}q \, \langle\phi|\hat{H}_{I,q}|\phi'\rangle \, \hat{b}_q \frac{\sin\left[\left(q - \frac{(\omega_\phi - \omega_{\phi'})}{v_0}\right) v_0 t\right]}{\left(q - \frac{(\omega_\phi - \omega_{\phi'})}{v_0}\right)} \\ &\overset{t\to\infty}{=} -i\frac{L}{\hbar v_0} \sum_{\phi,\phi'} \langle\phi|\hat{H}_{I,q_{\phi,\phi'}}|\phi'\rangle \, |\phi\rangle\langle\phi'| \, \hat{b}_{q_{\phi,\phi'}},\end{aligned} \tag{4.25}$$

where we used that $\lim_{t\to\infty} {}^{\sin(xt)}/_{x} = \pi\delta(x)$ and have defined $q_{\phi,\phi'} \equiv {}^{(\omega_\phi - \omega_{\phi'})}/_{v_0}$, which is the electron-target momentum exchange (set by energy conservation and the non-recoil approximation). By further defining the dimentionless, integrated interaction-Hamiltonian matrix elements as

$$\hbar_{I,\phi,\phi'} = \tfrac{L}{\hbar v_0} \langle\phi| \hat{H}_{I,q_{\phi,\phi'}} |\phi'\rangle , \tag{4.26}$$

we can write the scattering matrix, $\hat{S} \equiv \lim_{t\to\infty} \hat{S}(t,-t)$, connecting the initial and final states to first order in the Magnus expansion as

$$\hat{S} = \exp\left\{ -i \sum_{\phi,\phi'} \hbar_{I,\phi,\phi'} |\phi\rangle\langle\phi'| \hat{b}_{q_{\phi,\phi'}} \right\}. \tag{4.27}$$

Note that by inspection of Hamiltonians in Eqs. (4.18) and (4.12), $\hbar_{I,\phi,\phi'}$ will be proportional to a linear combination of the interaction strengths between the electron and the various entities composing the target (e.g. $g^{e-c}_{q_{\phi,\phi'}}$ or $g^{e-QE}_{q_{\phi,\phi'}}$), that for now we will simply call g. Then Equation (4.27) shows that for the Magnus expansion to be valid, the parameter $\beta \equiv Lg/v_0$ must fulfil $\beta < 1$. We will refer to this dimensionless β parameter as the integrated coupling strength throughout this chapter, and in subsequent sections we will particularize it for the different targets under consideration. Moreover, we reiterate that the structure of Eq. (4.27) can be understood as a consequence of energy conservation: the target interaction with the free electron connects every pair of eigenstates of the quantum target, $|\phi\rangle$ and $|\phi'\rangle$ through the interaction Hamiltonian matrix elements, and then reflects this transition with a momentum shift of the electronic wavefunction equal to $q_{\phi,\phi'}$ to satisfy energy conservation in the non-recoil approximation. In the following sections, we will use scattering matrices like that in Eq. (4.27) to study the interaction between a free electron and two different kinds of targets: isolated QEs, characterised by a very simple energy landscape, and polaritonic targets, in which the anharmonic polariton energy ladder introduces some very interesting degrees of freedom into the problem.

4.3 Quantum state preparation and readout with free electrons

In this section, armed with the theoretical framework for the quantum description of the coherent interaction between free electrons and arbitrary optical and material excitations shown in Section 4.2, we tackle the general problem of the assessment of free electrons as tools for QE state generation and interrogation.

The ability to control the state of a qubit is crucial for all emergent branches of quantum technologies. Applications such as quantum computing, communication or metrology benefit from having precise control over the state of quantum systems. Proposals of the exploitation of optical fields to prepare and manipulate quantum states date back to the early stages of quantum mechanics itself [327], when both quantum and semi-classical formulations showed that optical pulses and oscillatory fields provide a useful toolkit for such purpose. Despite the undeniable success in the use of light fields in quantum technologies, free space optical excitations suffer from being diffraction-limited, which imposes a strong limitation on the minimal size that elements must present in order to be individually addressable. As such, free electrons, due to their highly short-range interaction, and the recent developments in the electronic wavefunction engineering, appear as very appealing candidates to be used in quantum platforms for quantum state preparation and readout.

To retain clarity, we choose to parametrize our models in a phenomenological fashion (within realistic bounds), avoiding the question of their actual physical implementation. The section is structured as follows: in subsection 4.3.1 we introduce the Hamiltonian describing the interaction between modulated electrons and single QEs and particularize the scattering matrix for such case. Next, we explore perfectly modulated electrons in subsection 4.3.2, and show how single electron interaction and continuous electron pumping can be used to perform QE state preparation. We then proceed to analyse realistic, finitely modulated electronic wavefunctions and QE spontaneous emission to

set the constraints that the system parameters must fulfil for the implementation of targeted QE states in subsection 4.3.3. Finally, in subsection 4.3.4, we outline the potential of free electrons, and their quantum nature, as tools for quantum state tomography.

4.3.1 Model

The interaction of a localized exciton transition and a passing electron can be described through the Hamiltonian given in Eq. (4.11) (and in Refs. [P5, 310, 312, 317]), which can be equivalently written in an explicitly hermitian form as:

$$\hat{H}_I = \hbar \sum_q [g_q^{e-QE} \hat{\sigma}^\dagger \hat{b}_q + (g_q^{e-QE})^* \hat{\sigma} \hat{b}_q^\dagger], \tag{4.28}$$

where the definition of the magnitudes in Eq. (4.28) is the same as previously introduced. Although not relevant, for completeness we mention that the bare Hamiltonian of this system reads $\hat{H}_0 = \sum_k E_k \hat{c}_k^\dagger \hat{c}_k + \hbar\omega \hat{\sigma}^\dagger \hat{\sigma}$. To analyze the effect of the passing electron on the QE, we calculate the final state of the system using the scattering matrix formalism by application of the Magnus expansion [326], as introduced in subsection 4.2.3. Particularizing Eq. (4.27) for the interaction Hamiltonian above, the scattering matrix up to the first order in the Magnus expansion [312] can be written as

$$\hat{S} = \exp\left[-i \left(\beta \hat{\sigma}^\dagger \hat{b} + \beta^* \hat{\sigma} \hat{b}^\dagger \right) + \hat{O}(\beta^2) \right], \tag{4.29}$$

where we have introduced the integrated coupling strength, β, which throughout this section will be defined as $\beta \equiv g_{q_0}^{e-QE} L / v_0$. In this expression, v_0 is the central velocity of the electron beam, and L is the length of the imaginary box used to quantize the free-electron momentum eigenstates. We remark, that throughout this section we will phenomenologically parametrize β, exploring a range of values within realistic bounds, but independent of any actual physical implementation. Note that in Appendix G we demonstrate the validity of the first order Magnus expansion and the feasibility of the explored parameter

range for the case of a free electron and QE interacting through free space by extending the propagator above to the third order of the Magnus expansion. Note that we have dropped the q subindex as energy conservation fixes $q = q_0 \equiv \omega/v_0$, with ω being the natural frequency of the QE. Using that $(\beta\hat{\sigma}^\dagger\hat{b} + \beta^*\hat{\sigma}\hat{b}^\dagger)^2 = |\beta|^2\,\mathbb{1}$, neglecting contributions higher than β^2 in the Magnus expansion and absorbing complex phase of β in the QE ground state, the scattering matrix can then be written as [312, 315]

$$\hat{S} = \mathbb{1}\cos(|\beta|) - i(\hat{\sigma}^\dagger\hat{b} + \hat{\sigma}\hat{b}^\dagger)\sin(|\beta|). \tag{4.30}$$

This simple expression allows describing the free-electron-QE interaction, keeping in mind that corrections of order β^2 would need to be included in Equation (4.29) for large coupling strengths. In what follows, we omit the absolute value of the coupling strength, β, and assume that it is real and positive. For QE state preparation and readout, the initial state of the compound system can be written as the product state of QE and free-electron initial density matrices, $\rho_0 = \rho_0^{\mathrm{QE}} \otimes \rho_0^e$, and the final state after interaction is simply given by $\rho = \hat{S}\rho_0\hat{S}^\dagger$. In the next sections, we employ the closed-form approach outlined here to investigate different free-electron and QE configurations.

4.3.2 Ideally modulated electrons

Similarly to the concept of coherent states in quantum optics, $|\alpha\rangle$, which are the eigenstates of the bosonic annihilation operator as $\hat{a}\,|\alpha\rangle = \alpha\,|\alpha\rangle$, we define the ideally modulated electron wavefunctions to be eigenstates of the electron ladder operator, $\hat{b}_q$. A particular choice that fulfils this condition may be written as [328]

$$|C_\phi\rangle = \mathcal{D}\sum_{n=-\infty}^{\infty} e^{in\phi}\,|k_0 - nq\rangle\,, \tag{4.31}$$

with $\mathcal{D}$ being a normalization factor. Note that the choice in Eq. (4.31) is not unique, and particle-like wavefunctions[3] can also be used to describe ideally modulated electrons [311, 315, 316]. The action of the ladder

[3] Particularly, describing the electronic wavefunction in momentum space as a Gaussian distribution around k_0 as $|\psi\rangle = \int \mathrm{d}k\, B(k)\,|k\rangle$, with $B(k) =$

operator on this state is just $\hat{b}\,|C_\phi\rangle = e^{-i\phi}\,|C_\phi\rangle$, and conversely $\hat{b}^\dagger\,|C_\phi\rangle = e^{i\phi}\,|C_\phi\rangle$.

The action of the scattering matrix in Eq. (4.30) on an initial state characterized by the product of this electronic wavefunction, and any arbitrary QE state, ρ_0^{QE}, has the form

$$\rho = \left[\hat{S}_r \rho_0^{\mathrm{QE}} \hat{S}_r{}^\dagger\right] \otimes |C_\phi\rangle\langle C_\phi|\,, \tag{4.32}$$

with $\hat{S}_r = \mathbb{1}\cos(\beta) - i(\hat{\sigma}^\dagger e^{-i\phi} + \hat{\sigma} e^{i\phi})\sin(\beta)$. Thus, the final state turns out to be a product state of the initial electronic comb and an unitary operation applied onto the inial QE state. Hence, free electron and QE remain disentangled, and the passing electron does not retain any information about the emitter. This indicates that ideally modulated electrons will perform poorly as tools for quantum state readout. Nevertheless, by tracing out the free-electron degrees of freedom in the final density matrix, one finds $\rho^{\mathrm{QE}} = \mathrm{Tr}_e[\rho] = \hat{S}_r \rho_0^{\mathrm{QE}} \hat{S}_r{}^\dagger$. Due to the unitary character of $\hat{S}_r$ then one has $\mathrm{Tr}\{(\rho^{\mathrm{QE}})^2\} = \mathrm{Tr}\{(\rho_0^{\mathrm{QE}})^2\}$, and therefore the purity of the QE state,

$$\mathcal{P} = \sqrt{2\,\mathrm{Tr}\{(\rho^{\mathrm{QE}})^2\} - 1}, \tag{4.33}$$

is preserved in its interaction with a perfectly modulated electron beam regardless of the interaction parameters, which is a very desirable property for quantum state preparation. Note that $\mathcal{P} = 1$ ($\mathcal{P} = 0$) for pure (maximally mixed) QE states in Equation (4.33).

To investigate the effect of the modulation on the final QE state, we consider now that the QE is initially in the pure state $|\psi^{\mathrm{QE}}\rangle = \cos(\theta)\,|g\rangle + \sin(\theta)e^{-i\gamma}\,|e\rangle$ and the electron is ideally modulated with wavefunction given by Equation (4.31). It can be shown that the probability of finding the QE in the ground state after interaction (i.e., the final ground state population) is given by

$$\langle g|\rho^{\mathrm{QE}}|g\rangle_{\mathrm{ideal}} = \cos^2(\theta) - \sin^2(\beta)\cos(2\theta)$$

$(2\pi\sigma_k^2)^{-1/4}\exp\{-((k-k_0)/(\sqrt{2}\sigma_k))^2\}$, such that $\sigma_k \ll q$ one sees that $\langle\psi|\hat{b}_q|\psi\rangle = \exp\{-q^2/8\sigma_k\}$, which in the particle-like limit of $\sigma_k \to \infty$ tends to 1.

$$+\frac{1}{2}\sin(\phi-\gamma)\sin(2\theta)\sin(2\beta). \tag{4.34}$$

Conversely, if the initial state of the electron is monochromatic (mc), i.e equal to $|k_0\rangle$, then the same probability becomes $\langle g|\rho^{\mathrm{QE}}|g\rangle_{mc} = \cos^2(\theta)-\sin^2(\beta)\cos(2\theta)$. Hence, we can identify the second line of Equation (4.34) as the contribution due to electron modulation. This term presents a dependence on $\sin(2\theta) = 2\sin(\theta)\cos(\theta)$, which can be related to the coherences of ρ_0^{QE}, and indicates that the contribution to the final populations takes place through interference with the initial state. The modulation contribution is maximal when $|\sin(2\theta)| = 1$, a condition that coincides with the maximum expectation value for the QE dipole moment operator, $\hat{\mathbf{d}} \equiv \mathbf{d}\hat{\sigma} + \mathbf{d}^*\hat{\sigma}^\dagger$, given by

$$\left\langle \psi^{\mathrm{QE}}\middle|\hat{\mathbf{d}}\middle|\psi^{\mathrm{QE}}\right\rangle = \hat{u}_{\mathbf{d}}|\mathbf{d}|\sin(2\theta)\cos(\zeta_{\mathbf{d}}-\gamma), \tag{4.35}$$

where $\hat{u}_{\mathbf{d}}$ is the unitary vector in the dipole moment direction, and $\zeta_{\mathbf{d}}$ is its complex phase argument. Interestingly, the final ground state probability in Eq. (4.34) is also sensitive to the initial phase, γ, through ϕ, and therefore one may have access to complete information of the QE state through modulation.

Even though large coupling strengths are attainable under sufficiently precise electron positioning [P5] and, therefore, single electron-QE interaction events are already of practical relevance, in general, the coupling between a QE and a single free electron will be weak. It is therefore of interest to investigate setups in which the QE sequentially interacts with identically prepared modulated electrons. We assume that these arrive at the emitter with a constant rate $\gamma_e = 1/\tau$ (much slower than the QE-electron interaction), and using that each of them alter the target state by $\Delta\rho^{\mathrm{QE}} = \hat{S}_r\rho^{\mathrm{QE}}\hat{S}_r{}^\dagger - \rho_0^{\mathrm{QE}}$, we can construct a Von Neumann equation for the QE dynamics. In the limit of weak coupling, $\hat{S}_r \to \mathbb{1} - i\beta(\hat{\sigma}^\dagger e^{-i\phi} + \hat{\sigma}e^{i\phi})$ and

$$\dot{\rho}^{\mathrm{QE}} \approx \frac{\Delta\rho^{\mathrm{QE}}}{\tau} \approx -\frac{i}{\hbar}[\hat{H}_{\mathrm{eff}}, \rho^{\mathrm{QE}}], \tag{4.36}$$

where $\hat{H}_{\mathrm{eff}} = \frac{\hbar}{\tau}\beta(\hat{\sigma}^\dagger e^{-i\phi} + \hat{\sigma}e^{i\phi})$. This effective Hamiltonian has the

form of a coherent optical driving of the QE in the rotating frame [329], and therefore we can expect the emergence of Rabi oscillations in the interaction with the train of modulated electrons.

To get a deeper intuition of the induced QE dynamics, throughout this section we will represent the evolution of the QE state by the associated trajectories in the Bloch sphere. For that matter, we now introduce the Pauli matrices $\hat{\sigma}_i$, defined as $\hat{\sigma}_1 \equiv |e\rangle\langle g| + |g\rangle\langle e|$, $\hat{\sigma}_2 \equiv -i\,|e\rangle\langle g| + i\,|g\rangle\langle e|$ and $\hat{\sigma}_3 \equiv |e\rangle\langle e| - |g\rangle\langle g|$, which enable us to parametrize the QE state as $\rho^{\mathrm{QE}} = (\mathbb{1} + x\hat{\sigma}_1 + y\hat{\sigma}_2 + z\hat{\sigma}_3)/2$, with associated $\{x, y, z\}$ coordinates in the Bloch sphere. In this representation, the z component codifies the excited state probability of the state ($\langle|e\rangle\langle e|\rangle = (1+z)/2$), while the x and y coordinates codify the coherences of the state ($\langle|e\rangle\langle g|\rangle = (x+iy)/2$). The two eigenstates of $\hat{H}_{\mathrm{eff}}$ above have coordinates $[x, y, z] = \pm[\cos(\phi), \sin(\phi), 0]$, and therefore, the component of any QE state along these eigenvectors is preserved over time, while its normal component oscillates in the plane normal to this vector. Thus, the effective Hamiltonian above induces a state precession around the axis defined by ϕ, the relative phase between consecutive terms in Equation (4.31). As this vector is normal to the z-axis, a QE initially in the ground state (or, in general, any state normal to the eigenvectors of H_{eff}), will experience Rabi-like oscillations in its dynamics, with frequency $\beta\gamma_e$, and the phase of the coherences in ρ^{QE} fixed in time[4]. Note that, by adiabatically modifying the modulation phase ϕ of the incoming electrons, it is also possible to rotate the phase of the coherences in ρ^{QE}. This, together with the Rabi dynamics above, constitutes a complete mechanism for arbitrary QE state preparation.

4.3.3 State preparation with non-ideally modulated electrons

We have shown that perfectly modulated electrons present promising features for the preparation of quantum states in QE targets. In this

[4] Again, this is due to the oscillations taking place in the plane defined by the normal vector $[\cos(\phi), \sin(\phi), 0]$. Since this vector lies on the $x-y$ plane, as the state oscillates, the values of $atan(y/x)$ will remain constant, and so will the complex phase of the state's coherence, indicated above.

subsection, we explore the constraints that emerge for this purpose when non-ideal, more realistic electron modulations are considered. As in the previous section, we begin by taking a look at the single electron-QE interaction event, and then proceed to study the phenomenology that arises under continuous electron driving.

Single electron-QE interaction

We consider arbitrary electron wavefunctions spanning a continuum of wavevector components, with the general form $|\psi_0^e\rangle = \int dk B(k)\,|k\rangle$. Thus, the initial state of the QE-electron system is $\rho_0 = \rho_0^{\mathrm{QE}} \otimes |\psi_0^e\rangle\langle\psi_0^e|$. Applying Equation (4.30) and taking the partial trace over the free electron, $\rho^{\mathrm{QE}} = \int dk\,\langle k|\,\hat{S}\rho_0\hat{S}^\dagger\,|k\rangle$, the state of the QE after interaction reads

$$\begin{aligned}\rho^{\mathrm{QE}} = \rho_0^{\mathrm{QE}} &+ i\frac{\sin(2\beta)}{2}\left[\rho_0^{\mathrm{QE}}, I_1'\hat{\sigma}_1 + I_1''\hat{\sigma}_2\right] \\ &+ \frac{\sin^2(\beta)}{2}\Bigg\{\left(\hat{\sigma}_1\rho_0^{\mathrm{QE}}\hat{\sigma}_1 + \hat{\sigma}_2\rho_0^{\mathrm{QE}}\hat{\sigma}_2 - 2\rho_0^{\mathrm{QE}}\right) \\ &\qquad + I_2'\left(\hat{\sigma}_1\rho_0^{\mathrm{QE}}\hat{\sigma}_1 - \hat{\sigma}_2\rho_0^{\mathrm{QE}}\hat{\sigma}_2\right) \\ &\qquad + I_2''\left(\hat{\sigma}_1\rho_0^{\mathrm{QE}}\hat{\sigma}_2 + \hat{\sigma}_2\rho_0^{\mathrm{QE}}\hat{\sigma}_1\right)\Bigg\},\end{aligned} \tag{4.37}$$

where the effect of the initial electronic wavefunction is completely encoded in the overlapping integrals $I_1 \equiv \left\langle \hat{b} \right\rangle_e = \int dk\, B(k)B^*(k+q)$ and $I_2 \equiv \left\langle \hat{b}^2 \right\rangle_e = \int dk\, B(k)B^*(k+2q)$. The prime and double prime notation is used to indicate the real and imaginary part of these magnitudes, respectively. One can see that when $B(k)$ is composed of a single wavevector component narrower than $q = \omega/v_0$, these integrals vanish, while $|I_1| = |I_2| = 1$ for a perfectly modulated wavefunction like Equation (4.31). Thus, I_1 and I_2 account for the impact that the free-electron modulation has on the final QE state.

Since all the electronic degrees of freedom are contained within the modulation integrals, I_i, Equation (4.37) indicates that, as long as these integrals are the same, the induced dynamics of the QE will also be identical, regardless of the particular choice of $|\psi_0^e\rangle$, and thus allows

the comparison among different wavefunction configurations within the validity of the Magnus expansion in Equation (4.29). Several different strategies for electron modulation have been currently investigated in the literature. In Ref. [311], Gaussian-shaped $B(k)$ were investigated, for which $I_{1,2} \to 1$ in the particle-like limit of diverging momentum width, as shown in footnote 3 on page 133, while $I_{1,2} \to 0$ in the limit of vanishing momentum spread. This translates into a large impact of electron modulation in ρ^{QE} for particle-like electrons, while it is irrelevant in the limit of wave-like, unmodulated monochromatic electrons. A different wavefunction shaping strategy, based on PINEM, has been investigated recently [285, 305], as it enables the preparation of free electrons with a comb-like wavevector distribution of the form $|\psi_e\rangle = \sum_l J_l(2\beta)\,|k_0 + lq\rangle$, where J_l is the l-th order Bessel function and β, defined as in Eq. (4.29) and subsection 4.2.3, is the integrated interaction strength with the PINEM field [317]. It can be shown that $I_n = \delta_{n,0}$ in this case (see Appendix H), which indicates that the instantaneous modulation induced by the interaction with a classical optical field will not produce measurable changes in the state of the QE. However, if the free electrons are left to drift after the PINEM interaction [314, 315], contributions to the overlapping integrals appear for relativistic velocities. In Appendix H, we explore this mechanism and, in agreement with Refs. [310, 330], we find that $|I_1| \lessapprox 0.581$ in this configuration. Other works in the literature have proposed more sophisticated setups involving multi-stage, single colour PINEM preparation steps, for which the modulation integrals are predicted to achieve values as high as $|I_1| \approx 0.998$ [330, 331]. Other approaches, more complex, but more easily integrable in conventional electron microscopes, involve an initial interaction of the free electrons with an optical resonator to generate CL emission and electron modulation. These resonators are engineered as planar metasurfaces that focus the generated CL into a target of interest [332] with which the free electrons subsequently interact [333]. Since the modulated electrons interact with the target after it has been placed on a quantum superposition, then from quantum interference, one is able of extracting information, such as the coherence lifetime of the samples [312, 334].

The difference between drifted-PINEM-like and particle-like electron wavepackets will become apparent when considering targets in which different transition energies are present, as in Section 4.4. In a nutshell, $I_{1,2}$ have the form of autocorrelation functions in k-space. Therefore, since a particle-like electron has a very broad wavevector distribution, it will be self-similar upon any wavevector translation, interacting in the same way with all the optical transitions present in the target. On the other hand, the comb-shaped wavefunction of PINEM electrons is only self-similar upon the translation of certain momentum values, and therefore allow to selectively address certain transitions of the target [P5]. This means that the effect of electron modulation must be understood as a result of quantum interference, rather than classical charge localization or bunching [311], and that strategies employing quantum-optical fields [280], multiple resonant frequencies [287, 297], multi-stage, single colour preparation processes [330, 335], or general multi-stage preparation processes [331] are required to fully exploit modulated electron wavepackets for QE state preparation.

Back to Equation (4.37), its first line contains the term that gives rise to the Rabi dynamics discussed in Section 4.3.2 (note that $\sin(2\beta)/2 \approx \beta$ in the weak coupling limit). Importantly, it shows that the Rabi frequency is proportional to $|I_1|$, and therefore originates from the electron modulation. Moreover, for small coupling strengths, this is the leading order term in β, since that $\sin^2(\beta) \approx \beta^2$ in the rest of terms [310], which reveals that the phenomenology for realistic electron modulation resembles the ideal one for sufficiently weak coupling strength. The last two lines in Equation (4.37) also present a dependence on the electron modulation through I_2. As we will later show, these contributions are responsible for cancelling the electron-induced dephasing that takes place for non-modulated electrons at relatively large coupling strengths.

To illustrate the difference in quantum state preparation between realistic and perfect electron modulation, we choose a free-electron wavefunction consisting of a finite comb of N identical peaks,

$$|\psi_0^e\rangle = \tfrac{1}{\sqrt{N}} \sum_{m=1}^{N} |k - mq\rangle \,, \tag{4.38}$$

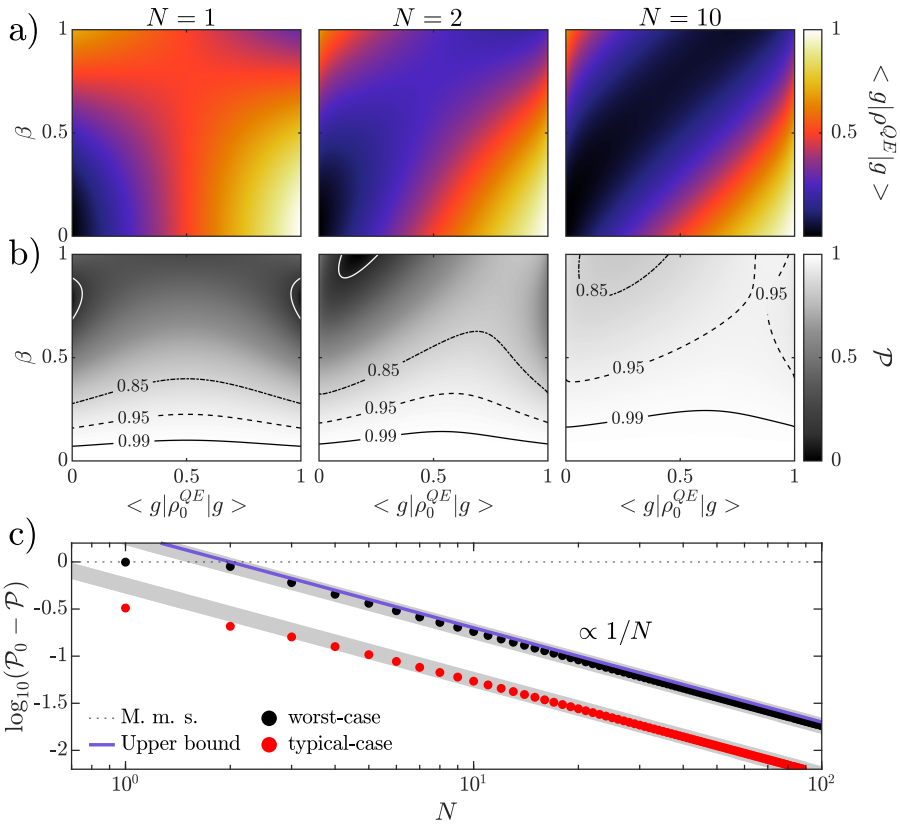

FIGURE 4.1: Final state of the QE after its interaction with a realistic (non-ideally modulated) electron wavefunction. The initial QE state is $\left|\psi_0^{QE}\right\rangle = \cos(\theta)\,|g\rangle + \sin(\theta)e^{i\frac{\pi}{2}}\,|e\rangle$. a) Ground state probability and b) purity of the final QE state as a function of initial ground state probability $\langle g|\rho_0^{\mathrm{QE}}|g\rangle = \cos^2(\theta)$, and integrated coupling strength, β. On each row, panels left to right correspond to electron combs of sizes $N = 1$, 2 and 10 respectively, as indicated on top of each column. Panel (c) renders the purity loss, $\Delta\mathcal{P} = \mathcal{P}_0 - \mathcal{P}$ as a function of the electron comb size, N.

for which $I_n = 1 - n/N$ ($I_2 = 0$ for $N = 1$). We first assume that this electron interacts with a QE that is initially in the pure state $\left|\psi_0^{\mathrm{QE}}\right\rangle = \cos(\theta)\,|g\rangle + \sin(\theta)e^{i\frac{\pi}{2}}\,|e\rangle$. Figure 4.1 (a) shows the probability of finding the QE in the ground state after the interaction and Fig. 4.1 (b) the purity of its final state as a function of the initial ground state population, $\langle g|\rho_0^{\mathrm{QE}}|g\rangle = \cos^2(\theta)$, and the coupling strength, β. Note that despite the perturbative character of our description, we have taken the

liberty to range β up to unity, where, in general, higher order corrections in the Magnus expansion would be required. In the panels depicting the purity, black contour lines indicate regions of high final purity, while white contours are used to indicate regions in which the purity falls below 0.2. The three columns in Fig. 4.1 (a,b) show the results for combs of three different sizes, $N = 1$, 2 and 10, as indicated on top of the figure. In the case of a monochromatic electron ($N = 1$), we can observe two different regions in the dependence of the ground state population on β. At very low couplings, the final ground state population follows the initial one, and, as β is increased, more population is shifted by the interaction with the electron. At $\beta = \pi/4$ the QE has $\langle g|\rho^{\mathrm{QE}}|g\rangle = 1/2$ for every possible initial state, point beyond which the electron interaction is able to move more than 50% of the QE's population in the single interaction event, indicating that the effect of the interaction with the free electrons is the largest [315, 317]. Note that as the interaction strength is increased, the purity of ρ^{QE} is progressively reduced, reaching the limiting case of vanishing $\mathcal{P}$ for $\beta = \pi/4$ and $\langle g|\rho_0^{\mathrm{QE}}|g\rangle = 0$, 1, which reveals that the QE is left in a maximally mixed state. This is detrimental for quantum state preparation, but potentially beneficial for the readout of the QE state, which can become highly entangled with the passing electrons (see Section 4.3.4). Note that the purity of the final state approaches unity in most QE and electron wavefunction configurations apart from this particular region of the map.

The $N = 1$ configuration represents the opposite of the ideally modulated electron treated in Section 4.3.2. As the number of wavevector components of the electron comb increases, the purity loss, $\Delta\mathcal{P} = \mathcal{P}_0 - \mathcal{P}$, is reduced in the whole parameter plane, as shown in Figure 4.1(b). This trend is accompanied by a modification of the landscape of final ground state probabilities, which develops a more complex dependence on $|\psi_0^e\rangle$ and coupling strength, approaching Equation (4.34) as N increases. This allows, for instance, to prepare the QE in the excited state with a wider range of system parameters [317]. Considering the case of general N, it can be shown that maximum purity loss takes place for QEs initially in a equally weighted superposition of ground and excited state. Like in the perfectly modulated case, this can be linked to the maximum

expectation value of the QE dipole moment, a condition in which the coherences in ρ_0^{QE} acquire a relevant role in the QE-electron interaction (see Section 4.3.2). In this particular configuration, an upper bound for the QE purity loss can be extracted, having

$$\Delta\mathcal{P} \leq 1 - \frac{1}{N}\sqrt{(N - 2\sin^2(\beta))^2 + \sin^2(2\beta)} \leq \frac{2}{N}, \tag{4.39}$$

where, in the last step, the limit $N \to \infty$ is taken. Equation (4.39) reveals the impact of finite size effects in the electron comb on the purity of the QE state. It also unveils that $\Delta\mathcal{P}$ scales as $\sin^2(\beta) \approx \beta^2$ in the weak coupling limit, vanishing faster than the Rabi frequency in the QE dynamics (proportional to β in Equation (4.36)).

In Figure 4.1(c) the purity loss of the QE state is plotted against the number of wavevector components in the electron wavefunction. The worst (largest loss) and typical (averaged) $\Delta\mathcal{P}$ are shown in black and red dots, respectively. They are extracted numerically from calculations for all possible values of $\{\beta, \theta\}$ in Fig. 4.1(a,b) and for N ranging from 1 to 1000. The purple solid line renders the upper bound given by Equation (4.39), i.e. $\Delta\mathcal{P} \leq 2/N \approx 2(1 - |I_1|)$, where in the last step we have reverted back to the modulation integral. The faint gray thick lines are a guide for the eye of the N^{-1} dependence featured by both sets of data for large enough electron comb. The dotted horizontal line corresponds to $\Delta\mathcal{P} = 1$, for which the QE is in a maximally mixed state (M. m. s., $\mathcal{P} = 0$) and can be maximally entangled with the passing electron. Notice that, unexpectedly, this condition can be very closely met for $N = 2 > 1$, which opens the door to exploiting the coherence of modulated electrons for quantum state tomography.

Continuous electron-QE interaction

In what follows, we study the phenomenology of continuous electron-QE interaction for non-perfectly periodic wavepackets. Following the same arguments that led to Equation (4.36), now fed with the density matrix in Equation (4.37), a master equation for the QE dynamics induced by its continuous, sequential interaction with non-ideally modulated electron

wavepackets (with rate γ_e) can be written as [310]

$$\dot{\rho}^{QE} \approx \gamma_e \left(\rho^{\mathrm{QE}} - \rho_0^{\mathrm{QE}}\right) - \frac{\gamma_0}{2}\mathcal{L}_\sigma[\rho]. \tag{4.40}$$

Importantly, note that in a refinement of our model, a Lindblad term given by $\mathcal{L}[\rho] = (\sigma^\dagger\sigma\rho + \rho\sigma^\dagger\sigma - 2\sigma\rho\sigma^\dagger)$ has been included to account for spontaneous decay of the QE. Expressing the initial density matrix of the QE in the Bloch basis as $\rho_0^{\mathrm{QE}} = (\mathbb{1} + x\hat{\sigma}_1 + y\hat{\sigma}_2 + z\hat{\sigma}_3)/2$, and its time derivative as $\dot{\rho}^{\mathrm{QE}} = (\mathbb{1} + \dot{x}\hat{\sigma}_1 + \dot{y}\hat{\sigma}_2 + \dot{z}\hat{\sigma}_3)/2$, it can then be shown that the coordinates of the QE's state in the Bloch sphere evolve according to the first order differential equation

$$\begin{pmatrix}\dot{x}\\ \dot{y}\\ \dot{z}\end{pmatrix} = \left[\begin{pmatrix} g_1 I_2^{'} & g_1 I_2^{''} & g_2 I_1^{''} \\ g_1 I_2^{''} & -g_1 I_2^{'} & -g_2 I_1^{'} \\ -g_2 I_1^{''} & g_2 I_1^{'} & -g_1 - \frac{\gamma_0}{2}\end{pmatrix} - \left(\frac{\gamma_0}{2} + g_1\right)\mathbb{1}\right]\begin{pmatrix}x\\ y\\ z\end{pmatrix} - \begin{pmatrix}0\\ 0\\ \gamma_0\end{pmatrix}, \tag{4.41}$$

where, for compactness, we have defined $g_1 = \gamma_e \sin^2(\beta)$ and $g_2 = \gamma_e \sin(2\beta)$, and $I_{1,2}$ are the k-space overlapping integrals. Remarkably, in absence of modulation the roles of g_1 and spontaneous decay are very similar, with the main difference being the steady state towards which each mechanism gravitates. To shed light into the dynamics described by Equation (4.41), let us first examine the steady state ($\dot{x} = \dot{y} = \dot{z} = 0$), and subsequently analyze how it is reached. In absence of modulation ($I_{1,2} = 0$, i.e. for a monochromatic electron), the QE steady state is

$$\begin{pmatrix}x_{\mathrm{ss}}\\ y_{\mathrm{ss}}\\ z_{\mathrm{ss}}\end{pmatrix} = -\begin{pmatrix}0\\ 0\\ \frac{\gamma_0}{\gamma_0 + 2\gamma_e \sin^2(\beta)}\end{pmatrix}, \tag{4.42}$$

which nicely showcases the interplay between the two mechanisms governing the dynamics: radiative decay tends to bring the QE to its ground state ($z = -1$ in the Bloch sphere), while the incoming electrons tend to drive the QE to a maximally mixed state at the origin of the Bloch sphere. Evaluating the probability of finding the QE in its excited state, $\langle e|\rho^{\mathrm{QE}}|e\rangle = \frac{1+z_{\mathrm{ss}}}{2}$, we find that its maximum value is 1/2 [310, 313,

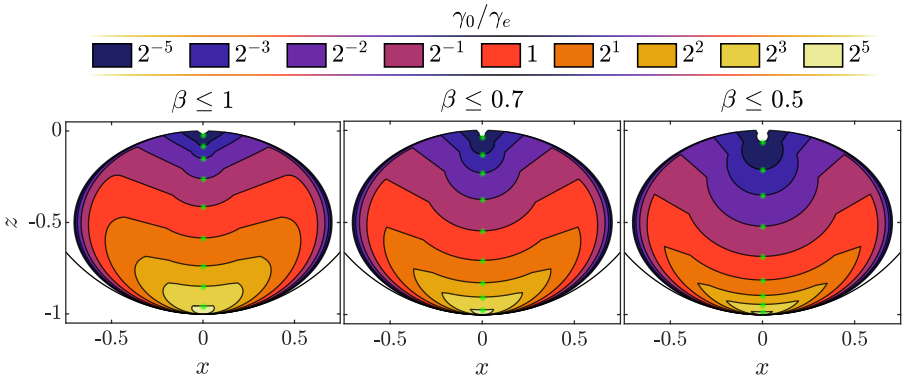

FIGURE 4.2: QE steady states accessible through the continuous interaction with modulated electrons. Each colour corresponds to a value of γ_0/γ_e, the ratio between QE radiative decay and electron driving rates. The modulation integrals are free to vary, and the coupling strength, β is limited to 1, 0.7, and 0.5 in the three different panels. Each region contains all the states attainable for larger γ_0/γ_e. The green dots represent the steady states with maximum excited state probability for the non-modulated case for each value of γ_0/γ_e and maximum allowed β. The solid black line represents the edge of the Bloch sphere.

317, 336], obtained for $\gamma_e \gg \gamma_0$. This condition yields $\mathcal{P} = |z_{\rm ss}| = 0$, which reveals that all the quantum coherence in the QE is erased by the incoming electrons. This result is the extension of the purity loss discussed in Fig. 4.1 for single electrons: in each interaction event, the QE state experiences some purity loss, and once the QE state is a statistical mixture, the steady state corresponds to equal ground and excited state populations (i.e. when the QE is in a maximally mixed state). We term this mechanism *electron-induced dephasing*, and it will also play a role in the QE dynamics even when modulation is introduced.

In contrast to the simple form of the steady state in absence of modulation given in Eq. (4.42), when modulation is introduced the steady state expression becomes rather obscure. It is then more instructive to show which regions of the Bloch sphere can be accessed in the different parametric regimes. In Figure 4.2, we show the steady states that may be reached through electron modulation for values of the ratio γ_0/γ_e ranging 3 orders of magnitude. Each color region contains the steady states accessible through variations in the overlapping integrals

and coupling strength. In particular, the modulus of the modulation integrals is allowed to vary within $|I_i| \in [0, 1]$, while their phases are set so that the QE states lay within the xz-plane[5], and the coupling strength is limited to $\beta \leq \{1, 0.7, 0.5\}$ for each of the panels in Fig. 4.2. As with monochromatic electrons, the set of accessible states lies close to the ground state for large QE radiative decay, while it encompasses a larger portion of the Bloch sphere for large incoming electron rate, approaching the point of maximally mixed states ($z = 0$) for $\gamma_0/\gamma_e \to 0$. As the maximum value of the coupling strength is limited, the region of accessible steady states shrinks towards the ground state, exactly like in the non-modulated case. However, electron modulation makes possible to have steady states with higher excited state probability. To demonstrate this, we add green points in Fig. 4.2 to indicate the steady states with maximum excited state probability in the non-modulated case for each value of γ_0/γ_e and maximum β. These points lay where the $x = 0$ axis intersects the top edge of the states accessible through modulation, and remarkably, always have lower z coordinate (i.e. lower excited state probability) than other accessible steady states with finite x coordinate. The maps shown in Fig. 4.2 correspond to numerical results, as no closed-form expression for the regions could be found. This makes the prediction of final QE states for a particular subset of electron wavefunction parameters a non-trivial task. However, an expression for the steady states in the limit of weak coupling strength can be found in [310]. Note that the solid black line in Figure 4.2 renders the edge of the Bloch sphere, where QE pure states are located. Thus, only accessible steady states in the vicinity of the ground state have high purity, which imposes an essential limitation for quantum state preparation purposes.

Since the continuous free-electron drive only leads to low purity steady states, we now shift our attention to the transient dynamics of the interaction between emitter and incoming free electrons. The principal timescales will be given by the eigenvalues of the coefficient matrix in Equation (4.41). In the case of monochromatic electrons, it is already diagonal, and all eigenvalues are real and negative: $\lambda_{1,2} = -(\gamma_0/2 + g_1)$

[5] These regions acquire azimuthal symmetry around the z-axis if the phases of I_i are set as free parameters.

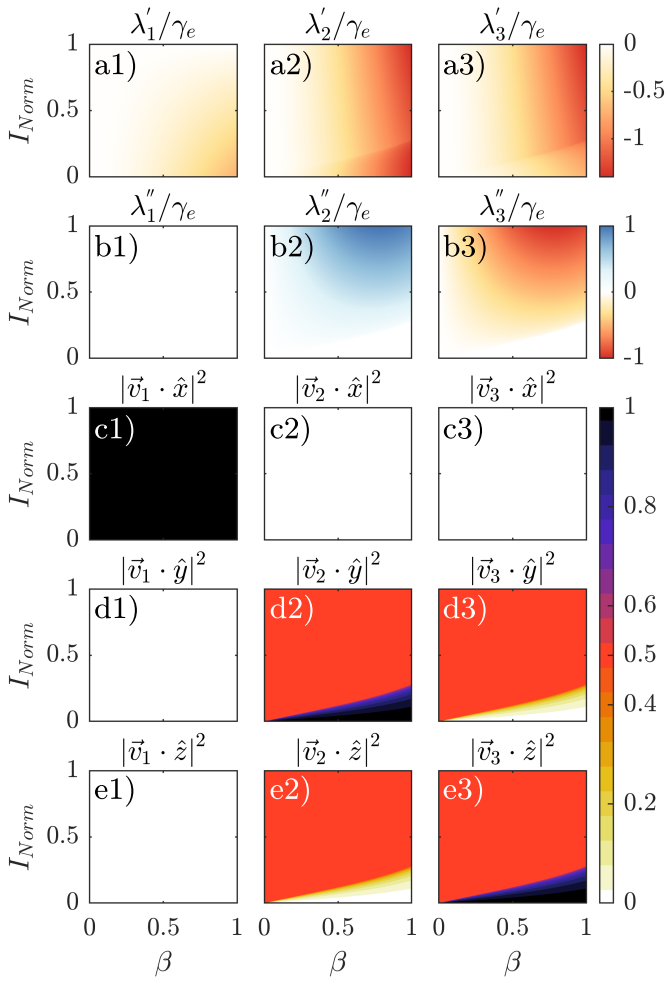

FIGURE 4.3: Real (a) and imaginary (b) part of the three eigenvalues, $\lambda_{1,2,3}$, of the coefficient matrix in Equation (4.41) for $I_1 = I_2 = I_{Norm}$ and $\gamma_0 = 0$. The eigenvalues are rendered versus the absolute value of the overlapping integral and QE-electron interaction strength. x (c), y (d) and z (e) components of the eigenvectors, $\vec{v}_{1,2,3}$, as a function of I_{Norm} and β/π.

and $\lambda_3 = -(\gamma_0 + 2g_1)$. The system dynamics therefore consists of an exponential decay of the Bloch vector to the steady state, which takes place even in the absence of radiative QE decay, through the electron-induced dephasing mechanisms introduced in the previous subsection, which is weighted by $g_1 \propto \sin^2(\beta)$. Figure 4.3 displays the real (a) and

imaginary (b) part of the eigenvalues, $\lambda_{1,2,3}$, for real $I_1 = I_2 = I_{Norm}$ and $\gamma_0 = 0$. These are rendered as a function of I_{Norm} and the coupling strength β. Note that, in the small radiative decay regime, γ_0 enters in the coefficient matrix of Equation (4.41) through the identity matrix, which means that its effect is limited to a shift in the real part of the eigenvalues. All eigenvalues have negative real part and present vanishing (b1), positive (b2) or negative (b3) imaginary part. Thus, all describe an exponential decay into the steady state, but also an oscillatory Rabi-like dynamics, which will give rise to transient states beyond those in Figure 4.2. This oscillatory behaviour only takes place in regions of panels (b2) and (b3), where $\lambda''_{2,3}/\gamma_e$ are non-zero. These are delimited by the inequality $|I_{Norm}\sin(2\beta)| > \sin^2(\beta)$ (Rabi frequency larger than electron dephasing rate).

In the limit of weak QE-electron coupling and weak radiative decay, the eigenvalues of the coefficient matrix acquire the form

$$\begin{aligned}
\frac{\lambda_1}{\gamma_e} &= -\frac{\gamma_0}{\gamma_e} - \beta^2\left[1 - |I_2|\,\cos\left(2\,\theta_1 - \theta_2\right)\right], \\
\frac{\lambda_2}{\gamma_e} &= -\frac{\gamma_0}{\gamma_e} - \beta^2\frac{\left(3 + |I_2|\,\cos\left(2\,\theta_1 - \theta_2\right)\right)}{2} + 2\mathrm{i}|I_1|\beta, \\
\frac{\lambda_3}{\gamma_e} &= -\frac{\gamma_0}{\gamma_e} - \beta^2\frac{\left(3 + |I_2|\,\cos\left(2\,\theta_1 - \theta_2\right)\right)}{2} - 2\mathrm{i}|I_1|\beta,
\end{aligned} \tag{4.43}$$

where we have written $I_n = |I_n|e^{i\theta_n}$ to highlight the different roles of their amplitude and phases. As anticipated above, the imaginary part of the eigenvalues is proportional to the absolute value of I_1, while I_2 only modifies the real part. Thus, one can write the Rabi-like frequency for the system in the weak coupling limit as $\Omega_R^{wc} = 2|I_1|\gamma_e\beta$ [310, 313], which recovers the result in Equation (4.36) for $|I_1| = 1$. Equations (4.43) reveal that for vanishing γ_0/γ_e, smaller β values lead the QE to experience longer oscillatory transients before reaching the steady state. Importantly, Eq. (4.43) also shows that the phases of the overlapping integrals have an important influence on the exponential relaxation, allowing to slow down or speed up these dynamics for QE states along the eigenvectors.

In Fig. 4.3 we also show the squared absolute value of the components

of the eigenvectors $\vec{v}_{1,2,3}$, associated to the three eigenvalues in panels (a)-(b). The components along x, y, and z are rendered against I_{Norm} and β in panels (c), (d), and (e), respectively. Figure 4.3(c) reveals that the projection along x of the Bloch vector representing any QE state is completely governed by $\vec{v}_1$, and therefore experiences a purely exponential decay in time. On the contrary, the Bloch vector projection within the yz-plane does not evolve monotonically, as it involves eigenvectors $\vec{v}_2$ and $\vec{v}_3$. This indicates that the QE excited and ground populations (given by the z-component of the state vector) undergo Rabi oscillations[6]. In fact, the plane of oscillation depends on the phase of the overlapping integrals $I_{1,2}$ (both are real in Figure 4.3). It can be shown that for negligible $|I_2|$, the plane always contains the z-axis, and that the angle it forms with x axis is $\varphi = -\operatorname{atan}(1/\tan(\theta_1)) = \theta_1 - \pi/2$. This behaviour is inherited from the ideally modulated case, and stems from the dependence of the QE final populations on the initial coherences, since this contribution becomes maximal when I_1 and QE coherences are $\pm\pi/2$ out of phase, as illustrated in Equation (4.34).

The dependence of the QE dynamics on θ_1, the phase of the overlapping integral I_1, is analysed in more detail in Figure 4.4(a). It renders the trajectories followed by the state vector of a QE initially in its ground state for various values of θ_1. The limit of negligible purity loss is taken: $\beta = 10^{-3}$ and $\gamma_0 = 0$. We can observe that the QE state lays always at the surface of the Bloch sphere and the trajectory plane rotates with θ_1. This mechanism allows reaching any point on the surface of the Bloch sphere, which shows the capability of modulated free electrons for QE state preparation for low β and large γ_e. The detrimental effect of increasing the QE-electron interaction is showcased in Figure 4.4(b), where $\theta_1 = -\pi/2$ so that the dynamics take place within

[6] In absence of radiative loss, for weak modulation, the z component of the Bloch vector exponentially relaxes to a maximally mixed state and for a QE initially in the ground state one has $z = -e^{\lambda_i' t}$, with an associated excited state probability $P_e(t) = \frac{1+z(t)}{2}$, which at early times $P_e(t) \propto t$. On the contrary, for strong modulation, the complex eigenvalues will appear in complex-conjugate pairs giving $z = -e^{\lambda_2' t}\cos\left(\lambda_2'' t\right)$, which in the Rabi-dominated regime presents a quadratic excited state probability at early times $P_e(t) \propto t^2$, in agreement with predictions in Ref. [316].

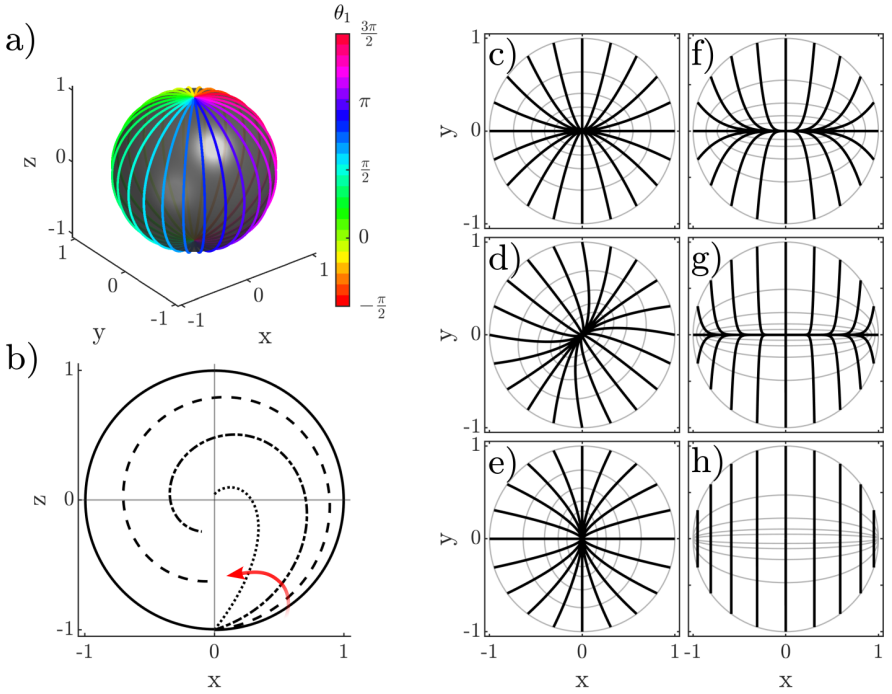

FIGURE 4.4: QE dynamics under continuous driving with modulated electrons. a) QE paths along the surface of the Bloch sphere from the ground to the excited state for $\gamma_0 = 0$ and different θ_1, the phase of I_1. b) QE trajectories for different β values (θ_1 is chosen so that the QE state remains within the xz-plane). The different trajectories correspond to β values of 10^{-3}, 0.1, 0.3 and 0.9, where the red arrow points towards trajectories of higher β values. Panels (c-e) represent the trajectories (black) and equal-time contours (grey) for QEs initially in various pure states within the xy-plane. $I_1 = 0$, $|I_2| = 0.2$, and three values of θ_2: 0 (c), $\pi/2$ (d) and π (e). Panels (f-h) show the same situation as before but for $\theta_2 = 0$ and three values of $|I_2|$: 0.5 (f), 0.9 (g), and 1 (h) respectively.

the xz-plane. The paths followed by the QE state over a single Rabi period, $2\pi/\Omega_R^{sc} = \gamma_e\,|I_1 \sin(2\beta)|$, are displayed for different β. Note that we have corrected the expression of the Rabi frequency to follow the dependence obtained from Eq. (4.30). The trajectories in Fig. 4.4(b) show the purity loss caused by electron-induced dephasing, which is larger for higher coupling strength, making the QE trajectory depart from the edge of the Bloch sphere and towards the maximally mixed state at $z = 0$.

As illustrated in Equations (4.43), the overlapping integral I_2 allows modifying the decay dynamics of QE state vector. As described in Appendix I, I_2 breaks the symmetric decay of the real and imaginary parts of the QE coherences, and introduces two distinct decay rates for them, which in absence of I_1 are $\lambda_\pm = -g_1(1 \pm |I_2|)$ (note that we take $\gamma_0 = 0$). The corresponding eigenvectors read

$$\vec{v}_\pm = \frac{\pm\sqrt{1 \pm \cos(\theta_2)}\text{sign}(\sin(\theta_2))\hat{x} + \sqrt{1 \mp \cos(\theta_2)}\hat{y}}{\sqrt{2}}. \tag{4.44}$$

In the limit $|I_2| \to 1$, λ_- vanishes and $\vec{v}_-$ is preserved in time, while $\vec{v}_+$ decay the fastest. By tuning θ_2, it is possible to tailor the x and y-components of $\vec{v}_-$, and therefore, to select the phase of the coherences in ρ^{QE}. As shown in Appendix I, the phase preserved fulfils[7] $\vartheta \equiv \text{atan}\,(y/x) = \theta_2/2 + N\pi$. This phenomenology is explored numerically in Figure 4.4(c)-(h), which display QE trajectories (black lines) within the xy plane for various initial pure states (located at the edge of the Bloch sphere) and for different values of $|I_2| > 0$ and θ_2. We make $I_1 = 0$, which can be realized by modulating the electrons to twice the QE frequency. As a guide for the eye, we show in light grey lines the equal-time contours for initially pure states in the xy plane, as an illustration of their temporal evolution. These clearly demonstrate the asymmetric decay. Again, we take $\beta = 10^{-3}$ and $\gamma_0 = 0$. In the left panels, $|I_2| = 0.2$ and $\theta_2 = 0$ (c), $\pi/2$ (d) and π (e), showcasing the rotation of the preserved phase from the horizontal to the vertical direction. Right panels correspond to $\theta_2 = 0$ and $|I_2| = 0.5$ (f), 0.9 (g), and 1 (h). They exhibit a slow dynamics along $\vartheta = 0$, and QE trajectories approaching the steady state tangentially to it. Importantly, in Figure 4.4(h), a complete preservation of the phase along $\vartheta = 0$ is apparent, accompanied by a minimal $\Delta\mathcal{P}$. Note, in contrast, that initial phases orthogonal to it decay into the maximally mixed state. Figure 4.4(c)-(h) point towards a strategy to coherently rotate ρ^{QE} within the xy-plane by tuning the phase of I_2 over time. As detailed in the

[7] If one wishes to preserve the coherences in the plane in which Rabi-oscillations take place, then the phase relationship between the modulation integrals must fulfil $\theta_2 = 2\theta_1 + (2N+1)\pi$, ($N \in \mathbb{Z}$), in agreement with the weak coupling limit eigenvalues in Eq. (4.43).

Appendix I, by varying the phase of this overlapping integral in time as $\theta_2(t) = \theta_2(0) + \omega t$ it will possible to keep the QE's state phase-locked to ϑ as long as $\omega \leq 2|I_2|g_1$. This, together with the Rabi oscillations depicted in Fig. 4.4 are mechanisms that are present in the case of ideally modulated electrons and that persist when considering non-ideal modulation. These therefore constitute a complete toolset for quantum state preparation in isolated QEs, even when considering realistically prepared free electron wavefunctions.

The main limitation of the outlined quantum state preparation schemes is that they require a weak QE-electron coupling. Note that β determines the timescale of the coherent dynamics, and therefore, its magnitude relative to the radiative QE lifetime and the electron arrival time set the physical bounds for its implementation. On the one hand, in order to observe Rabi oscillations, the condition $2|I_1|\beta\gamma_e > \gamma_0$ must be fulfilled [310]. On the other hand, for too large coupling, the incoming electrons make the QE state collapse into the maximally mixed state. To avoid this electron-induced dephasing, the condition $2|I_1|\beta\gamma_e > 2\gamma_e\beta^2$ must be met. Both inequalities combined yield

$$\frac{1}{2|I_1|}\frac{\gamma_0}{\gamma_e} < \beta < |I_1|. \tag{4.45}$$

State-of-the-art electron sources of transmission electron microscopes present repetition rates of up to 40 MHz [337], which sets the order of magnitude for γ_e above. Depending on the material platform for the QE realization, decay rates many orders of magnitude apart are available. Here we take two as reference: excitons formed in WSe_2/hBN heterostructures, presenting lifetimes of the order of 200 ns [338] ($\gamma_0 \simeq 4$ MHz), while lifetimes as long as 500 μs have been reported in superconducting qubits [339] ($\gamma_0 \simeq 2$ kHz). This means that for perfectly modulated electrons ($|I_1| = 1$), the integrated coupling strength, β, must lay within $\{0.005, 1\}$ in the former case, and within $\{2 \times 10^{-6}, 1\}$ in the latter. Note that for single-colour, multi-stage preparation methods, theoretical analysis predict attainable modulation integrals as high as $|I_1| = 0.998$ [330], with already existing experimental demonstrations of the proof of concept [335], indicating the technological feasibility of

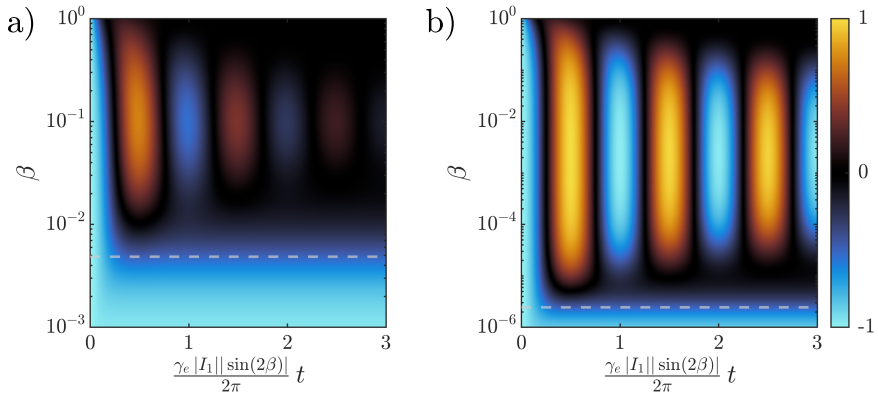

FIGURE 4.5: a,b) Rabi dynamics undergone by the z-component of the Bloch vector as a function of coupling strength for realistic γ_e and two QE realizations: solid-state excitons (a) and superconducting qubits (b). Horizontal white lines plot the bounds established by Equation (4.45), while the upper bound at $\beta = 1$ coincides with vertical axis limit. Both panels share the same colour scale.

the realization of Rabi dynamics with modulated electrons. Figure 4.5 displays the z-component of the QE state vector as a function of coupling strength and time for parameters corresponding to the solid-state exciton (a) and superconducting qubit (b). The time axes are normalized to the Rabi period, $2\pi/\Omega_R^{sc}$. The white horizontal lines on each panel correspond to the lower bound imposed by Equation (4.45), which are in excellent agreement with the region of coupling strengths where the oscillatory dynamics takes place. As expected, the oscillations in the QE population are much longer-lived in the superconducting qubit; even so, oscillatory dynamics are observed in both systems at appropriate coupling strengths. Note that, in both panels, the QE tends towards its ground state ($z = -1$) for β below the radiative decay threshold. On the contrary, as β approaches the electron-dephasing threshold, the QE state tends to the maximally mixed state ($z = 0$).

4.3.4 Quantum state tomography

So far, we have investigated the exploitation of ideal and realistic (non-ideal) modulated electron wavepackets to perform QE state preparation.

In this subsection, we study the use of the latter as a tool for quantum state readout, which comes as an opportunity that only non-perfectly periodic electron combs offer, as briefly discussed in Section 4.3.2. Let us assume that we have prepared an electron in an initial state given as a linear combination of wavevector eigenstates

$$|\psi_e\rangle = \frac{\sum_{n=-\infty}^{\infty} f_n e^{in\phi} |k_0 - nq\rangle}{\sqrt{\sum_{n=-\infty}^{\infty} f_n^2}}, \tag{4.46}$$

where f_n is a real constant and ϕ is the phase difference between consecutive wavevector peaks. This electron interacts with a two-level system in an arbitrary state, ρ_0^{QE}, so that the initial state of the system is $\rho_0 = \rho_0^{\mathrm{QE}} \otimes |\psi_e\rangle\langle\psi_e|$, and the final state, obtained by the use of the scattering matrix in Equation (4.29), is $\rho = \hat{S}\rho_0\hat{S}^\dagger$. Contrary to previous sections, we trace now over the QE degrees of freedom to obtain the free-electron density matrix after the interaction, $\rho^e = \mathrm{Tr}_{\mathrm{QE}}\{\rho\}$. This allows us to compute the expectation value for the electron population with wavevector k, $\langle\hat{n}_k\rangle = \mathrm{Tr}\{\hat{c}_k^\dagger\hat{c}_k\rho^e\}$ (with $\hat{c}_k$ being the annihilation operator for an electron of wavevector k [P5, 310]), having

$$\begin{aligned}\langle\hat{n}_k\rangle =& \frac{1}{\sum_n f_n^2}\sum_n \Big\{ \cos(\beta)^2 f_n^2 \\ &+ \frac{\sin(\beta)^2}{2}\left[f_{n+1}^2 + f_{n-1}^2 + z\left(f_{n+1}^2 - f_{n-1}^2\right)\right] \\ &- \frac{|d|}{2}\sin(2\beta)\sin(\phi_d - \phi) f_n\left(f_{n+1} - f_{n-1}\right)\Big\}\delta_{k,k_0-nq},\end{aligned} \tag{4.47}$$

where we have written the initial state of the QE in Bloch basis in the usual form, $\rho_0^{\mathrm{QE}} = (\mathbb{1} + x\hat{\sigma}_1 + y\hat{\sigma}_2 + z\hat{\sigma}_3)/2$, and for compactness we have defined $d \equiv x + iy$, and $\phi_d \equiv \arg(d)$. Equation (4.47) reveals that the final electron wavevector distribution is composed by peaks distributed integer multiples away from k_0 (the central wavevector of the initial electron wavefunction), and that the final distribution is sensitive to the three degrees of freedom of ρ_{QE} [312, 315]. Importantly, this indicates that, in principle, it is possible to perform quantum state reconstruction of QE states by modulated free electrons.

The amount of information carried by the free-electron wavefunction

after the interaction can be measured through its degree of entanglement with the QE state. As we are dealing with a bipartite system in a pure state, we can use the Wooters concurrence [340] as the witness of the electron-QE degree of entanglement

$$\mathcal{C} \equiv \sqrt{2(1 - \mathrm{Tr}\{(\rho^e)^2\}} = \sqrt{1 - \mathcal{P}}, \tag{4.48}$$

where $\mathcal{P}$ is the purity of the free-electron reduced density matrix, defined as in Equation (4.33). $\mathcal{C}$ ranges from 0, for a separable state, to 1, for a maximally entangled one. Equation (4.48) establishes that the concurrence is uniquely determined by $\mathcal{P}$, depending monotonically on it, and vanishing as it approaches unity. For the initial electron wavefunction in Equation (4.46) interacting with a QE with an arbitrary density matrix $\rho_0^{\mathrm{QE}} = (\mathbb{1} + x\hat{\sigma}_1 + y\hat{\sigma}_2 + z\hat{\sigma}_3)/2$, we have

$$\begin{aligned}\frac{\mathcal{C}^2(\rho)}{\sin(\beta)^2} =& 2(2 - |d|^2)(1 - {I_1}^2)\cos(\beta)^2 \\ &+(1 - z^2)(1 - {I_2}^2)\sin(\beta)^2 \\ &+2z|d|\sin(\phi - \phi_d)\sin(2\beta)I_1(I_2 - 1) \\ &+2({I_1}^2 - I_2)|d|^2\cos(2(\phi - \phi_d))\cos(\beta)^2,\end{aligned} \tag{4.49}$$

where we have used that $\sqrt{|d|^2 + z^2} = 1$ (QE initially in a pure state), and I_i are the modulation integrals of the electronic wavefunction. Note that Eq. (4.49) has been written in such a way that in order for the concurrence to vanish, both I_1 and I_2 must tend to 1. Consider for instance that the initial electronic wavefunction is formed by N equal amplitude peaks, then the two modulation integrals behave as $I_1 = \max\{(N-1)/N, 0\}$ and $I_2 = \max\{(N-2)/N, 0\}$. From these expressions, the limiting forms of the concurrence for monochromatic and perfectly modulated electrons are

$$\mathcal{C}(\rho) \overset{N=1}{=} \sin(\beta)\sqrt{4 - 2|d|^2 - (3 + z^2 - 2|d|^2)\sin(\beta)^2}, \tag{4.50}$$

$$\mathcal{C}(\rho) \overset{N\to\infty}{=} 0. \tag{4.51}$$

For an electron wavefunction consisting in a single wavevector peak, the

final entanglement depends both on the initial state of the QE and the coupling parameters. In particular, Eq. (4.50) predicts that maximal entanglement is possible when the QE is initially in the fully excited or ground state ($z = \pm 1$), and $\beta = \pi/4$, as can be seen from the zero final QE purity shown in Fig.4.1(a) after interaction. In the case of a perfectly modulated electron, the final concurrence tends to zero. This limiting behaviour was already discussed in Section 4.3.2, where we discarded perfectly modulated electrons as tools for QE quantum state reconstruction. In Figure 4.6, we display the maximum concurrence attainable for each free-electron configuration, labelled through the pair of parameters $\{N, \beta\}$ and computed over all possible combinations of ${\rho_0}^{\mathrm{QE}}$ and electronic modulation phase, ϕ. It shows that the degree of entanglement monotonically diminishes with decreasing coupling strength and comb size. High concurrence is possible for $N > 1$, which indicates that, in principle, information can be extracted efficiently from the system, while having access to the phase properties of the QE coherences. In what follows, we explore this idea of using electron combs with few modulation wavevector peaks to readout the state of a QE, and compare this strategy with using monochromatic wavefunctions ($N = 1$).

We analyse first the case of a monochromatic wavefunction by feeding Equation (4.47) with $f_n = \delta_{n0}$. The final electronic state is composed by three wavevector components: zero-loss peak, energy loss and energy gain sidebands. Their amplitudes encode the probabilities for the electron wavevector to remain as before the interaction, or to gain, or lose a quanta matching the QE optical transition. These are given by

$$\langle \hat{n}_{k_0} \rangle = \cos(\beta)^2, \tag{4.52}$$

$$\langle \hat{n}_{k_0 \pm q} \rangle = \frac{\sin(\beta)^2}{2} \left[1 \pm z\right]. \tag{4.53}$$

Equation (4.52) makes evident that the zero-loss peak depletion gives information about the QE-electron coupling strength, while the imbalance between energy gain and loss sidebands in Equation (4.53) reveals the presence of an initial population in the QE excited state. Crucially, no information about the QE coherences can be extracted from the free-electron wavefunction, and thus it is impossible to ascertain the quantum

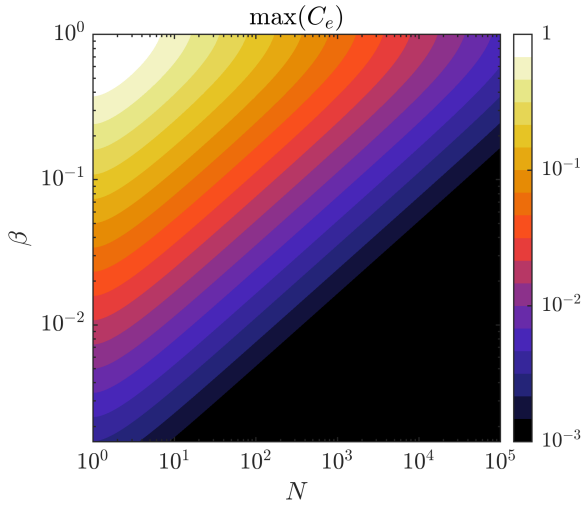

FIGURE 4.6: Maximum possible electron-QE entanglement as measured by the concurrence as a function of coupling strength and number of momentum peaks in the initial electronic wavefunction. The maximum is taken over the set of all possible modulation phases, ϕ, and initial QE states (x, y, z), with $\sqrt{x^2 + y^2 + z^2} \leq 1$.

nature of the emitter state, since pure and mixed states sharing the same Bloch z-component would lead to exactly the same electron wavevector spectra. This we show in Figure 4.7, where panel (a) plots the spectrum for a monochromatic wavefunction before (black) and after (purple) the interaction with a QE prepared in a certain initial state. One can see how the zero-loss peak is depleted by the interaction with the QE and the energy loss and gain sidebands appear with different amplitudes. From this spectrum, the QE state reconstruction in Figure 4.7(b) was obtained. The lack of information about the coherences (represented by question marks) makes the assessment of the purity of the QE state impossible.

Equation (4.47) shows that at least two wavevector components spaced by q are needed in the initial electron wavefunction to probe the QE coherences [312]. Considering an electron wavepacket with initial wavevector components $|k_0\rangle$ and $|k_0 \pm q\rangle$, with $f_1 = f_{-1}$, 5 different

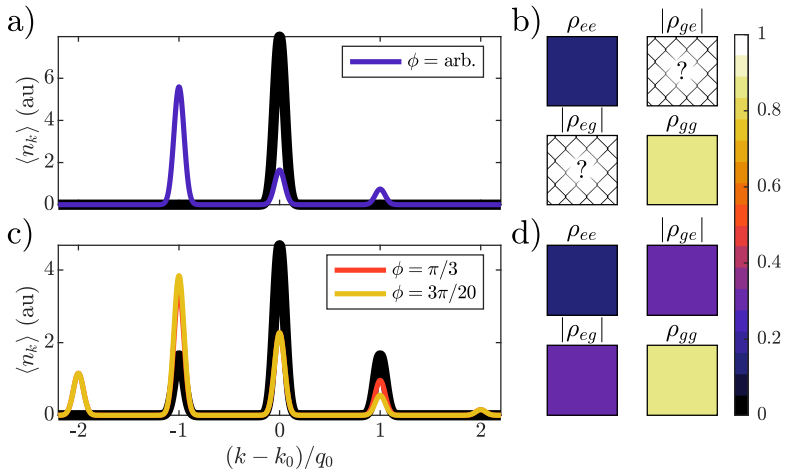

FIGURE 4.7: Quantum state tomography with free electrons. b,d) Electronic wavevector distribution before (black) and after interaction with the QE in the case of a monochromatic electron (b) and non-ideal modulated electron (d). c,e) Quantum state reconstruction from the data obtained in the experiments shown in panels (b,d) respectively, displaying incomplete (c) and complete (e) state reconstruction for the monochromatic and non-ideal modulated electron respectively.

wavevector components emerge in the final electron state after the interaction with the QE, with spectral amplitudes given by

$$\langle \hat{n}_{k_0} \rangle = \cos(\beta)^2 \alpha_0^2 + \frac{\sin(\beta)^2}{2} \alpha_1^2 \tag{4.54}$$

$$\langle \hat{n}_{k_0 \pm q} \rangle = \frac{\cos(\beta)^2}{2} \alpha_1^2 + \frac{\sin(\beta)^2}{2} [1 \pm z] \alpha_0^2, \mp \frac{|d|}{2\sqrt{2}} \sin(2\beta) \sin(\phi_d - \phi) \alpha_0 \alpha_1, \tag{4.55}$$

$$\langle \hat{n}_{k_0 \pm 2q} \rangle = \frac{\sin(\beta)^2}{4} \alpha_1^2 [1 \pm z], \tag{4.56}$$

where $\alpha_1 = \sqrt{2} f_1 / \sqrt{f_0^2 + 2f_1^2}$ and $\alpha_0 = f_0 / \sqrt{f_0^2 + 2f_1^2}$. We now introduce the symmetric and antisymmetric combination of the n-th spectral amplitude as $n_j^S \equiv \langle \hat{n}_{k_0 + jq} \rangle + \langle \hat{n}_{k_0 - jq} \rangle$ and $n_j^A \equiv \langle \hat{n}_{k_0 + jq} \rangle - \langle \hat{n}_{k_0 - jq} \rangle$. These can be evaluated from Equations (4.55) and (4.56), and the magnitudes characterizing the initial state of the system can be obtained

from these as

$$z = \frac{n_2^A}{n_2^S}, \tag{4.57}$$

$$\sin(\beta)^2 = \frac{2n_2^S}{\alpha_1^2}, \tag{4.58}$$

$$|d|\sin(2\beta)\sin(\phi - \phi_d) = \frac{\sqrt{2}}{\alpha_0\alpha_1}\left(n_1^A - 2\frac{\alpha_0^2}{\alpha_1^2}n_2^A\right). \tag{4.59}$$

The initial QE populations are uniquely specified by Equation (4.57), and assuming weak electron-QE interaction, Equation (4.58) gives $\beta = \sin^{-1}(\sqrt{2n_2^S}/|\alpha_1|)$ [P4]. To extract the QE coherences, one can perform the measurement with different ϕ (in the initial modulated wavefunction). It can be shown that two different phases are sufficient to determine coherences of the system. By defining $\gamma_j = \frac{\sqrt{2}}{\alpha_0\alpha_1}\left(n_1^A - 2\frac{\alpha_0^2}{\alpha_1^2}n_2^A\right)$ as the evaluation of the right-hand side of Eq. (4.59) corresponding to the phase ϕ_j, the coherences are given by

$$d = \frac{1}{\sin(2\beta_0)}\frac{\left[\gamma_1 e^{i\phi_2} - \gamma_2 e^{i\phi_1}\right]}{\sin(\phi_1 - \phi_2)}, \tag{4.60}$$

which shows that complete arbitrary QE state retrieval is possible under modulated electron probing. We showcase this protocol in Figure 4.7(c), where the initial (black) and final (orange, yellow) wavevector spectra for a QE in a certain state are displayed. Note that the free-electron spectra after the interaction are different for the two modulation phases, $\phi_{1,2}$. This proves that the initial QE state has non-zero coherences, and it is therefore not merely a statistical mixture. By applying the strategy outlined above, we can construct the initial QE density matrix, as shown in Figure 4.7(d) where, in contrast to Figure 4.7(b), a full characterization of the QE coherences is possible.

Let us clarify that the QE coherences in Figure 4.7(d) were obtained under the assumption that the interaction strength is positive and real. For general complex β, we can follow the procedure described in Section 4.3.2: by performing a basis change and absorbing the phase of the coupling strength into the ground state of the QE, the scattering matrix takes the same form as if the coupling strengths were real and

positive. This means that it is enough to multiply the QE coherence in Figure 4.7(d) by $\exp\{-i\phi_\beta\}$ to extend the result to complex coupling strengths, while the z-component of the Bloch vector remains unchanged. Therefore, in general, to perform proper state readout it is needed to have characterized the complex QE-electron coupling strength in a previous experiment. This can be done by extending recently proposed, homodyne-based ideas in the realm of bosonic modes [293] to QEs. Note that that for interactions with an isolated QE, this phase factor is irrelevant, while for ensembles of interacting QEs, the relative phases of their ground states can have an important role. Finally, we remark that, even in the situation in which the coupling strength is complex valued, our protocol allows determining unequivocally the purity of the initial QE state, as $\mathcal{P} = \sqrt{z^2 + |d|^2}$, is insensitive to phase shifts in d.

4.4 Modulated electrons to probe and manipulate polaritonic targets

Much research attention has focused lately on the strong-coupling (SC) phenomena that emerge when quantum emitters (QEs), such as organic molecules, solid-state vacancies, or quantum dots, are placed within the near-field of photonic resonators, such as Fabry-Perot cavities, metamaterial devices, or nanoantennas [235, 341, 342]. In setups involving macroscopic ensembles of QEs, the formation of polaritons (hybrid light-matter states) has opened the way for the manipulation of matter for purposes such as the modification of material properties or the control of chemical reactions [56, 343]. The high complexity of these systems, however, makes their theoretical description extremely challenging, which severely limits the capability of current theories to reproduce experimental results [342, 344]. Complementarily, polariton formation in systems comprising a single (or few) QEs [51, 265, 345] have been investigated for quantum light generation [42, 346] in studies that have also shed light into different aspects of light-matter SC at the macroscopic scale [233]. However, the inherent dark character of these microscopic systems [347], which must feature large light-matter interaction strengths and small

radiative losses, prevents their full characterization by far-field, optical means. This makes near field probes very interesting candidates for the study of strong light-matter interaction, as shown in Sec. 3.3 of this thesis.

In this section, we use the model Hamiltonian derived from mQED principles [27, 39, 321, 348] in Sec. 4.2 to describe the quantum interaction between a modulated electron wavepacket and a polaritonic target comprising a single QE (treated as a two-level system) and a nanophotonic cavity. For simplicity, we consider a cavity with spherical symmetry, and to unveil clearly quantum-coherent effects in the light-matter SC, we restrict its Hilbert space to the lowest (degenerate), dipolar modes that it supports. In this section, we explore the polariton energy ladder of the hybrid photonic-excitonic system through both the free-electron wavepacket and photon spectra in EELS-, CL- and PINEM-like setups, and finally, we demonstrate the power of modulated electron beams to probe and control light-matter states in the SC regime. Particularly, we will show that, since modulated electrons modify the state of the target through quantum interference, it is possible for modulated electrons to address specific transitions independently in a system in which several energy scales coexist. This points to the possibility of transforming traditional free-electron microscope setups, incoherent and broadband in nature, to perform coherent imaging with simultaneous nanoscale resolution [293].

4.4.1 Target-probe system and Hamiltonian

In this section, we first introduce the polaritonic target for our study and particularize the Hamiltonian derived in Section 4.2.

The target-probe system that we have chosen to assess the ability of free electrons to explore light-matter SC is depicted in Fig. 4.8. We consider a nanophotonic cavity (typically a metallic nanoparticle), sustaining dipolar-like confined modes overlapping with the dipole moment, $\mu_{QE} = 1\,\mathrm{e}\cdot\mathrm{nm}$ (parallel to x-axis), of a QE placed in close proximity of the nanoparticle surface (the QE-cavity distance is similar to the cavity radius itself, $b_{c-QE} \approx R$), also along the x-direction. The free-electron

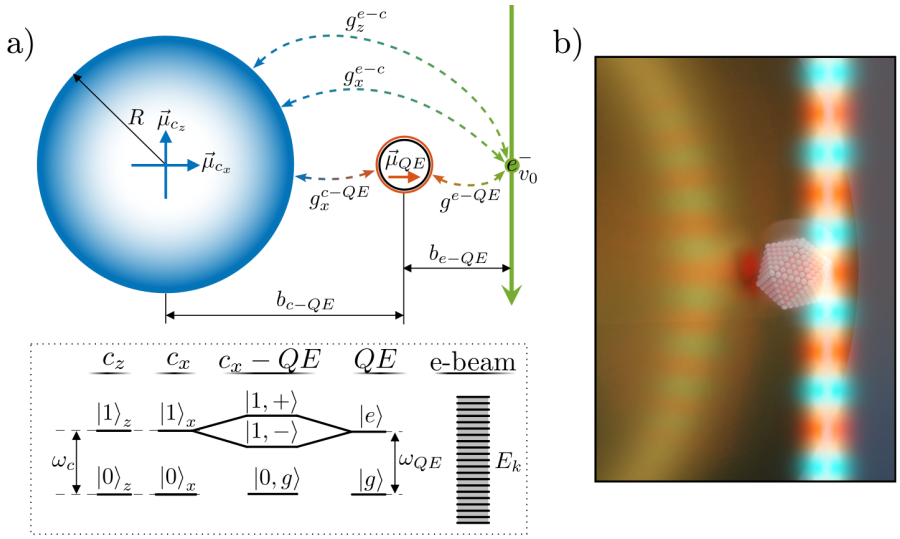

FIGURE 4.8: a) Sketch of the system under consideration. Top: an electron wavepacket with central velocity $v_0\hat{z}$ and kinetic energy E_k passes through a target system composed of a nanoparticle cavity and a QE. The nanoparticle radius is 10 nm and its spectrum is restricted to two degenerate dipolar cavity modes with energy $\hbar\omega_c = \hbar\omega_{QE} = 2$ eV, at resonance with the QE. Bottom: illustration of the energy levels of $\hat{H}_0$ for target (left) and electron beam (right). The z-dipolar cavity mode is uncoupled from the QE, while the x-dipolar one is strongly coupled to it, giving rise to non-degenerate polaritonic states. Note that we represent the energy levels of the electron as a quasi-continuum, as any final momentum value is *a priori* allowed. b) Rendering of system sketched in (a), where a modulated free electron passes in close proximity to the polaritonic target formed by a QE (represented as a quantum dot) and a gold nanoparticle.

wavepacket, with energies in the order of 10 keV, passes through the compound target along the $\hat{z}$ direction with impact parameters b_{e-c} and b_{e-QE} with respect to cavity and QE, respectively. QE and cavity are, unless specified otherwise, at resonance, with $\hbar\omega_c = \hbar\omega_{QE} = 2$ eV. This enables us to neglect the contribution from higher order, multipolar modes in the QE-cavity interaction. To maximize their coupling, we set $R = 10$ nm, which corresponds to modal dipole moments of $\mu_{c_{x,y}} = 40\, e{\cdot}$nm, as given per Eq. (4.21). This idealized, but feasible, system serves as a test-bed to explore the phenomenology resulting from

the electron probing of polaritonic states.

The Hamiltonian describing the interaction is given in Sec. 4.2.2. It accounts for the coupling between free electrons, a QE and the three degenerate dipolar modes of a small nanoparticle, treated within the quasi-static approximation[8]. The system Hamiltonian can be written as $\hat{H} = \hat{H}_0 + \hat{H}_I$, with

$$\hat{H}_0 = \hbar \sum_{i=x,z} \omega_c \hat{a}_i^\dagger \hat{a}_i + \hbar\omega_{QE} \hat{\sigma}^\dagger \hat{\sigma} + \sum_k E_k \hat{c}_k^\dagger \hat{c}_k + \hbar g_x^{c-QE} \left[\hat{a}_x^\dagger \hat{\sigma} + \hat{a}_x \hat{\sigma}^\dagger \right], \tag{4.61}$$

$$\begin{aligned} \hat{H}_I =& \sum_q \hat{H}_{I,q}\, \hat{b}_q \\ =& \hbar \sum_{i=x,z} \sum_q g_{q,i}^{e-c} \hat{b}_q \left[\hat{a}_i^\dagger - \hat{a}_i \right] \mathrm{sign}(q) + \hbar \sum_q g_q^{e-QE} \hat{b}_q \left[\hat{\sigma} - \hat{\sigma}^\dagger \right] \mathrm{sign}(q). \end{aligned} \tag{4.62}$$

$\hat{H}_0$ describes the free dynamics of target and electron beam independently, and $\hat{H}_I$ their interaction. This Hamiltonian captures the terms previously used to study free electron interaction with optical modes [280, 302, 303], QEs [310, 312, 317], and polaritonic systems [318, 319]. We also note that the parametrization through macroscopic QED allows retrieving the classical results from EELS theory (see Sec. E.4).

In Eqs. (4.61)-(4.62), $\hat{a}_i$ $(i = x, z)$ are the annihilation operators for the degenerate dipolar cavity modes (note that, by symmetry, we can consider only those within the xz-plane in 4.1), $\hat{\sigma} = |g\rangle\langle e|$ is the two-level-system lowering operator for the QE excitons, and $\hat{c}_k$ is the operator describing the annihilation of free-electron population in the wavepacket component with momentum k and energy $E_k = (\hbar k)^2/2m_e$. The fourth term in Equation (4.61) accounts for the cavity-emitter coupling in the rotating wave approximation with strength given in Sec. 4.2.2, that we

[8] The impact of retardation and nonlocal effects, beyond the quasi-static picture, are discussed in Section E.4 and in Ref. [P5], indicating that no qualitative changes take place upon considering a more sophisticated description of the nanoparticle behaviour.

reproduce here as

$$g_x^{c-QE} = \frac{\omega_{QE}}{3}\sqrt{\frac{\pi}{2}\left(\frac{R}{b_{c-QE}}\right)^3 \frac{\mu_{QE}^2}{\hbar\omega_c\epsilon_0 b_{c-QE}^3}}. \tag{4.63}$$

Note that since μ_{QE} is oriented along the $\hat{x}$ direction, the couplings in Eq. (4.19) indicate that the QE only couples to the cavity mode with an effective dipole moment along x-direction. The two Holstein-like terms in Equation (4.62) describe the target-probe interaction, where $\hat{b}_q = \sum_k \hat{c}_{k-q}^\dagger \hat{c}_k$ is the ladder operator that shifts the free-electron momentum by an amount q, which is transferred to or from the cavity modes (first terms) or QE exciton (last term). Note that, contrary to the QE, the passing electrons couple to both the x- and z-dipolar cavity modes. The electron-cavity and electron-QE coupling strenghts, given in Sec. 4.2.2, can be written as

$$g_{q,x}^{e-c} = \frac{e\hbar k_0}{3m_e L} q^2 K_1(|q|b_{e-c})\sqrt{\frac{1}{\hbar\epsilon_0}\frac{\pi}{2}\frac{R^3}{\omega_c}}, \tag{4.64}$$

$$g_{q,z}^{e-c} = \frac{e\hbar k_0}{3m_e L} q^2 K_0(|q|b_{e-c})\sqrt{\frac{1}{\hbar\epsilon_0}\frac{\pi}{2}\frac{R^3}{\omega_c}}, \tag{4.65}$$

$$g_q^{e-QE} = \frac{ek_0 q^2 \mu_{QE}}{2\pi m_e L\epsilon_0\omega_{QE}} K_1(|q|b_{e-QE}), \tag{4.66}$$

where $\hbar k_0 = m_e v_0 \gg \hbar|q|$ is the incoming momentum of the passing electrons, which is ~ 4 orders of magnitude larger than the momentum they exchange with the cavity/emitter ($|q| \sim \omega_{c,QE}/v_0$). This fact enables us to operate under the nonrecoil approximation [151]. $K_{0,1}(\cdot)$ are modified Bessel functions of the second kind, and we have assumed positive impact parameters ($b_{i-j} > 0$ for all i, j). L is the length scale introduced in the particle-in-a-box quantization of the electron momentum. As shown in Sec. 4.2.3, the scattering matrix elements will depend on the integrated coupling strength, β, which is defined as $\beta = Lg/v_0$ for the different couplings under consideration. From the structure of the couplings given in Sec. 4.2.2, one sees that all the physical observables will not depend on the L lengthscale, formally introduced for clarity.

We are interested in employing the electron beam as a tool to explore light-matter SC in the target. Therefore, we will proceed by diagonalizing (analytically) the bare Hamiltonian, $\hat{H}_0$, accounting for the cavity-QE interactions at all orders in the coupling strength g_x^{c-QE} and obtaining the polaritonic eigenstates of the target. On the contrary, taking advantage of the fact that the incoming electrons only alter the target weakly, the interaction Hamiltonian, $\hat{H}_I$, will be treated perturbatively, only considering processes up to the first interaction order in $g_{q,i}^{e-c}$ and g_q^{e-QE} in the Magnus expansion, presented in subsection 4.2.3.

The bottom panel of Fig. 4.8(a) illustrates the energy levels of the target (left) and electrons (right). The sketch of the ground and first excitation manifolds for the target shows an uncoupled z-dipolar cavity mode and the emergence of polaritonic states as a result of the hybridization of the x-dipolar cavity mode and the QE exciton. The eigenstates of $\hat{H}_0$ can be expressed as a product of the free electron states, $|k\rangle$, the Fock states of the uncoupled cavity mode, $|n\rangle_z$, and the polaritonic states. If cavity and QE are at resonance (which is the reference configuration for our study), these can be simply written as $|N,\pm\rangle = (|N\rangle_x |g\rangle \pm |N-1\rangle_x |e\rangle)/\sqrt{2}$ in the N-th manifold, with energies $\hbar\omega_{N,\pm} = \hbar(N\omega_{c,QE} \pm \sqrt{N} g_x^{c-QE})$ [56, 235, 341]. Therefore, we have

$$\hat{H}_0 |\phi\rangle \otimes |k\rangle = [E_\phi + E_k] |\phi\rangle \otimes |k\rangle \,, \tag{4.67}$$

for the bare system, where we have written the bare Hamiltonian eigenstates as a product of the target eigenstates, $|\phi\rangle = |n\rangle_z \otimes |N,\pm\rangle$ with $E_\phi = \hbar\omega_c n_z + \hbar\omega_{N,\pm}$, and the free electron eigenstates, $|k\rangle$ with eigenenergies E_k. On the other hand, precisely due to the complexity of the polariton energy ladder, the electrons may acquire any energy value E_k and therefore their energy spectrum in Fig. 4.8(a) is represented as a quasi-continuum. In contrast, when free electrons interact with quantum targets with a single relevant energy scale, like isolated QEs [310, 312, 317] (see Sec. 4.3), or single optical modes [280, 302, 303], the state of the free electrons after interaction can be simply characterized by the number of exchanged photons, greatly simplifying the problem. The contrast will become more apparent when we construct the general form

of the scattering matrix in the next section.

4.4.2 Electron-target interaction

In this section we apply the scattering matrix formalism [304, 310, 312] introduced in subsection 4.2.3 to describe the change of the target states by the passing electrons. This amounts to applying the propagator for the interaction Hamiltonian in the interaction picture. The plasmonic nature of the cavity translates into optical mode lifetimes in the range of several tens of femtoseconds, while the QE lifetime is of the order of hundreds of ps. The electron-target interaction time can be estimated from the ratio $\lambda_c/4v_0 \simeq 2$ fs (where we have assumed a size for the subwavelengh-confined cavity mode of $\lambda_c/4$), which is at least one order of magnitude faster than the lifetime of the target states [59]. Thus, using the quasi-instantaneous character of the electron-target interaction, we can describe the mixing of the target eigenstates, $|\phi\rangle$, induced by the free electron through

$$\hat{S} = \exp\left\{-i\sum_{\phi,\phi'} \hbar_{I,\phi,\phi'} \left|\phi\right\rangle\!\left\langle\phi'\right| \hat{b}_{q_{\phi,\phi'}}\right\}, \tag{4.68}$$

$$\hbar_{I,\phi,\phi'} = \frac{L}{\hbar v_0} \left\langle\phi\right|\hat{H}_{I,q_{\phi,\phi'}}\left|\phi'\right\rangle . \tag{4.69}$$

The quantity $q_{\phi,\phi'} \equiv \frac{(E_\phi - E_{\phi'})}{\hbar v_0}$, accounts for energy conservation in the electron-target interaction, and it appears together with the L/v_0 factor from integrating over all possible momentum exchange, as shown in Eq. (4.25). This L factor in Equation (4.69) cancels with the $1/L$ factors in the expectation values $\langle\phi|\,\hat{H}_I\,|\phi'\rangle$ embedded in the coupling strengths in Eqs. (4.64)-(4.66), which makes the propagator $\hat{S}$ independent of this auxiliary length scale. By relating the initial and final free-electron momenta through the momentum exchanged with the target, $k = k' - q$ and making use of the non-recoil approximation, it is possible to write

$$q_{\phi,\phi'} = \frac{\omega_c(n_z - n_z') + \omega_{N,\pm} - \omega_{N',\pm'}}{v_0}, \tag{4.70}$$

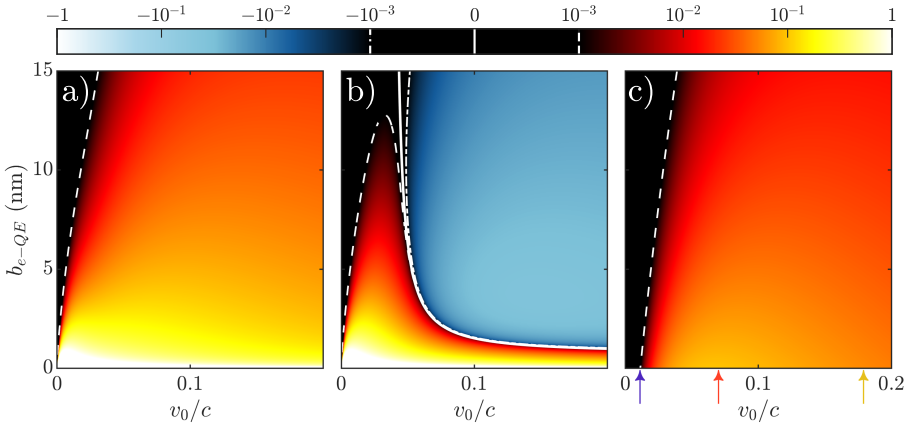

FIGURE 4.9: Matrix elements, $\hbar_{I,G,\phi'}$, connecting the target ground state with states of the first excitation manifold as a function of the free electron-QE distance and the electron speed. a) Upper polariton $|1_+\rangle$, b) Lower polariton $|1_-\rangle$, c) $z-$dipolar mode $|1_z\rangle$. Note that we are omitting the electronic part of the wavefunction, see main text. Solid, dashed, and dotted-dashed white lines plot the isocurves $\hbar_{I,G,\phi'} = 0$, $\hbar_{I,G,\phi'} = 10^{-3}$, and $\hbar_{I,G,\phi'} = -10^{-3}$, respectively. The vertical colour arrows in (c) indicate the configurations considered in 4.10.

As mentioned before, previous works exploring the electron-beam-probing of optical cavities [280] and QEs [310], all the momentum and energy exchanged with the target was in multiples of $\omega_{c,QE}/v_0$ and $\omega_{c,QE}$, since the latter was the only energy scale present in the system. Here, the cavity-QE SC and the resulting polaritonic ladder gives rise to a much more complex landscape of electron-target interactions.

Figure 4.9 shows the adimensional matrix elements $\hbar_{I,\phi,\phi'}$ that connect the ground state of the target, $|\phi\rangle = |G\rangle = |0\rangle_z \otimes |0\rangle_\pm$ and the different states of the first excitation manifold of $\hat{H}_0$. With the cavity and QE parameters introduced above, we obtain $g_x^{c-QE} \approx 80$ meV, which is in accordance with the light-matter interaction strengths reported experimentally in different nanophotonic-based polaritonic systems at the single QE level [51, 265]. Due to the structure of the interaction Hamiltonian, the evaluation of Equation (4.69) for $|\phi'\rangle = |1_\pm\rangle = |0\rangle_z \otimes |1, \pm\rangle$

and $|\phi'\rangle = |1_z\rangle = |1\rangle_z \otimes |0\rangle$ yields [318]

$$\hbar_{I,G,1_\pm} = \frac{L}{\hbar v_0}\left[g^{e-c}_{\omega_{1,\pm}/v_0,x} \pm g^{e-QE}_{\omega_{1,\pm}/v_0}\right], \tag{4.71}$$

$$\hbar_{I,G,1_z} = \frac{L}{\hbar v_0} g^{e-c}_{\omega_c/v_0,z}. \tag{4.72}$$

Equation (4.71) illustrates the power of electron beams for the exploration of light-matter SC. In optical-based spectroscopic techniques, which operate under the far-field, laser-like pumping of the polaritonic target, the driving amplitude of the cavity is orders of magnitude larger than the QE. This is a consequence of the dipole mismatch between them, which is $\mu_{c_{x,z}}/\mu_{QE} \simeq 40$ for the small nanoparticle in our system (see Section E.4.2). In these setups, the polariton population takes place through the cavity, and hence, it is exactly the same (except for dispersion effects) for lower and upper states. When employing a very localized excitation, the electron beam in our case, it is possible to make the absolute value of two terms in Equation (4.71) similar through the tuning of the probe parameters that come into play in the interaction with the target. In this regime, one of the polariton states becomes completely dark to the passing electron, enabling the selective probing of the other one, as all the interaction dynamics will occur solely through it. This phenomenology is similar to the *polariton-blockade* mechanism [319] recently proposed as a resource for quantum information processing.

Figure 4.9 renders $\hbar_{I,G,1_+}$ (a), $\hbar_{I,G,1_-}$ (b) and $\hbar_{I,G,1_z}$ (c), as a function of the electron-QE impact parameter, b_{e-QE}, and the central velocity of the electron wavepacket normalized to the speed of light, v_0/c. We can observe that all the matrix elements decrease with larger distance and lower velocity (see dashed white lines), although only $\hbar_{I,G,1-}$ completely vanishes within the parameter range considered, as indicated by the white solid line in panel (b). As expected from the setup we have chosen (see Fig. 4.8) the electron probes more efficiently the polaritonic states than the z-dipolar cavity mode at small b_{e-QE}. Only at large v_0/c, the three panels acquire similar absolute values, although the elements for the lower polariton change sign and become negative in this regime. The study provided in these three panels serves as a guide for

designing the most appropriate electron-beam configuration to interrogate a given state of the first excitation manifold in the light-matter SC target.

The adimensional matrix elements in Fig. 4.9 acquire values that range between -1 and 1, which means that the propagator in Equation (4.68) can be treated perturbatively in different orders of electron-target interaction for most of the configurations analysed. Note that all the results that follow lie within this perturbative regime. Using the Taylor expansion for the exponent function, and due to the algebraic properties of the $\hat{b}_q$ operators, the scattering matrix of the electron-target interaction may then be written as

$$\hat{S} = \sum_{\phi,\phi'} \mathcal{S}_{\phi,\phi'} \left|\phi\right\rangle\!\left\langle\phi'\right| \hat{b}_{q_{\phi,\phi'}}, \tag{4.73}$$

$$\mathcal{S}_{\phi,\phi'} = \delta_{\phi\phi'} - i\hbar_{I,\phi,\phi'} - \tfrac{1}{2}\sum_{\phi''} \hbar_{I,\phi,\phi''}\hbar_{I,\phi'',\phi'} + \ldots,. \tag{4.74}$$

which shows explicitly the mixing of the states of $\hat{H}_0$ by the passing electrons to all orders in the coupling strengths given by Eqs. (4.64)-(4.66). Since we will be considering quantum states that initially can be written as a product state of free electron and target states, the structure of the scattering matrix then allows to perform operations within the reduced system of the target, and then carry out corresponding operations on the free electron wavefunction. This quasi-analytical character provides us with deep insights into the phenomenology of target-probe interactions. In the following sections, we will use it to unveil how the electron-induced state mixing described by Eq. (4.74) can be exploited for the probing of the polaritonic states in our model cavity-QE system. We will focus first on incoming electrons with a well-defined momentum, and then proceed to explore how modulated electron beams can be used to further characterize light-matter SC phenomena through the engineering of the electron wavefunction.

4.4.3 CL, EELS and PINEM in polaritonic targets

There are two strategies that allow extracting information from the target by electron probing: through the radiation spectrum of the cavity (we neglect the emission from the QE) into the far-field, as done in CL setups, and through measuring the energy lost/gained by the electron beam itself, like in EELS or PINEM experiments. We consider the former first, whose characterization is given by its radiation power spectrum [274]. The expression for this quantity, already given in Eq. (3.16) and reproduced here, reads

$$I(\omega) = \lim_{T\to\infty} \frac{1}{2\pi T} \int_{-\frac{T}{2}}^{\frac{T}{2}} dt \int_{-\infty}^{\infty} d\tau \left\langle \hat{\xi}^{\dagger}(t+\tau)\hat{\xi}(t) \right\rangle e^{-i\omega\tau}, \tag{4.75}$$

where $\hat{\xi} = \mu_{c_{x,z}}(\hat{a}_x + \hat{a}_z)$ is the dipole moment operator of the cavity (describing the coherent light emission [42] by its two degenerate modes) and $\hat{\xi}(t) = e^{i\hat{H}_0 t/\hbar}\hat{\xi}e^{-i\hat{H}_0 t/\hbar}$ describes its evolution in time under the bare Hamiltonian in Equation (4.61). The expectation value in Equation (4.75) is firstly taken over the state $|\phi_f\rangle = \hat{S}\,|G\rangle \otimes |k_0\rangle$, which results from the fast target-probe interaction when the former is initially in its ground state. We have briefly discussed the lifetime of the target states to justify the approximations inherent to Equation (4.68). However, our model is based on a purely Hamiltonian description of the target, given by Equation (4.67). Therefore, the spectrum obtained from Equation (4.75) will consist of a weighted sum of Dirac delta functions. In the following, we will introduce a phenomenological broadening, σ, for the spectral features, to account for the finite lifetime of the target states, by making the replacement $\delta(\omega) \to \frac{\sigma}{2\pi}\frac{1}{\omega^2+\sigma^2/4}$. This Lorentzian lineshape is obtained in the Lindbladian description of open quantum systems [31, 40].

Figure 4.10(a) shows CL-like spectra obtained for aloof electrons with impact parameters $b_{e-QE} = 1$ nm, $b_{e-c} = 11$ nm, and different velocities, indicated by the vertical color arrows in 4.9(c). The far-field intensity spectra are broadened by σ, set to 0.02 eV, an optimistic estimation for plasmonic lifetimes [59] ($1/\sigma = 30$ fs). They are normalized to I_0, the intensity at the polariton maxima in the limit $v_0 \to 0$ (see

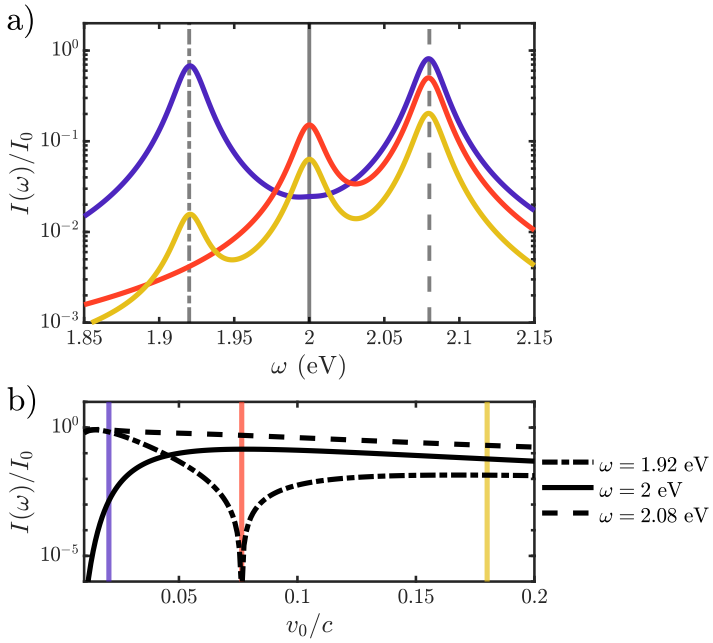

FIGURE 4.10: Far-field light intensity versus photon frequency for passing electrons with $b_{e-QE} = 1$ nm and $b_{e-c} = 11$ nm. a) Power spectra for three different electron velocities, indicated by the vertical arrows in 4.9: $0.02c$ (purple), $0.08c$ (orange) and $0.18c$ (yellow). b) Height of the three maxima in $I(\omega)$ as a function of v_0/c. Vertical lines indicate the configurations considered in (a). Selected frequencies in (b) are shown in (a) as vertical grey lines with matching line styles.

below). Three spectral maxima are apparent, which originate from the upper and lower polaritons, at 2.08 and 1.92 eV, respectively, and the uncoupled $z-$dipole cavity mode at 2 eV. For slow electrons (purple, $v_0 = 0.02c$), the spectrum is dominated by the polariton peaks, which have similar weights. This indicates that the electron-target interaction is mainly taking place through one of the polariton constituents. Indeed, $|g_x^{e-QE}| \gg |g^{e-c}_{\omega_{1,\pm}/v_0,x}|$ in this case, due to the small value of the QE impact parameter. As expected from 4.9(c), there is not an intermediate peak in this spectrum, as $g^{e-c}_{\omega_c/v_0,z}$ is negligible in this configuration.

The spectrum for higher electron velocities, $v_0 = 0.08c$ (orange), does not present the peak at 1.92 eV, which indicates that the lower polariton has become dark to the incoming electron beam. Note that

$g_x^{e-QE} \simeq g_{\omega_{1,\pm}/v_0,x}^{e-c}$ and $h_{I,G,-}$ vanishes in this case, as seen in Fig. 4.9(b). At even larger velocities, $v_0 = 0.18c$ (yellow), the spectral peaks are, in general, lower, but the three of them are clearly visible. In this configuration, all the matrix elements acquire comparable values. Our results reveal the complex dependence of $I(\omega)$ on v_0/c, far from any monotonic trend. In 4.10(b) we analyze it in more detail, by displaying the peak intensity contribution to the CL signal from the three states in the first excitation manifold as a function of the electron velocity. We find that the upper polariton peak is always the largest, while the lower polariton ($z-$dipole mode) is the second largest for low (large) v_0. In the limit $v_0 \to 0$, the upper and lower polariton maxima acquire the same value, I_0, employed for normalization. We can also observe that three far-field intensity maxima approach in the limit of large electron velocity in 4.10(b).

We investigate next the fingerprint of the target-probe interaction in the wavefunction of the passing electron beam. For this purpose, we focus on the reshaping of the momentum distribution of the electron wavepacket, measured by the difference in the population of the states $|k\rangle$ before and after the coupling with the QE-cavity system. Expressed in terms of the number operator $\hat{n}_k = \hat{c}_k^\dagger \hat{c}_k$, this difference is given by

$$\Delta n_k = \langle \hat{n}_k \rangle - \langle \hat{n}_k \rangle^0 , \tag{4.76}$$

where the superscript 0 indicates that the expectation value is evaluated for the electron wavefunction prior to the interaction. 4.11(a)-(c) plots this population difference versus $(k - k_0)\frac{v_0}{\omega_c}$ (where k_0 is the central electron wavevector) and half the detuning between the cavity mode and the QE, $\Delta = (\omega_c - \omega_{QE})/2$ (no longer at resonance in our analysis). The panels correspond to different initial states of the cavity-QE target, parametrized through the variable f, the amplitude of the first excited state of the x-dipole cavity mode,

$$|\phi_0\rangle = |0\rangle_z \otimes \left[\sqrt{1-f^2}\,|0\rangle_x + f\,|1\rangle_x\right] \otimes |g\rangle . \tag{4.77}$$

This eigenstate of $\hat{H}_0$ for vanishing g_x^{c-QE} mimics the weak, coherent

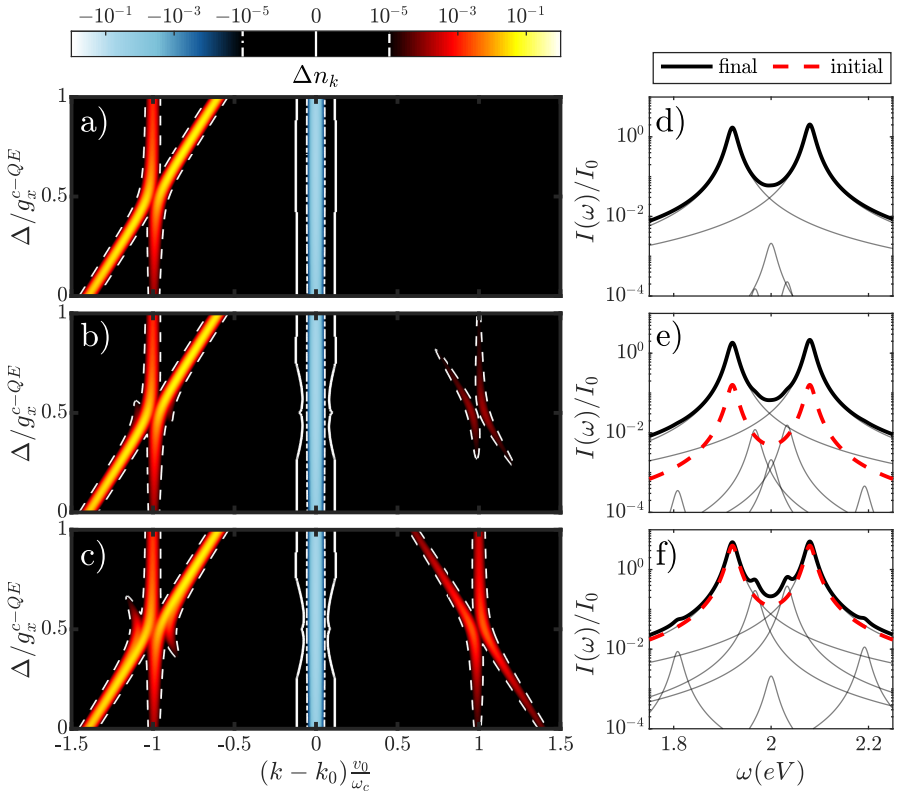

FIGURE 4.11: Momentum reshaping experienced by an incident monochromatic electron beam ($k = k_0$, $v_0 = 0.02c$) in its interaction with a polaritonic target as a function of the half cavity-QE detuning $\Delta = (\omega_c - \omega_{QE})/2$. In panel (a), the cavity is initially in its ground state in an EELS-like configuration. In panels (b) and (c), the initial state of the cavity is given by Equation (4.77) with $f = 0.1$ and 0.5, respectively, mimicking a PINEM setup. Panels (d-f) shows far-field emission spectra for the targets in the same initial state as in panels (a-c) (i.e. $f = 0$, $f = 0.1$ and $f = 0.5$) and $\Delta = 0$. Black solid (red dashed) lines plot the intensity after (before) the interaction with the incoming electrons. Thin grey lines render the different contributions to $I(\omega)$. They correspond to the transitions between the ground state and the $|1, \pm\rangle$ polaritons and z-dipolar optical mode, and between polaritonic states $|2, \pm\rangle$ and $|1, \pm'\rangle$.

driving of the cavity by a laser field polarized along x-direction. Note that, we have used the bare basis above, instead of the polaritonic basis employed in the previous subsection.

In Figure 4.11(a), we consider an EELS-like configuration, with the

target initially in its ground state, $|\phi_0\rangle = |G\rangle$ ($f = 0$). This setup has been previously investigated in the context of polariton formation in nanophotonic systems [281, 282, 318]. The incoming electron beam is monochromatic, presenting a single wave-vector component, $k = k_0$ and $v_0 = 0.02c$ (purple arrow in Fig. 4.9). We can observe that the electron population is transferred to $k < k_0$, the region of energy loss, while, as expected, the energy gain region ($k > k_0$) remains null. At zero detuning, $\Delta = 0$, two maxima in $\Delta n_k > 0$ (yellow color) are apparent, corresponding to the polaritonic states in the first excitation manifold, $|1, \pm\rangle$. These emerge in the region $k - k_0 \simeq -\frac{\omega_c}{v_0}$. The momentum transfer maxima for non-zero detuning disperses, giving rise to the imprint of the anticrossing profile characteristic of light-matter SC [51, P3, 265, 318, 343] into the electron wavepacket. At $|\Delta| > |g_x^{c-QE}|$, two asymptotic branches are apparent, one vertical, corresponding to the x-dipole cavity mode (fixed ω_c), and one diagonal, given by the QE exciton (varying ω_{QE}). Like in Fig. 4.10, a phenomenological wave-vector broadening σ/v_0 has been introduced in the map. The resulting lineshapes are indicated by the solid and dashed lines, which correspond to the isocurves $\Delta n_k = 0$ and $|\Delta n_k| = 10^{-5}$, respectively.

As shown in Figure 4.11(b), by pumping weakly the cavity mode ($f = 0.1$), and under a monochromatic electron beam with $k = k_0$ and $v_0 = 0.02c$, a region of $\Delta n_k > 0$ emerges in the energy-gain side of the momentum transfer map. This indicates that, as a result of the interaction with the target, the electron wavepacket can acquire momentum components larger than k_0 thanks to the population in the first excitation manifold of the cavity. This setup mimics a PINEM experiment, in which the passing electrons exchange energy with an optically-driven resonator. We can observe that the anticrossing profile in the energy-gain region is the fainted mirror image of the energy-loss one, with asymptotic branches given by fixed ω_c and $-\Delta$. At higher driving, $f = 0.5$ in Fig. 4.11(c), the magnitude of the energy gain anti-crossing becomes comparable to its energy loss counterpart, as the amplitude of $|0\rangle_x$ and $|1\rangle_x$ in Equation (4.77) are the same. We can also observe extra branches in the energy loss region, that follow $-\Delta$ instead of Δ. These Δn_k maxima originate from the promotion of polaritonic population from the first

to the second excitation manifold in the interaction with the passing electrons (discussed in more detail below), and illustrates that the power of PINEM in polaritonic systems for electron wavepacket shaping is well beyond that of EELS.

To complement our study, we plot in Fig. 4.11(d-f) the emission spectrum calculated from Equation (4.75) under the driving conditions in panels (a)-(c) and for zero cavity-QE detuning ($\Delta = 0$). Red dashed and black solid lines render $I(\omega)$ (in log scale) before and after the interaction with the electron beam. At $f = 0$ (EELS-CL configuration), $I(\omega) = 0$ prior to the electron arrival, and the final spectrum is dominated by two maxima originated from the radiative decay of the $|1,\pm\rangle$ polaritons to the ground state. The lineshapes for these two contributions are rendered in thin grey lines. Due to their lower weight, other spectral contributions also plotted in grey thin lines, are not apparent in $I(\omega)$. The central one corresponds to the $z-$dipole cavity mode (weakly excited by the passing electrons), and the small ones next to it result from the $|2,\pm\rangle$ to $|1,\pm\rangle$ transitions, with frequencies $\omega_{2,\pm} - \omega_{1,\pm} = \omega_{c,QE} \pm (\sqrt{2}-1)g_x^{c-QE}$. Figure 4.11(d) also presents intensity spectra for the two optically-driven cavities in panels (b) and (c), evaluated at $f = 0.1$ and 0.5, respectively. In both cases, the initial spectra present the two main polaritonic peaks only, whose height increases with f. In the final $I(\omega)$, multiple contributions can be identified. Apart from the two main ones, whose amplitude barely varies with respect to $f = 0$, and the central $z-$dipole feature which is independent of f, we can observe that the weight of the $|2,\pm\rangle$ to $|1,\pm\rangle$ transitions grow considerably with increasing optical driving. Moreover, two additional side peaks are apparent, due to another set of second-to-first manifold transitions, $|2,\pm\rangle$ to $|1,\mp\rangle$, with frequencies $\omega_{2,\pm} - \omega_{1,\mp} = \omega_{c,QE} \pm (\sqrt{2}+1)g_x^{c-QE}$. These transitions are also behind the extra branches in the energy-loss side branches of 4.11(c) at small detuning. Our results evidence that the modification of $I(\omega)$ due to the passing electron is negligible for cavities under significant optical pumping, a direct consequence of the weak character of the target-probe

interaction [310, 312]. Thus, to fully exploit the probing abilities of electron wavepackets, the strength of their coupling to the polaritonic target must be enhanced. In the next subsection we explore the use of the quantum degrees of freedom of the incoming electron for this purpose.

4.4.4 Modulated electron beams and polaritons

Thus far, we have demonstrated that free electrons can indeed be used to extract information from polaritonic targets, both by inducing far field emission from the target, and by driving the different possible transitions, which are then reflected in the electron energy loss/gain spectrum. However, as demonstrated in Fig. 4.11(d-f), the typically weak electron-target interaction leads to a small target population modification, which can easily become obscured by any pre-existing excitations in the case of a driven configuration. In Section 4.3 of this thesis we demonstrated that when considering a monochromatic electron interacting with an isolated QE, the population modification of the target scaled with β^2 in the limit of weak electron-QE target. In contrast, this scaling became directly proportional to β in the case of modulated electrons, therefore effectively increasing the interaction strength between the free electron and the QE. In this section, we explore the effects of electron modulation in the interaction of a free electron with the polaritonic target under study.

The starting point is the scattering matrix in Eq. (4.73), which states that for a free electron interacting with some polaritonic target, the general form of the scattering matrix will be

$$\hat{S} = \sum_{\phi_i,\phi_j} \mathcal{S}_{\phi_i,\phi_j} \, |\phi_i\rangle\langle\phi_j| \; \hat{b}_{q_{\phi_i,\phi_j}},$$

with $q_{\phi_i,\phi_j} = (E_{\phi_i} - E_{\phi_j})/\hbar v_0$. The scattering matrix matrix elements, $\mathcal{S}_{\phi_i,\phi_j}$, are given in a series expansion form in Eq. (4.74), and analytical expressions can be easily obtained from the interaction Hamiltonian. We now consider a modulated electron beam, initially prepared in a

superposition of momenta of the form:

$$|\varphi_e\rangle = \int \mathrm{d}k\, B(k)\, |k\rangle\,, \tag{4.78}$$

with $\int \mathrm{d}k\, |B(k)|^2 = 1$. This wavefunction can describe, for instance, a comb with a set of amplitude peaks equally spaced in momentum space, or the ideally modulated electrons, as in Sec. 4.3. In what follows, we will study two different scenarios: first we assume that the target is prepared initially in one of its polaritonic eigenstates, $|\phi_m\rangle = |n\rangle_z \otimes |N, \pm\rangle$, and then, we will assume that the target is prepared in a superposition of states, to highlight the effect of modulation in both scenarios. Employing a density matrix description of the target, in the first case we have: $\rho_t^0 = |\phi_m\rangle\langle\phi_m|$. After the interaction with the modulated electrons, the reduced density matrix of the target may be written as

$$\begin{aligned}\rho_t &= \int \mathrm{d}k\, \langle k|\, \hat{S}\, |\varphi_e\rangle\, \rho_t^0\, \langle\varphi_e|\, \hat{S}^\dagger\, |k\rangle = \\ &= \sum_{\phi_i,\phi_j} \mathcal{S}_{\phi_i,\phi_m}\, \mathcal{S}^*_{\phi_j,\phi_m}\, I(q_{\phi_j,\phi_i})\; |\phi_i\rangle\langle\phi_j|\,,\end{aligned} \tag{4.79}$$

where, in analogy to Section 4.3, we have introduced the modulation integrals, $I(q) \equiv \langle\varphi_e|\hat{b}_q|\varphi_e\rangle = \int \mathrm{d}k\, B(k)B^*(k+q)$, which quantify the effect of the electronic wavefunction on the quantum target. Note that, $I(0) = 1$ for every choice of $B(k)$. Eq. (4.79) shows that the population of the target states are completely independent from the electron momentum distribution [304], as $\langle\phi_s|\, \rho_t\, |\phi_s\rangle = |\mathcal{S}_{\phi_s,\phi_m}|^2$, which depends only on the form of the interaction Hamiltonian, and not on the initial free electron state. Furthermore, considering that $\mathcal{S}_{\phi,\phi} = 1$ to first order in the electron-target interaction, then $\langle\phi_s|\, \rho_t\, |\phi_s\rangle \simeq \langle\phi_s|\, \rho_t^0\, |\phi_s\rangle = \delta_{s,m}$, which shows that initial populations remain largely unaltered after the interaction with the electron. On the other hand, the coherences in Eq. (4.79) can be manipulated by appropriately designing the electron wavefunction [304]. Thus, by shaping $B(k)$ as a momentum comb with spacing q_{ϕ_1,ϕ_2}, then $I(q_{\phi_1,\phi_2}) \neq 0$ and the final coherences $\langle\phi_1|\, \rho_t\, |\phi_2\rangle$ will be modified, while leaving the rest of the target density matrix unaltered. This is in fact the phenomenology previously showcased in Sec. 4.3.3 for

a free electron interacting with an isolated QE, for which this general treatment also holds. Note that while in Fig. 4.1 we observed how, in general, the interaction of an isolated QE with a monochromatic electron led to purity loss in the QE, Eq. (4.79) shows that when the quantum target is initially in one of its eigenstates, in absence of modulation (i.e., $I(q) = \delta_{q,0}$), the final state of the target will be characterized as a classical statistical mixture, indicating that monochromatic free electrons are not able to induce quantum coherence in a target.

Next, we focus our attention on targets prepared in a superposition of polaritonic states of the form $\left|\psi_t^0\right\rangle = \cos\theta\left|\phi_{m_1}\right\rangle + e^{i\gamma}\sin\theta\left|\phi_{m_2}\right\rangle$. Then, the population of a given polaritonic state $|\phi_s\rangle$ after interaction with the modulated electron beam has the form

$$\begin{aligned}\langle\phi_s|\,\rho_t\,|\phi_s\rangle = &\cos^2\theta\left|\mathcal{S}_{\phi_s,\phi_{m_1}}\right|^2 + \sin^2\theta\left|\mathcal{S}_{\phi_s,\phi_{m_2}}\right|^2 \\ &+\mathrm{Re}\Big\{\sin(2\theta)\,e^{-i\gamma}\,\mathcal{S}_{\phi_s,\phi_{m_1}}\,\mathcal{S}^*_{\phi_s,\phi_{m_2}}\,I(q_{\phi_{m_1},\phi_{m_2}})\Big\},\end{aligned} \tag{4.80}$$

which explicitly shows that for arbitrary initial target state, the final polaritonic populations can vary thanks to the initial coherences in ρ_t^0, as indicated by the $\sin(2\theta) = 2\sin(\theta)\cos(\theta)$ factor above, and the modulation of the electron beam encoded in $I(q)$. The last term indicates that by targeting the transition between the polaritonic states involved in $\left|\psi_t^0\right\rangle$, the impact of the modulation on the populations can be maximized. This ability (showcased here for a general target) of modulated electrons to transform coherences into populations is what enables them to induce Rabi dynamics in QEs [310] and makes it possible to employ them to implement quantum state tomography protocols [312], as shown in Sec. 4.3.

To illustrate the implications of Equation (4.80), we consider a particular target-probe configuration. The initial electron wavefunction is set to a comb of the form $|\psi_e\rangle = \sum_{n=-N/2}^{N/2}\frac{|k_0+nq_{mod}\rangle}{\sqrt{N+1}}$ with $N = 100$. Note that it implies the exchange of up to 50 photons in its preparation (well within reach of recent PINEM experiments [320]). The polaritonic target is initially in the state

$$\left|\psi_t^0\right\rangle = \frac{1}{2}\left|0\right\rangle_z \otimes \left[\sqrt{3}\left|0\right\rangle_x + e^{i\theta}\left|1\right\rangle_x\right] \otimes |g\rangle\,, \tag{4.81}$$

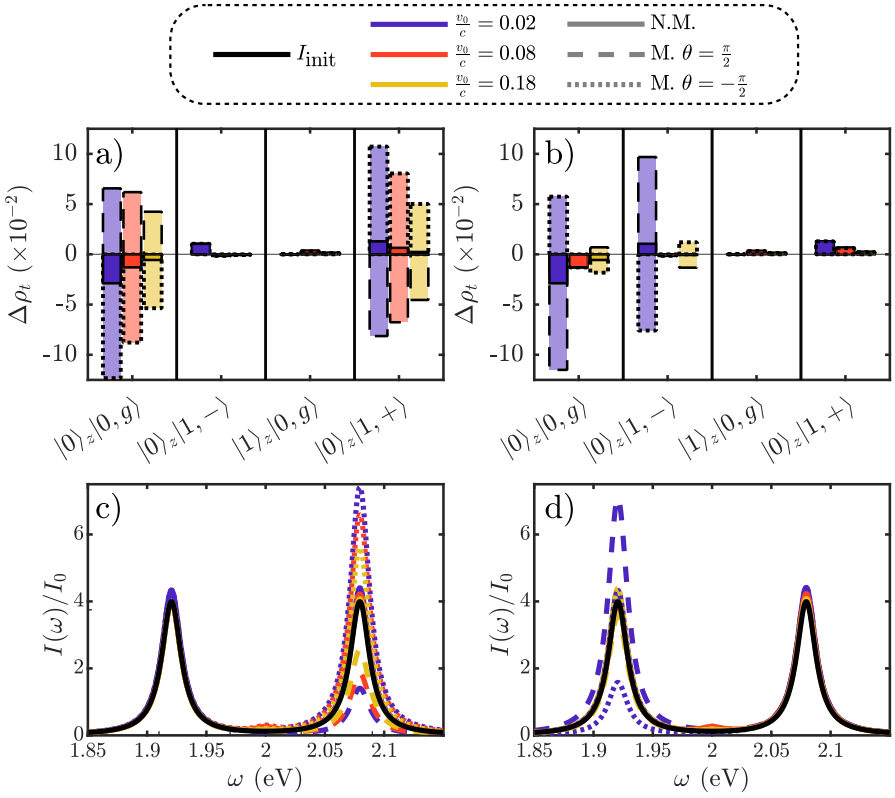

FIGURE 4.12: Impact of the electron modulation on the target population transfer (a)-(b) and cavity power spectrum (c)-(d). In the top (bottom) panels, the momentum modulation is at resonance with the transition between the ground state and upper (lower) polariton state, $q_{mod} = \omega_{1,+}/v_0$ ($q_{mod} = \omega_{1,-}/v_0$). Three different electron central velocities are considered: $0.02c$ (blue), $0.08c$ (orange) and $0.2c$ (green), and the impact parameter b_{e-c} is set to 11 nm. In all panels, two different initial state phases, θ are considered: $\pi/2$ (dashed lines) and $-\pi/2$ (dotted lines). The solid lines correspond to a non-modulated (N.M.) electron beam, and the solid black lines in (c) and (d) plot the cavity spectrum before the interaction with the passing electrons.

where θ is a real number. Note that this wavefunction can be expressed as a linear combination of the QE ground state and the $|0\rangle_z \otimes |1,\pm\rangle$ polaritonic states. In Fig. 4.12(a-b), we analyse the population differences (given by the diagonal terms of $\Delta\rho_t = \rho_t - \rho_t^0$) induced by the passing electrons on the ground and the three first-excitation target states. We consider the three central electron velocities indicated in

Fig. 4.9 (purple, orange and yellow in increasing v_0/c), and two different initial state configurations, given different values of θ in Equation (4.81) (dashed and dotted lines). In all cases, $b_{e-c} = 11$ nm. For reference, the population differences for a non-modulated (N.M.) electron beam are plotted in solid lines (note that these are independent of θ). In panel (a), the modulation spacing is at resonance with the upper polariton, $q_{mod} = \omega_{1,+}/v_0$, in panel (b), with the lower one, $q_{mod} = \omega_{1,-}/v_0$.

As expected, Figure 4.12(a) displays a significant population transfer only between the ground state (left) and the upper polariton (right), which is larger for lower electron velocity, following the monotonic dependence in the emitter-target coupling in Fig. 4.9(a). Moreover, we can observe that for $\theta = -\pi/2$ the upper polariton gains population (as in the non-modulated case), while it gets depopulated for $\theta = \pi/2$. Note that this parameter sets the phase, and therefore the sign, of the contribution of the initial coherences to the final populations given by the last term in Equation (4.80). We can see how this can be leveraged to control the flow of population among polaritonic states. The momentum spacing in $B(k)$ is set to yield the most efficient energy transfer between the ground and lower polariton states in Fig. 4.12(b). The non-monotonic dependence of the populations on the electron velocity in this case is inherited from Fig. 4.9(b). Again, varying θ inverts the direction of the population transfer.

Apart from analysing the effect of electron modulation on the target populations, we also investigate its impact on the cavity power spectrum given by Equation (4.75), now evaluated for the state that results from applying the scattering matrix on Equation (4.81). Importantly, this is a far-field magnitude that can be easily accessed experimentally. Fig. 4.12(c) and (d) plot $I(\omega)$ for $q_{mod} = \omega_{1,+}/v_0$, and $q_{mod} = \omega_{1,-}/v_0$, respectively. The black solid line renders the cavity spectrum before the interaction with the electron beam, I_{init}. We can observe that only the upper polariton peak is shaped by the passing electrons in (c), and the lower polariton one in (d). This illustrates the far-field fingerprint of the population manipulation in panels (a) and (b). In both cases, only the emission from the targeted transition through q_{mod} is modified, keeping the spectrum around the other features unaltered. Importantly, as we

observed in the polariton populations, the initial coherences, whose contribution to the spectrum depends on θ, set whether the altered emission peak increases or decreases with respect to I_{init}.

Figure 4.12 indicates that the coherences, rather than the populations, in ρ_t^0 dictate the manner in which the population transfer and the spectrum reshaping take place through the interaction with the modulated electron beam. To gain insight into this result, we simply evaluate Equation (4.80) for polaritonic states that are initially populated, i.e., by making $s = m_1$, for example. The final population of the m_1 state of the polariton then reads

$$\begin{aligned}\langle\phi_{m_1}|\,\rho_t\,|\phi_{m_1}\rangle = &\cos^2\theta\left|\mathcal{S}_{\phi_{m_1},\phi_{m_1}}\right|^2 + \sin^2\theta\left|\mathcal{S}_{\phi_{m_1},\phi_{m_2}}\right|^2 \\ &+\mathrm{Re}\Big\{\sin(2\theta)\,e^{-i\gamma}\,\mathcal{S}_{\phi_{m_1},\phi_{m_1}}\,\mathcal{S}^*_{\phi_{m_1},\phi_{m_2}}\,I(q_{\phi_{m_1},\phi_{m_2}})\Big\}.\end{aligned}$$

One can then see that, in the first two terms, $|\mathcal{S}_{\phi_{m1},\phi_{m1}}|^2 = 1$ and $|\mathcal{S}_{\phi_{m1},\phi_{m2}}|^2 = |\hbar_{I,\phi_{m1},\phi_{m2}}|^2$ to first order in the electron-target interaction. On the contrary, we have $\mathcal{S}_{\phi_{m1},\phi_{m1}}\mathcal{S}^*_{\phi_{m1},\phi_{m2}} = \hbar_{I,\phi_{m1},\phi_{m2}}$ to first order in the last one. Thus, we find that, while the first terms are independent or quadratic on the electron-target interaction strength, the last is linear, which makes it the leading one. Moreover, for a finite, but long electron comb, one has[9] $I(q_{mod}) = \int \mathrm{d}k\, B(k)B^*(k+q_{mod}) = N/(N+1) \simeq 1$, also contributing to make the initial coherences crucial in establishing the effect of the passing electrons on the target.

Finally, we pay attention to the effect that the target-probe interaction has on the modulated electron beam. The fact that the population transferences induced by modulated beams are larger than the non-modulated ones means that the energy balance of the interaction can be altered through the modulation itself. Thus, it is possible, in principle, to pump or deplete the target. In Fig. 4.13, we explore the net energy change experienced by the passing electrons

$$\Delta E = \sum_k E_k \Delta n_k, \tag{4.82}$$

[9] See Section 4.3.

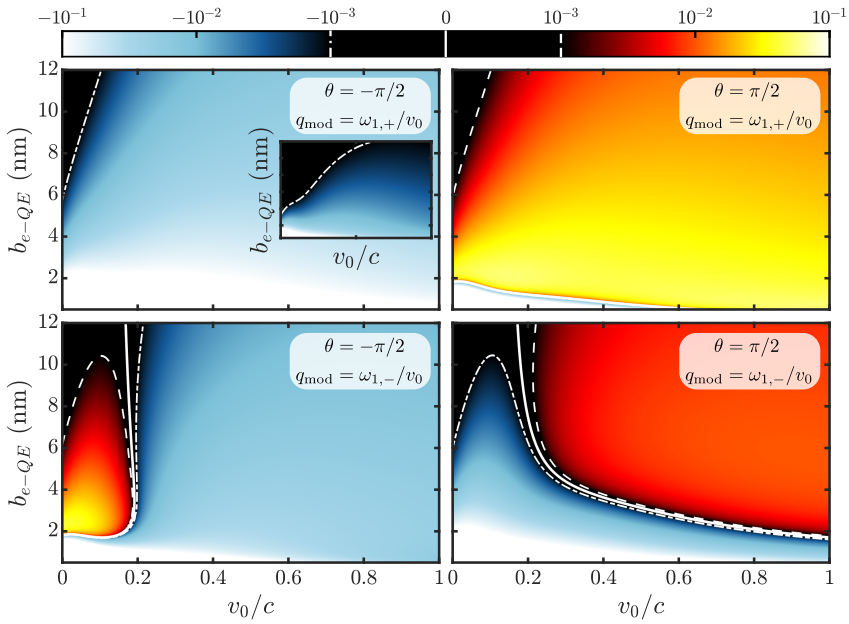

FIGURE 4.13: Expectation value of the energy change of the electron in units $\hbar\omega_c$. Main panels show the case of modulated electrons, showcasing that net energy gain and loss is achievable by modulating the electron. On each panel we show the modulation spacing and also the phase factor of the initial target state. The inset corresponds to the case of a non-modulated electron, where there always is net energy loss. The result in this case is independent of the phase factor.

where Δn_k is defined in Equation (4.76). As the initial electron wavefunction, we take the finite comb used in Fig. 4.12 and the target is prepared in the state given by Equation (4.81). The four panels in Fig. 4.13 display ΔE in units of $\hbar\omega_c$ as a function of the central electron velocity and impact parameter, b_{e-QE}. The results for the initial target state with $\theta = -\pi/2$ ($\theta = \pi/2$) are shown in the left (right) maps, and the modulation is set at resonance with the ground transition to the upper (top) and lower (bottom) polariton. For reference, the map for non-modulated electrons is shown as an inset with the same parameter range, illustrating that the passing electrons can only lose energy in the non-modulated setup, and ΔE is larger for smaller impact parameter and electron velocity. The situation is rather similar for $\theta = -\pi/2$.

For this state phase, there emerges only a narrow region of small v_0/c where the electron beam gains energy for $q_{mod} = \omega_{1,-}/v_0$. Apart from it, the maps resemble the EELS one, and the target population always increases by the effect of the passing electrons. For $\theta = \pi/2$ (right), the net energy change maps are very different. Fast electron beams gain energy for both q_{mod} (although ΔE is larger for the transition between the ground and upper polariton), and lose it at low velocities and impact parameters. Here, the target is populated/depopulated depending on v_0 and b_{e-QE}. The richness of the net energy loss/gain landscape in Fig. 4.13 follows from the coupling strengths in Fig. 4.9, as the leading order in the electron-target interaction is linear in $\hbar_I$. Thus, we can link the gain-loss transitions in the lower maps with the change in sign in $\hbar_{I,G,1\_}$ in Fig. 4.9(b). All maps are equivalent in the limit of small v_0 and b_{e-QE}, where $\hbar_I \to 1$ and electron modulation becomes irrelevant. Our results also showcase the power of polaritonic systems to re-shape and alter modulated electron beams through the energy of its natural transitions and the phase involved in its initial state preparation.

4.5 Conclusions

In this chapter, we have delved into the study of how the quantum coherence properties of free electrons affect their interaction with quantum targets. This, together the generation of quantum-coherent free electrons, constitutes one of the most active areas of research within nanophotonics, as can be seen by the breadth of recently published works on the subject. Of course, free electrons have been one of the most fruitful tools for exploring physics at the nanoscale for decades, however, the latest advancements in attosecond electron-spectroscopy led to the discovery that free electrons in microscopes are able to carry quantum coherence, as indicated by early PINEM experiments [283, 284, 295], and subsequent refinements in the theoretical description of electron-photon interactions [296–298, 349]. Therefore this sparked the quest for understanding the optimal mechanisms for electron state preparation [285, 287, 289, 290, 299], which naturally leads to the proposal of employing

such free electrons imbued with quantum coherence to perform quantum optics at the nanoscale [284, 296, 297, 299, 301, 320].

The existing literature studies the interaction of free electrons with optical modes [280, 300–309], QEs [310–317] and hybdrid excitonic-photonic systems in the SC regime [318, 319], respectively. In this chapter, we have provided a unified framework rooted in the formalism of mQED to treat the interaction between a general set of electronic transitions and optical fields by extending previous results, only valid to study the interaction between idealized, dipolar two-level QEs [39]. In doing so, we have been able to put on equal footing the description of light-matter, and light-mediated matter-matter interaction. Since this framework is derived in terms of generic electronic eigenfunctions, it allows to study a wide range of electronic transitions, which we then particularize to free electrons, and dipolar QEs, but could nevertheless be employed to describe the interaction of more complex and extended electronic eigenfunctions, such as those present in organic molecules. Furthermore, since our approach is based on the Dyadic Green's Function, the results shown in this chapter can be straightforwardly extended to more complex nanophotonic systems, for which analytical solutions may not be available, and in which quantization of the optical modes becomes challenging. The inherent flexibility of the present framework therefore points to its applicability in a wide range of problems.

We have explored the quantum interaction of modulated free-electrons with single quantum emitters, and then with more complex polaritonic targets. We have made special emphasis on the quantum properties of the states that the free electron creates in the targets, and the dynamics that this interaction can induce. Throughout this chapter, we first considered single electron-QE interaction events, and revealed that the relevant figure of merit for the electron wavefunction preparation is the autocorrelation function in reciprocal space, which persists in the case of polaritonic targets with more complex energy landscapes. In the limit of perfectly periodic (ideal) modulation, we have shown that the purity of a QE state is preserved upon interaction, and emitter and free electrons remain disentangled after their encounter. Moving then into a configuration of continuous electron driving, we have revealed Rabi-like

dynamics in the emitter state, and explored its interplay with two decoherent effects: radiative losses and electron-induced dephasing. Finally, we have focused on quantum state tomography, and by analysing the degree of entanglement between emitter and free electron, we have determined that small electron combs are best suited for the task. Thus, a measurement protocol capable of uniquely determining the purity of the emitter state has been proposed.

We have also employed our Hamiltonian description of the electron-target interaction to analyse the effect of electron-polariton interactions on different key observables, such as the electron momentum redistribution and net energy change, and the polaritonic state populations and light emission spectrum from the target. In contrast to far-field probes, in which both polaritons of a strongly coupled light-matter system are symmetrically driven due to the typically much larger optical cross section of the cavity mode compared to the involved QEs, the near field nature of electron excitation allows to symmetrically couple to both excitonic and photonic polariton components, which enables to individually address either the upper or lower polariton. Our investigation has proceeded by increasing the complexity on the electron beam and target preparation, from EELS and CL to PINEM, and finally PINEM with modulated electron beams, all these described within the same unifying theoretical model. In this manner, we have mapped the typical anticrossing behavior of polaritonic systems both for the first and second excitation manifolds, and found that electron modulation allows to selectively address transitions in targets with complex energy landscapes, providing a degree of spectral selectivity to what otherwise behaves as a broadband source.

Our theoretical findings prove that free electrons, beyond their extremely high spatial resolution, are in general very relevant tools for the probing of the energy landscape and populations present in quantum targets. Nevertheless, monochromatic free electrons, as produced in electron microscopes, are not able to extract any information about the quantum coherences present in any given system, and moreover, their interaction generally leads to purity loss and coherence erasure. By modulating the free electrons prior to their interaction with the target,

these gain a series of abilities such as effectively larger electron-target interaction strength, purity preservation of the quantum target state and sensitivity to the coherences of the target, making them suitable tools for quantum state manipulation and characterization and therefore, a promising tool for quantum technologies, where their power and versatility can be exploited to address and manipulate complex qubits one by one.

Chapter 5

Conclusions and outlook

English

In this thesis, we have explored the theoretical modelling of phenomena associated with the coexistence of different families of interactions in nanophotonic settings. Through a mixture of analytical and numerical methods, we have developed predictive tools for complex nanophotonic systems. This effort has included (but not been limited to) close collaboration with several experimental groups, where we contributed to the design, modelling, and ultimate interpretation of observed phenomenology.

A key advantage of theoretical physics, compared with the complementary experimental counterpart is that when modelling complex, real-world problems, one may often neglect certain degrees of freedom by applying approximations and focusing only on the relevant parameters. Thus, a key aspect of the PhD work is learning to identify the essential elements to provide a valid description of the particular physical setup under study. The approximations applied follow from the physics that one expects to observe. Some of them are ubiquitously employed within the same field of study: the linear response in the constitutive relations of Maxwell's equations, the rotating wave approximation in the Jaynes Cummings Hamiltonian, or the non-recoil approximations for the interaction of energetic free electrons with nanostructures are some examples of approximations used throughout this thesis that implicitly reflect which physical mechanisms play the key roles. Yet, it is possible to find systems that defy these expectations. For instance, in Chapter 2, we modelled the interaction of a plasmonic resonance with a non-linear

medium. In these systems, the detuning between the resonant mode and the optical driving usually plays a central role [82, 90], mainly due to the large field enhancement around the metallic particles, and the large sensitivity of the plasmonic resonances to the environment's refractive index. Remarkably, due to the extended nature of the system we study, the non-linear effects arise through the extended interaction of the diffraction orders in the non-linear medium, which results in effects that are only weakly dependent on the excitation wavelength, as demonstrated by the semi-analytical treatment we developed.

This extended photon-photon interaction thus leads to the development of self-sustained oscillations and symmetry-breaking transitions. These dynamical phases, which we first report for a diffractive system, are furthermore of practical interest to the field of time-varying media, where material properties must vary at length scales comparable to the wavelength of light, λ, and on timescales of the optical frequency, $\tau \sim 1/\nu$. Therefore, extending the treatment presented in this thesis to materials with an instantaneous non-linearity brings the prospect of *self-modulating time-varying media*, which, by avoiding the need for complicated external optical setups, can provide an experimental platform to demonstrate the very interesting predictions of broadband amplification [142], Fresnel drag [140], photon pair production [139, 350], and other intriguing phenomena in the emerging field of time-varying media [138].

Beyond non-linear dynamics and self-modulating media in extended interactions, we have also explored the properties of near-field interactions, such as those that occur between tunnelling currents or free electrons and nanometrically confined excitations. This was studied using both classical and quantum mechanical descriptions, as described in Chapters 3 and 4, respectively. On the one hand, we showed that these near-field interactions can be leveraged as probes for nanophotonic phenomena, where far-field probing requires special setups. In particular, our use of tunnelling currents in Chapter 3 to probe the strong coupling between few-layers of a TMD and a nanophotonic cavity serves as a proof of concept for using electrically driven light sources to probe interactions at the nanoscale. Our findings are of particular interest to the

STM community, where strong coupling between the tip-substrate nanophotonic cavity and excitons or molecules has yet to be realized. This is puzzling considering the extraordinary control achieved over the tip geometry and tip-substrate distance, which, according to conventional understanding of strong coupling in plasmonic nanocavities, should chiefly determine the interaction strength. Therefore, studying the differences between our implementation and previous STM studies may highlight relevant factors that hinder the demonstration of strong coupling, such as charge-transfer effects, exciton hybridization with metallic conduction bands, or misalignment of the molecular/excitonic dipole moment with the dominant cavity modes.

In Chapter 3, we also studied the use of free charges directly as a broadband source, particularly as sources to trigger fluorescence in molecules coupled to nanophotonic cavities designed to enhance the fluorescence signal. These nanophotonic cavities are spherically symmetric, multilayered metallo-dielectric systems, similar to planar bulk hyperbolic metamaterials. By tuning the few degrees of freedom present in this multilayered design (primarily the radii of the spherical shells), we demonstrated that the fluorescence signal could be enhanced by orders of magnitude. The search for an optimal design was conducted through numerical optimization, positioning our work within the growing field of inverse design in nanophotonics [P6, 351, 352]. Our analytical solution for a spherically symmetric system grants high efficiency and evaluation speed, though it sacrifices some geometric flexibility, a feature that characterizes systems developed through more general inverse-design methods. Given the unprecedented computational power available today, the advent of GPU-based parallel computing for electromagnetic simulations [353, 354], together with the development of *surrogate models* [355–358], and the accessibility of consumer-grade numerical optimization tools [359], we can expect that the design process in the near future will be heavily driven by inverse design optimization methods, alongside more traditional design strategies based on physical principles and intuition.

In Chapter 4, we studied the interaction of free electrons with nanophotonic targets, this time using a quantum mechanical description.

The need for a quantum description arises from the realization that free electrons can carry quantum coherence, as demonstrated by PINEM experiments [283]. This calls for a model beyond the traditional classical current approach, as used in the theory of EELS [151].

We begin Chapter 4 by introducing the formalism devised to treat interactions between free electrons and quantum targets. The value of our theoretical approach is that, rooted in the mQED framework [27] and extending previous work [39], it treats field-mediated interactions between arbitrary electronic transitions. Thus, instead of postulating a model Hamiltonian for quantum systems formed by several quantum-mechanical entities, our framework provides a comprehensive description of the entire system, putting the various light and matter resonances and their interactions on equal footing. We particularize our theory to parametrize the interaction between free electrons, quantum emitters, and optical modes. Moreover, thanks to the central role of the electromagnetic Dyadic Green's Function in mQED, our results can be extended to handle more complex electronic wavefunctions (see Appendix F) and electromagnetic environments through numerical methods.

This description enabled us to first study the simplest case of a free electron interacting with an isolated QE, where we predict promising capabilities of free electrons for quantum state preparation and tomography. We identify the electron's self-correlation in momentum space as a key figure of merit for the preparation of free-electron wavefunctions, as it measures the impact of the free-electron wavefunction on the final state and effective dynamics of the QE, along with the enhanced sensitivity of the electron to the QE's coherences.

By coupling the QE to a nanophotonic cavity, we further explore a polaritonic target for interaction with the free electron. We find that electron self-correlation remains the relevant parameter for quantifying the effect of the electron's wavefunction, and wavefunction engineering of the free electron yields an effectively larger coupling strength. Notably, due to the anharmonic nature of the polaritonic energy ladder, electron modulation contributes transition-dependent effects. In contrast to the broadband nature of monochromatic free electrons, this allows the targeting of specific electronic transitions within polaritonic targets

or other systems with complex energy landscapes, providing selectivity that is unavailable with non-modulated free electrons.

Given the inherently nanometric spatial resolution, recent advances in attosecond temporal resolution, and progress in probing and controlling quantum coherence, free electrons are poised to become a central tool for quantum system control. This holds particular relevance for nanophotonics, where the diffraction limit imposes a hard boundary on the utility of free-space optics in sub-wavelength applications. This is evidenced by recent demonstrations of using free electrons in interferometric setups to extract attosecond-resolved phase information from optical fields [293, 294] and phonon-assisted decoherence times from colour centers in hBN [334].

Castellano

En esta tesis, hemos investigado el modelado teórico de fenómenos que surgen de la coexistencia de diferentes tipos de interacciones en entornos nanofotónicos. A través de una combinación de métodos analíticos y numéricos, hemos desarrollado herramientas de predicción para sistemas nanofotónicos complejos. Este trabajo ha contado con la estrecha colaboración con varios grupos experimentales, donde hemos contribuido al diseño, modelado e interpretación de la fenomenología observada.

Una de las grandes ventajas de la física teórica, en comparación con la vertiente experimental, es que al abordar problemas complejos, a menudo uno puede omitir ciertos grados de libertad aplicando aproximaciones y centrándose solo en los parámetros más relevantes. Así, un aspecto fundamental del doctorado es aprender a identificar los elementos esenciales que permiten ofrecer una descripción válida de cada sistema físico. Las aproximaciones que aplicamos se derivan de la física que esperamos observar. Algunas de estas aproximaciones son de uso común dentro de diversos campos de estudio: la respuesta lineal en las relaciones constitutivas de las ecuaciones de Maxwell, la aproximación de onda rotante en el Hamiltoniano de Jaynes-Cummings, o las aproximaciones de no-desvío (non-recoil) para la interacción de electrones libres energéticos con nanostructuras son solo algunos ejemplos de

aproximaciones utilizadas a lo largo de esta tesis, que reflejan de manera implícita qué mecanismos físicos desempeñan roles clave.

Sin embargo, hay sistemas que desafían estas expectativas. Por ejemplo, en el Capítulo 2, modelamos la interacción de una resonancia plasmónica con un medio no lineal. En estos sistemas, el desvío espectral entre el modo resonante y la excitación óptica suele jugar un papel fundamental [82, 90], principalmente debido a la gran concentración de campo alrededor de las partículas metálicas y a la elevada sensibilidad de las resonancias plasmónicas al índice de refracción del entorno. De manera inesperada, en el sistema que estudiamos, los efectos no lineales surgen a través de la interacción extendida de los órdenes de difracción a través del medio no lineal, lo que da lugar a un efecto que solo depende débilmente de la longitud de onda de excitación, como demostramos en el tratamiento semi-analítico que presentamos. Esta interacción extendida fotón-fotón da lugar a la aparición de oscilaciones auto-sostenidas y transiciones acompañadas de ruptura espontánea de simetría. Estas fases dinámicas, además de ser interesantes por ser esta la primera vez que se reportan en medios difractivos, son de interés práctico para el campo de los medios que varían en el tiempo (time-varying media), donde las propiedades materiales deben cambiar en escalas de longitud comparables a la longitud de onda de la luz, λ, y en escalas de tiempo de la frecuencia óptica, $\tau \sim 1/\nu$. Por tanto, extender nuestro tratamiento a materiales con una no-linealidad instantánea abre la puerta a medios *auto-modulados que varían en el tiempo*, lo que evitaría la necesidad de montajes ópticos externos complejos y pueden proporcionar una plataforma experimental para demostrar las interesantes predicciones, como la amplificación de señal no resonante [142], el rozamiento de Fresnel [140], la producción de pares entrelazados de fotones [139, 350] u otros fenómenos fascinantes en el campo emergente de los medios que varían en el tiempo [138].

Más allá de la dinámica no lineal y los medios auto-modulados en interacciones extendidas, también hemos estudiado las propiedades de

las interacciones de campo cercano, como aquellas que ocurren entre corrientes túnel o electrones libres y excitaciones confinadas nanométricamente. Este estudio se realizó tanto desde perspectiva del electromagnetismo clásico, como desde una formulación cuántica, como se detalla en los Capítulos 3 y 4, respectivamente. Por un lado, mostramos que estas interacciones de campo cercano pueden utilizarse como sondas para fenómenos nanofotónicos, donde el uso de sondas de campo lejano requeriría el uso de montajes especializados. En particular, nuestro uso de corrientes de túnel en el Capítulo 3 para investigar el acoplamiento fuerte entre unas pocas capas de un TMD y una cavidad nanofotónica sirve como prueba de concepto para usar fuentes de luz nanométricas alimentadas eléctricamente en la exploración de interacciones a escala nanométrica. Nuestros hallazgos son de especial interés para la comunidad de STM, donde aún no se ha logrado el acoplamiento fuerte entre la cavidad nanofotónica, formada por la punta-substrato, y excitones o moléculas. Esto es desconcertante dado el extraordinario control que se tiene sobre la geometría de la punta y la distancia punta-substrato, que, según el entendimiento general del acoplamiento fuerte en nanocavidades plasmónicas, determinar como factor principal la intensidad de la interacción. Por tanto, estudiar las diferencias entre nuestra implementación y estudios anteriores de STM podría recalcar los factores relevantes que puedan dificultan la demostración del acoplamiento fuerte, como pueden ser efectos de transferencia de carga, hibridación de excitones con la banda de conducción del metál, o la desalineación del momento dipolar de las moléculas/excitones con los modos dominantes de la cavidad.

En el Capítulo 3, también exploramos el uso de cargas libres directamente como una fuente de luz, especialmente como fuentes para activar la fluorescencia de moléculas acopladas a cavidades nanofotónicas diseñadas para mejorar la señal de fluorescencia. Estas cavidades nanofotónicas son sistemas metalo-dieléctricos multicapa con simetría esférica, similares a los metamateriales hiperbólicos multicapa planares. Al ajustar los pocos grados de libertad presentes en este diseño multicapa (principalmente los radios de las capas esféricas), demostramos que la señal de fluorescencia puede aumentarse en varios órdenes de magnitud. La búsqueda de un diseño óptimo se llevó a cabo mediante optimización

numérica, situando nuestro trabajo dentro del creciente campo del diseño inverso en nanofotónica [P6, 351, 352]. Nuestra solución analítica para un sistema esféricamente simétrico nos garantiza alta eficiencia y velocidad de evaluación al precio de sacrificar la flexibilidad geométrica por la que se caracterizan los sistemas desarrollados mediante métodos de diseño inverso en general.

Dado el crecimiento mantenido del poder de cálculo experimentado durante las últimas décadas, el surgimiento de la computación paralela basada en GPUs para simulaciones electromagnéticas [353, 354], junto con el desarrollo de *modelos surrogados*[355–358] y la accesibilidad de herramientas de optimización numérica para el usuario no-experto[359], podemos prever que el proceso de diseño en un futuro próximo estará fuertemente influenciado por métodos de optimización de diseño inverso, junto con estrategias de diseño más tradicionales basadas en principios físicos e intuición.

En el Capítulo 4, estudiamos la interacción de electrones libres con objetivos nanofotónicos, esta vez utilizando una descripción cuántica. La necesidad de una descripción cuántica surge del descubrimiento de que los electrones libres son capaces de transportar coherencia cuántica, como lo demuestran los experimentos de PINEM [283]. En consecuencia, la descripción de estos problemas requiere un modelo que vaya más allá del enfoque clásico, basado en considerar a los electrones como una densidad de corriente, tal y como se hace en la teoría de EELS [151].

Comenzamos el Capítulo 4 introduciendo el formalismo que hemos desarrollado para tratar las interacciones entre electrones libres y objetivos cuánticos. La relevancia de nuestro enfoque teórico radica en que, utilizando el marco de mQED [27] y ampliando trabajos previos [39], describimos las interacciones mediadas por el campo electromagnético entre transiciones electrónicas arbitrarias. De este modo, en lugar de postular un Hamiltoniano modelo para sistemas cuánticos compuestos por varias entidades mecánico-cuánticas, nuestro formalismo nos proporciona una descripción integral del sistema, poniendo las diversas resonancias de luz y materia y sus interacciones en pie de igualdad. En el resto del capítulo, particularizamos nuestra teoría para parametrizar la interacción entre electrones libres, emisores cuánticos y modos ópticos.

Es importante recalcar que gracias al papel central de la Función de Green Diádica electromagnética en mQED, nuestros resultados pueden extenderse para tratar funciones de onda electrónicas (ver Apéndice F) y entornos electromagnéticos más complejas que las consideradas en el capítulo mediante métodos numéricos.

Esta descripción nos permitió, primero, estudiar el caso simple de un electrón libre interactuando con un emisor cuántico (QE) aislado. En esta situación predecimos que los electrones libres presentan capacidades prometedoras para la preparación y tomografía de estados cuántico. Identificamos la auto-correlación de la función de onda del electrón libre en el espacio de momentos como una magnitud clave en la preparación de funciones de onda de electrones libres, ya que mide el impacto que estas funciones de onda tienen sobre el estado final y la dinámica efectiva del QE, y también proveen al electroón de sensibilidad a las coherencias del QE.

Después, acoplamos el QE a una cavidad nanofotónica, dando lugar a un objetivo polaritónico para la interacción con el electrón libre. En este caso, encontramos que la auto-correlación del electrón sigue siendo el parámetro clave para cuantificar el efecto de la función de onda electrónica, ya que da lugar a fuerzas de acoplamiento efectivas mayores entre electron y objetivo, y por tanto, esta magnitud se presenta como una figura de mérito de interés general a la hora de guiar la ingeniería de la función de onda del electrón libre. Notablemente, debido a la anharmonicidad de la escalera de energía polaritónica, descubrimos que la modulación del electrón produce efectos que pueden ser muy sensibles a la diferencia de energías entre estados polaritonicos, en contraste con la naturaleza de fuente de banda ancha por la que los electrones libres se caracterizan. esto permite afectar de manera selectiva a transiciones electrónicas específicas dentro de objetivos polaritónicos u otros sistemas con estructuras de niveles de energía complejos, proporcionando una selectividad que no está disponible con electrones libres no modulados.

Dada la resolución espacial inherentemente nanométrica, los avances recientes en resolución temporal en attosegundos y el progreso como sonda y herramienta para controlar el flujo de coherencia cuántica, es de esperar que los electrones libres se conviertan en una herramienta central

para el control de sistemas cuánticos. Esto es particularmente cierto para el campo de la nanofotónica, donde el límite de difracción impone una frontera estricta a la utilidad de montajes ópticos para aplicaciones donde las longitudes características son menores que la longitud de onda. Esta futura relevancia se empieza a evidenciar en las demostraciones recientes del uso de electrones libres en configuraciones interferométricas para extraer información sobre la fase de campos resuelta con resolución de attosegundos [293, 294], o la extracción de los tiempos de decoherencia en centros de color en hBN [334].

Appendix A

Details of the linear stability analysis derivation

Our starting point is Eq. (2.13), which we reproduce here:

$$\tau\,\dot{\Delta n}(\boldsymbol{r},t)+\Delta n\left(\boldsymbol{r},t\right)=-\gamma\left|\mathbf{E}_0\left(\boldsymbol{r}\right)\right|^2 + 2k_\omega^2\gamma\int d\boldsymbol{r}'\left[F(\boldsymbol{r},\boldsymbol{r}')+F^*(\boldsymbol{r},\boldsymbol{r}')\right]\Delta n(\boldsymbol{r}',t). \tag{A.1}$$

Where $F(\boldsymbol{r},\boldsymbol{r}')=n_0\mathbf{E}_0^*\left(\boldsymbol{r}\right)\cdot\overline{\overline{G}}\left(\boldsymbol{r}-\boldsymbol{r}'\right)\cdot\mathbf{E}_0\left(\boldsymbol{r}'\right)$. We start by spliting the refractive index change, $\Delta n(\boldsymbol{r},t)$, into a static and a dynamic part: $\Delta n\left(\boldsymbol{r},t\right)=\delta n_s\left(\boldsymbol{r}\right)+\delta n(\boldsymbol{r},t)$. Using the linear field solution, we arrive to an expression for the steady-state index modification

$$\delta n_s\left(\boldsymbol{r}\right)=-\gamma\left|\mathbf{E}_0\left(\boldsymbol{r}\right)\right|^2+2k_\omega^2\gamma\int d\boldsymbol{r}'\left[F(\boldsymbol{r},\boldsymbol{r}')+F^*(\boldsymbol{r},\boldsymbol{r}')\right]\delta n_s\left(\boldsymbol{r\prime}\right), \tag{A.2}$$

and for the time evolution of the different perturbations

$$\tau\,\dot{\delta n}\left(\boldsymbol{r},t\right)+\delta n\left(\boldsymbol{r},t\right)= 2k_\omega^2\gamma\int d\boldsymbol{r}'\left[F(\boldsymbol{r},\boldsymbol{r}')+F^*(\boldsymbol{r},\boldsymbol{r}')\right]\delta n(\boldsymbol{r}',t). \tag{A.3}$$

Since we are interested in perturbations that grow over time, we focus on the dynamic part. We first introduce the Dyadic Green's Function for a 2D system:

$$\overline{\overline{G}}_{ij}\left(\boldsymbol{r}-\boldsymbol{r}'\right)=\left[\delta_{i,j}+\frac{\partial_i\partial_j}{k_0^2}\right]g\left(\boldsymbol{r}-\boldsymbol{r}'\right) \tag{A.4}$$

$$g\left(\boldsymbol{r}-\boldsymbol{r}'\right)=\frac{i}{4}H_0\left(k_0\left|\boldsymbol{r}-\boldsymbol{r}'\right|\right)=\int\frac{d\boldsymbol{k\prime}}{4\pi^2}\frac{e^{i\ \boldsymbol{k}'\cdot\left(\boldsymbol{r}-\boldsymbol{r}'\right)}}{k'^2-k_0^2-i\eta}, \tag{A.5}$$

where $g\left(\boldsymbol{r}-\boldsymbol{r}'\right)$ is the scalar Green's Function of the Helmholtz wave equation in 2D, and η is a regularizing factor that tends to 0. Putting these two together, the complete dyadic can be written as:

$$\overline{\overline{G}}\left(\boldsymbol{r}-\boldsymbol{r}'\right)=\int\frac{d\boldsymbol{k\prime}}{4\pi^2}\ \overline{\overline{O}}\left(\boldsymbol{k}'\right)\ \frac{e^{i\boldsymbol{k}'\cdot\left(\boldsymbol{r}-\boldsymbol{r}'\right)}}{k'^2-k_0^2-i\eta}, \tag{A.6}$$

where

$$\overline{\overline{O}}\left(\boldsymbol{k}\right)=\begin{pmatrix}1-\frac{k_x^2}{k_0^2} & -\frac{k_xk_y}{k_0^2} & 0\\ -\frac{k_xk_y}{k_0^2} & 1-\frac{k_y^2}{k_0^2} & 0\\ 0 & 0 & 1\end{pmatrix} \tag{A.7}$$

contains all the tensorial character of the Dyadic Green's Function. By introducing that the linear system solution admits a expansion as a sum of plane waves as $\mathbf{E}_0\left(\boldsymbol{r}\right)=\sum_\alpha\mathcal{E}_\alpha e^{i\ \boldsymbol{k}_\alpha\cdot\boldsymbol{r}}$, one can write

$$F(\boldsymbol{r},\boldsymbol{r}')=n_0\sum_{\alpha,\beta}\int\frac{d\boldsymbol{k\prime}}{4\pi^2}\frac{\mathcal{E}_\alpha^*\cdot\overline{\overline{O}}\left(\boldsymbol{k}'\right)\cdot\mathcal{E}_\beta}{k'^2-k_0^2-i\eta}e^{i(\boldsymbol{k}'-\boldsymbol{k}_\alpha)\cdot\boldsymbol{r}}e^{i(\boldsymbol{k}_\beta-\boldsymbol{k}')\cdot\boldsymbol{r}'}. \tag{A.8}$$

To investigate how the refractive index modulation of a certain wavevector evolve in time, we multiply each side of Eq. (A.3) by $e^{i\ \boldsymbol{k}\cdot\boldsymbol{r}}/4\pi^2$ and integrate over all space. By writing the refractive index in terms of its Fourier components as $\delta n\left(\boldsymbol{r}\right)=\int d\boldsymbol{k}''\ \delta n\left(\boldsymbol{k}''\right)\ e^{-i\ \boldsymbol{k}''\cdot\boldsymbol{r}}$, and dropping the explicit time dependence for compactness, we have

$$\begin{aligned}&\tau\,\dot{\delta n}\left(\boldsymbol{k}\right)+\delta n\left(\boldsymbol{k}\right)=\\ &2k_\omega^2\gamma|E_0|^2\sum_{\alpha,\beta}\left[n_0\left(\frac{F_{\alpha\beta}(\boldsymbol{k}_\alpha-\boldsymbol{k})}{\left|\boldsymbol{k}_\alpha-\boldsymbol{k}\right|^2-k_0^2}\right)+n_0^*\ \left(\frac{F_{\beta\alpha}^*(\boldsymbol{k}_\beta+\boldsymbol{k})}{\left|\boldsymbol{k}_\beta+\boldsymbol{k}\right|^2-\left(k_0^*\right)^2}\right)\right]\\ &\times\delta n\left(\boldsymbol{k}+\boldsymbol{k}_\beta-\boldsymbol{k}_\alpha\right).\end{aligned} \tag{A.9}$$

Here we have assumed that the nonlinear domain extends infinitely, and that the homogeneous medium refractive index has a non-zero imaginary part, which allows to drop η. For brevity, we introduce $F_{\alpha\beta}\left(\boldsymbol{k}\right)=\frac{\mathcal{E}_\alpha^*}{|E_0|}\cdot$

$\left[\mathbb{I} - \frac{\mathbf{kk}}{k_0^2}\right] \cdot \frac{\mathcal{E}_\beta}{|E_0|}$, with $|E_0|$ being the amplitude of the incident plane wave. Writing the refractive index as $n_0 = n_{0,r} + in_{0,i} = n_{0,r}\,(1 + i\chi) \approx |n_0|(1 + i\chi)$, where $\chi \ll 1$, then the term in square brackets from the equation above can be rewritten as

$$n_0 \left(\frac{F_{\alpha\beta}(\boldsymbol{k}_\alpha - \boldsymbol{k})}{|\boldsymbol{k}_\alpha - \boldsymbol{k}|^2 - k_0^2} \right) + n_0^* \left(\frac{F^*_{\beta\alpha}(\boldsymbol{k}_\beta + \boldsymbol{k})}{|\boldsymbol{k}_\beta + \boldsymbol{k}|^2 - (k_0^*)^2} \right) =$$

$$\frac{1}{|n_0|k_\omega^2} \left[(1 + i\chi) \frac{F_{\alpha\beta}(\boldsymbol{k}_\alpha - \boldsymbol{k})}{\frac{|\boldsymbol{k}_\alpha - \boldsymbol{k}|^2}{(|n_0|k_\omega)^2} - (1 + i\chi)^2} + (1 - i\chi) \frac{F^*_{\beta\alpha}(\boldsymbol{k}_\beta + \boldsymbol{k})}{\frac{|\boldsymbol{k}_\beta + \boldsymbol{k}|^2}{(|n_0|k\omega)^2} - (1 - i\chi)^2} \right] \approx$$

$$\frac{1}{|n_0|k_\omega^2} \left[\frac{F_{\alpha\beta}(\boldsymbol{k}_\alpha - \boldsymbol{k})}{\frac{|\boldsymbol{k}_\alpha - \boldsymbol{k}|^2}{k_0^2} - 1 - 2i\chi} + \frac{F^*_{\beta\alpha}(\boldsymbol{k}_\beta + \boldsymbol{k})}{\frac{|\boldsymbol{k}_\beta + \boldsymbol{k}|^2}{k_0^2} - 1 + 2i\chi} \right].$$

Which finally allows to write Eq. (A.9) as presented in the main text:

$$\tau\, \dot{\delta n}\,(\boldsymbol{k}) + \delta n\,(\boldsymbol{k}) = \frac{2}{|n_0|} \frac{\gamma\,|E_0|^2}{\chi} \sum_{\alpha,\beta} \mathcal{M}_{\alpha\beta}(\boldsymbol{k}) \delta n\,(\boldsymbol{k} + \boldsymbol{k}_\alpha - \boldsymbol{k}_\beta)\ , \quad \text{(A.10)}$$

$$\mathcal{M}_{\alpha\beta}(\boldsymbol{k}) = \frac{\chi F_{\beta\alpha}\,(\boldsymbol{k}_\beta - \boldsymbol{k})}{\frac{|\boldsymbol{k} - \boldsymbol{k}_\beta|^2}{k_0^2} - 1 - 2i\chi} + \frac{\chi F^*_{\alpha\beta}\,(\boldsymbol{k} + \boldsymbol{k}_\alpha)}{\frac{|\boldsymbol{k} + \boldsymbol{k}_\alpha|^2}{k_0^2} - 1 + 2i\chi}. \quad \text{(A.11)}$$

Besides the linearization procedure, the strongest assumption made in this derivation is that the non-linear medium has infinite extent. Throughout the literature of pattern-forming systems, it is well known that the boundaries of non-linear media play a big role in the emergence of non-linear phenomena [360]. This may happen for instance for symmetry reasons i.e. The boundaries don't allow perturbations of certain patterns to emerge, or simply because the non-linear thresholds increase. In our case, the non-linear medium is much larger than the reciprocals of the characteristic wavevectors that appear in this treatment, however, the finite extent of the experimental system leads the thresholds to increase. This can be understood by relaxing the conditions in the derivation and letting the non-linear medium have a finite extent. What one sees from doing this is that the instead of coupling non-locally to particular wavevectors, the coupling takes place to a whole neigbourhood

through a convolution operation. This has the effect of joining together wavevectors that tend to get amplified through the non-linearity with others that tend to get attenuated, therefore raising the NL-threshold as a consequence.

Appendix B

Details about transfer matrix derivation and implementation

B.1 Transfer matrix and spherical vector harmonics expansion

For isotropic linear media, Maxwell's equations can be written assuming harmonic time dependence as

$$\mathbf{E} = \frac{ic}{\omega\varepsilon}(\nabla \times \mathbf{H}) \qquad \mathbf{H} = -\frac{ic}{\omega\mu}(\nabla \times \mathbf{E}). \tag{B.1}$$

To fully exploit the spherical symmetry of the system, one expands the electromagnetic (EM) fields in the basis of the orthogonal vector spherical harmonics, which are defined as

$$\begin{aligned} \mathbf{Y}_{lm}^{(e)} &= \frac{ir}{\sqrt{l(l+1)}}\nabla Y_{lm}, \\ \mathbf{Y}_{lm}^{(o)} &= \frac{ir^2}{\sqrt{l(l+1)}}\nabla \times (\nabla \times \mathbf{Y}_{lm}^{(e)}), \\ \mathbf{Y}_{lm}^{(m)} &= r(\nabla \times \mathbf{Y}_{lm}^{(e)}). \end{aligned} \tag{B.2}$$

In these expressions, Y_{lm} are the orthonormal spherical harmonics as defined in the Condon-Shortley convention. With these, it is possible to

construct a basis of normalized transverse vector multipoles

$$\mathbf{F}_{Mlm}(k_n, \mathbf{r}) = f_{Ml}(k_n r)\mathbf{Y}^{(m)}_{lm}(\mathbf{r}), \tag{B.3}$$

$$\mathbf{F}_{Elm}(k_n, \mathbf{r}) = \frac{1}{k_n r}\left[\sqrt{l(l+1)} f_{El}(k_n r)\mathbf{Y}^{(o)}_{lm}(\mathbf{r}) + \frac{d}{dr}(r f_{El}(k_n r))\mathbf{Y}^{(e)}_{lm}(\mathbf{r})\right], \tag{B.4}$$

where the subscripts E and M stand for the TE and TM polarizations. In these expressions, $f_{\alpha l}$ can be any combination of spherical bessel functions, and in particular we choose Bessel and Hankel functions, $f_{\alpha l} = j_l$ and $f_{\alpha l} = h^{(1)}_l$, and will denote the associated vector multipoles as $\mathbf{J}_{\alpha lm}$ and $\mathbf{H}_{\alpha lm}$. This choice sets the EM powerflow along the positive radial direction, and also allows to separate well and badly behaved solutions at the origin. A general solution for the electric field in the n-th layer of the hyperbolic cavity can be written as

$$\mathbf{E}_\alpha = \sum_{l,m}\left[A_{\alpha lm}(n)\mathbf{J}_{\alpha lm}(k_n\mathbf{r}) + B_{\alpha lm}(n)\mathbf{H}_{\alpha lm}(k_n\mathbf{r})\right]. \tag{B.5}$$

By applying continuity conditions of fields across boundaries, one constructs the forward-scattering transfer matrix, which relates the fields in two adjacent layers through the amplitude coefficients in Eq. (B.5) as

$$\begin{pmatrix} A_{\alpha lm}(n+1) \\ B_{\alpha lm}(n+1) \end{pmatrix} = T^+_{\alpha l}(n) \begin{pmatrix} A_{\alpha lm}(n) \\ B_{\alpha lm}(n) \end{pmatrix}. \tag{B.6}$$

The backwards-scattering matrices are obtained from Eq. (B.6) by inversion. The expressions for the scattering matrices [207] for the TE and TM modes are given by

$$T^+_{Ml}(n) = -i\begin{pmatrix} \kappa_n\xi'_l(y_n)\psi_l(x_n) - \xi_l(y_n)\psi'_l(x_n) & \kappa_n\xi'_l(y_n)\xi_l(x_n) - \xi_l(y_n)\xi'_l(x_n) \\ \psi_l(y_n)\psi'_l(x_n) - \kappa_n\psi'_l(y_n)\psi_l(x_n) & \psi_l(y_n)\xi'_l(x_n) - \kappa_n\psi'_l(y_n)\xi_l(x_n) \end{pmatrix},$$

$$T^+_{El}(n) = -i\begin{pmatrix} \xi'_l(y_n)\psi_l(x_n) - \kappa_n\xi_l(y_n)\psi'_l(x_n) & \xi'_l(y_n)\xi_l(x_n) - \kappa_n\xi_l(y_n)\xi'_l(x_n) \\ \kappa_n\psi_l(y_n)\psi'_l(x_n) - \psi'_l(y_n)\psi_l(x_n) & \kappa_n\psi_l(y_n)\xi'_l(x_n) - \psi'_l(y_n)\xi_l(x_n) \end{pmatrix}, \tag{B.7}$$

Where $\xi_l(z)$ and $\psi_l(z)$ are Riccati-Bessel functions, defined as $\psi_l(z) = zj_l(z)$ and $\xi_l(z) = zh_l^{(1)}(z)$, and the prime denotes the derivative with respect to the argument. The other magnitudes appearing are $\kappa_n = \sqrt{\epsilon_{n+1}/\epsilon_n}$, the ratio between the permittivities between adjacent layers, r_n, the outer radius, $k_n = \sqrt{\epsilon_n}\omega/c$, the EM wavevector modulus for the nth layer, and $x_n = k_n r_n$ and $y_n = k_{n+1} r_n$.

In our calculations, we are particularly interested in linking the external fields and the EM fields at the center of the nanocavity. Thus, for a core shell consistent of N layers, and labelling the core as the zero-th region, we define the ordered product of transfer matrices as

$$\begin{aligned} \mathcal{M}_{\alpha l} &= \prod_{n=0}^{N} T^{+}_{\alpha l}(n) \\ &\equiv T^{+}_{\alpha l}(N) T^{+}_{\alpha l}(N-1) \dots T^{+}_{\alpha l}(1) T^{+}_{\alpha l}(0). \end{aligned} \tag{B.8}$$

The computation of the matrices in Eq. (B.8) gives us access to the relevant magnitudes of our study.

B

B.2 Expressions for relevant magnitudes

In this section, we outline the derivation of the expressions of field enhancement, and radiative and total Purcell factors. Finally, the simplification of Eq. (B.7) is also briefly discussed.

B.2.1 Field Enhancement

We focus our attention first into the field enhancement taking place at the center of the nanocavities under positron beam excitation, which allows us to describe the absorption amplification experienced by any fluorescent agent placed in this position. As mentioned, defining $\mathbf{J}_{\alpha lm}$ and $\mathbf{H}_{\alpha lm}$ allows to separate well and badly behaved solutions at the origin. Since upon external excitation the field has to be finite at the origin, then solutions must not include $\mathbf{H}_{\alpha lm}$ in the central region ($B_{\alpha lm}(n = 0) = 0$). Furthermore, evaluating $\mathbf{J}_{Mlm}$ we find that it always vanishes at the origin for every value of l and m, and moreso, $\mathbf{J}_{Elm}$

is only non-vanishing at the origin for $l = 1$, which allows to write

$$\mathbf{E}(\mathbf{r} = 0) = \sum_{m=-1}^{1} A_{E1m}(1)\mathbf{J}_{E1m}(k_n, \mathbf{r} = 0). \tag{B.9}$$

It is straightforward to link Eq. (B.9) with the TE external fields as

$$\begin{pmatrix} A_{E1m}(N+1) \\ B_{Elm}(N+1) \end{pmatrix} = \mathcal{M}_{E1} \begin{pmatrix} A_{E1m}(1) \\ 0 \end{pmatrix}, \tag{B.10}$$

so that the field at the cavity center can be expressed as

$$\mathbf{E}(0) = \frac{1}{\langle \mathcal{M}_{E1} \rangle_{11}} \left[\sum_{m=-1}^{1} A_{E1m}(N+1)\mathbf{J}_{E1m}(k_n, 0) \right]. \tag{B.11}$$

Note that in absence of cavity the transfer matrices become the identity, and therefore, one can simply identify the term in brackets as the external incident field evaluated at $\boldsymbol{r} = 0$. Eq. (B.11) shows that the optical modes sustained by the hyperbolic nanocavities are given by the zeroes of $\langle \mathcal{M}_{E1} \rangle_{11}$. This result is formally identical to the usual calculation of Mie resonances [208]. Finally, the field enhancement with respect to a given reference configuration can be calculated as

$$\frac{|E|}{|E_0|} = \frac{|\langle \mathcal{M}^0_{E1} \rangle_{11}|}{|\langle \mathcal{M}_{E1} \rangle_{11}|}, \tag{B.12}$$

where the zero sub- and super-scripts denote the reference magnitudes, corresponding to silica spheres of the same outer radius as the nanocavities. It is worth noting that this normalization absorbs all the spectral features of the excitation source, and thus the result only depends on the cavity geometric and material parameters.

We now give an explicit expression of the field generated by the positron at the center of the cavity. As justified before, the modal expansion at the origin in absence of the cavity is the same as the electric field produced by a passing electron in free space [185], thus we can then

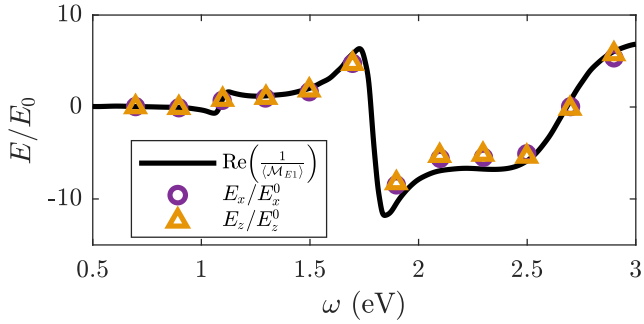

FIGURE B.1: Comparison between fully numerical (isolated points) and quasi-analytical predictions (solid line) for the field enhancement at the center of the 7-layer periodic nanocavity considered in Fig. 3.4.

use

$$\begin{aligned}\mathbf{E}_{\text{free}}(\mathbf{r}=0) &= \sum_{m=-1}^{1} A^{\text{free}}_{E1m}(N+1)\mathbf{J}_{E1m}(k_0,\mathbf{r}=0) = \\ &= \frac{2e\omega}{v^2\gamma}\left[\frac{i}{\gamma}K_0\left(\frac{\omega b}{v\gamma}\right)\hat{\mathbf{z}} - K_1\left(\frac{\omega b}{v\gamma}\right)\hat{\mathbf{x}}\right],\end{aligned} \tag{B.13}$$

where we have chosen the electron to have positive velocity v along the z axis and along the line $x=-b$, $y=0$. In Eq. (B.13), $\gamma = 1/\sqrt{1-(v/c)^2}$ is the Lorentz contraction factor, and K_i are modified bessel functions of the second kind. The field in the presence of the structure will then be given by

$$\mathbf{E}(0) = \frac{1}{\langle\mathcal{M}_{E1}\rangle_{11}}\frac{2e\omega}{v^2\gamma}\left[\frac{i}{\gamma}K_0\left(\frac{\omega b}{v\gamma}\right)\hat{\mathbf{z}} - K_1\left(\frac{\omega b}{v\gamma}\right)\hat{\mathbf{x}}\right]. \tag{B.14}$$

In Fig. B.1, I plot the ratio between Eqs. (B.14) and (B.13) versus frequency for the structure considered in Fig. 3.4, a periodic 7-layer nanocavity with $R_{\text{in}} = 11$ nm and $R_{\text{tot}} = 60$ nm. Transfer matrix calculations are compared against COMSOL simulations. We can observe the excellent agreement between quasi-analytical and fully numerical spectra for both x- and z-components of the electric field at the cavity center.

B

B.2.2 Radiative Purcell

Now we obtain the expressions that characterize the radiative and total Purcell factors needed to calculate the total fluorescence quantum yield. We describe the molecules as EM oscillating point-dipoles with dipole moment $\mathbf{p}$. The fields radiated by such EM sources in a medium of permittivity ϵ and at location $\boldsymbol{r}_d$ is given by [207]

$$\mathbf{E}_d(\mathbf{r}) = \sum_{lm} \left[a^d_{Mlm} \mathbf{H}_{Mlm}(k, \mathbf{r}) + a^d_{Elm} \mathbf{H}_{Elm}(k, \mathbf{r}) \right]. \tag{B.15}$$

where the coefficients are given by the expressions

$$\begin{aligned} a^d_{Mlm} &= 4\pi i \frac{k^3}{\epsilon} \mathbf{p} \cdot \mathbf{J}^*_{Mlm}(k, \mathbf{r}_d), \\ a^d_{Elm} &= 4\pi i \frac{k^3}{\epsilon} \mathbf{p} \cdot \mathbf{J}^*_{Elm}(k, \mathbf{r}_d). \end{aligned} \tag{B.16}$$

The asterisks in the coefficients above denote the complex conjugate of the vector spherical harmonics, not the Bessel functions. As mentioned before, $\mathbf{J}_{Mlm}(k, \mathbf{r}_d)$ vanishes for $\mathbf{r}_d = 0$ for any l and m, while $\mathbf{J}_{Elm}(k, \mathbf{r}_d)$ is only non-zero at the origin for $l = 1$. The electric field radiated by a point-dipole source located at the coordinate origin (cavity center) is then

$$\begin{aligned} \mathbf{E}_d(\mathbf{r}) = 4\pi i \frac{k^3}{\epsilon} \sum_{m=-1}^{1} \left[\mathbf{p} \cdot \mathbf{J}^*_{E1m}(k, 0) \mathbf{H}_{E1m}(k, \mathbf{r}) \right] = \\ = \sum_{m=-1}^{1} \left[B_{E1m}(1) \mathbf{H}_{E1m}(k, \mathbf{r}) \right] \end{aligned} \tag{B.17}$$

Note that the radial dependence of Eq (B.17) is given by $h^{(1)}_l$, describing EM powerflow along the positive radial direction. In the exterior of the nanocavities, there will be only EM fields behaving in a similar way, and thus we can make $A_{E1m}(N+1) = 0$ in Eq. (B.5). Using the ordered product of transfer matrices, $\mathcal{M}_{E1}$, we can relate the field coefficients

outside the cavity and inside its core,

$$\begin{pmatrix} 0 \\ B_{Elm}(N+1) \end{pmatrix} = \mathcal{M}_{E1} \begin{pmatrix} A_{E1m}(1) \\ B_{E1m}(1) \end{pmatrix}. \tag{B.18}$$

Which upon solving allows to obtain

$$A_{E1m}(1) = -\frac{\langle \mathcal{M}_{E1} \rangle_{12}}{\langle \mathcal{M}_{E1} \rangle_{11}} B_{E1m}(1), \tag{B.19}$$

$$B_{Elm}(N+1) = \frac{\det(\mathcal{M}_{E1})}{\langle \mathcal{M}_{E1} \rangle_{11}} B_{E1m}(1). \tag{B.20}$$

With this, we know the fields in the central region of the cavity and on the outside, which allows to calculate the far-field radiated power, which is related to the radiative Purcell, and the near-field total power emitted by the fluorescent agent, which yields the total Purcell.

Eq. (B.20) shows that the electric field in the exterior of the cavities is equal to the free-space dipole field scaled by a transfer matrix factor. Hence, the relation between the radiated power in the presence of the cavity and in free space is simply $P_R = |\det(\mathcal{M}_{E1})/\langle \mathcal{M}_{E1} \rangle_{11}|^2 n_{core}^2 P_{\text{free}}$, with P_{free} being the power radiated in free-space by the same dipole and n_{core} is the refractive index of the central region. If we consider a different normalization, a reference different from free-space, we can express the radiative Purcell factor as

$$\mathcal{P}_R = \frac{P_R}{P_R^0} = \left| n_{\text{core}}^2 \frac{\det(\mathcal{M}_{E1})}{\langle \mathcal{M}_{E1} \rangle_{11}} \right|^2 \Bigg/ \left| n_{\text{core},0}^2 \frac{\det(\mathcal{M}_{E1}^0)}{\langle \mathcal{M}_{E1}^0 \rangle_{11}} \right|^2. \tag{B.21}$$

Note that technically, the radiative Purcell should be calculated as the ratio of the radiated power to the total dissipated energy by the reference, and therefore, the expression above for the radiative Purcell will only be valid if the reference configuration is lossless.

B.2.3 Total Purcell

As we have shown in the previous subsection, the total field (including the scattering due to the multilayer structure) within the core of the

cavity can be written as

$$\mathbf{E}_T(\mathbf{r}) = \sum_{m=-1}^{1} B_{E1m}(1)\left[\mathbf{H}_{E1m}(k,\mathbf{r}) - \frac{\langle \mathcal{M}_{E1}\rangle_{12}}{\langle \mathcal{M}_{E1}\rangle_{11}}\mathbf{J}_{E1m}(k,\mathbf{r})\right]. \quad \text{(B.22)}$$

Computing the magnetic field associated to (B.22), we can calculate the total power radiated by the dipole within the core region, which turns out to be

$$\begin{aligned} P_T &= \frac{c^2}{2\omega^2}\frac{1}{\sqrt{\epsilon}}\,\mathrm{Re}\left[1 - \frac{\langle \mathcal{M}_{E1}\rangle_{12}}{\langle \mathcal{M}_{E1}\rangle_{11}}\right]\left[\sum_{m=-1}^{1}|B_{E1m}(1)|^2\right] = \\ &= n_{\mathrm{core}} P_{\mathrm{free}}\,\mathrm{Re}\left[1 - \frac{\langle \mathcal{M}_{E1}\rangle_{12}}{\langle \mathcal{M}_{E1}\rangle_{11}}\right], \end{aligned} \quad \text{(B.23)}$$

where we have grouped terms corresponding to the power radiated in free space. Again, one can normalize this magnitude to a different situation and obtain the total Purcell factor as

$$\mathcal{P}_T = \frac{P_T}{P_T^0} = \sqrt{\frac{\epsilon_{\mathrm{core}}}{\epsilon_{\mathrm{core},0}}}\,\mathrm{Re}\left(1 - \frac{\langle \mathcal{M}_{E1}\rangle_{12}}{\langle \mathcal{M}_{E1}\rangle_{11}}\right) \Big/ \mathrm{Re}\left(1 - \frac{\langle \mathcal{M}^0_{E1}\rangle_{12}}{\langle \mathcal{M}^0_{E1}\rangle_{11}}\right), \quad \text{(B.24)}$$

where $\epsilon_{\mathrm{core},0} = \epsilon_{\mathrm{core}} = \epsilon_{\mathrm{SiO_2}}$ in our calculations.

With the expressions presented in this section, the calculation of fluorescence enhancement factors has been reduced to the computation of ordered products of transfer matrices. We have shown that all the relevant magnitudes (field enhancement and Purcell factors) can be written in a compact, quasi-analytical form in terms of $\mathcal{M}_{E1}$.

B.3 Particle Swarm Optimization

To find the optimal geometric configuration for hyperbolic cavities we implemented a particle swarm optimization (PSO) algorithm [217]. The inspiration for these algorithms is that groups of animals are somehow able of efficiently locating food sources. The hypothesis is that local correlations in the motion of the members of a swarm lead to global behaviors, due to the sharing of information among individuals. The

algorithm that we implement is largely based on the original PSO formulation in Ref. [217], with some later modifications proposed by the same authors [218].

The PSO algorithm works as follows. We define first a hypercube that represents the solution space, and set the lower and upper bounds for every variable. Next, we create a population of n individuals scattered randomly across this volume and assign a random initial velocity to each one. Then the fitness function is evaluated for every individual, and velocities are updated as

$$\vec{v}' = w\vec{v} + \phi_p(\vec{p}_{best} - \vec{x}) + \phi_g(\vec{g}_{best} - \vec{x})$$
$$\vec{x}' = \vec{x} + \vec{v}$$

In these expressions, w is the inertia weight, $\vec{p}_{best}$ is best achieved position of each individual, and $\vec{g}_{best}$ is the best position achieved among all individuals in the swarm. After calculating the new set of positions, the fitness function is re-evaluated and the values of $\vec{p}_{best}$ and $\vec{g}_{best}$ are updated. This is done until convergence.

The expression above illustrates that the motion of every individual gravitates towards the particular and general best, and that the strength of the pull towards any of these is given by the ratio ϕ_p and ϕ_g. In each iteration, we set $\phi_p = 2 * Rand()$ and $\phi_g = 2 * Rand()$, where $Rand$ indicates a randomly generated number between 0 and 1. This way, both have the same expectation value, while random kicks are included to drive the search process. The role of the inertia weight is to foster exploration of the solution space [218]. In our implementation, we set its initial value to 0.9 and decrease it linearly until reaching $w = 0.4$. This causes the first iterations of the algorithm to have a search-like behavior, while late iterations tend to refine the optimum positions. We consider large swarm populations (10^5 individuals) and limit the number of iterations to 10^3. Due to the stocastic element introduced in the parameter values, we repeat the whole optimization process 20 times and keep the best outcome.

B

Appendix C

Evaluating the hyperbolic character of multilayer nanocavities

In Section 3.2, we evaluated the hyperbolic character of the nanocavities by employing the expression for the effective permittivity tensor of a planar system. In this section we show that these results hold when considers the more complicated expressions for the effective permittivity tensor of a spherical layered system. For a multi-shell of internal radius R_0 and external radius R, where the boundaries between materials are given by r_i, the effective permittivity tensors are given by [211]

$$\epsilon_\theta = \epsilon_\phi = \frac{1}{R - R_0} \sum_i \epsilon_i (r_{i+1} - r_i), \tag{C.1}$$

$$\frac{1}{\epsilon_r} = \frac{R_0 R}{R - R_0} \sum_i \frac{1}{\epsilon_i} \left(\frac{1}{r_i} - \frac{1}{r_{i+1}} \right). \tag{C.2}$$

For a system composed of alternating silver and silica layers (like in our case) the angular components of the permittivity tensor simply read:

$$\epsilon_\theta = \epsilon_\phi = \epsilon_{\mathrm{Ag}}\, \eta_{\mathrm{linear}} + \epsilon_{\mathrm{SiO_2}}\, (1 - \eta_{\mathrm{linear}}), \tag{C.3}$$

which is exactly the same as the expression for the tangential components of the planar, bulk case but with the filling fraction being defined in terms of the radial, and not volumetric distribution, hence the linear subscript.

For a general multilayer made of isotropic materials, the hyperbolic

character can be checked by evaluating $\epsilon_r \epsilon_\theta$, which if one defines $\Delta_i \equiv r_{i+1} - r_i$ and $\overline{r_i} \equiv (r_{i+1} + r_i)/2$ can be straightforwardly obtained as

$$\epsilon_\theta \epsilon_r = \frac{1}{R_0 R} \frac{\sum_i \epsilon_i \Delta_i}{\sum_i \frac{1}{\epsilon_i} \frac{\Delta_i}{(\overline{r_i})^2 - \left(\frac{\Delta_i}{2}\right)^2}}. \tag{C.4}$$

In Fig. C.1 we show the real part of this magnitude for the periodic nanocavities treated in Sec. 3.2.2, and one can see that this magnitue is negative in the majority of the parameter space treated and therefore, the multilayered shells do behave hyperbolically. We have included a solid black line that shows the condition $\mathrm{Re}(\epsilon_r \epsilon_\theta) = 0$ to make the distinction between hyperbolic and non-hyperbolic regions more clear.

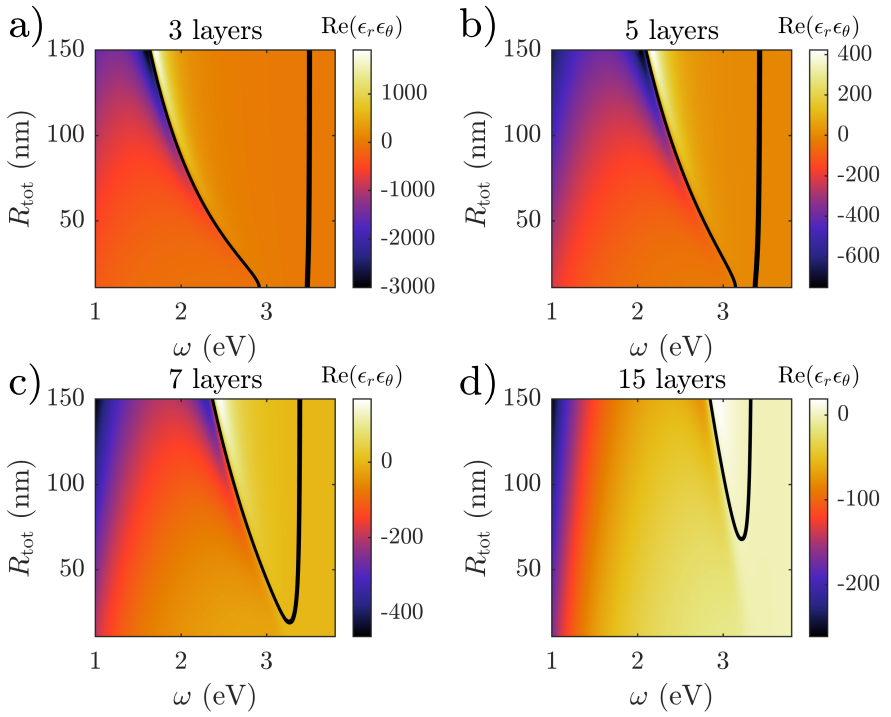

FIGURE C.1: Demonstration of the hyperbolic character of periodic multilayered cavities with 3 (a), 5 (b), 7 (c) and 15 layers (d), showing that below roughly 3 eV and when the layersizes are much smaller than the wavelength, these spherical multilayers behave hyperbolically.

In the same way, one can check that the PSO-designed cavities shown

in Sec. 3.2.3 are also of hyperbolic character. In Fig. C.2 we show $\mathrm{Re}(\epsilon_r \epsilon_\theta)$ at the optimization frequency for these cavities of different number of layers. The negative character of this quantity indicates that the optimization procedure yields hyperbolic cavities for target operation frequencies below 2.8 eV.

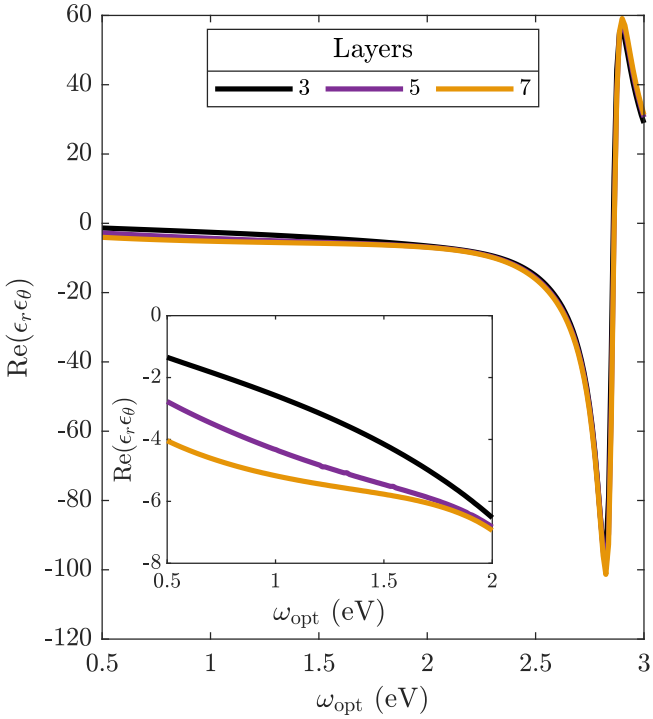

FIGURE C.2: Demonstration of hyperbolic character of PSO-designed nanocavities for operation frequencies below 3 eV. Inset showcases the different behavior of the optimization at lower photon energies.

C

Appendix D

Far-field model of EL from plasmonic structures

To fully capture the far-field experimental phenomenology we develop a model. This is meant to reproduce experimental features that, according to our numerical simulations, are not related to the strong light-matter interactions that take place within the micron-sized volume around the nanowire junction. In particular, the model allows us to introduce a far-field maximum observed in the experiment, blue-detuned from the TMD exciton frequency, that we link to the strong radiation losses experienced by the surface plasmon waves that scatter at the nanowire edges, microns away from the region of electron tunnelling. By construction, this maximum is absent in the numerical simulations, where the lateral boundary conditions prevent any power radiation in the vertical direction originated from propagating surface plasmons. In our model, we have included two optical modes, and the exciton transition. The Hamiltonian that describes the interaction and pumping of the system is given by, $\hat{H} = \hat{H}_0 + \hat{H}_{\text{pump}}$, with

$$\hat{H}_0 = \hbar\omega_1\,\hat{a}_1^\dagger\hat{a}_1 + \hbar\omega_\sigma\,\hat{\sigma}^\dagger\hat{\sigma} + \hbar g(\hat{a}_1^\dagger\hat{\sigma} + \hat{a}_1\hat{\sigma}^\dagger) + \hbar\omega_2\,\hat{a}_2^\dagger\hat{a}_2, \tag{D.1}$$

$$\hat{H}_{\text{pump}} = \hbar\nu_1\,(\hat{a}_1^\dagger + \hat{a}_1) + \hbar\nu_2\,(\hat{a}_2^\dagger + \hat{a}_2), \tag{D.2}$$

where $\hat{a}_1$ is the bosonic annihilation operator for the optical mode around 1.8 eV that our COMSOL simulations reproduce, the one responsible for the coupling to the exciton (where $\hat{\sigma}$ is the excitonic annihilation operator). Both are coupled through a Jaynes-Cummings term with strength g. On the other hand, $\hat{a}_2$ is the annihilation operator for the

exciton-decoupled, blue-detuned mode observed in the experiments. The electron static-like current couples to both optical modes, and not the TMD excitons, with relative strengths given by ν_i. Assuming that the pumping is small, and in order to account for optical and excitonic radiative decay [41], we build an effective non-hermitian Hamiltonian of the form

$$\hat{H}_{\text{eff}} = \hat{H}_{\text{pump}} + \hbar\Omega_1\,\hat{a}_1^\dagger\hat{a}_1 + \hbar\Omega_\sigma\,\hat{\sigma}^\dagger\hat{\sigma} + \hbar g(\hat{a}_1^\dagger\hat{\sigma} + \hat{a}_1\hat{\sigma}^\dagger) + \hbar\Omega_2\,\hat{a}_2^\dagger\hat{a}_2, \tag{D.3}$$

where $\Omega_i = \omega_i - i\gamma_i/2$ and, in the same fashion, $\Omega_\sigma = \omega_\sigma - i\gamma_\sigma/2$. Note that the γ's are the radiative decay rates of the different elements of the system. We can diagonalize the terms that couple the optical mode $\hat{a}_1$ and the exciton $\hat{\sigma}$ above. These give rise to the polaritons observed experimentally. The polaritonic Hamiltonian is then given by $\hat{H}_{\text{pol}} = \hbar\Omega_1\hat{a}_1^\dagger\hat{a}_1 + \hbar\Omega_\sigma\hat{\sigma}^\dagger\hat{\sigma} + \hbar g(\hat{a}_1^\dagger\hat{\sigma} + \hat{a}_1\hat{\sigma}^\dagger)$, and is diagonalized as $\hat{H}_{\text{pol}}\,|N,\pm\rangle = \hbar\Omega_\pm(N)\,|N,\pm\rangle$, with $\Omega_\pm(N) = N\Omega_1 - \Delta \pm \sqrt{\Delta^2 + Ng^2}$, and

$$\begin{aligned} |N,\pm\rangle &= \frac{g\sqrt{N}\,|N,g\rangle + (\Delta \mp \sqrt{\Delta^2 + Ng^2})\,|N-1,e\rangle}{\sqrt{Ng^2 + \left|\Delta \mp \sqrt{\Delta^2 + Ng^2}\right|^2}} \\ &\equiv A_\pm\,|N,g\rangle + B_\pm\,|N-1,e\rangle\,, \end{aligned} \tag{D.4}$$

where $\Delta = (\Omega_1 - \Omega_\sigma)/2$, and $|g\rangle$ and $|e\rangle$ correspond, respectively, to the ground and excited state of the exciton, and $|N\rangle$ is the number of photons in mode $\hat{a}_1$. Then, one can treat the pump term using first-order perturbation theory [273], and find the perturbed ground state of the system, which turns out to be

$$|0'\rangle \approx |0,g\rangle \otimes \left[|0\rangle_2 - \frac{\nu_2}{\Omega_2^*}\,|1\rangle_2\right] - \nu_1\left[\frac{A_+^*}{\Omega_+^*}\,|1,+\rangle + \frac{A_-^*}{\Omega_-^*}\,|1,-\rangle\right] \otimes |0\rangle_2\,. \tag{D.5}$$

D

Once this perturbed ground state is known, we can compute the power spectrum (under weak-pumping), given by [274]

$$I(\omega) = \mathrm{Re}\left(\lim_{T\to\infty} \frac{1}{2\pi T} \int_{-T/2}^{T/2} dt \int_{-\infty}^{\infty} d\tau \left\langle 0' \middle| \hat{\xi}^{\dagger}(t)\hat{\xi}(t-\tau) \middle| 0' \right\rangle e^{-i\omega\tau} \right), \tag{D.6}$$

where $\hat{\xi}_i = \vec{\mu}_i \hat{a}_i$, with $\vec{\mu}_i$ being the effective dipole moment of the optical modes. We assume that detected emission mainly comes from the optical modes, and since the pumping is incoherent, we consider separately the intensity emitted by each optical mode (thus neglecting cross-correlation terms). The lineshapes for both modes are therefore

$$\begin{aligned} I_1(\omega) =& \frac{|\nu_1\mu_1|^2}{2\pi} \left| \frac{A_+^2}{\Omega_+} \right|^2 \frac{|\Gamma_+|}{(\omega-\omega_+)^2+\Gamma_+^2} \\ &+ \frac{|\nu_1\mu_1|^2}{2\pi} \left| \frac{A_-^2}{\Omega_-} \right|^2 \frac{|\Gamma_-|}{(\omega-\omega_-)^2+\Gamma_-^2}, \end{aligned} \tag{D.7}$$

$$I_2(\omega) = \frac{|\nu_2\mu_2|^2}{2\pi} \left| \frac{1}{\Omega_2} \right|^2 \frac{|\Gamma_2|}{(\omega-\omega_2)^2+\Gamma_2^2}, \tag{D.8}$$

where $\omega_i = \mathrm{Re}(\Omega_i)$, and $\Gamma_i = \mathrm{Im}(\Omega_i)$. Finally, the measured intensity is given by the projection of the far field amplitude over the polarizer, which can be calculated as

$$I_T(\omega) = I_1(\omega)\cos^2(\phi-\phi_1) + I_2(\omega)\cos^2(\phi-\phi_2), \tag{D.9}$$

where ϕ is the polarizer angle and ϕ_i is the orientation of the dipole moment of mode i. We set the parameters of the TMD exciton and first cavity mode to the values obtained from our numerical simulations: $\phi_1 = 45°$, $\omega_1 = 1.75$ eV, $\gamma_1 = 2\Gamma_1 = 90$ meV, g=35 meV, $\omega_\sigma = 1.75$ eV, $\gamma_\sigma = 10$ meV. For the second cavity mode, we take $\omega_2 = 1.81$ eV, $\gamma_2 = 2\Gamma_2 = 140$ meV, and ϕ_2 as described in the main text of the thesis and in the caption of Fig. 3.13. The other free parameter is the ratio $f = |\nu_2\mu_2/\nu_1\mu_1|^2$, which weights how much more (or less) the two different cavity modes get excited in the near field by the tunneling current (ν_2/ν_1), and how relatively bright they are (μ_2/μ_1). These two mechanisms are indistinguishable from the far field. We know from

experimental data that the $\hat{a}_2$ mode is brighter, so we have set $f = 3$, with which we produce the results shown in the thesis.

Appendix E

MQED for nanophotonics

E.1 Outline of the hamiltonian derivation

In this section, we give an overview of the way the Hamiltonian of the system has been postulated. For a more detailed description of the followed procedure we refer the reader to the corresponding sections of this appendix. The starting point is a macroscopic QED (mQED) Hamiltonian [28, 321] describing EM fields in a minimal coupling scheme and a term that describes a collection of arbitrary electronic eigenstates:

$$\hat{H} = \iint \mathrm{d}\boldsymbol{r}\, \mathrm{d}\omega\, \hbar\omega \hat{\boldsymbol{f}}^{\dagger}(\boldsymbol{r},\omega)\hat{\boldsymbol{f}}(\boldsymbol{r},\omega) + \sum_i E_i \hat{c}_i^{\dagger}\hat{c}_i + \frac{e}{m}\hat{\mathbf{p}}\cdot\hat{\boldsymbol{A}}, \tag{E.1}$$

where $\hat{\boldsymbol{f}}(\boldsymbol{r},\omega)$ are the usual bosonic operators representing the fields created by an infinitesimal dipole moment, $\hat{c}_i$ is the annihilation operator of an electron in an eigenstate described by the wavefunction $\phi_i(r)$, $\hat{\mathbf{p}}$ is the momentum operator of the charged particles and $\hat{\boldsymbol{A}}$ is the vector potential operator, which can be written in terms of the $\hat{\boldsymbol{f}}(\boldsymbol{r},\omega)$ operators as

$$\hat{\boldsymbol{A}}(\boldsymbol{r}) = -i\int \frac{\mathrm{d}\omega}{\omega}\int \mathrm{d}\boldsymbol{r}' \left[\mathbf{G}(\boldsymbol{r},\boldsymbol{r}',\omega)\cdot\hat{\boldsymbol{f}}(\boldsymbol{r}',\omega) - \hat{\boldsymbol{f}}^{\dagger}(\boldsymbol{r}',\omega)\cdot\mathbf{G}^{\dagger}(\boldsymbol{r},\boldsymbol{r}',\omega)\right], \tag{E.2}$$

where $\mathbf{G}$ is the Dyadic Green's Function. We can also write the momentum operator in terms of the basis of electronic eigenfunctions, $\{\phi_i\}$ as

$$\hat{\mathbf{p}}(\boldsymbol{r}) = -i\hbar\sum_{i,j}\hat{c}_i^{\dagger}\hat{c}_j\phi_i^{*}(\boldsymbol{r})\nabla\phi_j(\boldsymbol{r}), \tag{E.3}$$

which motivates defining a dipole moment density $\boldsymbol{d}_{ij}(\boldsymbol{r}) \equiv \phi_i^*(\boldsymbol{r})\nabla\phi_j(\boldsymbol{r})$, and an operator describing the electronic jump between eigenstates $\phi_j \to \phi_i$ as $\hat{\sigma}_{ij} = \hat{c}_i^\dagger \hat{c}_j$. The Hamiltonian above only contains direct couplings between electronic transitions and EM fields, and as such, all the interactions between different electronic transitions appear as second order processes. In this appendix, we will obtain an effective Hamiltonian that describes the direct interaction of these electronic transitions mediated by the EM environment following a procedure similar to that of Ref. [39]. The core idea of the derivation is that one may split the total EM response, codified in the Dyadic Green's Function, $\mathbf{G}$, into the part that is resonant with the electronic transitions, $\mathbf{G}^{(\mathrm{R})}$, and the non-resonant part to which electronic transitions are only weakly coupled and thus acts as a background, $\mathbf{G}^{(\mathrm{NR})}$. Therefore one has that $\mathbf{G} = \mathbf{G}^{(\mathrm{R})} + \mathbf{G}^{(\mathrm{NR})}$, and consequently, the vector potential will also be written in this manner as $\hat{\boldsymbol{A}} = \hat{\boldsymbol{A}}^{(\mathrm{R})} + \hat{\boldsymbol{A}}^{(\mathrm{NR})}$. We then find that the dynamics of the system can be described by an effective Hamiltonian

$$\begin{aligned}\hat{H}_{\mathrm{eff}} = &\iint \mathrm{d}\boldsymbol{r}\,\mathrm{d}\omega\,\hbar\omega\,\hat{\boldsymbol{f}}^\dagger(\boldsymbol{r},\omega)\hat{\boldsymbol{f}}(\boldsymbol{r},\omega) + \sum_i (E_i - \hbar\delta_i)\,\hat{c}_i^\dagger\hat{c}_i \\ &+ \frac{e}{m}\hat{\mathbf{p}}\cdot\hat{\boldsymbol{A}}^{(\mathrm{R})} - \hbar \sum_{\substack{i,j \\ k,l\neq i,j}} g_{ij,kl}^{m-m}\hat{\sigma}_{ij}\hat{\sigma}_{kl}^\dagger \end{aligned} \tag{E.4}$$

where only the resonant part of the fields remains in the light-matter interaction term, as the non-resonant background has given rise to the direct matter-matter interaction term. The expressions for the Lamb-shift, δ_i and coupling between electronic transitions $g_{ij,kl}^{m-m}$ are given by

$$g_{ij,kl}^{m-m} = \frac{e^2\hbar\mu_0}{2m^2}\iint \mathrm{d}\boldsymbol{r}\,\mathrm{d}\boldsymbol{r}'\,\boldsymbol{d}_{ij}(\boldsymbol{r})\cdot\mathrm{Re}\left\{\mathbf{G}^{(\mathrm{NR})}(\boldsymbol{r},\boldsymbol{r}',\Omega)\right\}\cdot\boldsymbol{d}_{kl}^*(\boldsymbol{r}'), \tag{E.5}$$

$$\delta_i = \sum_j g_{ij,ij}^{m-m}. \tag{E.6}$$

One of the assumptions needed for the above expression to hold is that the energy difference associated with transitions $i \to j$ and $k \to l$ are similar so that $\Omega = \omega_{ij} \approx \omega_{kl}$. This effective Hamiltonian also holds in

the case that the Dyadic Green's Function varies sufficiently smoothly over the frequency range of interest. Note that since $\boldsymbol{d}_{ij}^{*} = -\boldsymbol{d}_{ji}$, and the dyadic is symmetric with respect to index exchange, it can be shown that this coupling satisfies: $g_{ij,kl}^{m-m} = (g_{kl,ij}^{m-m})^{*}$ and $g_{ij,kl}^{m-m} = g_{lk,ji}^{m-m}$.

Once that a direct, field-mediated, coupling between electronic transitions has been derived from the non-resonant EM background, we proceed to define new bosonic operators describing the EM field in the spirit of the emitter-centered modes, as described in [321]. This is done in Section E.2.2, and the final Hamiltonian reads

$$\begin{aligned}\hat{H}_{\text{eff}} = &\sum_{ij}\int \mathrm{d}\omega\ \hbar\omega\, \hat{a}_{ij}^{\dagger}(\omega)\hat{a}_{ij}(\omega) + \sum_{i}(E_i - \hbar\delta_i)\,\hat{c}_i^{\dagger}\hat{c}_i \\ &+\hbar\sum_{ij}\int \mathrm{d}\omega\ g_{ij}^{l-m}(\omega)\left[\hat{a}_{ij}(\omega) + \hat{a}_{ji}(\omega)^{\dagger}\right]\hat{\sigma}_{ij} \\ &-\hbar\sum_{\substack{i,j\\k,l}} g_{ij,kl}^{m-m}\hat{\sigma}_{ij}\hat{\sigma}_{kl}^{\dagger},\end{aligned} \tag{E.7}$$

where the new set of bosonic operators $\hat{a}_{ij}$ is defined as

$$\hat{a}_{ij}(\omega) = \frac{-e}{m\omega g_{ij}^{l-m}(\omega)}\iint d\boldsymbol{r}\, d\boldsymbol{r}'\, \boldsymbol{d}_{ij}(\boldsymbol{r})\cdot\mathbf{G}^{(\mathrm{R})}(\boldsymbol{r},\boldsymbol{r}',\omega)\cdot\hat{\boldsymbol{f}}(\boldsymbol{r}',\omega), \tag{E.8}$$

and satisfy the canonical conmutation relation of bosonic operators by construction: $[\hat{a}_{ij}(\omega), \hat{a}_{ij}^{\dagger}(\omega)] = 1$, which leads to the following expression for the couplings

$$g_{ij}^{l-m}(\omega) = \frac{e}{m}\sqrt{\frac{\hbar\mu_0}{\pi}}\sqrt{\iint dr\, dr'\, \boldsymbol{d}_{ij}(r)\cdot\mathrm{Im}\Big\{\mathbf{G}^{(\mathrm{R})}(r,r',\omega)\Big\}\cdot\boldsymbol{d}_{ij}^{*}(r')}. \tag{E.9}$$

We remark that until this point, no knowledge about the particular electronic transitions under study have been assumed, and therefore this treatment can be applied to a wide variety of systems beyond the present one. In Section E.3, we find that the current densities, $\vec{d_{ij}}(r)$, associated to transitions in dipolar QE and free electrons propagating along the $\hat{z}$ axis, which are the central part of our studies in this thesis, are given

by:

$$\boldsymbol{d}_{ij}^{QE}(\boldsymbol{r}) = -\frac{m\omega_{ij}}{e\hbar}\boldsymbol{\mu}_{ij}\delta^3(\boldsymbol{r}-\boldsymbol{r}_0), \tag{E.10}$$

$$\boldsymbol{d}_{ij}^{e}(\boldsymbol{r}) = ik_0\frac{\delta^2(\boldsymbol{r}-\boldsymbol{r}_\perp)}{L}e^{i(k_j-k_i)z}\hat{z}, \tag{E.11}$$

where $\boldsymbol{\mu}_{ij} = -e\langle j|\hat{r}|i\rangle$ is the usual transition dipole moment, $k_0 = mv_0/\hbar$ is the initial momentum of the incoming electron and L is the length of a fictitious box used to quantise the momentum values of the electron. We have also introduced $\boldsymbol{r}_0$ as the location of the dipolar QE and $\boldsymbol{r}_{\perp,0}$ for the location of the free electron on the $x-y$ plane. To obtain the light-matter interaction coupling strengths, we derive the Dyadic Green's Function for a metallic sphere in Section E.4, and noting that it can be written as $\mathbf{G}^{(\mathrm{R})}(\boldsymbol{r},\boldsymbol{r}',\omega) \approx \boldsymbol{\mathcal{G}}(\boldsymbol{r},\boldsymbol{r}',\omega_C)\delta(\omega-\omega_C)$, where ω_C is the resonance frequency of the cavity, the coupling strength and interaction Hamiltonian for dipolar QE interacting with a single cavity mode are given by:

$$\hat{H}_I^{c-QE} = \hbar g^{c-QE}\left[\hat{\sigma}\hat{a}^\dagger + \hat{\sigma}^\dagger\hat{a}\right], \tag{E.12}$$

$$g^{c-QE} = \frac{\omega_{QE}}{\hbar}\sqrt{\frac{\hbar\mu_0}{\pi}\boldsymbol{\mu}\cdot\mathrm{Im}\left\{\boldsymbol{\mathcal{G}}(\boldsymbol{r}_0,\boldsymbol{r}_0,\omega_c)\right\}\cdot\boldsymbol{\mu}^*}. \tag{E.13}$$

The spherical nanoparticle supports three degenerate dipolar modes that can be considered to be oriented along the $\hat{x}$, $\hat{y}$ and $\hat{z}$ axis respectively. The coupling between a QE, placed along the $\hat{x}$ axis to each of these degenerate modes is given in Equation (E.68). In the case we are considering, with the dipole moment of the QE's transition oriented along the $\hat{x}$ axis, then only the coupling to the $\hat{x}$-mode of the cavity is non-zero and is given by:

$$g_x^{c-QE} = \frac{\omega_{QE}}{3}\sqrt{\frac{\pi}{2}\left(\frac{R}{b_{c-QE}}\right)^3\frac{1}{\hbar\omega_c}\frac{\mu_{QE}^2}{\epsilon_0\, b_{c-QE}^3}}.$$

E

On the other hand, the Hamiltonian describing the coupling between free electrons and the cavity is given by

$$\hat{H}_I^{e-c} = \hbar \sum_q g_q^{e-c} \hat{b}_q \left(\hat{a}^\dagger - \hat{a}\right) \mathrm{sign}(q), \tag{E.14}$$

$$g_q^{e-c} = \frac{ek_0}{mL}\sqrt{\frac{\hbar\mu_0}{\pi}\iint \mathrm{d}z\,\mathrm{d}z', \mathrm{Im}\left\{\hat{z}\cdot\boldsymbol{\mathcal{G}}(\boldsymbol{r},\boldsymbol{r}',\omega_c)\cdot\hat{z}\right\}e^{iq(z-z')}}, \tag{E.15}$$

where for compactess we have defined $\boldsymbol{r} = [\boldsymbol{r}_{\perp,0}, z]$ and $\boldsymbol{r}' = [\boldsymbol{r}_{\perp,0}, z']$. Introducing the GF of the cavity we find that the free-electron-cavity couplings can be written as

$$g_{q,x}^{e-c} = \frac{e\hbar k_0}{3mL}\left|q\right|^2 K_1(|qb_{e-c}|)\sqrt{\frac{1}{\epsilon_0\hbar\omega_c}\frac{\pi R^3}{2}}, \tag{E.16}$$

$$g_{q,y}^{e-c} = 0, \tag{E.17}$$

$$g_{q,z}^{e-c} = \frac{e\hbar k_0}{3mL}\left|q\right|^2 K_0(|qb_{e-c}|)\sqrt{\frac{1}{\epsilon_0\hbar\omega_c}\frac{\pi R^3}{2}}, \tag{E.18}$$

which shows that the $\hat{y}$ dipolar mode of the cavity is decoupled from the electron and QE and therefore remains outside of the dynamics, while the $\hat{x}$ mode couples to free-electron and QE and the $\hat{z}$ mode couples only to the free electron.

Finally, the interaction between the free electron and dipolar transition inside the QE can be described through the matter-matter interaction term in the mQED Hamiltonian. Upon introducing the particular definition of the current densities associated to both transitions, the interaction Hamiltonian and coupling strength are given by:

$$\hat{H}_I^{e-QE} = -\hbar \sum_q g_q^{e-QE}\left[\hat{\sigma} - \hat{\sigma}^\dagger\right]\hat{b}_q, \tag{E.19}$$

$$g_q^{e-QE} = ik_0\frac{e\mu_0\omega_{QE}}{mL}\int \mathrm{d}z'\ \boldsymbol{\mu}\cdot\mathrm{Re}\left\{\mathbf{G}^{(\mathrm{NR})}\left(\boldsymbol{r}_0,\boldsymbol{r}',|\omega_{QE}|\right)\right\}\cdot\hat{z}e^{iqz'}. \tag{E.20}$$

As the non-resonant EM background, we assume that the QE-free electron interaction will be mediated by the free-space GF. Upon integration, the coupling for an arbitrary dipole orientation is given by Equation

(E.64). Particularizing for a QE oriented along the $\hat{x}$ direction yields a coupling strength:

$$g_q^{e-QE} = -\frac{e\,k_0\,|q|^2}{2\pi m L \epsilon_0 \omega_{QE}} \mu_{QE} \text{sign}(q b_{e-QE}) K_1(|q b_{e-QE}|) \tag{E.21}$$

Putting all these interaction terms together, and introducing the energies for the bare optical modes $\hbar\omega_c \hat{a}_x^\dagger \hat{a}_x$, $\hbar\omega_c \hat{a}_z^\dagger \hat{a}_z$, electronic eigenstates $\sum_i E_i \hat{c}_i^\dagger \hat{c}_i$ and bare QE energies $\hbar\omega_{QE}\hat{\sigma}^\dagger\hat{\sigma}$ we have the complete Hamiltonian from the main text.

To end this section, we remark that the interaction between a free electron and optical cavity and QE have been studied before (mostly as separate processes, but recently also in conjunction [318]), and their coupling parametrized. However, in this work we have managed to unify their description in terms of the common starting framework of mQED. This ensures proper normalization of optical modes in arbitrary EM environments, and therefore, physically meaningful coupling stregths, even in situations in which the EM environment only serves as a non-resonant background. This work paves the way for exploring quantum phenomena in field mediated interactions between arbitrary electronic transitions, and in general light matter interaction phenomena beyond the dipolar approximation of quantum emitters.

E

E.2 General light matter interaction Hamiltonian for arbitrary electronic transitions

E.2.1 Matter-matter interaction through light

From a minimal coupling scheme within a mQED formalism, one is able to describe the coupling between electronic transitions and field photons. This in particular means that the field-mediated interactions between electronic transitions become a second order process. In what follows, we derive an effective Hamiltonian, in which the field mediated interaction between different electronic transitions is treated as a first order term. For that, we split the EM response of a given system into a part

that behaves resonantly with the matter transitions, $\mathbf{G}^{(\mathrm{R})}$, and other that acts as a non-resonant background to which the matter transitions weakly coupled, $\mathbf{G}^{(\mathrm{NR})}$. Therefore one has that $\mathbf{G} = \mathbf{G}^{(\mathrm{R})} + \mathbf{G}^{(\mathrm{NR})}$. To perform this separation, we follow the same strategy as Ref. [39], but generalise the formalism for an arbitrarily big set of electronic states. Most of the algebra done here mirrors that of said reference, and we refer the reader there for additional indications on how to perform the derivation. We start from the Hamiltonian in a minimal coupling scheme [28], by adapting the Coulomb gauge and neglecting the ponderomotive interaction term of the field, the minimal coupling Hamiltonian can be written as:

$$\hat{H} = \iint \mathrm{d}\boldsymbol{r}\ \mathrm{d}\omega\ \hbar\omega \hat{\boldsymbol{f}}^{\dagger}(\boldsymbol{r},\omega)\hat{\boldsymbol{f}}(\boldsymbol{r},\omega) \quad + \quad \frac{\hat{\mathbf{p}}^2}{2m} + V(\boldsymbol{r}) \quad + \quad \frac{e}{m}\hat{\mathbf{p}}\cdot\hat{\boldsymbol{A}} \tag{E.22}$$

where we see the terms corresponding respectively to the field Hamiltonian ($\hat{H}_F$), a term for the electronic eigenstates ($\hat{H}_e$), and the coupling term ($\hat{H}_{e,F}$). We have introduced the $\hat{f}$ operators, as defined in [28], which act as elemental field excitations, and follow bosonic conmutation relations:

$$[\hat{\boldsymbol{f}}(\boldsymbol{r},\omega),[\hat{\boldsymbol{f}}(\boldsymbol{r}',\omega')] = [\hat{\boldsymbol{f}}^{\dagger}(\boldsymbol{r},\omega),[\hat{\boldsymbol{f}}^{\dagger}(\boldsymbol{r}',\omega')] = \mathbf{0}, \tag{E.23}$$

$$[\hat{\boldsymbol{f}}(\boldsymbol{r},\omega),[\hat{\boldsymbol{f}}^{\dagger}(\boldsymbol{r}',\omega')] = \delta(\boldsymbol{r}-\boldsymbol{r}')\delta(\omega-\omega'). \tag{E.24}$$

Through the electronic Hamiltonian, we obtain the electronic wavefunctions that fulfill $\hat{H}_e\phi_i = E_i\phi_i$, and use these as a basis for the electronic states. As such we can write the electronic term as

$$\hat{H}_e = \sum_i \hat{c}_i^{\dagger}\hat{c}_i E_i, \tag{E.25}$$

where $\hat{c}_i$ is the annihilation operator of the state ϕ_i. In the same way, we may introduce these wavefunctions to describe the momentum of the electrons as

$$\hat{\mathbf{p}}(\boldsymbol{r}) = -i\hbar\sum_{i,j}\hat{c}_i^{\dagger}\hat{c}_j\phi_i^{*}(\boldsymbol{r})\nabla\phi_j(\boldsymbol{r}), \tag{E.26}$$

which motivates defining a dipole moment density $\boldsymbol{d}_{ij}(\boldsymbol{r}) \equiv \phi_i^*(\boldsymbol{r})\nabla\phi_j(\boldsymbol{r})$, and an operator describing the electronic jump between eigenstates $\phi_j \to \phi_i$ as $\hat{\sigma}_{ij} = \hat{c}_i^\dagger \hat{c}_j$. Therefore, the light-matter interaction term may be written as

$$\begin{aligned}\hat{\mathbf{p}}\cdot\hat{\boldsymbol{A}} &= -i\hbar \sum_{i,j} \hat{\sigma}_{ij} \int \mathrm{d}\boldsymbol{r}\ \boldsymbol{d}_{ij}(\boldsymbol{r}) \cdot \hat{\boldsymbol{A}}(\boldsymbol{r}) = \\ &= \frac{-i\hbar}{2} \sum_{i,j} \left[\hat{\sigma}_{ij} \left(\int \mathrm{d}\boldsymbol{r}\ \boldsymbol{d}_{ij}(\boldsymbol{r}) \cdot \hat{\boldsymbol{A}}(\boldsymbol{r}) \right) - \left(\int \mathrm{d}\boldsymbol{r}\ \hat{\boldsymbol{A}}(\boldsymbol{r}) \cdot \boldsymbol{d}_{ij}^*(\boldsymbol{r}) \right) \hat{\sigma}_{ij}^\dagger \right]\end{aligned} \tag{E.27}$$

where we have expressed the interaction term in a manifestly hermitian way. Note that the main difference between this work and reference [39] is that we are allowing for arbitrary electronic transitions mediated by photons to take place, which leads to the natural apparition of these extended transition dipole densities $\boldsymbol{d}_{ij}(\boldsymbol{r})$. This adds complexity in the expressions, but the spirit of the derivation remains unchanged. We now turn to express the vector potential as a function of the $\hat{\boldsymbol{f}}$ operators as:

$$\hat{\boldsymbol{A}}(\boldsymbol{r}) = -i \int \frac{\mathrm{d}\omega}{\omega} \int \mathrm{d}\boldsymbol{r}' \left[\mathbf{G}(\boldsymbol{r}, \boldsymbol{r}', \omega) \cdot \hat{\boldsymbol{f}}(\boldsymbol{r}', \omega) - \hat{\boldsymbol{f}}^\dagger(\boldsymbol{r}', \omega) \cdot \mathbf{G}^\dagger(\boldsymbol{r}, \boldsymbol{r}', \omega) \right] \tag{E.28}$$

Plugging this into the previous equation and making the aforementioned substitutions leads to

$$\begin{aligned}\hat{\mathbf{p}} \cdot \hat{\boldsymbol{A}} = \frac{-\hbar}{2} \sum_{i,j} \iiint \mathrm{d}\boldsymbol{r}\, \mathrm{d}\boldsymbol{r}' \frac{\mathrm{d}\omega}{\omega} \Big[&\hat{\sigma}_{ij}\, \boldsymbol{d}_{ij}(\boldsymbol{r}) \cdot \mathbf{G}(\boldsymbol{r}, \boldsymbol{r}', \omega) \cdot \hat{\boldsymbol{f}}(\boldsymbol{r}', \omega) + \\ &- \hat{\sigma}_{ij}\, \hat{\boldsymbol{f}}^\dagger(\boldsymbol{r}', \omega) \cdot \mathbf{G}^\dagger(\boldsymbol{r}, \boldsymbol{r}', \omega) \cdot \boldsymbol{d}_{ij}(\boldsymbol{r}) \\ &- \boldsymbol{d}_{ij}^*(\boldsymbol{r}) \cdot \mathbf{G}(\boldsymbol{r}, \boldsymbol{r}', \omega) \cdot \hat{\boldsymbol{f}}(\boldsymbol{r}', \omega)\, \hat{\sigma}_{ij}^\dagger \\ &+ \hat{\boldsymbol{f}}^\dagger(\boldsymbol{r}', \omega) \cdot \mathbf{G}^\dagger(\boldsymbol{r}, \boldsymbol{r}', \omega) \cdot \boldsymbol{d}_{ij}^*(\boldsymbol{r})\, \hat{\sigma}_{ij}^\dagger \Big]\end{aligned} \tag{E.29}$$

In order to obtain direct interaction terms between the different electronic transitions, it is necessary to obtain the dynamics of the $\hat{f}$ operators in terms of the electronic transition operators. The time evolution

of any operator in the Heisenberg picture is given by $\dot{\hat{O}}(t) = -\frac{i}{\hbar}[\hat{O}(t), \hat{H}]$. In particular, it is useful to split the complete Hamiltonian into the field + electronic system Hamiltonian, $\hat{H}_s$, and the interaction Hamiltonian $\hat{H}_I = e\,\hat{\mathbf{p}} \cdot \hat{\boldsymbol{A}}/m$. This way the evolution of $\hat{O}$ is given by:

$$\begin{aligned}\dot{\hat{O}}(t) = -\frac{i}{\hbar}[\hat{O}(t), \hat{H}_s] + i\frac{e}{2m}\sum_{i,j}\iiint \mathrm{d}\boldsymbol{r}\,\mathrm{d}\boldsymbol{r}'\,\frac{\mathrm{d}\omega}{\omega}\times \\ \Bigg[[\hat{O}, \hat{\sigma}_{ij}]\Big(\boldsymbol{d}_{ij}(\boldsymbol{r})\cdot\mathbf{G}(\boldsymbol{r},\boldsymbol{r}',\omega)\cdot\hat{\boldsymbol{f}}(\boldsymbol{r}',\omega) \\ - \hat{\boldsymbol{f}}^\dagger(\boldsymbol{r}'.\omega)\cdot\mathbf{G}^\dagger(\boldsymbol{r},\boldsymbol{r}',\omega)\cdot\boldsymbol{d}_{ij}(\boldsymbol{r})\Big) \\ - \Big(\boldsymbol{d}^*_{ij}(\boldsymbol{r})\cdot\mathbf{G}(\boldsymbol{r},\boldsymbol{r}',\omega)\cdot\hat{\boldsymbol{f}}(\boldsymbol{r}',\omega) \\ - \hat{\boldsymbol{f}}^\dagger(\boldsymbol{r}'.\omega)\cdot\mathbf{G}^\dagger(\boldsymbol{r},\boldsymbol{r}',\omega)\cdot\boldsymbol{d}^*_{ij}(\boldsymbol{r})\Big)[\hat{O}, \hat{\sigma}^\dagger_{ij}]\Bigg]\end{aligned} \tag{E.30}$$

In particular, the time evolution of the fundamental field operators $\hat{\boldsymbol{f}}$ reads:

$$\begin{aligned}\dot{\hat{\boldsymbol{f}}}(\boldsymbol{r}',\omega',t) =& -i\omega'\hat{\boldsymbol{f}}(\boldsymbol{r}',\omega',t) \\ &+\frac{ie}{2m\omega'}\sum_{i,j}\int \mathrm{d}\boldsymbol{r}\left[\mathbf{G}^\dagger(\boldsymbol{r},\boldsymbol{r}',\omega')\cdot\boldsymbol{d}^*_{ij}(\boldsymbol{r})\,\hat{\sigma}^\dagger_{ij} - \hat{\sigma}_{ij}\,\mathbf{G}^\dagger(\boldsymbol{r},\boldsymbol{r}',\omega')\cdot\boldsymbol{d}_{ij}(\boldsymbol{r})\right]\end{aligned}$$

Where we have used that $\left[\hat{\boldsymbol{f}}(\boldsymbol{r}',\omega',t), \hat{\boldsymbol{f}}^\dagger(\boldsymbol{r},\omega,t)\right] = \delta(\omega-\omega')\delta(\boldsymbol{r}-\boldsymbol{r}')$ and Equation (E.29). Solving this equation formally we find

$$\begin{aligned}\hat{\boldsymbol{f}}(\boldsymbol{r}',\omega,t) = \hat{\boldsymbol{f}}^{\mathrm{free}}(\boldsymbol{r}',\omega,t) - i\frac{e}{2m\omega}\sum_{k,l}\times \\ \Bigg\{\iint_0^t \mathrm{d}t'\,\mathrm{d}\boldsymbol{r}''\Big[\hat{\sigma}_{kl}(t')\mathbf{G}^\dagger(\boldsymbol{r}'',\boldsymbol{r}',\omega)\cdot\boldsymbol{d}_{kl}(\boldsymbol{r}'') \\ - \mathbf{G}^\dagger(\boldsymbol{r}'',\boldsymbol{r}',\omega)\cdot\boldsymbol{d}^*_{kl}(\boldsymbol{r}'')\,\hat{\sigma}^\dagger_{kl}(t')\Big]e^{-i\omega(t-t')}\Bigg\}\end{aligned}$$

E

plugging this back into Equation (E.30), expanding the product and making use of the identity $\int \mathrm{d}\mathbf{s}\, \mathbf{G}(\boldsymbol{r},\mathbf{s},\omega)\cdot\mathbf{G}^\dagger(\boldsymbol{r}'',\mathbf{s},\omega) = \frac{\hbar\mu_0}{\pi}\omega^2 \mathrm{Im}(\mathbf{G}(\boldsymbol{r},\boldsymbol{r}'',\omega))$ [28], the equation of motion for $\hat{O}$ reads

$$\begin{aligned}\dot{\hat{O}}(t) = -\frac{i}{\hbar}[\hat{O}(t),\hat{H}_s] + i\frac{e^2}{4m^2}\frac{\hbar\mu_0}{\pi}\sum_{\substack{i,j\\k,l}}\int_0^t \mathrm{d}t' \iiint \mathrm{d}\boldsymbol{r}\,\mathrm{d}\boldsymbol{r}''\,\mathrm{d}\omega \times \\ \Big[-i[\hat{O},\hat{\sigma}_{ij}]\hat{\sigma}_{kl}(t')\boldsymbol{d}_{ij}(\boldsymbol{r})\cdot \mathrm{Im}\left\{\mathbf{G}(\boldsymbol{r},\boldsymbol{r}'',\omega)\right\}\cdot \boldsymbol{d}_{kl}(\boldsymbol{r}'')e^{-i\omega(t-t')} \\ + i[\hat{O},\hat{\sigma}_{ij}]\hat{\sigma}^\dagger_{kl}(t')\boldsymbol{d}_{ij}(\boldsymbol{r})\cdot \mathrm{Im}\left\{\mathbf{G}(\boldsymbol{r},\boldsymbol{r}'',\omega)\right\}\cdot \boldsymbol{d}^*_{kl}(\boldsymbol{r}'')\, e^{-i\omega(t-t')} \\ - i[\hat{O},\hat{\sigma}_{ij}]\hat{\sigma}^\dagger_{kl}(t')\,\boldsymbol{d}^*_{kl}(\boldsymbol{r}'')\cdot \mathrm{Im}\left\{\mathbf{G}(\boldsymbol{r}'',\boldsymbol{r},\omega)\right\}\cdot \boldsymbol{d}_{ij}(\boldsymbol{r})e^{i\omega(t-t')} \\ + i[\hat{O},\hat{\sigma}_{ij}]\hat{\sigma}_{kl}(t')\boldsymbol{d}_{kl}(\boldsymbol{r}'')\cdot \mathrm{Im}\left\{\mathbf{G}(\boldsymbol{r}'',\boldsymbol{r},\omega)\right\}\cdot \boldsymbol{d}_{ij}(\boldsymbol{r})e^{i\omega(t-t')} \\ + i\boldsymbol{d}^*_{ij}(\boldsymbol{r})\cdot \mathrm{Im}\left\{\mathbf{G}(\boldsymbol{r},\boldsymbol{r}'',\omega)\right\}\cdot \boldsymbol{d}_{kl}(\boldsymbol{r}'')\hat{\sigma}_{kl}(t')[\hat{O},\hat{\sigma}^\dagger_{ij}]e^{-i\omega(t-t')} \\ - i\boldsymbol{d}^*_{ij}(\boldsymbol{r})\cdot \mathrm{Im}\left\{\mathbf{G}(\boldsymbol{r},\boldsymbol{r}'',\omega)\right\}\cdot \boldsymbol{d}^*_{kl}(\boldsymbol{r}'')\,\hat{\sigma}^\dagger_{kl}(t')[\hat{O},\hat{\sigma}^\dagger_{ij}]e^{-i\omega(t-t')} \\ + i\boldsymbol{d}^*_{kl}(\boldsymbol{r}'')\cdot \mathrm{Im}\left\{\mathbf{G}(\boldsymbol{r}'',\boldsymbol{r},\omega)\right\}\cdot \boldsymbol{d}^*_{ij}(\boldsymbol{r})\hat{\sigma}^\dagger_{kl}(t')[\hat{O},\hat{\sigma}^\dagger_{ij}]e^{i\omega(t-t')} \\ - i\boldsymbol{d}_{kl}(\boldsymbol{r}'')\mathrm{Im}\left\{\mathbf{G}(\boldsymbol{r}'',\boldsymbol{r},\omega)\right\}\cdot \boldsymbol{d}^*_{ij}(\boldsymbol{r})\,\hat{\sigma}_{kl}(t')[\hat{O},\hat{\sigma}^\dagger_{ij}]e^{i\omega(t-t')}\Big]\end{aligned}$$

Now we introduce a coarse-graining Markov approximation, by expressing the time dependency of the ladder operators by the natural frequency of the shifted eigenenergies[1]: $\hat{\sigma}_{ij}(t') \approx \tilde{\hat{\sigma}}_{ij}(t)e^{-i\omega_{ij}t'}$. This in turn means that $\tilde{\hat{\sigma}}_{ij}(t) = \hat{\sigma}_{ij}(t)e^{i\omega_{ij}t}$, and therefore $\hat{\sigma}_{ij}(t') \approx \hat{\sigma}_{ij}(t)e^{i\omega_{ij}(t-t')}$. Then we make the substitution $\int \mathrm{d}t'\, e^{i\Omega(t-t')} \to \xi(\Omega)$, where $\xi(x) = \pi\delta(x) + i\mathcal{P}\,(1/x)$ by virtue of the Sokhotski-Plemejl theorem, where $\mathcal{P}$ denotes the principal value. These two terms of the integral represent the resonant (the δ function) and the non resonant (the principal value) part of the interaction. As indicated above, we assume that the field-mediated interaction between the two electronic transitions is happening through the non-resonant electromagnetic environment, and therefore only consider the principal value contribution. In this situation $\xi(-x) = \xi^*(x)$,

[1] Solving a Heisemberg equation for the time evolution of these ladder operators one can see that $\omega_{ij} = \omega_j - \omega_i$. Thus depending on the initial and final states of the transition these frequencies may positive or negative.

E

and the time evolution of $\hat{O}$ reads:

$$\dot{\hat{O}}(t) = -\frac{i}{\hbar}[\hat{O}(t), \hat{H}_s] + i\frac{e^2}{4m^2}\frac{\hbar\mu_0}{\pi}\sum_{\substack{i,j\\k,l}}\iiint d\boldsymbol{r}\, d\boldsymbol{r}''\, \mathrm{d}\omega \times$$

$$\Bigg[- i[\hat{O}, \sigma_{ij}]\sigma_{kl}\boldsymbol{d}_{ij}(\boldsymbol{r}) \cdot \mathrm{Im}\left\{\mathbf{G}(\boldsymbol{r}, \boldsymbol{r}'', \omega)\right\} \cdot \boldsymbol{d}_{kl}(\boldsymbol{r}'')\xi(-(\omega - \omega_{kl}))$$

$$+ i[\hat{O}, \sigma_{ij}]\sigma^{\dagger}_{kl}\boldsymbol{d}_{ij}(\boldsymbol{r}) \cdot \mathrm{Im}\left\{\mathbf{G}(\boldsymbol{r}, \boldsymbol{r}'', \omega)\right\} \cdot \boldsymbol{d}^{*}_{kl}(\boldsymbol{r}'')\, \xi(-(\omega + \omega_{kl}))$$

$$- i[\hat{O}, \sigma_{ij}]\hat{\sigma}^{\dagger}_{kl}\, \boldsymbol{d}^{*}_{kl}(\boldsymbol{r}'') \cdot \mathrm{Im}\left\{\mathbf{G}(\boldsymbol{r}'', \boldsymbol{r}, \omega)\right\} \cdot \boldsymbol{d}_{ij}(\boldsymbol{r})\xi(\omega - \omega_{kl})$$

$$+ i[\hat{O}, \sigma_{ij}]\sigma_{kl}\boldsymbol{d}_{kl}(\boldsymbol{r}'') \cdot \mathrm{Im}\left\{\mathbf{G}(\boldsymbol{r}'', \boldsymbol{r}, \omega)\right\} \cdot \boldsymbol{d}_{ij}(\boldsymbol{r})\xi(\omega + \omega_{kl})$$

$$+ i\boldsymbol{d}^{*}_{ij}(\boldsymbol{r}) \cdot \mathrm{Im}\left\{\mathbf{G}(\boldsymbol{r}, \boldsymbol{r}'', \omega)\right\} \cdot \boldsymbol{d}_{kl}(\boldsymbol{r}'')\sigma_{kl}[\hat{O}, \hat{\sigma}^{\dagger}_{ij}]\xi(-(\omega - \omega_{kl}))$$

$$- i\boldsymbol{d}^{*}_{ij}(\boldsymbol{r}) \cdot \mathrm{Im}\left\{\mathbf{G}(\boldsymbol{r}, \boldsymbol{r}'', \omega)\right\} \cdot \boldsymbol{d}^{*}_{kl}(\boldsymbol{r}'')\, \sigma^{\dagger}_{kl}[\hat{O}, \hat{\sigma}^{\dagger}_{ij}]\xi(-(\omega + \omega_{kl}))$$

$$+ i\boldsymbol{d}^{*}_{kl}(\boldsymbol{r}'') \cdot \mathrm{Im}\left\{\mathbf{G}(\boldsymbol{r}'', \boldsymbol{r}, \omega)\right\} \cdot \boldsymbol{d}^{*}_{ij}(\boldsymbol{r})\hat{\sigma}^{\dagger}_{kl}[\hat{O}, \hat{\sigma}^{\dagger}_{ij}]\xi(\omega - \omega_{kl})$$

$$- i\boldsymbol{d}_{kl}(\boldsymbol{r}'')\mathrm{Im}\left\{\mathbf{G}(\mathrm{r}'', \mathrm{r}, \omega)\right\} \cdot \mathrm{d}^{*}_{\mathrm{ij}}(\mathrm{r})\, \sigma_{\mathrm{kl}}[\hat{\mathrm{O}}, \hat{\sigma}^{\dagger}_{\mathrm{ij}}]\xi(\omega + \omega_{\mathrm{kl}})\Bigg]$$

In analogy with the classical definition of a probability current, we can define $\boldsymbol{J}_{ij}(\boldsymbol{r}) \equiv i[\boldsymbol{d}_{ij}(\boldsymbol{r}) - \boldsymbol{d}^{*}_{ji}(\boldsymbol{r})]$, and $\boldsymbol{\Delta}_{ij}(\boldsymbol{r}) \equiv i[\boldsymbol{d}_{ij}(\boldsymbol{r}) + \boldsymbol{d}^{*}_{ji}(\boldsymbol{r})]$, where $\boldsymbol{J}_{ij}(\boldsymbol{r}) = \boldsymbol{J}^{*}_{ji}(\boldsymbol{r})$ and $\boldsymbol{\Delta}_{ij}(\boldsymbol{r}) = -\boldsymbol{\Delta}^{*}_{ji}(\boldsymbol{r})$. Using $\hat{\sigma}_{kl} = \hat{\sigma}^{\dagger}_{lk}$, and $\omega_{lk} = -\omega_{kl}$, allows to rewrite the previous Heisenberg equation in a more compact form

$$\dot{\hat{O}}(t) = -\frac{i}{\hbar}[\hat{O}(t), \hat{H}_s] + \frac{i}{\hbar}\frac{e^2}{4m^2}\frac{\hbar^2\mu_0}{\pi}\pi\sum_{\substack{i,j\\k,l}}\iint d\boldsymbol{r}\, d\boldsymbol{r}'' \times$$

$$\Bigg[[\hat{O}, \hat{\sigma}_{ij}]\hat{\sigma}_{kl}(i)\boldsymbol{d}_{ij}(\boldsymbol{r}) \cdot \mathrm{Re}\left\{\mathbf{G}(\boldsymbol{r}, \boldsymbol{r}'', \omega_{kl})\right\} \cdot \boldsymbol{J}_{kl}(\boldsymbol{r}'')$$

$$(-i)\boldsymbol{d}^{*}_{ji}(\boldsymbol{r}) \cdot \mathrm{Re}\left\{\mathbf{G}(\boldsymbol{r}, \boldsymbol{r}'', \omega_{kl})\right\} \cdot \boldsymbol{J}_{kl}(\boldsymbol{r}'')\hat{\sigma}_{kl}[\hat{O}, \hat{\sigma}_{ij}]\Bigg].$$

Where the integrals involving the imaginary part of the system's Dyadic Green's Function have been evaluated by the use of Kramers-Krönig relations as follows:

$$\mathcal{P}\int_0^{\infty} \mathrm{d}\omega\, \frac{\mathrm{Im}\left\{\mathbf{G}(\mathbf{s}, \mathbf{t}, \omega)\right\}}{\omega \pm \omega_0} =$$

E

$$= \mathcal{P}\int_{-\infty}^{\infty} \mathrm{d}\omega\ \frac{\mathrm{Im}\left\{\mathbf{G}(\mathbf{s},\mathbf{t},\omega)\right\}}{\omega \pm \omega_0} - \mathcal{P}\int_{-\infty}^{0} \mathrm{d}\omega\ \frac{\mathrm{Im}\left\{\mathbf{G}(\mathbf{s},\mathbf{t},\omega)\right\}}{\omega \pm \omega_0} =$$
$$= \pi \mathrm{Re}\left\{\mathbf{G}(\mathbf{s},\mathbf{t},\mp\omega_0)\right\} - \mathcal{P}\int_{0}^{\infty} \mathrm{d}\omega\ \frac{\mathrm{Im}\left\{\mathbf{G}(\mathbf{s},\mathbf{t},\omega)\right\}}{\omega \mp \omega_0}.$$

To arrive at the final result, we use the property of the Green's Function $\mathbf{G}^*(\mathbf{s},\mathbf{t},\omega) = \mathbf{G}(\mathbf{s},\mathbf{t},-\omega^*)$. We now define several quantities:

$$f_{ij,kl} \equiv \frac{1}{2}\iint \mathrm{d}\boldsymbol{r}\,\mathrm{d}\boldsymbol{r}''\,\boldsymbol{J}_{ij}(\boldsymbol{r}) \cdot \mathrm{Re}\left\{\mathbf{G}(\boldsymbol{r},\boldsymbol{r}'',\omega_{kl})\right\} \cdot \boldsymbol{J}_{kl}(\boldsymbol{r}''),$$
$$h_{ij,kl} \equiv \frac{1}{2}\iint \mathrm{d}\boldsymbol{r}\,\mathrm{d}\boldsymbol{r}''\,\boldsymbol{\Delta}_{ij}(\boldsymbol{r}) \cdot \mathrm{Re}\left\{\mathbf{G}(\boldsymbol{r},\boldsymbol{r}'',\omega_{kl})\right\} \cdot \boldsymbol{J}_{kl}(\boldsymbol{r}''),$$
$$\overline{f}_{ij,kl} = \frac{f_{ij,kl} + f_{kl,ij}}{2},$$
$$\delta f_{ij,kl} = \frac{f_{ij,kl} - f_{kl,ij}}{2},$$
$$\overline{h}_{ij,kl} = \frac{h_{ij,kl} + h_{kl,ij}}{2},$$
$$\delta h_{ij,kl} = \frac{h_{ij,kl} - h_{kl,ij}}{2}.$$

If we assume that the two electronic transitions interacting fulfil $\omega_{kl} \approx \omega_{ij}$, then these read

$$\overline{f}_{ij,kl} \approx \frac{1}{2}\iint \mathrm{d}\boldsymbol{r}\,\mathrm{d}\boldsymbol{r}''\,\boldsymbol{J}_{ij}(\boldsymbol{r}) \cdot \mathrm{Re}\left\{\mathbf{G}(\boldsymbol{r},\boldsymbol{r}'',\omega_{kl})\right\} \cdot \boldsymbol{J}_{kl}(\boldsymbol{r}''),$$
$$\delta f_{ij,kl} \approx 0,$$
$$\overline{h}_{ij,kl} = \frac{1}{2}\iint \mathrm{d}\boldsymbol{r}\,\mathrm{d}\boldsymbol{r}''\,\boldsymbol{d}^*_{ji}(\boldsymbol{r}) \cdot \mathrm{Re}\left\{\mathbf{G}(\boldsymbol{r},\boldsymbol{r}'',\omega_{kl})\right\} \cdot \boldsymbol{d}^*_{lk}(\boldsymbol{r}'')$$
$$- \frac{1}{2}\iint \mathrm{d}\boldsymbol{r}\,\mathrm{d}\boldsymbol{r}''\,\boldsymbol{d}_{ij}(\boldsymbol{r}) \cdot \mathrm{Re}\left\{\mathbf{G}(\boldsymbol{r},\boldsymbol{r}'',\omega_{kl})\right\} \cdot \boldsymbol{d}_{kl}(\boldsymbol{r}''),$$
$$\delta h_{ij,kl} = \frac{1}{2}\iint \mathrm{d}\boldsymbol{r}\,\mathrm{d}\boldsymbol{r}''\,\boldsymbol{d}_{ij}(\boldsymbol{r}) \cdot \mathrm{Re}\left\{\mathbf{G}(\boldsymbol{r},\boldsymbol{r}'',\omega_{kl})\right\} \cdot \boldsymbol{d}^*_{lk}(\boldsymbol{r}'')$$
$$- \frac{1}{2}\iint \mathrm{d}\boldsymbol{r}\,\mathrm{d}\boldsymbol{r}''\,\boldsymbol{d}^*_{ji}(\boldsymbol{r}) \cdot \mathrm{Re}\left\{\mathbf{G}(\boldsymbol{r},\boldsymbol{r}'',\omega_{kl})\right\} \cdot \boldsymbol{d}_{kl}(\boldsymbol{r}'').$$

Using these expressions, one can rewrite the Heisenberg equation as

$$\dot{\hat{O}}(t) = -\frac{i}{\hbar}[\hat{O}(t), \hat{H}_s] +$$

$$+\frac{i}{\hbar}\frac{e^2\hbar^2\mu_0}{4m^2}\sum_{\substack{i,j\\k,l}}[\hat{O},\hat{\sigma}_{ij}\hat{\sigma}_{kl}]\left(\overline{f}_{ij,kl}+\delta h_{ij,kl}\right)$$
$$+\frac{i}{\hbar}\frac{e^2\hbar^2\mu_0}{4m^2}\sum_{\substack{i,j\\k,l}}\left(\left\{\hat{O},\hat{\sigma}_{ij}\hat{\sigma}_{kl}\right\}-2\hat{\sigma}_{ij}\hat{O}\hat{\sigma}_{kl}\right)\overline{h}_{ij,kl}. \tag{E.31}$$

In this equation we recognize two terms of different natures: the first one is hermitian, and captures a coherent coupling between the two electronic transitions mediated by the EM fields. The second term has a Lindblad-like form, and describes the dissipative coupling between these two transitions. The expression can be further simplifyied by noting that $\delta h_{kl,ij} = -\delta h_{ij,kl}$. If transitions $i \to j$ and $k \to l$ take place between eigenstates of different electronic subsystems, or more generally, if $[\hat{\sigma}_{ij},\hat{\sigma}_{kl}] = 0$, then the terms $\delta h_{kl,ij}$ will cancel out, which leads the final Heisenberg equation to be written as:

$$\dot{\hat{O}}(t) = -\frac{i}{\hbar}[\hat{O}(t),\hat{H}_s]+$$
$$+\frac{i}{\hbar}\frac{e^2\hbar^2\mu_0}{4m^2}\sum_{\substack{i,j\\k,l}}[\hat{O},\hat{\sigma}_{ij}\hat{\sigma}_{kl}]\overline{f}_{ij,kl}$$
$$+\frac{i}{\hbar}\frac{e^2\hbar^2\mu_0}{4m^2}\sum_{\substack{i,j\\k,l}}\left(\left\{\hat{O},\hat{\sigma}_{ij}\hat{\sigma}_{kl}\right\}-2\hat{\sigma}_{ij}\hat{O}\hat{\sigma}_{kl}\right)\overline{h}_{ij,kl}. \tag{E.32}$$

Therefore, the field-mediated coherent coupling between two electronic transitions is parametrized by the quantity $\overline{f}_{ij,kl}$, which has the form of the power dissipated by two classical electrical currents, where in the expression, the transition probability currents of the involved electronic transitions play the role of these electrical currents. Furthermore, if the transitions under consideration are such that fulfil $\boldsymbol{d}_{ij} = -\boldsymbol{d}^*_{ji}$, then Eq. (E.32) can be majorly simplified[2], as then $\delta h_{ij,kl} = 0$ and $\overline{h}_{ij,kl} = 0$, and therefore the dynamics of the field mediated electronic interaction will be described by an effective Hamiltonian $\dot{\hat{O}}(t) = -\frac{i}{\hbar}[\hat{O}(t),\hat{H}_{eff}]$

[2] Transitions between localized eigenstates and and the free electron eigenstates we use in calculations down the line both fulfil this condition.

where the Hamiltonian is defined as:

$$\hat{H}_{eff} = \hat{H}_s - \sum_{ij} \hbar g^{m-m}_{ij,ij} \hat{c}^\dagger_i \hat{c}_i - \sum_{\substack{i,j \\ k,l \neq i,j}} \hbar g^{m-m}_{ij,kl} \hat{\sigma}_{ij} \hat{\sigma}^\dagger_{kl} \tag{E.33}$$

$$g^{m-m}_{ij,kl} = \frac{e^2 \hbar \mu_0}{2m^2} \iint \mathrm{d}\boldsymbol{r}\, \mathrm{d}\boldsymbol{r}'\; \boldsymbol{d}_{ij}(\boldsymbol{r}) \cdot \mathrm{Re}\left\{ \mathbf{G}^{(\mathrm{NR})}\left(\boldsymbol{r}, \boldsymbol{r}', \frac{|\omega_{kl}| + |\omega_{ij}|}{2} \right) \right\} \cdot \boldsymbol{d}^*_{kl}(\boldsymbol{r}'), \tag{E.34}$$

where we have introduced an effective matter-matter coupling strength $g^{m-m}_{ij,kl}$, and explicitely indicated that the Dyadic Green's Function that mediates this interaction corresponds to the non-resonant part. As previously indicated, the sign of ω_{ij} will depend on the particular initial and final states ($\omega_{ij} = -\omega_{ji}$), and due to the symmetry of the Dyadic Green's Function with respect to the sign of the frequency argument, we denote the frequency dependence by using the absolute values. Note that in Eq. (E.33) we distinguish between cases in which $\{kl\} \neq \{ij\}$, and those in which $\{kl\} = \{ij\}$. While the first summation terms describe this coherent coupling between electronic transitions, the second kind renormalizes the energy of the electronic eigenstates with an energy shift given by $\hbar\delta_i = \sum_j g^{m-m}_{ij,ij}$. From the definition of the coupling strength we see that $g^{m-m}_{ij,kl} = g^{m-m*}_{kl,ij}$, and also, since $\boldsymbol{d}_{ji} = -\boldsymbol{d}^*_{ij}$, $g^{m-m}_{ji,lk} = g^{m-m*}_{ij,kl}$. The complete Hamiltonian then reads:

$$\begin{aligned} \hat{H}_{\mathrm{eff}} = & \iint \mathrm{d}\boldsymbol{r}\, \mathrm{d}\omega\; \hbar\omega \hat{\boldsymbol{f}}^\dagger(\boldsymbol{r},\omega) \hat{\boldsymbol{f}}(\boldsymbol{r},\omega) + \sum_i \left(E_i - \hbar\delta_i\right) \hat{c}^\dagger_i \hat{c}_i \\ & + \frac{e}{m} \hat{\mathbf{p}} \cdot \hat{\boldsymbol{A}}^{(\mathrm{R})} - \sum_{\substack{i,j \\ k,l \neq i,j}} \hbar\, g^{m-m}_{ij,kl}\, \hat{\sigma}_{ij} \hat{\sigma}^\dagger_{kl} \end{aligned} \tag{E.35}$$

The first two terms in Eq. (E.35) correspond to the energies of the field and electronic states, while the second line describes the coupling between the electronic states with the resonant component of the EM environment, and among electronic transitions mediated by the non-resonant component of the fields[3]. On the next section, we will focus on writing the light-matter coupling term of the Hamiltonian in a similar fashion as we have done here.

[3] See the Sokhotski-Plemejl decomposition made in page 226.

E.2.2 Light-matter interaction: Current centered modes

Next, our interest lies in finding how to express the light matter couplings in terms of generalized bosonic operators. For that we revisit the resonant term in the minimal coupling in Equation E.29. Writing:

$$\hat{\mathbf{p}} = -i\frac{\hbar}{2}\sum_{i,j}\int \mathrm{d}\boldsymbol{r}\left[\hat{\sigma}_{ij}\,\phi_i^*(\boldsymbol{r})\nabla\phi_j(\boldsymbol{r}) - \hat{\sigma}_{ji}\,\phi_i(\boldsymbol{r})\nabla\phi_j^*(\boldsymbol{r})\right],$$

$$\hat{\boldsymbol{A}}(\boldsymbol{r}) = -i\int\frac{\mathrm{d}\omega}{\omega}\int \mathrm{d}\boldsymbol{r}'\left[\mathbf{G}(\boldsymbol{r},\boldsymbol{r}',\omega)\cdot\hat{\boldsymbol{f}}(\boldsymbol{r}',\omega) - \hat{\boldsymbol{f}}^\dagger(\boldsymbol{r}'.\omega)\cdot\mathbf{G}^\dagger(\boldsymbol{r},\boldsymbol{r}',\omega)\right],$$

The interaction Hamiltonian term looks like

$$\begin{aligned}
H_I = \frac{e}{m}\hat{\mathbf{p}}\cdot\hat{\boldsymbol{A}}^{(\mathrm{R})} = \\
= -\frac{e\hbar}{2m}\sum_{i,j}\int\frac{\mathrm{d}\omega}{\omega}\Bigg\{\hat{\sigma}_{ij}\iint d\boldsymbol{r}\,d\boldsymbol{r}'\,\boldsymbol{d}_{ij}(\boldsymbol{r})\cdot\mathbf{G}^{(\mathrm{R})}(\boldsymbol{r},\boldsymbol{r}',\omega)\cdot\hat{\boldsymbol{f}}(\boldsymbol{r}',\omega) \\
+\hat{\sigma}_{ji}\iint d\boldsymbol{r}\,d\boldsymbol{r}'\,\boldsymbol{d}_{ji}(\boldsymbol{r})\cdot\mathbf{G}^{(\mathrm{R})}(\boldsymbol{r},\boldsymbol{r}',\omega)\cdot\hat{\boldsymbol{f}}(\boldsymbol{r}',\omega) \\
+\hat{\sigma}_{ij}\iint d\boldsymbol{r}\,d\boldsymbol{r}'\,\hat{\boldsymbol{f}}^\dagger(\boldsymbol{r}',\omega)\cdot\left(\mathbf{G}^{(\mathrm{R})}(\boldsymbol{r},\boldsymbol{r}',\omega)\right)^\dagger\cdot\boldsymbol{d}_{ji}^*(\boldsymbol{r}) \\
+\hat{\sigma}_{ji}\iint d\boldsymbol{r}\,d\boldsymbol{r}'\,\hat{\boldsymbol{f}}^\dagger(\boldsymbol{r}',\omega)\cdot\left(\mathbf{G}^{(\mathrm{R})}(\boldsymbol{r},\boldsymbol{r}',\omega)\right)^\dagger\cdot\boldsymbol{d}_{ij}^*(\boldsymbol{r})\Bigg\}
\end{aligned} \tag{E.36}$$

where to get the last term we have just exchanged the indices and used that $\boldsymbol{d}_{ji}(\boldsymbol{r}) = -\boldsymbol{d}_{ij}^*(\boldsymbol{r})$. Following the spirit of emitter centered modes [27, 321] we rewrite the Hamiltonian by defining a new set of bosonic operators as

$$\begin{aligned}
H_I = \hbar\sum_{i,j}\int \mathrm{d}\omega\Big[g_{ij}(\omega)\hat{\sigma}_{ij}\,\hat{a}_{ij}(\omega) + g_{ji}(\omega)\hat{\sigma}_{ji}\,\hat{a}_{ji}(\omega) + \\
+g_{ij}^*(\omega)\hat{\sigma}_{ij}^\dagger\,\hat{a}_{ij}^\dagger(\omega) + g_{ji}^*(\omega)\hat{\sigma}_{ji}^\dagger\,\hat{a}_{ji}^\dagger(\omega)\Big]
\end{aligned} \tag{E.37}$$

$$\hat{a}_{ij}(\omega) = \frac{-e}{2m\omega g_{ij}(\omega)}\iint d\boldsymbol{r}\,d\boldsymbol{r}'\,\boldsymbol{d}_{ij}(\boldsymbol{r})\cdot\mathbf{G}^{(\mathrm{R})}(\boldsymbol{r},\boldsymbol{r}',\omega)\cdot\hat{\boldsymbol{f}}(\boldsymbol{r}',\omega) \tag{E.38}$$

E

From these expressions and the commutation properties of the $\hat{\boldsymbol{f}}$ operators, it can be shown that $[\hat{a}_{ij}, \hat{a}_{kl}] = 0$. By using the commutation relations of the $\hat{\boldsymbol{f}}$ operators and the identity $\int \mathrm{d}\mathbf{s}\, \mathbf{G}(\boldsymbol{r}, \mathbf{s}, \omega) \cdot \mathbf{G}^{\dagger}(\boldsymbol{r}'', \mathbf{s}, \omega) = \frac{\hbar\mu_0}{\pi}\omega^2 \mathrm{Im}(\mathbf{G}(\boldsymbol{r}, \boldsymbol{r}'', \omega))$, the commutation relation for these new bosonic operators is given by:

$$[\hat{a}_{ij}(\omega), \hat{a}^{\dagger}_{kl}(\omega')] = \\ = \delta(\omega - \omega') \frac{e^2 \hbar \mu_0}{4m^2 \pi g_{ij}(\omega) g^*_{kl}(\omega)} \iint \mathrm{d}\boldsymbol{r}\, \mathrm{d}\boldsymbol{r}''\, \boldsymbol{d}_{ij}(\boldsymbol{r}) \cdot \mathrm{Im}\left\{\mathbf{G}^{(\mathrm{R})}(\boldsymbol{r}, \boldsymbol{r}'', \omega)\right\} \cdot \boldsymbol{d}^*_{kl}(\boldsymbol{r}'')$$

In particular, by imposing $[\hat{a}_{ij}, \hat{a}^{\dagger}_{ij}] \equiv 1$, we find that the coupling between the photon mode and the electronic transition is given by:

$$g_{ij}(\omega) = \frac{e}{2m} \sqrt{\frac{\hbar\mu_0}{\pi} \iint \mathrm{d}\boldsymbol{r}\, \mathrm{d}\boldsymbol{r}'\, \boldsymbol{d}_{ij}(\boldsymbol{r}) \cdot \mathrm{Im}\left\{\mathbf{G}^{(\mathrm{R})}(\boldsymbol{r}, \boldsymbol{r}', \omega)\right\} \cdot \boldsymbol{d}^*_{ij}(\boldsymbol{r}')} \tag{E.39}$$

This is the central result of this section. It shows that the coupling strength between a given electronic transition and an optical mode can be written in a form very similar to the coupling strength between a QE and an optical mode, albeit replacing the puntual dipole moment by an extended current distribution. Using the fact that the Dyadic Green's Function function is a symmetric tensor, it can be seen that g_{ij} is a real constant, and that $g_{ij} = g_{ji}$. This then allows to rewrite the general commutator as

$$[\hat{a}_{ij}(\omega), \hat{a}^{\dagger}_{kl}(\omega')] = \delta(\omega - \omega') \frac{F^{kl}_{ij}}{\sqrt{F^{ij}_{ij} F^{kl}_{kl}}} \tag{E.40}$$

$$F^{cd}_{ab} = \iint \mathrm{d}\boldsymbol{r}\, \mathrm{d}\boldsymbol{r}'\, \boldsymbol{d}_{ab}(\boldsymbol{r}) \cdot \mathrm{Im}\left\{\mathbf{G}^{(\mathrm{R})}(\boldsymbol{r}, \boldsymbol{r}', \omega)\right\} \cdot \boldsymbol{d}^*_{cd}(\boldsymbol{r}') \tag{E.41}$$

Although we will not tackle this problem here, the modes defined in this manner are not orthogonal, since the conmutators for the modes from different transitions are non-zero. Some strategies have been proposed to tackle this problem and generate a set of field operators that do conmute among themselves [321]. We are particularly interested in

systems in which the Green's Function is sharply peaked around a resonant frequency: ω_c. By writting the resonant part of the Dyadic Green's Function as

$$\mathbf{G}^{(\mathrm{R})}(\boldsymbol{r},\boldsymbol{r}',\omega) = \boldsymbol{\mathcal{G}}(\boldsymbol{r},\boldsymbol{r}',\omega_c)\delta(\omega-\omega_c), \tag{E.42}$$

the interaction Hamiltonian in Eq. (E.37) can be written as a familiar Rabi interaction Hamiltonian:

$$H_I = \hbar\sum_{i,j} g_{ij}^{l-m}\left[\hat{\sigma}_{ij}\left(\hat{a}_{ij}+\hat{a}_{ji}^{\dagger}\right)+\hat{\sigma}_{ij}^{\dagger}\left(\hat{a}_{ji}+\hat{a}_{ij}^{\dagger}\right)\right] \tag{E.43}$$

$$\hat{a}_{ij} = \frac{-e}{2m\omega g_{ij}}\iint d\boldsymbol{r}\,d\boldsymbol{r}'\,\boldsymbol{d}_{ij}(\boldsymbol{r})\cdot\boldsymbol{\mathcal{G}}(\boldsymbol{r},\boldsymbol{r}',\omega_c)\cdot\hat{\boldsymbol{f}}(\boldsymbol{r}',\omega_c) \tag{E.44}$$

$$g_{ij}^{l-m} = \frac{e}{2m}\sqrt{\frac{\hbar\mu_0}{\pi}}\iint d\boldsymbol{r}\,d\boldsymbol{r}'\,\boldsymbol{d}_{ij}(\boldsymbol{r})\cdot\mathrm{Im}\left\{\boldsymbol{\mathcal{G}}(\boldsymbol{r},\boldsymbol{r}',\omega_c)\right\}\cdot\boldsymbol{d}_{ij}^{*}(\boldsymbol{r}') \tag{E.45}$$

Where we have now introduced a light-matter interaction strength denoted by g_{ij}^{l-m}. Finally, the effective Hamiltonian of a system that involves general electronic transitions interacting with a single mode field can be written as

$$\begin{aligned}\hat{H}_{\mathrm{eff}} =& \sum_{ij}\hbar\omega_c\hat{a}_{ij}^{\dagger}\hat{a}_{ij}+\sum_{i}\tilde{E}_i\hat{c}_i^{\dagger}\hat{c}_i\\ &+\hbar\sum_{i,j}g_{ij}^{l-m}\hat{\sigma}_{ij}\left(\hat{a}_{ij}+\hat{a}_{ji}^{\dagger}\right)\\ &-\sum_{\substack{i,j\\k,l\neq i,j}}\hbar\,g_{ij,kl}^{m-m}\,\hat{\sigma}_{ij}\hat{\sigma}_{kl}^{\dagger}\end{aligned} \tag{E.46}$$

with

$$g_{ij}^{l-m} = \frac{e}{m}\sqrt{\frac{\hbar\mu_0}{\pi}}\iint d\boldsymbol{r}\,d\boldsymbol{r}'\,\boldsymbol{d}_{ij}(\boldsymbol{r})\cdot\mathrm{Im}\left\{\boldsymbol{\mathcal{G}}(\boldsymbol{r},\boldsymbol{r}',\omega_c)\right\}\cdot\boldsymbol{d}_{ij}^{*}(\boldsymbol{r}') \tag{E.47}$$

$$g_{ij,kl}^{m-m} = \frac{e^2\hbar\mu_0}{2m^2}\iint d\boldsymbol{r}\,d\boldsymbol{r}'\,\boldsymbol{d}_{ij}(\boldsymbol{r})\cdot\mathrm{Re}\left\{\mathbf{G}^{(\mathrm{NR})}\left(\boldsymbol{r},\boldsymbol{r}',\frac{|\omega_{kl}|+|\omega_{ij}|}{2}\right)\right\}\cdot\boldsymbol{d}_{kl}^{*}(\boldsymbol{r}') \tag{E.48}$$

E.3 Electronic transitions of interest

One of the strengths of the above Hamiltonian is its applicability to a wide variety of electronic transitions. One could study the coupling of bloch electrons in materials, localised electronic transitions in molecules, or bound electrons in material defects on equal footing, provided one is capable of obtaining the initial and final electronic states involved in the transition. In this section, we will apply the above formalism to derive couplings for specific cases: localized dipolar electronic transitions and also free electrons.

E.3.1 Localized transitions: dipolar quantum emitters

One of the most relevant applications of this framework is when dealing with localised transitions. In this family we can include transitions inside quantum dots, molecules or defects in crystals. This is due to the fact that regardless of the actual shape of the electronic states taking place in the transition, the scale lengths associated with them is much smaller than the scale in which the EM fields change. As such, one could assume that the Dyadic Green's Function is constant over the span of the electronic wavefunctions of the quantum emitter (QE) and write:

$$\begin{aligned}\boldsymbol{d}_{ij}^{QE}(r) \approx \delta(r-r_0)\int \mathrm{d}\boldsymbol{r}'\,\boldsymbol{d}_{ij}(r') = \delta(r-r_0)\int \mathrm{d}\boldsymbol{r}'\,\phi_i^*(r')\nabla\phi_j(r') = \\ = \delta(r-r_0)\langle i|\nabla|j\rangle = -\delta(r-r_0)\frac{m}{\hbar^2}\langle i|[\hat{H}_e,\hat{r}]|j\rangle = \\ = -\delta(r-r_0)\frac{m}{e\hbar}(\omega_j-\omega_i)\langle i|-e\hat{r}|j\rangle = -\delta(r-r_0)\frac{m\omega_{ij}}{e\hbar}\boldsymbol{\mu}_{ij} \qquad \text{(E.49)}\end{aligned}$$

where in the end we have the energy difference between the initial and final state given by $\omega_{ij}=\omega_j-\omega_i$, and the usual transition dipole moment given by $\boldsymbol{\mu}_{ij}=\langle i|-e\hat{r}|j\rangle$, where e is the electron charge. To arrive at this expression we have used that, in general, the electronic Hamiltonian will be written as $\hat{H}_e = V(r)+\hat{\mathbf{p}}^2/2m$ and therefore $[\hat{H}_e,\hat{r}] = -i\hbar\hat{\mathbf{p}}/m = -\hbar^2\nabla/m$. Putting this transition current density into Eq. (E.47), we get the very familiar expression for the coupling between a dipolar QE and

an optical mode of a cavity:

$$g_{ij}^{c-QE} = \frac{|\omega_{ij}|}{\hbar}\sqrt{\frac{\hbar\mu_0}{\pi}\boldsymbol{\mu}_{ij}\cdot \mathrm{Im}\left\{\boldsymbol{\mathcal{G}}(\boldsymbol{r}_0,\boldsymbol{r}_0,\omega_c)\right\}\cdot\boldsymbol{\mu}_{ij}^*} \tag{E.50}$$

Since these couplings are real, $g_{ij}^{c-QE} = g_{ji}^{c-QE} \equiv g^{c-QE}$. For the case of a single QE, with eigenstates named by $|g\rangle$ and $|e\rangle$, for ground and excited state, the interaction between this QE and some EM environment is given (from Eq. (E.46)) by:

$$\begin{aligned}\hat{H}_I^{c-QE} =& g^{c-QE}\hbar\left[\hat{\sigma}_{ge}\left(\hat{a}_{ge}+\hat{a}_{eg}^\dagger\right)+\hat{\sigma}_{eg}\left(\hat{a}_{eg}+\hat{a}_{ge}^\dagger\right)\right]\\ \approx& \hbar g^{c-QE}\left[\hat{\sigma}\hat{a}_{eg}^\dagger+\hat{\sigma}^\dagger\hat{a}_{eg}\right] \qquad \text{(E.51)}\\ g^{c-QE} =& \frac{\omega_{QE}}{\hbar}\sqrt{\frac{\hbar\mu_0}{\pi}\boldsymbol{\mu}\cdot\mathrm{Im}\left\{\boldsymbol{\mathcal{G}}(\boldsymbol{r}_0,\boldsymbol{r}_0,\omega_c)\right\}\cdot\boldsymbol{\mu}^*} \qquad \text{(E.52)}\end{aligned}$$

where we have introduced the usual QE ladder operators given by $\hat{\sigma} = |g\rangle\langle e|$, defined the QE transition dipole moment as $\boldsymbol{\mu} \equiv \boldsymbol{\mu}_{ge} = \langle g|-e\hat{r}\,|e\rangle$, and applied the rotating wave approximation to the cavity-QE coupling, which leads to the interaction being written in terms of a single optical mode.

E.3.2 Free electrons

We will approximate free electron states as momentum eigenstates in the $\hat{z}$ direction with some lateral distribution: $\phi_k(\boldsymbol{r}) = g_\perp(\boldsymbol{r}_\perp)e^{ik_k z}/\sqrt{L}$ where L is the length of a fictitious box used to quantize the electron momenta, and $g_\perp(\boldsymbol{r}_\perp)$ is a function describing the thin lateral profile of the electron wavepacket. In principle we could say that

$$g_\perp(\boldsymbol{r}_\perp) = \sqrt{\frac{1}{2\pi\sigma^2}}\exp\left\{-\left(\frac{|\boldsymbol{r}_\perp-\boldsymbol{r}_{0,\perp}|}{2\sigma}\right)^2\right\},$$

which in the limit of small beam width behaves as a delta in the lateral direction. For a transition between free states we then have:

$$\boldsymbol{d}_{kl}(\boldsymbol{r}) = \phi_k^*\nabla\phi_l = \frac{1}{\sigma}\begin{pmatrix}\frac{(x_0-x)}{2\sigma}\\ \frac{(y_0-y)}{2\sigma}\\ ik_l\sigma\end{pmatrix}\frac{e^{-\frac{|\boldsymbol{r}_\perp-\boldsymbol{r}_{0,\perp}|^2}{2\sigma^2}}}{2\pi\sigma^2}\frac{e^{i(k_l-k_k)z}}{L} \tag{E.53}$$

E

$$\overset{\lim_{\sigma\to 0}}{\approx} ik_0 \frac{\delta^2(\boldsymbol{r}_\perp - \boldsymbol{r}_{0,\perp})}{L} e^{i(k_l - k_k)z}\hat{z}, \tag{E.54}$$

where we have approximated the free electron states as a punctual distribution in a lateral direction and assumed that the electron's momentum does not change much within the interaction, and therefore the initial and final electron momentum are given approximately by the incident electron's central momentum, k_0. Of course this also means that we assume that the electron wavepacket has a well defined central momentum. Putting this into Eq. (E.47)

$$g_{kl}^{e-c} = \frac{ek_0}{mL}\sqrt{\frac{\hbar\mu_0}{\pi}} \iint \mathrm{d}z\,\mathrm{d}z'\,\mathrm{Im}\left\{\hat{z}\cdot\boldsymbol{\mathcal{G}}(\boldsymbol{r},\boldsymbol{r}',\omega_c)\cdot\hat{z}\right\} e^{i(k_l-k_k)(z-z')}, \tag{E.55}$$

where we have used $\boldsymbol{r} = [\boldsymbol{r}_{\perp,0}, z]$, and $\boldsymbol{r}' = [\boldsymbol{r}_{\perp,0}, z']$. For an electron interacting with an arbitrary system, initially in the ground state, the first order interaction term will give a probability for the electron to loose a certain amount of momentum proportional to $(g_{kl}^{e-c})^2$. It is then nice to check that the classical EELS probability[151] indeed has the form $(g_{kl}^{e-c})^2$ if one makes the change $k_l - k_k \to \omega/v_0$, with v_0 being the initial velocity of the electron, with this substitution being just the consequence of energy conservation in the photon exchange between the optical modes and the electron. The fact that we have related the coupling strength to the classical EM Dyadic Green's Function through mQED allows to apply this strategy to arbitrary optical modes and we have the certainty that the normalization of the bosonic operators will be the right one by construction, which implies that this coupling strength expressions are physical.

Also note that the coupling strength above only depends on the momentum of the electron through the momentum change over the interaction. By writing $k_k \equiv k$ and $q \equiv k_l - k_k$ one can see that the above coupling strength can be parametrized just as g_q^{e-c}. The same applies to the optical modes defined in Eq. (E.44), albeit with the peculiarity that since the cavity's Dyadic Green's Function is purely imaginary at the resonance frequency (See Section E.4), then one can show from

Eq. (E.44) that $\hat{a}_q = -\hat{a}_{-q}$. With this, the interaction term between a free electron and an optical mode is given by

$$\begin{aligned}\hat{H}_I^{e-c} &= \hbar \sum_q g_q^{e-c} \hat{b}_q \left(\hat{a}_{-q}^\dagger - \hat{a}_{-q}\right) \\ &\approx \hbar \sum_q g_q^{e-c} \hat{b}_q \left(\hat{a}_{-q_0}^\dagger - \hat{a}_{-q_0}\right) \operatorname{sign}(q) \qquad \text{(E.56)}\end{aligned}$$

$$\hat{a}_q = \frac{-ik_0 e}{2m\omega L g_q} \iint \mathrm{d}z\, \mathrm{d}\boldsymbol{r}'\; {}^{iqz}\hat{z} \cdot \boldsymbol{\mathcal{G}}([\boldsymbol{r}_{\perp,0}, z], \boldsymbol{r}', \omega_c) \cdot \hat{\boldsymbol{f}}(\boldsymbol{r}', \omega_c) \qquad \text{(E.57)}$$

$$g_q^{e-c} = \frac{ek_0}{mL}\sqrt{\frac{\hbar\mu_0}{\pi}} \iint \mathrm{d}z\, \mathrm{d}z'\, \mathrm{Im}\left\{\hat{z} \cdot \boldsymbol{\mathcal{G}}([\boldsymbol{r}_{\perp,0}, z], [\boldsymbol{r}_{\perp,0}, z'], \omega_c) \cdot \hat{z}\right\} e^{iq(z-z')} \qquad \text{(E.58)}$$

Where we have approximated that the optical modes that the electron will interact with are given by those that exchange momentum $q_0 = \omega_c/v_0$. Upon studying the interaction of an electron with an isolated optical mode and enforcing energy conservation, this assertion can be seen to be correct. When considering the interaction of an electron with a polaritonic system, the energy exchanges will differ from ω_c, but since optical plamonic modes are highly spatially confined, their reciprocal space content will be very wide momenta distribution, and therefore, the error included by naming all the optical modes as $\hat{a}_{-q_0}$ is small.

In passing, note that the coupling strength above shows that a simple matching condition between the optical modes and the momentum exchange allows to maximize the coupling strength: for an electron interacting with an optical mode of frequency ω_c, energy conservation imposes $q = \omega_c/v_0$. The coupling strength above involves a Fourier transform of the associated field profiles, and therefore, for constructive interference one would want that the spatial frequency of the optical modes matches that of $\exp(iqz)$. If we consider a guided mode inside a waveguide, with guided momentum $k = k_0 n_{eff}$, where n_{eff} is the effective refractive index of the guided mode, then we see that by making $k = q = \omega_c/v_0 \rightarrow v_0 = c/n_{eff}$, will lead to enhanced interaction strength. This amounts to matching the phase velocity of the optical

mode in the waveguide to that of the momentum exchange of the free electron, just as done in [299].

E.3.3 Bound electron - free electron interaction

From Eq. (E.46), and having particularized the current densities for transitions in dipolar QE and free electrons, the Hamiltonian describing the free-electron bound electron interaction is given by:

$$\hat{H}_I^{e-QE} = -2\hbar \sum_{kl} \left[g_{ge,lk}^{e-QE}\, \hat{\sigma} + (g_{ge,kl}^{e-QE})^*\, \hat{\sigma}^\dagger \right] \sigma_{kl},$$

where we have introduced the ladder operators of the QE given by $\hat{\sigma} = |g\rangle\langle e|$, and explicit expressions for both couplings in the last term are:

$$g_{ge,lk}^{e-QE} = ik_0 \frac{e\mu_0\omega_{ge}}{2mL} \int \mathrm{d}z'\ \boldsymbol{\mu}_{ge} \cdot \mathrm{Re}\left\{ \mathbf{G}\left(\boldsymbol{r}_{QE}, \boldsymbol{r}', \omega_{ge}\right) \right\} \cdot \hat{z} e^{i(k_l - k_k)z'},$$
$$g_{ge,kl}^{e-QE} = ik_0 \frac{e\mu_0\omega_{ge}}{2mL} \frac{m\omega_{ge}}{e\hbar} \int \mathrm{d}z'\ \boldsymbol{\mu}_{ge} \cdot \mathrm{Re}\left\{ \mathbf{G}\left(\boldsymbol{r}_{QE}, \boldsymbol{r}', \omega_{ge}\right) \right\} \cdot \hat{z} e^{-i(k_l - k_k)z'},$$

where again, for compactness we have used $\boldsymbol{r}' = [\boldsymbol{r}_{0,\perp}, z']$. Defining $k_k = k$ and $k_l = k_k + q$, we see that the two couplings become independent of k

$$g_q^{e-QE} \equiv 2g_{ge,lk}^{e-QE} = ik_0 \frac{e\mu_0\omega_{ge}}{mL} \int \mathrm{d}z'\ \boldsymbol{\mu}_{ge} \cdot \mathrm{Re}\left\{ \mathbf{G}\left(\boldsymbol{r}_{QE}, \boldsymbol{r}', |\omega_{ge}|\right) \right\} \cdot \hat{z} e^{iqz'},$$
$$2g_{ge,kl}^{e-QE} \equiv g_{-q}^{e-QE} = -(g_q^{e-QE})^*,$$

which allows to parametrize the interaction Hamiltonian entirely in terms of the momentum exchange between the free electron and the QE: q. With this, the interaction Hamiltonian and coupling strengths read

$$\hat{H}_I^{e-QE} = -\hbar \sum_q g_q^{e-QE} \left[\hat{\sigma} - \hat{\sigma}^\dagger \right] \hat{b}_q, \tag{E.59}$$
$$g_q^{e-QE} = ik_0 \frac{e\mu_0\omega_{QE}}{mL} \int \mathrm{d}z'\ \boldsymbol{\mu} \cdot \mathrm{Re}\left\{ \mathbf{G}^{(\mathrm{NR})}\left(\boldsymbol{r}_{QE}, [\boldsymbol{r}_{0,\perp}, z'], |\omega_{QE}|\right) \right\} \cdot \hat{z} e^{iqz'},$$

Notice that the coupling between the QE and the passing electron depends on the non-resonant componet of the Dyadic Green's Function. In

our study, we will then asssume that the QE and free electron will interact through free-space, and therefore, the non-resonant Dyadic Green's Function corresponds to $\mathbf{G}^{(\mathrm{NR})} = \mathbf{G}_0$, the free-space Dyadic Green's Function [12]. In the near field, it reads:

$$\mathbf{G}_0(\boldsymbol{r},\boldsymbol{r}') \overset{NF}{\approx} \frac{e^{ikR}}{4\pi R}\frac{1}{k^2R^2}\left[-\bar{\bar{I}} + 3\frac{\boldsymbol{RR}}{R^2}\right].$$

where $\boldsymbol{R} = \boldsymbol{r} - \boldsymbol{r}'$, $R = |\boldsymbol{r}|$ and $\boldsymbol{rr}$ denotes the outer product. To calculate $\mathbf{G}(\boldsymbol{r}_{QE}, [\boldsymbol{r}_\perp, z], \Omega)$, we have $\boldsymbol{r}_{QE} = [x_{QE}, 0, z_{QE}]$ $\boldsymbol{r}_e = [x_{QE} + b_{e-QE}, 0, z]$, so $\boldsymbol{R} = \boldsymbol{r}_{QE} - \boldsymbol{r}_e = -[b_{e-QE}, 0, z - z_{QE}]$. If we define $\hat{u} = \boldsymbol{R}/R$ we then have

$$\begin{aligned}\boldsymbol{\mu}\cdot\mathbf{G}_0(\boldsymbol{r}_{QE},[\boldsymbol{r}_\perp,z])\cdot\hat{z} &= \frac{e^{ik\sqrt{b_{e-QE}^2+(z-z_{QE})^2}}}{4\pi\sqrt{b_{e-QE}^2+(z-z_{QE})^2}}\frac{-\boldsymbol{\mu}\cdot\hat{z}+3(\boldsymbol{\mu}\cdot\hat{u})(\hat{u}\cdot\hat{z})}{k^2\left[b_{e-QE}^2+(z-z_{QE})^2\right]}\\ &\overset{QS}{\approx}\frac{-(\boldsymbol{\mu}\cdot\hat{z})}{4\pi k^2\left[b_{e-QE}^2+(z-z_{QE})^2\right]^{3/2}}+\\ &+\frac{3(\boldsymbol{\mu}\cdot\hat{x})b_{e-QE}(z-z_{QE})}{4\pi k^2\left[b_{e-QE}^2+(z-z_{QE})^2\right]^{5/2}}+\\ &+\frac{3(\boldsymbol{\mu}\cdot\hat{z})(z-z_{QE})^2}{4\pi k^2\left[b_{e-QE}^2+(z-z_{QE})^2\right]^{5/2}},\end{aligned}$$

Where we have used the quasi-static (QS) limit. So the coupling between the free electron and the 2 level system is given by

$$\begin{aligned}g_q^{e-QE} = ik_0\frac{e\mu_0\omega_{QE}}{4\pi mLk^2}\frac{e^{iqz_{QE}}\boldsymbol{\mu}}{|b_{e-QE}|^2}\cdot\Big\{&\Big[2I_2(qb_{e-QE})-I_0(qb_{e-QE})\Big]\hat{z}+\\ &+\Big[3\,\mathrm{sign}(\mathrm{b_{e-QE}q})\mathrm{I_1(qb_{e-QE})}\Big]\hat{\mathrm{x}}\Big\},\end{aligned}$$

where we have defined the integrals

$$I_n(\phi) = \int_{-\infty}^{\infty}\mathrm{d}z\,\frac{z^n}{[1+z^2]^{5/2}}e^{i|\phi|z} \tag{E.60}$$

which evaluate to

$$I_0(\phi) = \frac{2}{3}\,|\phi|^2\,K_2(|\phi|), \tag{E.61}$$

$$I_1(\phi) = \frac{2i}{3}\,|\phi|^2\,K_1(|\phi|), \tag{E.62}$$

$$I_2(\phi) = \frac{2}{3}\left[|\phi|\,K_1(|\phi|) - |\phi|^2\,K_0(|\phi|)\right], \tag{E.63}$$

$$I_0(\phi) - 2I_2(\phi) = 2\,|\phi|^2\,K_0(|\phi|).$$

where in the last line we have used the recurrence relation [81] of modified bessel functions to rewrite the expression in a more compact form. From this, the interaction strength between the bound and free electron can be written as:

$$g_q^{e-QE} = -\frac{e\,k_0\,|q|^2\,e^{iqz_{QE}}}{2\pi m L\epsilon_0\omega_{QE}}\boldsymbol{\mu}\cdot\begin{pmatrix}\text{sign}(qb_{e-QE})K_1(|qb_{e-QE}|)\\ 0\\ iK_0(|qb_{e-QE}|)\end{pmatrix}. \tag{E.64}$$

In agreement with previous calculations for the free electron - bound electron interaction strength [310].

E.4 Quasi-static Dyadic Green's Function of a Sphere

Here, we aim at obtaining a closed expression for the $\boldsymbol{\mathcal{G}}(\boldsymbol{r},\boldsymbol{r}',\omega_c)$ tensor in the Dyadic Green's Function decomposition for the optical mode supported by a spherical cavity:

$$\mathbf{G}(\boldsymbol{r},\mathbf{r}',\omega) = \mathbf{G}_0(\boldsymbol{r},\mathbf{r}',\omega) + \boldsymbol{\mathcal{G}}(\boldsymbol{r},\mathbf{r}')\mathcal{L}(\omega)$$

where $\mathbf{G}_0(\boldsymbol{r},\mathbf{r}',\omega)$ is the vacuum Dyadic Green's Function and $\mathcal{L}(\omega)$ contains the frequency response of the sphere's contribution to the total GF. To do this we solve Poisson equation in the geometry presented in Fig. E.1 with the charge distribution of an electric dipole:

$$\rho(\boldsymbol{r}',\omega) = -\mu\cdot\nabla\delta(\boldsymbol{r}'-\boldsymbol{r}_\mu).$$

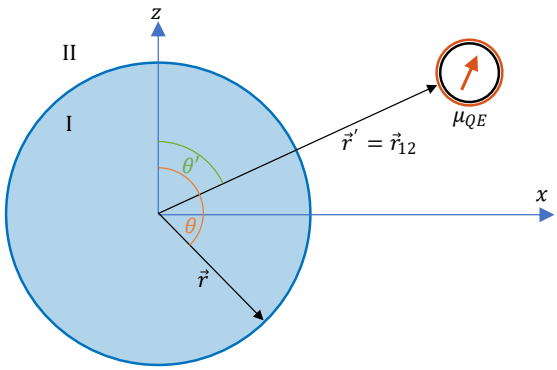

FIGURE E.1: Sketch of the system under consideration with relevant parameters.

We use that for $r' > r$, we can expand

$$\frac{1}{|\boldsymbol{r}-\boldsymbol{r}'|} = \sum_{n=0}^{\infty}\sum_{m=-n}^{n} \frac{4\pi}{2n+1} Y_n^{m*}(\theta',\phi') Y_n^m(\theta,\phi) \frac{r^n}{r'^{n+1}},$$

which allows to express the potential created by the dipole as

$$\phi_{inc}(\boldsymbol{r},\omega) = \frac{1}{4\pi\epsilon_0}\int \mathrm{d}\boldsymbol{r}' \frac{\rho(\boldsymbol{r}',\omega)}{|\boldsymbol{r}-\boldsymbol{r}'|} = \frac{1}{4\pi\epsilon_0}\sum_{n=0}^{\infty}\sum_{m=-n}^{n} \frac{4\pi}{2n+1} I_n^m Y_n^m(\theta,\phi) r^n,$$

with

$$I_n^m = \int \mathrm{d}\boldsymbol{r}' \frac{\rho(\boldsymbol{r}',\omega)}{r'^{n+1}} Y_n^{m*}(\theta',\phi') = -\nabla'\left(\frac{Y_n^{m*}(\theta',\phi')}{r'^{n+1}}\right)\cdot\boldsymbol{\mu}.$$

Now we can solve the scattering problem by expanding the potential on the different regions and matching spherical harmonics:

$$\begin{aligned}
\phi_{I}{}_n^m(\boldsymbol{r},\omega) =& \phi_{inc}{}_n^m(\boldsymbol{r},\omega) + \phi_{sc,I}{}_n^m(\boldsymbol{r},\omega) = \\
=& \frac{1}{\epsilon_0}\frac{1}{2n+1} I_n^m Y_n^m(\theta,\phi) r^n + A_n^m \frac{Y_n^m(\theta,\phi)}{r^{n+1}}, \\
\phi_{II}{}_n^m(\boldsymbol{r},\omega) =& \phi_{sc,II}{}_n^m(\boldsymbol{r},\omega) = B_n^m Y_n^m(\theta,\phi) r^n.
\end{aligned}$$

Imposing continuity of the potential and the normal component of the displacement field we find A_n^m, and hence the scattered field

$$\phi_{sc,I_n^m}(\boldsymbol{r},\omega) = -\left[\frac{1}{\epsilon_0}\frac{R^{2n+1}}{2n+1} I_n^m \frac{\epsilon_{sph}(\omega)-1}{\epsilon_{sph}(\omega)+\frac{n+1}{n}}\right]\frac{Y_n^m(\theta,\phi)}{r^{n+1}}.$$

Note that all the frequency dependence is contained within the permittivity of the sphere. If we assume a Drude model for the sphere $\epsilon_{sph} = 1-\omega_p^2/(\omega(\omega+i\gamma))$, then we can rewrite the permittivity quotient as

$$\frac{\epsilon_{sph}(\omega)-1}{\epsilon_{sph}(\omega)+\frac{n+1}{n}} = \frac{-\frac{\omega_p^2}{\omega(\omega+i\gamma)}}{\frac{2n+1}{n}-\frac{\omega_p^2}{\omega(\omega+i\gamma)}} = \frac{-\omega_{sp}^2}{\omega(\omega+i\gamma)-\omega_{sp}^2},$$

where we have defined $\omega_c = \omega_{sp} = \sqrt{n/(2n+1)}\,\omega_p$, the generalized Frölich poles. The above quotient has poles for $\omega = \pm\sqrt{\omega_{sp}^2-(\gamma/2)^2} - i\gamma/2$, which in the limit of small losses tends to ω_{sp}. This means that within the good resonator approximation, the above quotient will be only non-zero for a small region around ω_{sp}. Expressing $\omega = \omega_{sp}+\delta$, and expanding for small δ values we find:

$$\begin{aligned}\frac{\epsilon_{sph}(\omega)-1}{\epsilon_{sph}(\omega)+\frac{n+1}{n}} = \frac{-\omega_{sp}^2}{(\omega_{sp}+\delta)^2+i\gamma(\omega_{sp}+\delta)-\omega_{sp}^2} &\approx -\frac{1}{2}\frac{\omega_{sp}}{\omega-\omega_{sp}+i\frac{\gamma}{2}} \\ &= \frac{-\omega_{sp}}{2}\mathcal{L}(\omega,\omega_{sp},\gamma),\end{aligned}$$

which gives a lorentzian lineshape around every frölich pole, with $\mathcal{L}(\omega,\omega_{sp},\gamma) = (\omega-\omega_{sp}+i\gamma/2)^{-1}$. The scattered potential and corresponding field are then

$$\begin{aligned}\phi_{sc,I_n^m}(\boldsymbol{r},\omega) &= \frac{1}{2\epsilon_0}\frac{R^{2n+1}}{2n+1}\,\omega_{sp}\mathcal{L}(\omega,\omega_{sp},\gamma)\,\frac{Y_n^m(\theta,\phi)}{r^{n+1}}\nabla'\left(\frac{Y_n^{m*}(\theta',\phi')}{r'^{n+1}}\right)\cdot\boldsymbol{\mu}, \\ \mathbf{E}_{sc,I_n^m}(\boldsymbol{r},\omega) &= -\frac{1}{2\epsilon_0}\frac{R^{2n+1}}{2n+1}\,\omega_{sp}\mathcal{L}(\omega,\omega_{sp},\gamma)\,\nabla\left(\frac{Y_n^m(\theta,\phi)}{r^{n+1}}\right)\nabla'\left(\frac{Y_n^{m*}(\theta',\phi')}{r'^{n+1}}\right)\cdot\boldsymbol{\mu}.\end{aligned}$$

By definition the Dyadic Green's Function fulfils

$$\mathbf{E}_\mu = \frac{\omega^2}{c^2\epsilon_0}\mathbf{G}(\boldsymbol{r},\boldsymbol{r}',\omega))\cdot\boldsymbol{\mu},$$

and therefore the contributions of all the different spherical harmonics to the Dyadic Green's Functions are:

$$\mathbf{G}_n^m(\boldsymbol{r},\boldsymbol{r}',\omega) = -\frac{c^2}{\omega^2}\frac{R^{2n+1}\mathcal{L}(\omega,\omega_{sp},\gamma)}{2(2n+1)}\,\omega_{sp}\nabla\left(\frac{Y_n^m(\theta,\phi)}{r^{n+1}}\right)\otimes\nabla'\left(\frac{Y_n^{m*}(\theta',\phi')}{r'^{n+1}}\right).$$

In particular we are interested in the contributions given by the dipolar mode of the nanoparticle, corresponding to $l = 1$. Setting $l = 1$ immediately gives three possible values for m, which gives the expected three-fold degeneracy of the dipolar mode. Instead of using the complex formulation, we choose to work with the real-valued spherical harmonics, given by

$$\begin{aligned}\mathcal{Y}_x &= \frac{1}{\sqrt{2}}\left[Y_1^{-1} - Y_1^1\right] = \frac{1}{2}\sqrt{\frac{\pi}{3}}\frac{x}{r},\\ \mathcal{Y}_y &= \frac{1i}{\sqrt{2}}\left[Y_1^{-1} + Y_1^1\right] = \frac{1}{2}\sqrt{\frac{\pi}{3}}\frac{y}{r},\\ \mathcal{Y}_z &= Y_1^0 = \frac{1}{2}\sqrt{\frac{\pi}{3}}\frac{z}{r}.\end{aligned}$$

So the Dyadic Green's Functions can be expressed as

$$\mathbf{G}_{x,y,z}(\boldsymbol{r},\boldsymbol{r}',\omega) = -\frac{c^2}{\omega^2}\frac{\pi R^3}{72}\,\omega_{sp}\mathcal{L}(\omega,\omega_{sp},\gamma)\nabla\left(\frac{x,y,z}{r^3}\right)\otimes\nabla'\left(\frac{x',y',z'}{r'^3}\right).$$

To express this dyadic in the form of Eq. (E.42), it is enough to note that in the limit of vanishing absorption $\lim_{\gamma\to 0}\mathcal{L}(\omega,\omega_{sp},\gamma) = -i\pi\delta(\omega-\omega_{sp})$, and that $\mathcal{L}(\omega_{sp},\omega_{sp},\gamma) = -2i/\gamma$, so that:

$$\mathbf{G}x,y,z(\boldsymbol{r},\boldsymbol{r}',\omega) = \boldsymbol{\mathcal{G}}_{x,y,z}(\boldsymbol{r},\boldsymbol{r}',\omega_{sp})\delta(\omega-\omega_{sp}), \tag{E.65}$$

$$\boldsymbol{\mathcal{G}}_{x,y,z}(\boldsymbol{r},\boldsymbol{r}',\omega_{sp}) = -\frac{\gamma\pi c^2}{2\omega_{sp}}\frac{\pi R^3\mathcal{L}(\omega_{sp},\omega_{sp},\gamma)}{72}\,\nabla\left(\frac{x,y,z}{r^3}\right)\otimes\nabla'\left(\frac{x',y',z'}{r'^3}\right). \tag{E.66}$$

Finally, noting that $\partial_i(x_j/r^3) = (r^2\delta_{i,j} - 3x_ix_j)/r^5$, the entries of the Dyadic Green's Function of the three degenerated dipolar cavity modes

(denoted by x_k) can be written as:

$$[\mathcal{G}_{x_k}]_{ij}(\boldsymbol{r},\boldsymbol{r}',\omega_{sp}) = i\pi\frac{c^2}{\omega_{sp}}\frac{\pi R^3}{72}\,\partial_i\left(\frac{x_k}{r^3}\right)\otimes\partial'_j\left(\frac{x'_k}{r'^3}\right)$$
$$= i\pi\frac{c^2}{\omega_{sp}}\frac{\pi R^3}{72}\,\frac{(r^2\delta_{i,k}-3x_ix_k)(r'^2\delta_{j,k}-3x'_jx'_k)}{r^5r'^5}. \tag{E.67}$$

E.4.1 Evaluation of QE-cavity coupling

By using Eq. (E.52), and the Dyadic Green's Function of a sphere from above, the coupling between a QE of dipole moment $\boldsymbol{\mu}$, when the dipole is placed on the $\hat{x}$ axis at a distance b_{c-QE} from the nanoparticle is given by:

$$g_x^{c-QE} = \frac{\omega_{QE}}{3}\,|\boldsymbol{\mu}\cdot\hat{x}|\sqrt{\frac{\pi}{2}\left(\frac{R}{b_{c-QE}}\right)^3\frac{1}{\hbar\omega_{sp}}\,\frac{1}{\epsilon_0\,b_{c-QE}^3}} \tag{E.68a}$$

$$g_y^{c-QE} = \frac{\omega_{QE}}{6}\,|\boldsymbol{\mu}\cdot\hat{y}|\sqrt{\frac{\pi}{2}\left(\frac{R}{b_{c-QE}}\right)^3\frac{1}{\hbar\omega_{sp}}\,\frac{1}{\epsilon_0\,b_{c-QE}^3}} \tag{E.68b}$$

$$g_z^{c-QE} = \frac{\omega_{QE}}{6}\,|\boldsymbol{\mu}\cdot\hat{z}|\sqrt{\frac{\pi}{2}\left(\frac{R}{b_{c-QE}}\right)^3\frac{1}{\hbar\omega_{sp}}\,\frac{1}{\epsilon_0\,b_{c-QE}^3}} \tag{E.68c}$$

which shows that for a dipole oriented along one of the coordinate axis, it only couples to one of the three degenerated dipolar modes of the cavity.

E

E.4.2 Evaluation of free electron - cavity coupling

In the same way, using Eq. (E.58) and the Dyadic Green's Function of a spherical nanoparticle we find that an electron that passes a distance $\boldsymbol{r}_{\perp,0} = b_{e-c}\hat{x}$ of the cavity has a coupling to the different dipolar modes given by:

$$g_{q,x}^{e-c} = \frac{ek_0}{mL}\sqrt{\frac{\hbar}{\epsilon_0\omega_{sp}}\,\frac{\pi R^3}{8}\,\frac{1}{|b_{e-c}|^4}\,I_1(qb_{e-c})I_1^*(qb_{e-c})}$$

$$g_{q,y}^{e-c} = 0$$

$$g_{q,z}^{e-c} = \frac{ek_0}{3mL}\sqrt{\frac{\hbar}{\epsilon_0\omega_{sp}}\frac{\pi R^3}{8}\frac{1}{|b_{e-c}|^4}\left[I_0(qb_{e-c}) - 2I_2(qb_{e-c})\right]\left[I_0(qb_{e-c}) - 2I_2(qb_{e-c})\right]^*}$$

where we have used the integrals defined in Eq. (E.60). From this, the interaction strength between the passing electron and the dipolar modes of the cavity is given by

$$g_{q,x}^{e-c} = \frac{e\hbar k_0}{3mL}|q|^2 K_1(|qb_{e-c}|)\sqrt{\frac{1}{\epsilon_0\hbar\omega_{sp}}\frac{\pi R^3}{2}} \tag{E.69a}$$

$$g_{q,y}^{e-c} = 0 \tag{E.69b}$$

$$g_{q,z}^{e-c} = \frac{e\hbar k_0}{3mL}|q|^2 K_0(|qb_{e-c}|)\sqrt{\frac{1}{\epsilon_0\hbar\omega_{sp}}\frac{\pi R^3}{2}} \tag{E.69c}$$

Having seen before the coupling strength between a free electron and a QE (Eq. (E.64)), we can extract the dipole moment that the free electron induces in the cavity:

$$|\boldsymbol{\mu}_c| = \frac{2\pi}{3}\sqrt{\pi R^3\,\hbar\omega_{sp}\epsilon_0} \tag{E.70}$$

We further note that the amplitudes of this dipole moment satisfy: $|\boldsymbol{\mu}_c\cdot\hat{x}| = |\boldsymbol{\mu}_c\cdot\hat{z}|$ and $\boldsymbol{\mu}_c\cdot\hat{y} = 0$. From here one can see that for the parameters used in the main text $|\boldsymbol{\mu}_c^{ind}| \approx 40|\boldsymbol{\mu}_{QE}|$. This expression agrees well with the one derived from comparing the polarizability of a sphere with that of a quantum 2-level system [324].

If one calculates the integrated loss probability of an electron interacting with a spherical metallic nanoparticle in the non-retarded limit [151], and applies the good resonator approximation to the Drude description, the loss probability is calculated as:

$$\begin{aligned} P_L &= \int \mathrm{d}\omega\,\Gamma_{NR}^{sph}(\omega) = \\ &= \int \mathrm{d}\omega\,\frac{e^2}{\pi^2\epsilon_0\hbar v_0^2}\left[\left(\frac{\omega}{v}\right)^2 K_0^2\left(\frac{\omega b}{v}\right) + \left(\frac{\omega}{v}\right)^2 K_1^2\left(\frac{\omega b}{v}\right)\right]\mathrm{Im}\left\{\alpha_{NR}(\omega)\right\}, \end{aligned} \tag{E.71}$$

E

which upon insertion of the polarizability

$$\alpha_{NR}(\omega) = R^3 \frac{\epsilon(\omega) - 1}{\epsilon(\omega) + 2} \approx i \frac{\omega_{sp} \pi R^3}{2} \delta(\omega - \omega_{sp}),$$

reads

$$P_L = \frac{e^2}{\pi^2 \epsilon_0 \hbar \omega_{sp}} \left(\frac{\omega_{sp}^4}{v^4} \right) \left[K_0^2 \left(\frac{\omega_{sp} b}{v_0} \right) + K_1^2 \left(\frac{\omega_{sp} b}{v_0} \right) \right] \frac{\pi R^3}{2}. \tag{E.72}$$

Looking at the electron-cavity couplings above, and taking the limit of small coupling, one can see that the first order of interaction between a free electron and a spherical nanoparticle, with the nanoparticle initially in its ground state yields a probability for the electron to loose one photon that looks like

$$P_L \approx \left| \frac{L}{v_0} g^{e-c}_{\omega_{sp}/v_0, x} \right|^2 + \left| \frac{L}{v_0} g^{e-c}_{\omega_{sp}/v_0, z} \right|^2 \tag{E.73}$$

$$= \frac{e^2}{9 \epsilon_0 \hbar \omega_{sp}} \left(\frac{\omega_{sp}}{v_0} \right)^4 \left[K_0^2 \left(\left| \frac{\omega_{sp} b_{e-c}}{v_0} \right| \right) + K_1^2 \left(\left| \frac{\omega_{sp} b_{e-c}}{v_0} \right| \right) \right] \frac{\pi R^3}{2}, \tag{E.74}$$

which agrees with the classical result to a factor of $(\pi/3)^2$. The agreement between our formalism and the classical result is not a coincidence, and besides the analytical similarity of the calculations involved in the derivation, what matters is that through mQED we have been able to define properly normalized bosonic modes, which means that once the electromagnetic Dyadic Green's Function of an arbitrary system is known, the interaction can be studied in the way that we have outlined.

E.4.3 Validity of the quasi-static approximation

In this section, we explore the validity of the quasi-static approximation we have used for the Hamiltonian parametrization. The two conditions that need to be fulfilled in order to safely neglect retardation effects are $k_0 b \ll 1$, and $k_0 R \ll 1$. In our case $R = 10$ nm, and $b = 11$ nm, and, at the frequency range of our study ($\hbar\omega_{sp} = 2$ eV), these inequalities

evaluate to $k_0 b \approx 0.1 > k_0 R$, which makes the quasi-static approximation valid. To further verify this conclusion, we borrow the analytical expression [151] describing the energy loss probability for a free electron in the vicinity of a spherical nanoparticle including retardation effects

$$\Gamma^{\mathrm{R}}_{\mathrm{sph}}(\omega) = \frac{e^2}{4\pi\epsilon_0}\frac{R}{\pi\hbar c^2}\frac{\pi}{k_0 R}\sum_{l=1}^{\infty}\sum_{m=-l}^{l} K_m^2\left(\frac{k_0 b}{\beta\gamma}\right)\left[C_{lm}^{M}\mathrm{Im}(t_l^M) + C_{lm}^{E}\mathrm{Im}(t_l^E)\right],$$

where the definition of the different terms can be found in Ref. [151]. In the limit of small radius, R, the magnetic scattering coefficients, t_l^M, vanish, and the the dominant contribution is given by the electric dipole mode, which acquires the form

$$t_1^E \overset{k_0 R\to 0}{\approx} \frac{2}{3}(k_0 R)^3\frac{\epsilon(\omega)-1}{\epsilon(\omega)+2},$$

where $\epsilon(\omega)$ is the nanoparticle permittivity. This way, the expression for the energy-loss probability in the quasi-static approximation can be obtained

$$\Gamma^{\mathrm{QS}}_{\mathrm{sph,dip}}(\omega) = \frac{e^2}{4\pi\epsilon_0}\frac{R}{\pi\hbar c^2}\left(\frac{k_0 R}{\beta}\right)^2\frac{4}{\beta^2} \times\left[K_1^2\left(\frac{k_0 b}{\beta}\right) + K_0^2\left(\frac{k_0 b}{\beta}\right)\right]\mathrm{Im}\left(\frac{\epsilon(\omega)-1}{\epsilon(\omega)+2}\right),$$

where $\beta = v/c$.

Employing a hydrodynamical Drude model for the metal permittivity [361], the key parameter measuring the impact of nonlocality is $\mathcal{B} = \sqrt{3/5}\, v_F$, which depends on the Fermi velocity of the metal. Using a 3D Fermi gas model, this can be expressed in terms of the electron density as $v_F = \hbar/m(3\pi^2 n)^{1/3}$. Thus, the characteristic length-scale for nonlocality (which sets the emergence of relevant electron-electron interactions in the metal response) can be estimated as [362]

$$l_F \sim \frac{\mathcal{B}}{\omega_p} = (3\pi^2)^{1/3}\frac{\hbar}{e}\sqrt{\frac{\epsilon_0}{m}}n^{-1/6}$$

where $\omega_p = \sqrt{ne^2/\epsilon_0 m}$ is the Drude plasma frequency. For noble metals,

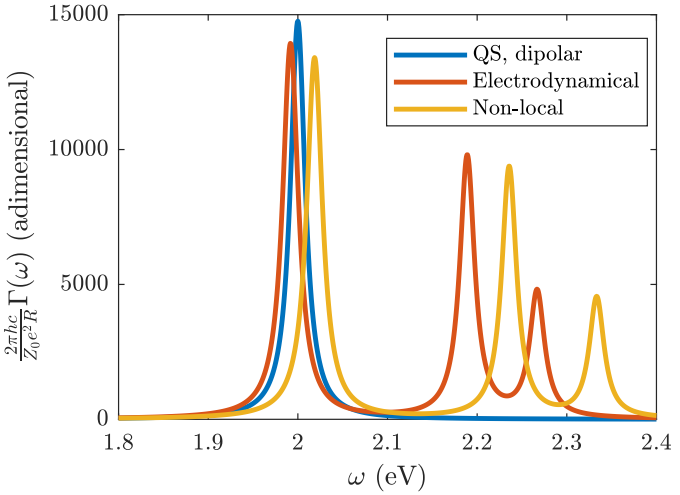

FIGURE E.2: Electron energy loss probability for an electron with $\beta = 0.1$ interacting with a sphere of radius $R = 10$ nm at an impact parameter $b = 11$ nm. The result is shown in the quasi-static limit, in the full electrodynamical picture, and with non-local corrections.

such as silver or gold, $\mathcal{B} \approx 0.01c$ and $l_F \approx 0.1$ nm, much smaller than R and b in our polaritonic model system. One of the first theoretical approaches accounting for non-local effects in the optical response of metallic nanospheres was proposed by Ruppin [363]. Employing a hidrodynamical Drude model, scattering coefficients, t_l^E and t_l^M, were obtained that included a non-local length-scale correction of the form

$$\delta_l^{NL} = l(l+1)\left(\epsilon(\omega)-1\right)\frac{j_l(x_{nl})}{x_{nl}j_l'(x_{nl})}, \text{ with } x_{nl} = \sqrt{\frac{\epsilon(\omega)}{1-\epsilon(\omega)}}\frac{\omega_p R}{\mathcal{B}}.$$

With the elements introduced above, we can compare electron energy loss probabilities for the nanophotonic cavity model in the main text, obtained under quasi-static, retarded, and non-local descriptions. We showcase the result up to the octupolar response in Fig. E.2. In agreement with our initial estimations, the electrodynamic, fully-retarded $\Gamma(\omega)$ does not deviate significantly from the quasi-static prediction. The only fingerprint of retardation is a few meV redshift in the dipolar mode (2 eV) of the cavity, which validates neglecting retardation effects in

the calculation of the electron-target coupling strengths. Similarly, the comparison with the non-local-corrected model, reveals that nonlocality does not have a significant impact either at frequencies in the vicinity of the dipolar resonance. It yields a blueshift of the dipolar mode, comparable in magnitude, to the redshift induced by retardation. Thus, in the ~ 2 eV range, both effects tend to counterbalance each other. Note however, that the deviation between retarded and nonlocal predictions become larger at higher frequencies, at the quadrupolar and octupolar cavity modes, which are not considered in the target system in the main text.

E

Appendix F

Free electron probing of the hydrogen atom wavefunctions

In this appendix, we particularize Eq. (4.5) for the case of the interaction between a free electron and the different transitions present in a hydrogen atom. The expression of the vacuum-mediated coupling between an arbitrary electronic transition and a free electron is given by

$$g_{ij,q} = -ik_0 \frac{e^2 \hbar \mu_0}{2m^2 L} \iint d\boldsymbol{r}\, dz'\, \boldsymbol{d}_{ij}(\boldsymbol{r}) \cdot \mathrm{Re}\left\{ \overline{\overline{G}}_0(\boldsymbol{r}, [\mathbf{r}_\perp, z'], \Omega) \right\} \cdot \hat{z} e^{iqz}. \tag{F.1}$$

We wish to particularize these expressions for transitions between the hydrogen's ground state and some excited state labelled by the usual quantum numbers: n, l and m. Labeling the eigenfunctions of the hydrogen atomas $\phi_{n,l,m}$, then the transition dipole densities of interest will be given by

$$\boldsymbol{d}_{ij}(\boldsymbol{r}) \rightarrow \boldsymbol{d}_{n,l,m}(\boldsymbol{r}) = \phi_{n,l,m} \nabla \phi^*_{1,0,0}.$$

Furthermore, from the derivation of the matter-matter interaction hamiltonian, the Dyadic Green's Function is to be evaluated at photon energy given by the energy difference between initial and final electronic state given by: $\Omega = \omega_n \approx (1 - 1/n^2) 13.6$ eV, while for energy conservation arguments, the momentum exchange of the electron within the non-recoil approximation is given by $q = \omega_n / v_0$ [P4, P5]. Moreover, note that hydrogenic wavefunctions are localized in the order of the Bohr radius, a_0, which is around 50 pm, while the lengthscales associated with photons

produced from these transitions are of the order of 100 nm. This implies that we can treat the Dyadic Green's Function within the quasi-static limit,where the dyadic is purely real, and therefore we can rewrite the coupling above in terms of the field produced by a volumetric charge distribution as [12]

$$g_{n,l,m} = -k_0 \frac{e^2\hbar}{2m^2 L\alpha\omega_n} \int dz\, \hat{z} \cdot \mathbf{E}_{n,l,m}([\mathbf{r}_\perp, z], \omega_n) e^{i\omega_n z/v_0}, \tag{F.2}$$

$$\mathbf{E}_{n,l,m}(\boldsymbol{r}', \omega) = i\omega\mu_0 \int d\boldsymbol{r}\, \overline{\overline{G}}_0(\boldsymbol{r}, \boldsymbol{r}', \omega) \cdot \alpha \boldsymbol{d}_{n,l,m}(\boldsymbol{r}), \tag{F.3}$$

where we have introduced α plainly as a factor that gives $\alpha \boldsymbol{d}_{ij}(\boldsymbol{r})$ units of current density. Then, to numerically calculate these couplings as a function of $\mathbf{r}_\perp$, one can numerically calculate $\mathbf{E}_{n,l,m}(\boldsymbol{r}', \omega)$ by using the analytical expression of the hydrogen atom's wavefunctions and a solver for Maxwell's equations (we for instance use COMSOL). Once the fields $\mathbf{E}_{n,l,m}$ are known, the integral in Eq. (F.2) can be numerically performed. In Fig. F.1 we show the normalized coupling strength in arbitrary units between the aforementioned transitions and the free electron travelling at $v_0 = 0.5c$. The extent of all the panels is $30a_0$ except for $l = 0$, in which the extent has been reduced to $10a_0$. Note that to obtain these we have implicitly assumed that the lateral extent of the incoming electron beam is vanishingly small compared to the features of the electronic wavefunctions involved, which is not realistic. However, this calculation allows to illustrate that, thanks to the mQED-based formulation of our model, it is rather simple to exploit the very powerfull numerical machinery developed for classical fields to parametrize the quantum mechanical couplings in more complicated situations than the ones treated in this thesis. For instance these simulations could be fed with the HOMO, LUMO eigenfunctions of chromophores obtained from DFT calculations to then calculate any magnitudes of interest, similarly to Ref. [364].

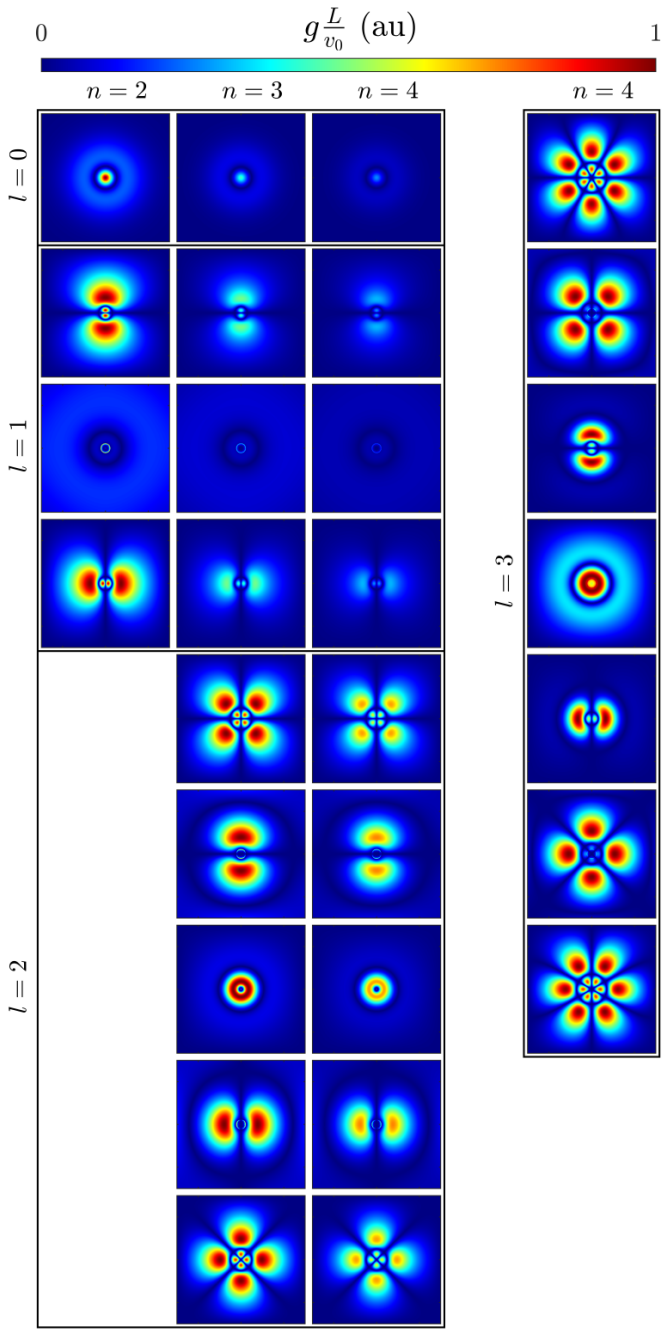

FIGURE F.1: Integrated coupling strength (dimensionless) in arbitrary scale between a transition $(1, 0, 0) \rightarrow (n, l, m)$ in the hydrogen atom and a free electron for all possible values of the quantum numbers up to $n = 4$.

F

Appendix G

Magnus expansion of electron-QE interaction

In this Appendix, we test the validity of Equation (4.29), which presents the calculation of the scattering matrix using the Magnus expansion [326] up to first order in the integrated interaction strength. Here, we compute it up to third order for a single QE in free space, and show that this approximation is valid for realistic values of the impact parameter, b, and the resonant electron wavevector, $q = \omega_{QE}/v_0$. We first determine the interaction Hamiltonian in the interaction picture in Sec. G.1, and proceed to obtain general expressions for the coefficients of the different orders of the Magnus expansion in Sec. G.2, which we finally evaluate them for the case of QE-free electron interaction through free space in Sec. G.3.

G.1 Interaction Hamiltonian in the interaction Picture

To obtain the different terms of the Magnus expansion, we first obtain the interaction Hamiltonian in the interaction picture. The interaction Hamiltonian for the free-electron-QE interaction is given by

$$\hat{H}_I = \hbar \sum_q \left(g_q \hat{\sigma} \hat{b}_q^\dagger + g_q^* \hat{\sigma}^\dagger \hat{b}_q \right). \tag{G.1}$$

In the interaction picture, it is given by $\hat{H}_{I,int}(t) = e^{i\frac{\hat{H}_0}{\hbar}t} \hat{H}_I e^{-i\frac{\hat{H}_0}{\hbar}t}$, with $\hat{H}_0 = \sum_k E_k \hat{c}_k^\dagger \hat{c}_k + E_e \sigma^\dagger \sigma + E_g \sigma \sigma^\dagger$, which by use of completitude

relations may be written as

$$\hat{H}_{I,int}(t) = \hbar \sum_{q,k'} \left(g_q \left|k'+q\right\rangle\!\left\langle k'\right| \hat{\sigma} e^{i\frac{(E_{k'+q}+E_g-E_{k'}-Ee)}{\hbar}t} + \text{h.c.} \right). \quad \text{(G.2)}$$

From the non-recoil approximation in the free electron dispersion one has that

$$E_{k+q} = \frac{\hbar^2(k+q)^2}{2m} \approx \frac{(\hbar k)^2 + \hbar^2 2qk}{2m} \approx E_k + \hbar v_0 q, \quad \text{(G.3)}$$

where we have assumed that $k \approx k_0 = mv_0/\hbar$. With this, and assuming that $E_e = \hbar\omega_{QE}$ and $E_g = 0$, the interaction Hamiltonian in the interaction picture reads

$$\hat{H}_{I,int}(t) = \hbar \sum_{q} \left(g_q \hat{b}_q^\dagger \hat{\sigma} e^{i(v_0 q - \omega_{QE})t} + g_q^* \hat{b}_q \hat{\sigma}^\dagger e^{i(-v_0 q + \omega_{QE})t} \right). \quad \text{(G.4)}$$

By considering spontaneous emission in the small excitation limit, one can describe the decay dynamics of the QE as predicted by a master equation by promoting the bare Hamiltonian to a non-hermitian one by including a imaginary part in the bare eigenfrequencies [41, 42]. Here, we take $\omega_{QE} \to \omega_{QE} - i\gamma/2$. It can then be shown that the interaction Hamiltonian under this description becomes

$$\hat{H}_{I,int}(t) = \hbar \sum_{q} \left(g_q \hat{b}_q^\dagger \hat{\sigma} e^{-i\left(\frac{\omega_{QE}}{v_0} - i\frac{\gamma}{2v_0} - q\right)v_0 t} + g_q^* \hat{b}_q \hat{\sigma}^\dagger e^{i\left(\frac{\omega_{QE}}{v_0} + i\frac{\gamma}{2v_0} - q\right)v_0 t} \right). \quad \text{(G.5)}$$

We now write the sum as an integral by dividing and multiplying by $\Delta q = 2\pi/L$, the momentum spacing that comes from the fictitious box used to quantize the free electron wavefunction. For compactness, we write $q = q_0 + \alpha$ and rename $Q \equiv \gamma/2v_0$. Thus, we have

$$\hat{H}_{I,int}(t) = \hbar \frac{L}{2\pi} \int \mathrm{d}\alpha \, \hat{O}(\alpha) \, \hat{b}_\alpha \, e^{i(-\alpha + iQ)v_0 t} \quad \text{(G.6)}$$

where we have defined $\hat{O}(\alpha) \equiv \left(g_{q_0-\alpha} \hat{b}_{q_0}^\dagger \hat{\sigma} + g_{q_0+\alpha}^* \hat{b}_{q_0} \hat{\sigma}^\dagger \right)$.

G

G.2 Scattering matrix and Magnus expansion

We now proceed to calculate the first three terms of the scattering matrix as given by the Magnus expansion. Considering a first order differential equation $d\left|\psi(t)\right\rangle/dt = \hat{U}(t)\left|\psi(t)\right\rangle$, the solution for the initial value problem is in general given by the time ordered product

$$\left|\psi(t)\right\rangle = \mathcal{T}\exp\left[\int_{-t_0}^{t} dt'\,\hat{U}(t')\right]\left|\psi(t_0)\right\rangle \equiv \hat{S}(t,t_0)\left|\psi(t_0)\right\rangle, \tag{G.7}$$

where we assume that the interaction starts at $-t_0$, and we will later take the limit $t_0 = t \to \infty$. By using the Magnus expansion, one may construct the propagator, $\hat{S}$, as the true exponential of a matrix as

$$\left|\psi(t)\right\rangle = e^{\hat{\Omega}(t,-t_0)}\left|\psi(t_0)\right\rangle,$$

where $\hat{\Omega}$ accepts a series decomposition $\hat{\Omega}(t) = \sum_n \hat{\Omega}_n(t)$, such that the first terms in the expansion read [326]

$$\hat{\Omega}_1(t,-t_0) = \int_{-t_0}^{t} \hat{U}(t_1)dt_1, \tag{G.8}$$

$$\hat{\Omega}_2(t,-t_0) = \frac{1}{2}\int_{-t_0}^{t} \mathrm{d}t_1 \int_{-t_0}^{t_1} \mathrm{d}t_2 \left[\hat{U}(t_1),\hat{U}(t_2)\right], \tag{G.9}$$

$$\hat{\Omega}_3(t,-t_0) = \frac{1}{6}\int_{-t_0}^{t} \mathrm{d}t_1 \int_{-t_0}^{t_1} \mathrm{d}t_2 \int_{-t_0}^{t_2} \mathrm{d}t_3\, \hat{L}(t_1,t_2,t_3), \tag{G.10}$$

$$\hat{L}(t_1,t_2,t_3) = \left[\hat{U}(t_1),\left[\hat{U}(t_2),\hat{U}(t_3)\right]\right] + \left[\left[\hat{U}(t_1),\hat{U}(t_2)\right],\hat{U}(t_3)\right].$$

Note that this expansion is perturbative in nature, and therefore its validity rests on whether the magnitude of subsequent interaction orders vanishes. For the Schrödinger equation, the $\hat{U}$ operator corresponds to the interaction Hamiltonian in the interaction picture as $\hat{U}(t) \equiv -i\hat{H}_{I,\mathrm{int}}(t)/\hbar$, with $\hat{H}_{I,int}(\tau)$ given in the previous section. Therefore, for our case the $\hat{U}$ operator reads:

$$\hat{U}(t) \equiv -\frac{iL}{2\pi}\int \mathrm{d}\alpha\, \hat{O}(\alpha)\,\hat{b}_\alpha\, e^{i(-\alpha+iQ)v_0 t} \tag{G.11}$$

In what follows, we calculate the first few terms of this expansion step by step in the limit $t_0 = t \to \infty$.

G.2.1 First term in the expansion: Ω_1

By direct integration from Eq. (G.9), it follows:

$$\lim_{t\to\infty} \hat{\Omega}_1(t,-t) = -\frac{iL}{2\pi v_0} \lim_{z\to\infty} \int \mathrm{d}\alpha\, \hat{O}(\alpha)\, \hat{b}_\alpha \int_{-z}^{z} \mathrm{d}z_1\, e^{i(-\alpha+iQ)z_1} = \tag{G.12}$$

$$= -\frac{iL}{v_0} \int \mathrm{d}\alpha\, \hat{O}(\alpha)\, \hat{b}_\alpha \delta(\alpha) = \tag{G.13}$$

$$= -i\left(\beta_{q_0} \hat{b}^\dagger_{q_0} \hat{\sigma} + \beta^*_{q_0} \hat{b}_{q_0} \hat{\sigma}^\dagger\right), \tag{G.14}$$

where we have used the limit $\lim_{x\to\infty} \sin(\alpha x)/\alpha = \pi\delta(\alpha)$, and defined $\beta_q \equiv L g_q / v_0$. The expression for this term is the same as given in the multiple references mentioned throuout this thesis. Note that in order to arrive at this expression, one has to assume that $\hat{O}(\alpha)$ (and therefore g_q) is an analytic function.

G.2.2 Second term in the expansion: Ω_2

We first we calculate the commutators in Eq. (G.9) needed to evaluate the second order contribution. Using the expression of $\hat{U}(t)$, one has

$$\left[\hat{U}(t_1), \hat{U}(t_2)\right] = \left(-\frac{iL}{2\pi}\right)^2 \times \iint \mathrm{d}\alpha\, \mathrm{d}\alpha' \left[\hat{O}(\alpha), \hat{O}(\alpha')\right] \hat{b}_{\alpha+\alpha'} e^{i(-\alpha+iQ)v_0 t_1} e^{i(-\alpha'+iQ)v_0 t_2}. \tag{G.15}$$

The commutator in the expression above is given by

$$\left[\hat{O}(\alpha), \hat{O}(\alpha')\right] = \left(g^*_{q_0+\alpha} g_{q_0-\alpha'} - g_{q_0-\alpha} g^*_{q_0+\alpha'}\right) \hat{\sigma}_z \equiv \tilde{\Gamma}(\alpha,\alpha')\hat{\sigma}_z,$$

where we have defined $\tilde{\Gamma}(\alpha,\alpha') \equiv g^*_{q_0+\alpha} g_{q_0-\alpha'} - g_{q_0-\alpha} g^*_{q_0+\alpha'}$ for compactness. We further define the dimentionless version of this magnitude as $\Gamma(\alpha,\alpha') \equiv (L/v_0)^2 \tilde{\Gamma}(\alpha,\alpha') = (\beta^*_{q_0+\alpha}\beta_{q_0-\alpha'} - \beta_{q_0-\alpha}\beta^*_{q_0+\alpha'})$, so the

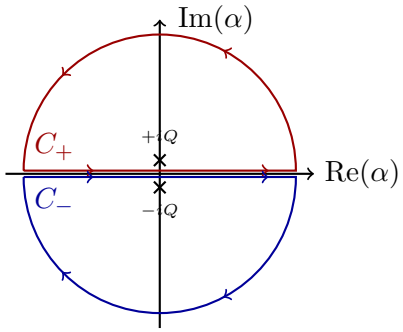

FIGURE G.1: Integration contours used in this calculation, together with the location of the relevant poles.

commutator above reads

$$\left[\hat{U}(t_1),\hat{U}(t_2)\right] = -\left(\frac{L}{2\pi}\right)^2 \hat{\sigma}_z \iint \mathrm{d}\alpha\,\mathrm{d}\alpha'\;\tilde{\Gamma}(\alpha,\alpha')\,\hat{b}_{\alpha+\alpha'}\,e^{i(-\alpha+iQ)v_0 t_1}e^{i(-\alpha'+iQ)v_0 t_2} \tag{G.16}$$

We now plug this commutator into Eq. (G.9), so that the second-order term in the Magnus expansion reads

$$\hat{\Omega}_2(t,-t_0) = -\frac{\hat{\sigma}_z}{8\pi^2}\iint \mathrm{d}\alpha\,\mathrm{d}\alpha'\,\Gamma(\alpha,\alpha')\,\hat{b}_{\alpha+\alpha'}\times \int_{-z_0}^{z}\mathrm{d}z_1\int_{-z_0}^{z_1}\mathrm{d}z_2\;e^{i(-\alpha+iQ)z_1}e^{i(-\alpha'+iQ)z_2}.$$

Focusing on the integrals over z, one has

$$\int_{-z_0}^{z}\mathrm{d}z_1\int_{-z_0}^{z_1}\mathrm{d}z_2\,e^{i(-\alpha+iQ)z_1}e^{i(-\alpha'+iQ)z_2} \overset{\lim_{z\to\infty}}{=} 2\pi\frac{\left[\delta\left(-\alpha-\alpha'+2iQ\right)-e^{-i(-\alpha'+iQ)z}\delta\left(-\alpha+iQ\right)\right]}{i\left(-\alpha'+iQ\right)},$$

where we have used that in the limit of $z = v_0 t \to \infty$, sinc functions can be recast as delta functions. Thus, the second contribution of the Magnus expansion reads

$$\hat{\Omega}_2 = -\frac{\hat{\sigma}_z}{4\pi}\left\{\iint \mathrm{d}\alpha\,\mathrm{d}\alpha'\;\frac{\Gamma(\alpha,\alpha')\,\hat{b}_{\alpha+\alpha'}}{i\left(-\alpha'+iQ\right)}\delta\left(-\alpha-\alpha'+2iQ\right)+\right.$$

$$- \iint \mathrm{d}\alpha\, \mathrm{d}\alpha'\, \Gamma(\alpha,\alpha')\, \hat{b}_{\alpha+\alpha'} \frac{e^{-i(-\alpha'+iQ)z}}{i\,(-\alpha'+iQ)} \delta\,(-\alpha+iQ) \Bigg\}.$$

To integrate the second line, we integrate over C_+ in Fig. G.1, which contains a simple pole at $\alpha' = iQ$, and apply the residue theorem. Then, integrate over α. For the first line, we first integrate over α. Thus, we obtain

$$\hat{\Omega}_2 = -\frac{\hat{\sigma}_z}{4\pi} \left\{ i\hat{b}_{2iQ} \int \mathrm{d}\alpha' \, \frac{\Gamma(-\alpha'+2iQ,\alpha')}{(\alpha'-iQ)} + 2\pi\Gamma(iQ,iQ)\hat{b}_{2iQ} \right\}.$$

Taking the limit of $Q \to 0$, on the one hand we have that $\Gamma(iQ,iQ) \to \Gamma(0,0) = 0$ and secondly, we invoke the Sokhotski–Plemelj theorem, which on the real line reads

$$\lim_{\epsilon\to 0^+} \frac{1}{x \pm i\epsilon} = \mp i\pi\delta(x) + \mathcal{P}\left(\frac{1}{x}\right). \tag{G.17}$$

Then the second contribution reads

$$\begin{aligned}
\hat{\Omega}_2 =& -i\frac{\hat{\sigma}_z}{4\pi}\mathcal{P}\int \mathrm{d}\alpha' \, \frac{\Gamma(-\alpha',\alpha')}{\alpha'} = \\
=& \frac{-i}{4\pi}\hat{\sigma}_z\mathcal{P}\int \mathrm{d}\alpha \, \frac{|\beta_{q_0-\alpha}|^2 - |\beta_{q_0+\alpha}|^2}{\alpha} = \\
=& \frac{i}{2\pi}\hat{\sigma}_z\,\mathcal{P}\left(\int_{-\infty}^{\infty} \mathrm{d}\alpha \, \frac{|\beta_{q_0+\alpha}|^2}{\alpha}\right),
\end{aligned} \tag{G.18}$$

where we remind that the definition $\Gamma(\alpha,\alpha') = \beta^*_{q_0+\alpha}\beta_{q_0-\alpha'} - \beta_{q_0-\alpha}\beta^*_{q_0+\alpha'}$. Finally, to write it in a more compact form, the second order contribution to the Magnus expansion reads

$$\hat{\Omega}_2 = -i\gamma_{q_0}\hat{\sigma}_z, \tag{G.19}$$

$$\gamma_{q_0} = -\frac{1}{2\pi}\,\mathcal{P}\left(\int_{-\infty}^{\infty} \mathrm{d}\alpha \, \frac{|\beta_{q_0+\alpha}|^2}{\alpha}\right), \tag{G.20}$$

which can be numerically computed upon knowing g_q.

G.2.3 Third term in the expansion: Ω_3

The third order contribution to the Magnus expansion has the form

$$\hat{\Omega}_3(t,-t_0) = \frac{1}{6}\int_{-t_0}^{t} \mathrm{d}t_1 \int_{-t_0}^{t_1} \mathrm{d}t_2 \int_{-t_0}^{t_2} \mathrm{d}t_3\, \hat{L}(t_1,t_2,t_3),$$
$$\hat{L}(t_1,t_2,t_3) = \left[\hat{U}(t_1),\left[\hat{U}(t_2),\hat{U}(t_3)\right]\right] + \left[\left[\hat{U}(t_1),\hat{U}(t_2)\right],\hat{U}(t_3)\right].$$

The commutators needed to evaluate the expansion are given by

$$\left[\left[\hat{U}(t_1),\hat{U}(t_2)\right],\hat{U}(t_3)\right] =$$
$$= i\left(\frac{L}{2\pi}\right)^3 \iiint \mathrm{d}\alpha\,\mathrm{d}\alpha'\,\mathrm{d}\alpha''\left[\left[\hat{O}(\alpha),\hat{O}(\alpha')\right],\hat{O}(\alpha'')\right]\hat{b}_{\alpha+\alpha'+\alpha''}\times$$
$$e^{i(-\alpha+iQ)v_0t_1}e^{i(-\alpha'+iQ)v_0t_2}e^{i(-\alpha''+iQ)v_0t_3},$$
$$\left[\hat{U}(t_1),\left[\hat{U}(t_2),\hat{U}(t_3)\right]\right] =$$
$$= i\left(\frac{L}{2\pi}\right)^3 \iiint \mathrm{d}\alpha\,\mathrm{d}\alpha'\,\mathrm{d}\alpha''\left[\hat{O}(\alpha),\left[\hat{O}(\alpha'),\hat{O}(\alpha'')\right]\right]\hat{b}_{\alpha+\alpha'+\alpha''}\times$$
$$e^{i(-\alpha+iQ)v_0t_1}e^{i(-\alpha'+iQ)v_0t_2}e^{i(-\alpha''+iQ)v_0t_3}.$$

Making use of the previously calculated commutator $\left[\hat{O}(\alpha),\hat{O}(\alpha')\right] = \tilde{\Gamma}(\alpha,\alpha')\hat{\sigma}_z$, we have

$$\left[\left[\hat{O}(\alpha),\hat{O}(\alpha')\right],\hat{O}(\alpha'')\right] = \tilde{\Gamma}(\alpha,\alpha')\left[\hat{\sigma}_z, g_{q_0-\alpha''}\hat{b}^\dagger_{q_0}\hat{\sigma} + g^*_{q_0+\alpha''}\hat{b}_{q_0}\hat{\sigma}^\dagger\right] =$$
$$= 2\,\tilde{\Gamma}(\alpha,\alpha')\left[g^*_{q_0+\alpha''}\hat{b}_{q_0}\hat{\sigma}^\dagger - g_{q_0-\alpha''}\hat{b}^\dagger_{q_0}\hat{\sigma}\right],$$
$$\left[\hat{O}(\alpha),\left[\hat{O}(\alpha'),\hat{O}(\alpha'')\right]\right] = \tilde{\Gamma}(\alpha',\alpha'')\left[g_{q_0-\alpha}\hat{b}^\dagger_{q_0}\hat{\sigma} + g^*_{q_0+\alpha}\hat{b}_{q_0}\hat{\sigma}^\dagger,\hat{\sigma}_z\right] =$$
$$= 2\,\tilde{\Gamma}(\alpha',\alpha'')\left[g_{q_0-\alpha}\hat{b}^\dagger_{q_0}\hat{\sigma} - g^*_{q_0+\alpha}\hat{b}_{q_0}\hat{\sigma}^\dagger\right],$$

where again we have used $\tilde{\Gamma}(\alpha,\alpha') \equiv g^*_{q_0+\alpha}g_{q_0-\alpha'} - g_{q_0-\alpha}g^*_{q_0+\alpha'}$. By defining the quantities

$$A(\alpha,\alpha',\alpha'') \equiv \tilde{\Gamma}(\alpha,\alpha')g^*_{q_0+\alpha''} - \tilde{\Gamma}(\alpha',\alpha'')g^*_{q_0+\alpha},$$
$$B(\alpha,\alpha',\alpha'') \equiv \tilde{\Gamma}(\alpha',\alpha'')g_{q_0-\alpha} - \tilde{\Gamma}(\alpha,\alpha')g_{q_0-\alpha''},$$

we compactly write the sum of these commutators as

$$\left[\hat{O}(\alpha),\left[\hat{O}(\alpha'),\hat{O}(\alpha'')\right]\right]+\left[\left[\hat{O}(\alpha),\hat{O}(\alpha')\right],\hat{O}(\alpha'')\right]=$$
$$2\left[A(\alpha,\alpha',\alpha'')\hat{b}_{q_0}\hat{\sigma}^{\dagger}+B(\alpha,\alpha',\alpha'')\hat{b}^{\dagger}_{q_0}\hat{\sigma}\right]\equiv\hat{F}(\alpha,\alpha',\alpha''),$$

where we again introduce $\hat{F}(\alpha,\alpha',\alpha'')$ as shorthand notation. Thus, the neccesary commutator is

$$[A(t_1),[A(t_2),A(t_3)]]+[[A(t_1),A(t_2)],A(t_3)]=$$
$$=i\left(\frac{L}{2\pi}\right)^3\iiint \mathrm{d}\alpha\,\mathrm{d}\alpha'\,\mathrm{d}\alpha''\hat{F}(\alpha,\alpha',\alpha'')\hat{b}_{\alpha+\alpha'+\alpha''}\times$$
$$e^{i(-\alpha+iQ)v_0t_1}e^{i(-\alpha'+iQ)v_0t_2}e^{i(-\alpha''+iQ)v_0t_3}.$$

From this, we now go back to the third order contribution of the Magnus expansion, which reads

$$\hat{\Omega}_3(t,-t_0)=\frac{i}{6}\left(\frac{L}{2\pi v_0}\right)^3\iiint \mathrm{d}\alpha\,\mathrm{d}\alpha'\,\mathrm{d}\alpha''\,\hat{F}(\alpha,\alpha',\alpha'')\hat{b}_{\alpha+\alpha'+\alpha''}\,I,$$

where we have wrapped inside of I all the integrals over time. Changing the variable of integration this integral reads

$$I=\int_{-z_0}^{z}\mathrm{d}z_1\,e^{i(-\alpha+iQ)z_1}\int_{-z_0}^{z_1}\mathrm{d}z_2 e^{i(-\alpha'+iQ)z_2}\int_{-z_0}^{z_2}\mathrm{d}z_3\,e^{i(-\alpha''+iQ)z_3}=$$
$$=\int_{-z_0}^{z}\mathrm{d}z_1\,e^{i(-\alpha+iQ)z_1}\int_{-z_0}^{z_1}\mathrm{d}z_2\left[\frac{e^{i(-\alpha''-\alpha'+2iQ)z_2}}{i\left(-\alpha''+iQ\right)}\right.$$
$$\left.-\frac{e^{-i(-\alpha''+iQ)z_0}e^{i(-\alpha'+iQ)z_2}}{i\left(-\alpha''+iQ\right)}\right].$$

Integrating and expanding the products:

$$I=\int_{-z_0}^{z}\mathrm{d}z_1\left\{e^{i(-\alpha-\alpha'-\alpha''+3iQ)z_1}\left[\frac{1}{i\left(-\alpha''-\alpha'+2iQ\right)i\left(-\alpha''+iQ\right)}\right]+\right.$$
$$-e^{i(-\alpha-\alpha'+2iQ)z_1}\left[\frac{e^{-i(-\alpha''+iQ)z_0}}{i\left(-\alpha'+iQ\right)i\left(-\alpha''+iQ\right)}\right]+$$
$$-e^{i(-\alpha+iQ)z_1}\left[\frac{e^{-i(-\alpha''-\alpha'+2iQ)z_0}}{i\left(-\alpha''-\alpha'+2iQ\right)i\left(-\alpha''+iQ\right)}\right]+$$

G

$$+e^{i(-\alpha+iQ)z_1}\left[\frac{e^{-i(-\alpha'-\alpha''+2iQ)z_0}}{i\,(-\alpha'+iQ)\,i\,(-\alpha''+iQ)}\right]\Bigg\}$$

Performing the last integral, and afte some manipulations and taking $z_0 = z$, one has

$$\begin{aligned}
I = 2\Bigg\{ & \frac{\sin\left[(-\alpha-\alpha'-\alpha''+3iQ)\,z\right]}{(-\alpha-\alpha'-\alpha''+3iQ)}\left[\frac{1}{i\,(-\alpha''-\alpha'+2iQ)\,i\,(-\alpha''+iQ)}\right]+ \\
& -\frac{\sin\left[(-\alpha-\alpha'+2iQ)\,z\right]}{(-\alpha-\alpha'+2iQ)}\left[\frac{e^{-i(-\alpha''+iQ)z}}{i\,(-\alpha'+iQ)\,i\,(-\alpha''+iQ)}\right]+ \\
& -\frac{\sin\left[(-\alpha+iQ)\,z\right]}{(-\alpha+iQ)}\left[\frac{e^{-i(-\alpha''-\alpha'+2iQ)z}}{i\,(-\alpha''-\alpha'+2iQ)\,i\,(-\alpha''+iQ)}\right]+ \\
& +\frac{\sin\left[(-\alpha+iQ)\,z\right]}{(-\alpha+iQ)}\left[\frac{e^{-i(-\alpha'-\alpha''+2iQ)z}}{i\,(-\alpha'+iQ)\,i\,(-\alpha''+iQ)}\right]\Bigg\}= \\
= 2\pi\Bigg\{ & -\delta\left(-\alpha-\alpha'-\alpha''+3iQ\right)\left[\frac{1}{(\alpha''+\alpha'-2iQ)\,(\alpha''-iQ)}\right]+ \\
& +\delta\left(-\alpha-\alpha'+2iQ\right)\left[\frac{e^{i(\alpha''-iQ)z}}{(\alpha'-iQ)\,(\alpha''-iQ)}\right]+ \\
& +\delta\left(-\alpha+iQ\right)\left[+\frac{e^{i(\alpha''+\alpha'-2iQ)z}}{(\alpha''+\alpha'-2iQ)\,(\alpha''-iQ)}\right]+ \\
& -\delta\left(-\alpha+iQ\right)\left[\frac{e^{i(\alpha'+\alpha''-2iQ)z}}{(\alpha'-iQ)\,(\alpha''-iQ)}\right]\Bigg\},
\end{aligned}$$

which we write by using the limit of the sinc function as a delta. Then, by direct use of the residue theorem this may be written as

$$\begin{aligned}
I = 2\pi\Bigg\{ & -\delta\left(-\alpha-\alpha'-\alpha''+3iQ\right)\left[\frac{1}{(\alpha''+\alpha'-2iQ)\,(\alpha''-iQ)}\right]+ \\
& +2\pi i\,\delta\left(-\alpha-\alpha'+2iQ\right)\,\delta(\alpha''-iQ)\,\frac{1}{(\alpha'-iQ)}+ \\
& -\delta\left(-\alpha+iQ\right)\left[(2\pi i)^2\delta(\alpha'-iQ)\delta(\alpha''-iQ)\right]+ \\
& +\delta\left(-\alpha+iQ\right)\left[\frac{e^{i(\alpha''+\alpha'-2iQ)z}}{(\alpha''+\alpha'-2iQ)\,(\alpha''-iQ)}\right]\Bigg\}.
\end{aligned}$$

Putting these terms back into the integral for $\hat{\Omega}_3$, and performing the complete integration, it reads

$$\begin{aligned}\hat{\Omega}_3 =& \frac{i\hat{b}_{3iQ}}{6(2\pi)^2}\left(\frac{L}{v_0}\right)^3\Bigg\{-\iint \mathrm{d}\alpha'''\,\mathrm{d}\alpha''\,\frac{\hat{F}(3iQ-\alpha''',\alpha'''-\alpha'',\alpha'')}{(\alpha'''-2iQ)\,(\alpha''-iQ)}+\\ &+2\pi i\int \mathrm{d}\alpha'\,\frac{\hat{F}(2iQ-\alpha',\alpha',iQ)}{(\alpha'-iQ)}+2\pi i\int \mathrm{d}\alpha''\,\frac{\hat{F}(iQ,2iQ-\alpha'',\alpha'')}{(\alpha''-iQ)}\\ &-(2\pi i)^2\hat{F}(iQ,iQ,iQ)\Bigg\}\end{aligned}$$

Now we repeatedly apply the Sokhotski–Plemelj theorem over the real line, given in Eq. (G.17), by taking the limit of $Q\to 0$. Thus, we find

$$\begin{aligned}\hat{\Omega}_3 = \frac{i}{6(2\pi)^2}\left(\frac{L}{v_0}\right)^3\Bigg\{&-\mathcal{P}\int \mathrm{d}\alpha''\,\mathcal{P}\int \mathrm{d}\alpha''\,\frac{\hat{F}(-\alpha''',\alpha'''-\alpha'',\alpha'')}{\alpha''\alpha'''}\\ &+i\pi\mathcal{P}\int \mathrm{d}\alpha'\,\frac{\hat{F}(-\alpha',\alpha',0)}{\alpha'}\\ &+i\pi\mathcal{P}\int \mathrm{d}\alpha''\,\frac{\hat{F}(0,-\alpha'',\alpha'')}{\alpha''}\\ &-(i\pi)^2\hat{F}(0,0,0)\Bigg\}.\end{aligned}$$

From the definition of $\hat{F}$, one may directly see that $\hat{F}(0,0,0)=\hat{0}$, and that the two single principal value integrals cancel each other. Thus, there is only one term left in the third order contribution, given by:

$$\hat{\Omega}_3 = -\frac{i}{6(2\pi)^2}\left(\frac{L}{v_0}\right)^3\mathcal{P}\int \mathrm{d}\alpha''\,\mathcal{P}\int \mathrm{d}\alpha''\,\frac{\hat{F}(-\alpha''',\alpha'''-\alpha'',\alpha'')}{\alpha''\alpha'''} \tag{G.21}$$

By inserting the particular form of the operator $\hat{F}$, we find

$$\hat{\Omega}_3 = -\frac{2i}{6(2\pi)^2}\left(\frac{L}{v_0}\right)^3\left[\mathcal{A}\,\hat{b}_{q_0}\hat{\sigma}^\dagger+\mathcal{B}\,\hat{b}^\dagger_{q_0}\hat{\sigma}\right] \tag{G.22}$$

$$\mathcal{A} = \mathcal{P}\int \mathrm{d}\alpha\,\mathcal{P}\int \mathrm{d}\alpha''\,\frac{A(-\alpha,\alpha-\alpha'',\alpha'')}{\alpha\alpha''} \tag{G.23}$$

$$\mathcal{B} = \mathcal{P}\int \mathrm{d}\alpha\,\mathcal{P}\int \mathrm{d}\alpha''\,\frac{B(-\alpha,\alpha-\alpha'',\alpha'')}{\alpha\alpha''} \tag{G.24}$$

Since every term in the Magnus expansion must be anti-Hermitian, then we know that $\mathcal{B} = \mathcal{A}^*$. By exploting the symmetry properties of the $\tilde{\Gamma}$ functions:

$$\tilde{\Gamma}(\alpha, \beta) = -\tilde{\Gamma}(\beta, \alpha),$$
$$\tilde{\Gamma}(-\alpha, -\beta) = -\tilde{\Gamma}^*(\alpha, \beta),$$

one may write these coefficients in a more compact form as

$$\mathcal{A} = \mathcal{P}\int \mathrm{d}\alpha\, \mathcal{P}\int \mathrm{d}\alpha' \frac{\tilde{\Gamma}(-\alpha, \alpha-\alpha')g^*_{q_0+\alpha'} - \tilde{\Gamma}(\alpha-\alpha', \alpha')g^*_{q_0-\alpha}}{\alpha'\alpha} =$$
$$= 2\mathcal{P}\int \mathrm{d}\alpha\, \mathcal{P}\int \mathrm{d}\alpha' \frac{\tilde{\Gamma}(-\alpha, \alpha-\alpha')g^*_{q_0+\alpha'}}{\alpha'\alpha},$$

and

$$\mathcal{B} = \mathcal{P}\int \mathrm{d}\alpha\, \mathcal{P}\int \mathrm{d}\alpha' \frac{\tilde{\Gamma}(\alpha-\alpha', \alpha')g_{q_0+\alpha} - \tilde{\Gamma}(-\alpha, \alpha-\alpha')g_{q_0-\alpha'}}{\alpha'\alpha} =$$
$$= 2\mathcal{P}\int \mathrm{d}\alpha\, \mathcal{P}\int \mathrm{d}\alpha' \frac{\tilde{\Gamma}(-\alpha, \alpha-\alpha')^* g_{q_0+\alpha'}}{\alpha'\alpha}$$

So indeed, $\mathcal{B} = \mathcal{A}^*$, and it is enough with calculating one of these magnitudes to parametrize the scattering matrix. Thus the third order contribution to the scattering matrix reads:

$$\hat{\Omega}_3 = -i\left[\kappa_{q_0}\,\hat{b}^\dagger_{q_0}\hat{\sigma} + \kappa^*_{q_0}\hat{b}_{q_0}\hat{\sigma}^\dagger\right] \tag{G.25}$$

$$\kappa_{q_0} = \frac{2}{3(2\pi)^2}\mathcal{P}\int \mathrm{d}\alpha\, \mathcal{P}\int \mathrm{d}\alpha' \frac{\Gamma(-\alpha, \alpha-\alpha')^*\beta_{q_0+\alpha'}}{\alpha'\alpha} \tag{G.26}$$

with $\Gamma(\alpha, \alpha') = \beta^*_{q_0+\alpha}\beta_{q_0-\alpha'} - \beta_{q_0-\alpha}\beta^*_{q_0+\alpha'}$, and $q_0 = \omega_{QE}/v_0$.

G.3 Evaluation for free electron-QE interaction through free space

From the previous sections, and noting that througout this section we use $q_0 \equiv q = \omega_{QE}/v_0$, the scattering matrix up to the third order in the

Magnus expansion reads

$$\hat{S} = e^{-i\left[(\beta_q+\kappa_q)\,\hat{b}_q^\dagger\hat{\sigma}+(\beta_q+\kappa_q)^*\hat{b}_q\hat{\sigma}^\dagger+\gamma_q\hat{\sigma}_z\right]+\mathcal{O}(\beta_q^4)}, \tag{G.27}$$

where β_q, γ_q and κ_q are the interaction strengths of the first, second, and third order of the Magnus expansion. Their expressions are given by

$$\beta_q = \frac{L}{v_0} g_q, \tag{G.28}$$

$$\gamma_q = -\frac{1}{2\pi}\mathcal{P}\int \mathrm{d}\alpha\, \frac{|\beta_{q+\alpha}|^2}{\alpha}, \tag{G.29}$$

$$\kappa_q = \frac{2}{3(2\pi)^2}\mathcal{P}\int \mathrm{d}\alpha'\, \frac{\beta_{q+\alpha'}}{\alpha'}\mathcal{P}\int \mathrm{d}\alpha\, \frac{\Gamma(-\alpha,\alpha-\alpha')^*}{\alpha}, \tag{G.30}$$

with $\Gamma(\alpha,\alpha') = \beta^*_{q+\alpha}\beta_{q-\alpha'} - \beta_{q-\alpha}\beta^*_{q+\alpha'}$. In these expressions, $\mathcal{P}$ is used to indicate the principal value of the integral. Equations (G.29) and (G.30) scale with the integrated coupling strength to the second and third power, respectively. For the case of a free electron travelling along z-direction and interacting with a dipolar QE, the analytical expression for the integration interaction strengths is given by [P5, 310, 312]

$$\beta_q = -\frac{e\,|\boldsymbol{\mu}|}{2\pi\epsilon_0 b^2\hbar\omega_{QE}}(qb)^2\frac{\boldsymbol{\mu}}{|\boldsymbol{\mu}|}\cdot\begin{pmatrix}\mathrm{sign}(qb)K_1(|qb|)\\ 0\\ -iK_0(|qb|)\end{pmatrix}. \tag{G.31}$$

In the expression above, $\boldsymbol{\mu}$ is the QE dipole moment, $K_{0,1}$ are modified Bessel function of the first kind, e is the electron charge and ϵ_0 is the vacuum permittivity. We note that the first factor in Equation (G.31) is independent of the momentum exchange, q, and therefore we can define a scaling parameter $\eta = e\,|\boldsymbol{\mu}|\,(2\pi\epsilon_0 b^2\hbar\omega_{QE})^{-1}$, as $\beta_q \propto \eta$, while $\gamma_q \propto \eta^2$, and $\kappa_q \propto \eta^3$. Furthermore, it can be shown that $\eta \approx 2.8774\frac{\mu_{\mathrm{e\cdot nm}}}{b^2_{\mathrm{nm}}\omega_{\mathrm{eV}}}$, which implies that this parameter can easily be of the order of unity for nanometric impact parameter, strong dipolar emitters and resonant energies in the optical regime. Thus, for feasible parameters, such as $b = 1$ nm, $\mu = 0.5\,e{\cdot}$nm, $\omega_{QE} = 3$ eV, we have $\eta = 0.47$.

Figure G.2 shows the numerical integration of the coupling strengths

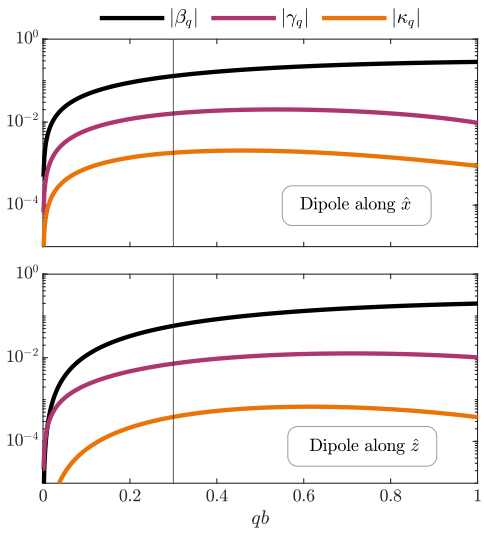

FIGURE G.2: Absolute value of the integrated interaction strengths in Equation (G.27) for an electron interacting with a QE with dipole moment along x-direction (top) and z-direction (bottom) as a function of qb and for $\eta = 0.47$.

in the Magnus expansion given in Eqs. (G.28-G.30) as a function of the product bq between 0 and 1 and for $\eta = 0.47$. Note that the interaction strengths are complex quantities, and we are rendering only their absolute value. The results obtained for QE dipole moments along x- and z-directions are plotted in the upper and lower panels, respectively. The black vertical lines correspond to $b = 1$ nm and an electron velocity (energy) of $0.05c$ (0.64 keV). These values correspond to slow electrons suffering negligible recoil effects [317, 322]. For x-oriented QEs, this configuration yields $|\beta_q| = 0.15 \approx 10|\gamma_q| \approx 100|\kappa_q|$ (for z-orientation, the overall values lower, but the proportionalities remain similar). Furthermore, note that by modifying the photonic environment, these couplings may be tailored to achieve larger β values while suppressing higher interaction orders [319]. These results justify the first-order perturbative treatment employed in Section 4.3 of this thesis.

G

Appendix H

Modulation integrals of relativistic PINEM electrons

From Ref. [315], the wavefunction of a free electron after a PINEM preparation step and a drift-time t_D is given by $|\psi\rangle = \int dk B(k)\,|k\rangle$ with

$$B(k) = \sum_m e^{-im\phi_0} \int dk \frac{e^{-iE_{\hbar k}t_D/\hbar}}{(2\pi\sigma_k^2)^{1/4}} J_m(2|\beta|) e^{-\frac{(k-k_0-mq_0)^2}{4\sigma_k^2}}, \tag{H.1}$$

where σ_k is the initial wavevector spread of the free electron, assumed to be much smaller than the recoil $\sigma_k \ll q_0$, β is the interaction strength with the PINEM field, k_0 is the initial wavevector of the free electron, and β is the integrated coupling strength, defined as in Section 4.2.3. We consider an energy dispersion relation for the free electron with relativistic corrections given by $E_p = E_0 + v_0(p-p_0) + \frac{1}{2\gamma^3 m_e}(p-p_0)^2$ [315]. Therefore, with this wavefunction, the overlapping integrals $I_n = \left\langle \hat{b}^n \right\rangle$, have the form

$$I_n = \exp\left[-in(\phi_0 + \hbar q_0 v_0 t_D) - i\frac{n^2}{2}\theta - \left(\frac{n\sigma_k}{\sqrt{2}q_0}\theta\right)^2\right] \times \\ \times \sum_m J_m(2|\beta|) J_{m+n}(2|\beta|) e^{-i\,m\,n\,\theta}. \tag{H.2}$$

We have introduced a new definition for the phase factor appearing in the summation as

$$\theta = \left(\frac{q_0 v_0}{\omega}\right)^2 \omega\, t_D \left(\frac{1-\eta^2}{\eta^2}\right) \frac{\hbar\omega}{\gamma m_e c^2}, \tag{H.3}$$

where $\eta = v_0/c$ and we have also made $q_0 = \omega/v_0$. Note that as a particular case of Neumann's addition theorem [81], it follows that $\sum_{m=-\infty}^{\infty} J_m(x)J_{m+n}(x) = \delta_{n,0}$, and therefore, the fact that this phase factor acquires non-zero values is key to achieve a significant degree of modulation through the drifting process. Also note that θ also appears as a damping term within the gaussian, which implies that when electrons have vanishing speeds, since $\theta \to \infty$, all the overlapping integrals are exponentially attenuated, just like predicted by the non-relativistic treatment. On the other hand, for electron speeds close to the speed of light, $\theta \to 0$, and the overlapping integrals vanish. This illustrates how a careful balance between electron speed and drift time must be attained.

In the case of the first overlapping integral, we have

$$I_1 \propto \sum_m J_m(z)J_{m+1}(z)e^{-i\,m\,\theta} =$$
$$= -\frac{1}{2}\frac{\partial}{\partial z}\left[\sum_{m=-\infty}^{\infty} J_m^2(z)e^{-i\,m\,\theta}\right] - \frac{2i}{z}\sum_{m=1}^{\infty} mJ_m(z)^2\sin(m\theta), \tag{H.4}$$

where we have used the recurrence relation of the bessel functions [81]. Although general solution of these sums couldn't be obtained, one can get analytical expressions for particular values of θ that will prove useful. Two of such cases correspond to θ being be an even or odd integer multiple of π, which yields

$$I_1 \propto \begin{cases} 0, & \text{if } \theta = 2N\pi, \\ J_1(4|\beta|), & \text{if } \theta = (2N+1)\pi, \end{cases} \tag{H.5}$$

with $N \in \mathbb{Z}$. To obtain these results, one can note that the second term in (H.4) directly evaluates to zero for both cases, and the sum in the first term can be obtained by using Neumann's addition theorem [81] as

$$\sum_{m=-\infty}^{\infty} J_m^2(z) = 1, \tag{H.6}$$

$$\sum_{m=-\infty}^{\infty} J_m^2(z)(-1)^m = \sum_{m=-\infty}^{\infty} J_m(z)J_{-m}(z) = J_0(2z), \tag{H.7}$$

which upon differentiation yield the results given in Eq. (H.5). Throughout Section 4.3 of this thesis we have shown that the closer the overlapping integrals are to unity, the closer the modulated electrons are to perfectly periodic electron combs. Therefore it is of interest to determine the upper bound of the overlapping integrals that can be attained in this way. We have numerically investigated this matter, and found that $\theta = \pi$ establishes a global upper bound for attainable modulation and therefore

$$|I_1| \leq \exp\left[-\left(\frac{\pi\sigma_k}{\sqrt{2}q_0}\right)^2\right] |J_1(4|\beta|)| \,. \tag{H.8}$$

The Bessel function acquires its maximum value at $4|\beta| = 0.46$, which in the limit of $\sigma_k \to 0$, gives that the first overlapping integral for an electron prepared with a PINEM experiment followed by a drift protocol can never surpass $|I_1| \lessapprox 0.581$, which is far from the required values for purity preservation during the interaction with QEs.

H

Appendix I

Phase locking with non-ideal modulated electrons

Equation (4.41) describes the evolution of the QE state vector in the Bloch sphere. By neglecting I_1 and γ_0, so as to focus on the phase locking behavior described in Section 4.3.3, the z-component becomes decoupled and we have

$$\begin{pmatrix}\dot{x}\\ \dot{y}\end{pmatrix} = \begin{pmatrix}-g_1\left(1-I_2'\right) & g_1 I_2''\\ g_1 I_2'' & -g_1\left(1+I_2'\right)\end{pmatrix}\begin{pmatrix}x\\ y\end{pmatrix} \tag{I.1}$$

By writing x (y) in polar coordinates, $x = r\cos(\vartheta)$ ($y = r\sin(\vartheta)$) we find that the EOM can be written as

$$\frac{\partial_\tau r}{r} = -1 + |I_2|\cos(\theta_2 - 2\vartheta), \tag{I.2}$$

$$\partial_\tau \vartheta = |I_2|\sin(\theta_2 - 2\vartheta), \tag{I.3}$$

where we have written $I_2 = |I_2|\exp(i\theta_2)$, and the time derivatives are with respect to $\tau = g_1 t$. Equations (I.2) and (I.3) reveal fixed points at $\vartheta = (n\pi + \theta_2)/2$, where n is an integer. Plugging these angles into Equation (I.2), we see that whenever n is even (odd) the radial decay is slowed (accelerated), and in the limit of $|I_2| \to 1$ the decay rate becomes zero. By linearizing Equation (I.3) around these fixed points, we see that whenever n is even (odd) the fixed point is stable (unstable). Thus, this interaction preserves the phases equal to $\theta_2/2$ or $\theta_2/2 + \pi$. We now make θ_2 time dependent, changing linearly in time, so that $\theta_2 = \omega t$.

This implies that the equations of motion can be casted as

$$\begin{aligned}\frac{\dot{r}}{r} &= \left(-1 + |I_2|\cos(\theta_2 - 2\vartheta)\right) g_1,\\ \dot{\vartheta} &= g_1 |I_2| \sin(\theta_2 - 2\vartheta),\\ \dot{\theta}_2 &= \omega.\end{aligned}$$

We now define a new variable, the phase difference as $\Delta\vartheta = \theta_2 - 2\vartheta$, which allows to write

$$\frac{\dot{r}}{r} = \left(-1 + |I_2|\cos(\Delta\vartheta)\right) g_1, \tag{I.4}$$

$$\dot{\Delta\vartheta} = \omega - 2g_1|I_2|\sin(\Delta\vartheta), \tag{I.5}$$

which shows that whenever $\kappa \equiv \omega/(2g_1|I_2|) \leq 1$, phase locking is possible between the impinging electron wavefunction and the QE state. Note that the fixed point in phase difference corresponds to $\Delta\vartheta_0 = \mathrm{asin}(\kappa)$.

By writing $\Delta\vartheta = \Delta\vartheta_0 + \delta$ and linearizing Equations (I.4) and (I.5) around the fixed point, we find that $\dot{r} = r\left(-1 + |I_2|\left[\sqrt{1-\kappa^2} - \kappa\delta(t)\right]\right) g_1$ and $\delta(t) = \delta_0 \exp\left(-2g_1|I_2|\sqrt{1-\kappa^2}t\right)$. Therefore, as long as $\kappa < 1$, the initial phase difference will tend to shrink to the one set by the fixed point. In the limit of $\kappa \to 0$, $|I_2| \to 1$ the QE vector state components become

$$r(t) = r_0 \exp\left[-\tfrac{g_1\kappa^2}{2}\left(t + \tfrac{\delta_0}{4\kappa g_1|I_2|}\left(1 - e^{-2g_1|I_2|t}\right)\right)\right], \tag{I.6}$$

$$\delta(t) = \delta_0 \exp\left(-2g_1|I_2|t\right), \tag{I.7}$$

$$\theta(t) = \tfrac{\omega}{2}t - \tfrac{\kappa}{2} + \tfrac{\theta_2(0) - [\theta_2(0) - 2\vartheta(0)]e^{-2g_1|I_2|t}}{2}. \tag{I.8}$$

We can see that in the transient in which the QE state reaches the phase locking, its purity is scaled by a factor of $\exp(-\delta_0\kappa/4|I_2|)$, and then it slowly decays as $\exp\left(-g_1\kappa^2 t\right)$. The steady state is phase locked with I_2, and the initial difference between the two phases vanish over time. This gives access to another way of inducing rotations in the Bloch sphere.

References

[1] J. C. Maxwell. 'VIII. A dynamical theory of the electromagnetic field'. In: *Philosophical Transactions of the Royal Society of London* 155 (1865) (cit. on pp. 3, 10).

[2] J. C. Maxwell. *A treatise on electricity and magnetism*. Clarendon Press, 1873 (cit. on p. 3).

[3] J. Schwinger. 'On Gauge Invariance and Vacuum Polarization'. In: *Physical Review* 82 (1951) (cit. on p. 3).

[4] J. A. Stratton. *The Field Equations*. John Wiley & Sons, Ltd, 2015 (cit. on p. 5).

[5] J. R. Reitz, F. J. Milford and R. W. Christy. *Foundations of Electromagnetic Theory (4th Edition)*. 4th ed. USA: Addison-Wesley Publishing Company, 2008 (cit. on pp. 5, 10, 13).

[6] R. W. Boyd. *Nonlinear Optics, Third Edition*. Elsevier, 2008 (cit. on pp. 6, 44).

[7] D. Strickland and G. Mourou. 'Compression of amplified chirped optical pulses'. In: *Optics Communications* 56.3 (1985) (cit. on p. 6).

[8] I.-W. Un, S. Sarkar and Y. Sivan. 'Electronic-Based Model of the Optical Nonlinearity of Low-Electron-Density Drude Materials'. In: *Physical Review Applied* 19.4 (2023) (cit. on p. 6).

[9] A. Y. Bykov, J. Deng, G. Li et al. 'Time-Dependent Ultrafast Quadratic Nonlinearity in an Epsilon-Near-Zero Platform'. In: *Nano Letters* 24.12 (2024) (cit. on p. 6).

[10] J. B. Khurgin, G. Sun, W. T. Chen et al. 'Ultrafast Thermal Nonlinearity'. In: *Scientific Reports* 5.1 (2015) (cit. on pp. 7, 32, 46, 72).

[11] Y. Sivan and S.-W. Chu. 'Nonlinear plasmonics at high temperatures'. In: *Nanophotonics* 6.1 (2017) (cit. on pp. 7, 32).

[12] L. Novotny and B. Hecht. *Principles of nano-optics*. 2009 (cit. on pp. 8, 9, 21, 52, 94, 124, 239, 252).

[13] H. A. Lorentz. *Versuch einer Theorie der electrischen und optischen Erscheinungen in bewegten Körpern*. B.G. Teubner, 1906 (cit. on p. 10).

[14] F. J. Dyson. 'Why is Maxwell's theory so hard to understand?' In: *IET Seminar Digest* 2007 (2007) (cit. on p. 10).

[15] J. J. Thomson. 'J. J. Thomson on "Cathode Rays"'. In: *Nature* 162 (1948) (cit. on p. 10).

[16] H. A. Lorentz. *The theory of electrons and its applications to the phenomena of light and radiant heat*. English. Leipzig: B. New York, 1909 (cit. on p. 10).

[17] F. Wooten and S. P. Davis. 'Optical Properties of Solids'. In: *American Journal of Physics* 41.7 (1973) (cit. on pp. 11, 13).

[18] B. Y.-K. Hu. 'Kramers–Kronig in two lines'. In: *American Journal of Physics* 57 (1989) (cit. on p. 12).

[19] G. B. Arfken, H. J. Weber and F. E. Harris. *Mathematical Methods for Physicists*. Elsevier, 2013 (cit. on p. 12).

[20] K. E. Oughstun. *Electromagnetic and Optical Pulse Propagation 1*. Vol. 125. Springer Series in Optical Sciences. New York, NY: Springer New York, 2007 (cit. on p. 13).

[21] J. B. Pendry, A. J. Holden, D. J. Robbins et al. 'Low frequency plasmons in thin-wire structures'. In: *Journal of Physics: Condensed Matter* 10.22 (1998) (cit. on pp. 13, 47).

[22] J. B. Pendry, A. J. Holden, D. J. Robbins et al. 'Magnetism from conductors and enhanced nonlinear phenomena'. In: *IEEE Transactions on Microwave Theory and Techniques* 47.11 (1999) (cit. on pp. 13, 47).

[23] J. B. Pendry. 'A Chiral Route to Negative Refraction'. In: *Science* 306.5700 (2004) (cit. on pp. 13, 47).

[24] L. Kelvin. 'I. Nineteenth century clouds over the dynamical theory of heat and light'. In: *The London, Edinburgh, and Dublin Philosophical Magazine and Journal of Science* 2.7 (1901) (cit. on p. 14).

[25] W. E. Lamb. 'Anti-photon'. In: *Applied Physics B* 60.2-3 (1995) (cit. on p. 15).

[26] R. Loudon. *The quantum theory of light*. Oxford University Press, 2000 (cit. on pp. 15, 21).

[27] S. Scheel and S. Buhmann. 'Macroscopic quantum electrodynamics, Van der Waals forces, Casimir'. In: *Acta Physica Slovaca* 58.5 (2008) (cit. on pp. 16, 159, 188, 192, 231).

[28] S. Y. Buhmann. *Dispersion Forces I*. Vol. 247. Springer Tracts in Modern Physics. Berlin, Heidelberg: Springer Berlin Heidelberg, 2012 (cit. on pp. 16, 120, 217, 223, 226).

[29] S. Franke, S. Hughes, M. K. Dezfouli et al. 'Quantization of Quasinormal Modes for Open Cavities and Plasmonic Cavity Quantum Electrodynamics'. In: *Physical Review Letters* 122.21 (2019) (cit. on pp. 16, 32).

[30] J. Ren, S. Franke and S. Hughes. 'Quasinormal Modes, Local Density of States, and Classical Purcell Factors for Coupled Loss-Gain Resonators'. In: *Physical Review X* 11.4 (2021) (cit. on p. 16).

[31] I. Medina, F. J. García-Vidal, A. I. Fernández-Domínguez et al. 'Few-Mode Field Quantization of Arbitrary Electromagnetic Spectral Densities'. In: *Physical Review Letters* 126.9 (2021) (cit. on pp. 16, 32, 95, 126, 168).

[32] M. Lednev, F. J. García-Vidal and J. Feist. 'Lindblad Master Equation Capable of Describing Hybrid Quantum Systems in the Ultrastrong Coupling Regime'. In: *Physical Review Letters* 132 (2024) (cit. on p. 16).

[33] C. J. Sánchez Martínez, J. Feist and F. J. García-Vidal. 'A mixed perturbative-nonperturbative treatment for strong light-matter interactions'. In: *Nanophotonics* 13.14 (2024) (cit. on p. 16).

[34] J. R. Rydberg. 'La constitution des spectres d'émission des éléments chimiques'. In: *Kongliga Svenska Vetenskaps-Akademiens Handlingar* (1890) (cit. on p. 17).

[35] E. Schrödinger. 'An Undulatory Theory of the Mechanics of Atoms and Molecules'. In: *Physical Review* 28.6 (1926) (cit. on p. 17).

[36] L. De Broglie. 'Recherches sur la théorie des Quanta'. In: *Annales de Physique* 10.3 (1925) (cit. on p. 17).

[37] P. Dirac. 'The quantum theory of the electron'. In: *Proceedings of the Royal Society of London. Series A, Containing Papers of a Mathematical and Physical Character* 117.778 (1928) (cit. on p. 18).

[38] E. M. Purcell, H. C. Torrey and R. V. Pound. 'Resonance Absorption by Nuclear Magnetic Moments in a Solid'. In: *Physical Review* 69.1-2 (1946) (cit. on p. 21).

[39] H. T. Dung, L. Knöll and D.-G. Welsch. 'Resonant dipole-dipole interaction in the presence of dispersing and absorbing surroundings'. In: *Physical Review A* 66.6 (2002) (cit. on pp. 23, 121, 159, 182, 188, 192, 218, 223, 224).

[40] H.-P. Breuer and F. Petruccione. *The Theory of Open Quantum Systems*. Vol. 9780199213. Oxford University PressOxford, 2007 (cit. on pp. 23, 168).

[41] R. Sáez-Blázquez, J. Feist, A. I. Fernández-Domínguez et al. 'Enhancing photon correlations through plasmonic strong coupling'. In: *Optica* 4.11 (2017) (cit. on pp. 24, 93, 94, 104, 109, 111, 214, 256).

[42] R. Sáez-Blázquez, J. Feist, F. J. García-Vidal et al. 'Photon statistics in collective strong coupling: Nanocavities and microcavities'. In: *Physical Review A* 98.1 (2018) (cit. on pp. 24, 29, 158, 168, 256).

[43] A. Kavokin, J. J. Baumberg, G. Malpuech et al. *Microcavities*. Oxford University Press, 2007 (cit. on pp. 27, 76).

[44] S. A. Maier. *Plasmonics: Fundamentals and Applications*. New York, NY: Springer US, 2007 (cit. on p. 29).

[45] N. W. A. N. D. Mermin. *Solid State Physics*. Holt, Rinehart and Winston, 1976 (cit. on p. 29).

[46] H. Raether. *Excitation of Plasmons and Interband Transitions by Electrons*. Vol. 88. Springer-Verlag, 1980 (cit. on p. 29).

[47] K. Drexhage. 'Influence of a dielectric interface on fluorescence decay time'. In: *Journal of Luminescence* 1-2 (1970) (cit. on p. 29).

[48] D. Kleppner. 'Inhibited Spontaneous Emission'. In: *Physical Review Letters* 47.4 (1981) (cit. on p. 29).

[49] V. Giannini, A. I. Fernández-Domínguez, S. C. Heck et al. 'Plasmonic Nanoantennas: Fundamentals and Their Use in Controlling the Radiative Properties of Nanoemitters'. In: *Chemical Reviews* 111.6 (2011) (cit. on pp. 29, 75, 81).

[50] L. Novotny and N. van Hulst. 'Antennas for light'. In: *Nature Photonics* 5.2 (2011) (cit. on p. 29).

[51] R. Chikkaraddy, B. de Nijs, F. Benz et al. 'Single-molecule strong coupling at room temperature in plasmonic nanocavities'. In: *Nature* 535.7610 (2016) (cit. on pp. 29, 75, 158, 165, 172).

[52] J. del Pino, J. Feist and F. J. Garcia-Vidal. 'Quantum theory of collective strong coupling of molecular vibrations with a microcavity mode'. In: *New Journal of Physics* 17.5 (2015) (cit. on p. 29).

[53] M. Ramezani, A. Halpin, A. I. Fernández-Domínguez et al. 'Plasmon-exciton-polariton lasing'. In: *Optica* 4.1 (2017) (cit. on p. 29).

[54] A. M. Berghuis, R. H. Tichauer, L. M. A. de Jong et al. 'Controlling Exciton Propagation in Organic Crystals through Strong Coupling to Plasmonic Nanoparticle Arrays'. In: *ACS Photonics* 9.7 (2022) (cit. on p. 29).

[55] R. H. Tichauer, I. Sokolovskii and G. Groenhof. 'Tuning the Coherent Propagation of Organic Exciton-Polaritons through the Cavity Q-factor'. In: *Advanced Science* 10.33 (2023) (cit. on p. 29).

[56] F. J. Garcia-Vidal, C. Ciuti and T. W. Ebbesen. 'Manipulating matter by strong coupling to vacuum fields'. In: *Science* 373.6551 (2021) (cit. on pp. 29, 158, 163).

[57] B. Munkhbat, A. Canales, B. Küçüköz et al. 'Tunable self-assembled Casimir microcavities and polaritons'. In: *Nature* 597.7875 (2021) (cit. on p. 29).

[58] C. F. Bohren and D. R. Huffman. *Absorption and Scattering of Light by Small Particles*. Vol. 1. 1. Wiley, 1998 (cit. on p. 31).

[59] N. Kholmicheva, L. Royo Romero, J. Cassidy et al. 'Prospects and applications of plasmon-exciton interactions in the near-field regime'. In: *Nanophotonics* 8.4 (2019) (cit. on pp. 31, 164, 168).

[60] H. M. Doeleman, E. Verhagen and A. F. Koenderink. 'Antenna–Cavity Hybrids: Matching Polar Opposites for Purcell Enhancements at Any Linewidth'. In: *ACS Photonics* 3.10 (2016) (cit. on pp. 32, 93).

[61] P. Peng, Y.-C. Liu, D. Xu et al. 'Enhancing Coherent Light-Matter Interactions through Microcavity-Engineered Plasmonic Resonances'. In: *Physical Review Letters* 119.23 (2017) (cit. on pp. 32, 93).

[62] B. Gurlek, V. Sandoghdar and D. Martín-Cano. 'Manipulation of Quenching in Nanoantenna–Emitter Systems Enabled by External Detuned Cavities: A Path to Enhance Strong-Coupling'. In: *ACS Photonics* 5.2 (2018) (cit. on pp. 32, 93).

[63] I. Shlesinger, J. Vandersmissen, E. Oksenberg et al. 'Hybrid cavity-antenna architecture for strong and tunable sideband-selective molecular Raman scattering enhancement'. In: *Science Advances* 9 (2023) (cit. on pp. 32, 93).

[64] S. R. K. Rodriguez, A. Abass, B. Maes et al. 'Coupling Bright and Dark Plasmonic Lattice Resonances'. In: *Physical Review X* 1.2 (2011) (cit. on p. 32).

[65] L. Cerdán, J. R. Deop-Ruano, J. J. Alvarez-Serrano et al. 'Perfect Absorption with Independent Electric and Magnetic Lattice Resonances in Metallo-Dielectric Arrays'. In: *Advanced Optical Materials* 12.13 (2024) (cit. on p. 32).

[66] J. J. Alvarez-Serrano, J. R. Deop-Ruano, V. Aglieri et al. 'Normal Incidence Excitation of Out-of-Plane Lattice Resonances in Bipartite Arrays of Metallic Nanostructures'. In: *ACS Photonics* 11.1 (2024) (cit. on p. 32).

[67] D. R. Abujetas, N. van Hoof, S. ter Huurne et al. 'Spectral and temporal evidence of robust photonic bound states in the continuum on terahertz metasurfaces'. In: *Optica* 6.8 (2019) (cit. on p. 32).

[68] J. L. Pura, J. R. Deop-Ruano, D. R. Abujetas et al. 'Tunable bound states in the continuum in active metasurfaces of graphene disk dimers'. In: *Nanophotonics* 12.24 (2023) (cit. on p. 32).

[69] A. Krasnok and A. Alu. 'Active Nanophotonics'. In: *Proceedings of the IEEE* 108.5 (2020) (cit. on p. 32).

[70] H. Zhao and L. Feng. 'Parity–time symmetric photonics'. In: *National Science Review* 5.2 (2018) (cit. on p. 32).

[71] c. K. Özdemir, S. Rotter, F. Nori et al. 'Parity–time symmetry and exceptional points in photonics'. In: *Nature Materials* 18.8 (2019) (cit. on p. 32).

[72] W. Liu, Q. Liu, X. Ni et al. 'Floquet parity-time symmetry in integrated photonics'. In: *Nature Communications* 15.1 (2024) (cit. on p. 32).

[73] A. O. Govorov and H. H. Richardson. 'Generating heat with metal nanoparticles'. In: *Nano Today* 2.1 (2007) (cit. on p. 32).

[74] G. Baffou and R. Quidant. 'Thermo-plasmonics: using metallic nanostructures as nano-sources of heat'. In: *Laser & Photonics Reviews* 7.2 (2013) (cit. on p. 32).

[75] G. Baffou, F. Cichos and R. Quidant. 'Applications and challenges of thermoplasmonics'. In: *Nature Materials* 19.9 (2020) (cit. on p. 32).

[76] A. S. Shalin, A. Canós Valero and A. Miroshnichenko, eds. *All-Dielectric Nanophotonics*. Elsevier, 2024 (cit. on p. 32).

[77] S. Manzeli, D. Ovchinnikov, D. Pasquier et al. '2D transition metal dichalcogenides'. In: *Nature Reviews Materials* 2.8 (2017) (cit. on pp. 32, 76).

[78] R. Verre, D. G. Baranov, B. Munkhbat et al. 'Transition metal dichalcogenide nanodisks as high-index dielectric Mie nanoresonators'. In: *Nature Nanotechnology* 14.7 (2019) (cit. on p. 32).

[79] S. H. Strogatz. *Nonlinear Dynamics and Chaos*. CRC Press, 2018 (cit. on pp. 38, 63).

[80] P. Cvitanovic. *Universality in chaos : a reprint selection*. Adam Hilger, 1989 (cit. on p. 39).

[81] M. Abramowitz, I. A. Stegun and R. H. Romer. 'Handbook of Mathematical Functions with Formulas, Graphs, and Mathematical Tables'. In: *American Journal of Physics* 56 (1988) (cit. on pp. 42, 240, 270).

[82] Z Geng, K. J. H. Peters, A. A. P. Trichet et al. 'Universal Scaling in the Dynamic Hysteresis, and Non-Markovian Dynamics, of a Tunable Optical Cavity'. In: *Physical Review Letters* 124.15 (2020) (cit. on pp. 45, 46, 61, 186, 190).

[83] K. J. H. Peters, Z. Geng, K. Malmir et al. 'Extremely Broadband Stochastic Resonance of Light and Enhanced Energy Harvesting Enabled by Memory Effects in the Nonlinear Response'. In: *Physical Review Letters* 126.21 (2021) (cit. on pp. 45, 46, 61).

[84] H. H. Li. 'Refractive index of silicon and germanium and its wavelength and temperature derivatives'. In: *Journal of Physical and Chemical Reference Data* 9.3 (1980) (cit. on p. 45).

[85] F. G. Della Corte, G. Cocorullo, M. Iodice et al. 'Temperature dependence of the thermo-optic coefficient of InP, GaAs, and SiC from room temperature to 600 K at the wavelength of 1.5 μm'. In: *Applied Physics Letters* 77.11 (2000) (cit. on p. 45).

[86] S. Uma, A. D. McConnell, M. Asheghi et al. 'Temperature-dependent thermal conductivity of undoped polycrystalline silicon layers'. In: *International Journal of Thermophysics* 22.2 (2001) (cit. on p. 45).

[87] K. Cui, Q. Zhao, X. Feng et al. 'Thermo-optic switch based on transmission-dip shifting in a double-slot photonic crystal waveguide'. In: *Applied Physics Letters* 100.20 (2012) (cit. on p. 45).

[88] M. Radhouene, M. Najjar, M. K. Chhipa et al. 'Design and analysis a thermo-optic switch based on photonic crystal ring resonator'. In: *Optik* 172 (2018) (cit. on p. 45).

[89] O. Marbello, S. Valbuena and F. Racedo. 'Study of the nonlinear optical response and thermal stability of edible oils using the Z-scan technique'. In: *Talanta* 206 (2020) (cit. on p. 46).

[90] K. J. H. Peters and S. R. K. Rodriguez. 'Limit cycles and chaos induced by a nonlinearity with memory'. In: *The European Physical Journal Special Topics* 231.3 (2022) (cit. on pp. 46, 186, 190).

[91] B Braeckeveldt, K. J. H. Peters, B Verdonschot et al. 'Memory-induced excitability in optical cavities'. In: *Physical Review Research* 6.2 (2024) (cit. on p. 46).

[92] G Keijsers, T Ham, Z Geng et al. 'Photon superfluidity through dissipation'. In: *Physical Review Research* 6.2 (2024) (cit. on p. 46).

[93] S. R. Rodriguez. 'Enhancing the Speed and Sensitivity of a Nonlinear Optical Sensor with Noise'. In: *Physical Review Applied* 13.2 (2020) (cit. on p. 46).

[94] K. J. H. Peters and S. R. K. Rodriguez. 'Exceptional Precision of a Nonlinear Optical Sensor at a Square-Root Singularity'. In: *Physical Review Letters* 129.1 (2022) (cit. on p. 46).

[95] V. G. Ramesh, K. J. H. Peters and S. R. K. Rodriguez. 'Arcsine Laws of Light'. In: *Physical Review Letters* 132.13 (2024) (cit. on p. 46).

[96] V. G. Ramesh and S. R. K. Rodriguez. 'Weak Ergodicity Breaking in Optical Sensing'. In: (2024) (cit. on p. 46).

[97] E Noether. 'Invariante Variationsprobleme'. In: *Nachrichten von der Gesellschaft der Wissenschaften zu Göttingen, Math. Klasse* 1918 (1918) (cit. on p. 47).

[98] D. Hsieh, D. Qian, L. Wray et al. 'A topological Dirac insulator in a quantum spin Hall phase'. In: *Nature* 452.7190 (2008) (cit. on p. 47).

[99] C.-K. Chiu, J. C. Y. Teo, A. P. Schnyder et al. 'Classification of topological quantum matter with symmetries'. In: *Reviews of Modern Physics* 88.3 (2016) (cit. on p. 47).

[100] A. B. Khanikaev, S. Hossein Mousavi, W.-K. Tse et al. 'Photonic topological insulators'. In: *Nature Materials* 12.3 (2013) (cit. on p. 47).

[101] T. Ozawa, H. M. Price, A. Amo et al. 'Topological photonics'. In: *Reviews of Modern Physics* 91.1 (2019) (cit. on p. 47).

[102] M. S. Rider, S. J. Palmer, S. R. Pocock et al. 'A perspective on topological nanophotonics: Current status and future challenges'. In: *Journal of Applied Physics* 125.12 (2019) (cit. on p. 47).

[103] A. Vakulenko, S. Kiriushechkina, D. Smirnova et al. 'Adiabatic topological photonic interfaces'. In: *Nature Communications* 14.1 (2023) (cit. on p. 47).

[104] W. M. Robertson, G. Arjavalingam, R. D. Meade et al. 'Measurement of photonic band structure in a two-dimensional periodic dielectric array'. In: *Physical Review Letters* 68.13 (1992) (cit. on p. 47).

[105] J. D. Joannopoulos, P. R. Villeneuve and S. Fan. 'Photonic crystals: putting a new twist on light'. In: *Nature* 386.6621 (1997) (cit. on p. 47).

[106] J. D. Joannopoulos, S. G. Johnson, J. N. Winn et al. *Photonic Crystals: Molding the Flow of Light - Second Edition*. REV - Revised, 2. Princeton University Press, 2008 (cit. on p. 47).

[107] A. D. Rakić. 'Algorithm for the determination of intrinsic optical constants of metal films: application to aluminum'. In: *Applied Optics* 34.22 (1995) (cit. on p. 47).

[108] F. Bloch. 'Über die Quantenmechanik der Elektronen in Kristallgittern'. In: *Zeitschrift für Physik* 52.7-8 (1929) (cit. on p. 49).

[109] P. W. Anderson. 'More Is Different'. In: *Science* 177.4047 (1972) (cit. on p. 50).

[110] M. Endres, T. Fukuhara, D. Pekker et al. 'The 'Higgs' amplitude mode at the two-dimensional superfluid/Mott insulator transition'. In: *Nature* 487.7408 (2012) (cit. on pp. 50, 71).

[111] N. Navon, A. L. Gaunt, R. P. Smith et al. 'Critical dynamics of spontaneous symmetry breaking in a homogeneous Bose gas'. In: *Science* 347.6218 (2015) (cit. on pp. 50, 71).

[112] A. Beekman, L. Rademaker and J. van Wezel. 'An introduction to spontaneous symmetry breaking'. In: *SciPost Physics Lecture Notes* (2019) (cit. on pp. 50, 71).

[113] T. Zibold, E. Nicklas, C. Gross et al. 'Classical Bifurcation at the Transition from Rabi to Josephson Dynamics'. In: *Physical Review Letters* 105.20 (2010) (cit. on p. 50).

[114] B. A. Malomed, ed. *Spontaneous Symmetry Breaking, Self-Trapping, and Josephson Oscillations*. Vol. 1. Progress in Optical Science and Photonics. Berlin, Heidelberg: Springer Berlin Heidelberg, 2013 (cit. on p. 50).

[115] P. Hamel, S. Haddadi, F. Raineri et al. 'Spontaneous mirror-symmetry breaking in coupled photonic-crystal nanolasers'. In: *Nature Photonics* 9.5 (2015) (cit. on p. 50).

[116] Q.-T. Cao, H. Wang, C.-H. Dong et al. 'Experimental Demonstration of Spontaneous Chirality in a Nonlinear Microresonator'. In: *Physical Review Letters* 118.3 (2017) (cit. on p. 50).

[117] B. Garbin, J. Fatome, G.-L. Oppo et al. 'Asymmetric balance in symmetry breaking'. In: *Physical Review Research* 2.2 (2020) (cit. on p. 50).

[118] G. Xu, A. U. Nielsen, B. Garbin et al. 'Spontaneous symmetry breaking of dissipative optical solitons in a two-component Kerr resonator'. In: *Nature Communications* 12.1 (2021) (cit. on p. 50).

[119] B. Garbin, A. Giraldo, K. J. H. Peters et al. 'Spontaneous Symmetry Breaking in a Coherently Driven Nanophotonic Bose-Hubbard Dimer'. In: *Physical Review Letters* 128.5 (2022) (cit. on p. 50).

[120] A. Krasnok and A. Alù. 'Low-Symmetry Nanophotonics'. In: *ACS Photonics* 9.1 (2022) (cit. on p. 50).

[121] L. Hill, G.-L. Oppo and P. Del'Haye. 'Multi-stage spontaneous symmetry breaking of light in Kerr ring resonators'. In: *Communications Physics* 6.1 (2023) (cit. on p. 50).

[122] A. Micheli, D. Jaksch, J. I. Cirac et al. 'Many-particle entanglement in two-component Bose-Einstein condensates'. In: *Physical Review A* 67.1 (2003) (cit. on p. 50).

[123] W. Casteels and C. Ciuti. 'Quantum entanglement in the spatial-symmetry-breaking phase transition of a driven-dissipative Bose-Hubbard dimer'. In: *Physical Review A* 95.1 (2017) (cit. on p. 50).

[124] Z. Xu, H. Yang, X. Song et al. 'Topical review: recent progress of charge density waves in 2D transition metal dichalcogenide-based heterojunctions and their applications'. In: *Nanotechnology* 32.49 (2021) (cit. on p. 50).

[125] P. A. Kalozoumis, C. Morfonios, F. K. Diakonos et al. 'Invariants of Broken Discrete Symmetries'. In: *Physical Review Letters* 113.5 (2014) (cit. on p. 50).

[126] N. de Gaay Fortman, R. Kolkowski, D. Pal et al. 'Spontaneous symmetry breaking in plasmon lattice lasers'. In: *Science Advances* 10 (2024) (cit. on p. 50).

[127] F. Wilczek. 'Quantum Time Crystals'. In: *Physical Review Letters* 109.16 (2012) (cit. on p. 71).

[128] P. Nozières. 'Time crystals: Can diamagnetic currents drive a charge density wave into rotation?' In: *EPL (Europhysics Letters)* 103.5 (2013) (cit. on p. 71).

[129] P. Bruno. 'Impossibility of Spontaneously Rotating Time Crystals: A No-Go Theorem'. In: *Physical Review Letters* 111.7 (2013) (cit. on p. 71).

[130] H. Watanabe and M. Oshikawa. 'Absence of Quantum Time Crystals'. In: *Physical Review Letters* 114.25 (2015) (cit. on p. 71).

[131] F. Wilczek. 'Quantum Time Crystals'. In: *Physical Review Letters* 109.16 (2012) (cit. on p. 71).

[132] F. Iemini, A. Russomanno, J. Keeling et al. 'Boundary Time Crystals'. In: *Physical Review Letters* 121.3 (2018) (cit. on p. 71).

[133] B. Buča, J. Tindall and D. Jaksch. 'Non-stationary coherent quantum many-body dynamics through dissipation'. In: *Nature Communications* 10.1 (2019) (cit. on p. 71).

[134] H. Keßler, J. G. Cosme, M. Hemmerling et al. 'Emergent limit cycles and time crystal dynamics in an atom-cavity system'. In: *Physical Review A* 99.5 (2019) (cit. on p. 71).

[135] P. Kongkhambut, J. Skulte, L. Mathey et al. 'Observation of a continuous time crystal'. In: *Science* 377.6606 (2022) (cit. on p. 71).

[136] H. Taheri, A. B. Matsko, L. Maleki et al. 'All-optical dissipative discrete time crystals'. In: *Nature Communications* 13.1 (2022) (cit. on p. 71).

[137] T. Liu, J.-Y. Ou, K. F. MacDonald et al. 'Photonic metamaterial analogue of a continuous time crystal'. In: *Nature Physics* 19.7 (2023) (cit. on p. 71).

[138] E. Galiffi, R. Tirole, S. Yin et al. 'Photonics of time-varying media'. In: *Advanced Photonics* 4.01 (2022) (cit. on pp. 71, 186, 190).

[139] J. Sloan, N. Rivera, J. D. Joannopoulos et al. 'Controlling two-photon emission from superluminal and accelerating index perturbations'. In: *Nature Physics* 18 (2022) (cit. on pp. 71, 186, 190).

[140] P. A. Huidobro, E. Galiffi, S. Guenneau et al. 'Fresnel drag in space–time-modulated metamaterials'. In: *Proceedings of the National Academy of Sciences* 116.50 (2019) (cit. on pp. 71, 186, 190).

[141] E. Galiffi, M. G. Silveirinha, P. A. Huidobro et al. 'Photon localization and Bloch symmetry breaking in luminal gratings'. In: *Physical Review B* 104.1 (2021) (cit. on p. 71).

[142] E. Galiffi, P. A. Huidobro and J. B. Pendry. 'Broadband Nonreciprocal Amplification in Luminal Metamaterials'. In: *Physical Review Letters* 123.20 (2019) (cit. on pp. 71, 186, 190).

[143] R. Tirole, S. Vezzoli, E. Galiffi et al. 'Double-slit time diffraction at optical frequencies'. In: *Nature Physics* 19.7 (2023) (cit. on p. 71).

[144] M. Z. Alam, I. De Leon and R. W. Boyd. 'Large optical nonlinearity of indium tin oxide in its epsilon-near-zero region'. In: *Science* 352.6287 (2016) (cit. on p. 72).

[145] S. Vezzoli, V. Bruno, C. DeVault et al. 'Optical Time Reversal from Time-Dependent Epsilon-Near-Zero Media'. In: *Physical Review Letters* 120.4 (2018) (cit. on p. 72).

[146] J. B. Khurgin. 'Nonlinear optics from the viewpoint of interaction time'. In: *Nature Photonics* 17.7 (2023) (cit. on p. 72).

[147] M. Kerker, D.-S. Wang and H. Chew. 'Surface enhanced Raman scattering (SERS) by molecules adsorbed at spherical particles: errata'. In: *Applied Optics* 19.24 (1980) (cit. on p. 73).

[148] S. A. Maier. 'Plasmonic field enhancement and SERS in the effective mode volume picture'. In: *Optics Express* 14.5 (2006) (cit. on p. 73).

[149] R. Zhang, Y. Zhang, Z. C. Dong et al. 'Chemical mapping of a single molecule by plasmon-enhanced Raman scattering'. In: *Nature* 498 (2013) (cit. on p. 73).

[150] R. C. de Campos Ferreira, A. Sagwal, J. Doležal et al. 'Resonant Tip-Enhanced Raman Spectroscopy of a Single-Molecule Kondo System'. In: *ACS Nano* 18 (2024) (cit. on p. 73).

[151] F. J. García de Abajo. 'Optical excitations in electron microscopy'. In: *Reviews of Modern Physics* 82.1 (2010) (cit. on pp. 74, 77, 118, 162, 188, 192, 236, 245, 247).

[152] P. E. Stamatopoulou, W. Zhao, Á. Rodríguez Echarri et al. 'Electron beams traversing spherical nanoparticles: Analytic and numerical treatment'. In: *Physical Review Research* 6.1 (2024) (cit. on pp. 74, 77, 118).

[153] H. Duan, A. I. Fernández-Domínguez, M. Bosman et al. 'Nanoplasmonics: Classical down to the Nanometer Scale'. In: *Nano Letters* 12.3 (2012) (cit. on pp. 74, 118).

[154] M. J. Lagos, A. Trügler, U. Hohenester et al. 'Mapping vibrational surface and bulk modes in a single nanocube'. In: *Nature* 543.7646 (2017) (cit. on pp. 74, 77, 118).

[155] D. L. Mills, M. Weber and B. Laks. 'Light Emission from Tunnel Junctions'. In: *Tunneling Spectroscopy: Capabilities, Applications, and New Techniques*. Ed. by P. K. Hansma. Boston, MA: Springer US, 1982 (cit. on pp. 74, 97).

[156] R. Berndt. 'Photon Emission from the Scanning Tunneling Microscope'. In: *Scanning Probe Microscopy: Analytical Methods*. Ed. by R. Wiesendanger. Berlin, Heidelberg: Springer Berlin Heidelberg, 1998 (cit. on pp. 74, 97).

[157] J. Kern, R. Kullock, J. Prangsma et al. 'Electrically driven optical antennas'. In: *Nature Photonics* 9.9 (2015) (cit. on pp. 74, 97).

[158] M. Parzefall and L. Novotny. 'Light at the End of the Tunnel'. In: *ACS Photonics* 5.11 (2018) (cit. on pp. 74, 97).

[159] S. P. Gurunarayanan, N. Verellen, V. S. Zharinov et al. 'Electrically Driven Unidirectional Optical Nanoantennas'. In: *Nano Letters* 17.12 (2017) (cit. on pp. 74, 97).

[160] J. S. Cho, R. Taschereau, S. Olma et al. 'Cerenkov radiation imaging as a method for quantitative measurements of beta particles in a microfluidic chip'. In: *Physics in medicine and biology* 54.22 (2009) (cit. on pp. 74, 77).

[161] R Robertson, M. S. Germanos, C Li et al. 'Optical imaging of Cerenkov light generation from positron-emitting radiotracers'. In: *Physics in Medicine and Biology* 54.16 (2009) (cit. on pp. 74, 77).

[162] L. Cui, Y. Zhu, M. Abbasi et al. 'Electrically Driven Hot-Carrier Generation and Above-Threshold Light Emission in Plasmonic Tunnel Junctions'. In: *Nano Letters* 20.8 (2020) (cit. on pp. 74, 96, 98–102, 107, 110).

[163] M. Brune, F. Schmidt-Kaler, A. Maali et al. 'Quantum Rabi Oscillation: A Direct Test of Field Quantization in a Cavity'. In: *Physical Review Letters* 76.11 (1996) (cit. on pp. 75, 94).

[164] J. Ye, D. W. Vernooy and H. J. Kimble. 'Trapping of Single Atoms in Cavity QED'. In: *Physical Review Letters* 83.24 (1999) (cit. on pp. 75, 94).

[165] V. Agranovich and G. Bassani. *Electronic Excitations in Organic Nanostructures*. Vol. 31. Thin Films and Nanostructures. Academic Press, 2003 (cit. on p. 76).

[166] C. Robert, D. Lagarde, F. Cadiz et al. 'Exciton radiative lifetime in transition metal dichalcogenide monolayers'. In: *Physical Review B* 93.20 (2016) (cit. on p. 76).

[167] C. Meineke, J. Schlosser, M. Zizlsperger et al. 'Ultrafast Exciton Dynamics in the Atomically Thin van der Waals Magnet CrSBr'. In: *Nano Letters* 24 (2024) (cit. on p. 76).

[168] A. Krasnok, S. Lepeshov and A. Alú. 'Nanophotonics with 2D transition metal dichalcogenides [Invited]'. In: *Optics Express* 26.12 (2018) (cit. on p. 76).

[169] X. Liu, T. Galfsky, Z. Sun et al. 'Strong light–matter coupling in two-dimensional atomic crystals'. In: *Nature Photonics* 9.1 (2015) (cit. on p. 76).

[170] M.-E. Kleemann, R. Chikkaraddy, E. M. Alexeev et al. 'Strong-coupling of WSe2 in ultra-compact plasmonic nanocavities at room temperature'. In: *Nature Communications* 8.1 (2017) (cit. on pp. 76, 95).

[171] A. B. Yankovich, B. Munkhbat, D. G. Baranov et al. 'Visualizing Spatial Variations of Plasmon–Exciton Polaritons at the Nanoscale Using Electron Microscopy'. In: *Nano Letters* 19.11 (2019) (cit. on pp. 76, 77, 95, 118).

[172] K. He, N. Kumar, L. Zhao et al. 'Tightly Bound Excitons in Monolayer WSe_2'. In: *Physical Review Letters* 113.2 (2014) (cit. on p. 76).

[173] Y. Li, A. Chernikov, X. Zhang et al. 'Measurement of the optical dielectric function of monolayer transition-metal dichalcogenides: MoS_2, $MoSe_2$, WS_2 and WSe_2'. In: *Physical Review B* 90.20 (2014) (cit. on pp. 76, 106).

[174] C. Poellmann, P. Steinleitner, U. Leierseder et al. 'Resonant internal quantum transitions and femtosecond radiative decay of excitons in monolayer WSe2'. In: *Nature Materials* 14.9 (2015) (cit. on p. 76).

[175] G. Moody, C. Kavir Dass, K. Hao et al. 'Intrinsic homogeneous linewidth and broadening mechanisms of excitons in monolayer transition metal dichalcogenides'. In: *Nature Communications* 6.1 (2015) (cit. on p. 76).

[176] J. Klein, B. Pingault, M. Florian et al. 'The Bulk van der Waals Layered Magnet CrSBr is a Quasi-1D Material'. In: *ACS Nano* 17 (2023) (cit. on p. 76).

[177] A. Polman, M. Kociak and F. J. García de Abajo. 'Electron-beam spectroscopy for nanophotonics'. In: *Nature Materials* 18.11 (2019) (cit. on pp. 77, 118).

[178] P. A. Čerenkov. 'Visible Radiation Produced by Electrons Moving in a Medium with Velocities Exceeding that of Light'. In: *Physical Review* 52.4 (1937) (cit. on p. 77).

[179] G. S. Mitchell, R. K. Gill, D. L. Boucher et al. 'In vivo Cerenkov luminescence imaging: a new tool for molecular imaging'. In: *Philosophical Transactions of the Royal Society A: Mathematical, Physical and Engineering Sciences* 369.1955 (2011) (cit. on p. 77).

[180] E. C. Pratt, T. M. Shaffer, Q. Zhang et al. 'Nanoparticles as multimodal photon transducers of ionizing radiation'. In: *Nature Nanotechnology* 13.5 (2018) (cit. on pp. 77, 80).

[181] D. L. Thorek, R. Robertson, W. A. Bacchus et al. 'Cerenkov imaging - a new modality for molecular imaging.' In: *American journal of nuclear medicine and molecular imaging* 2.2 (2012) (cit. on pp. 77, 79).

[182] T. M. Shaffer, E. C. Pratt and J. Grimm. 'Utilizing the power of Cerenkov light with nanotechnology'. In: *Nature Nanotechnology* 12.2 (2017) (cit. on pp. 77, 79).

[183] H. Hu, X. Lin, D. Liu et al. 'Broadband Enhancement of Cherenkov Radiation Using Dispersionless Plasmons'. In: *Advanced Science* 9.26 (2022) (cit. on pp. 77, 79).

[184] I. Frank and I. Tamm. 'Coherent Visible Radiation of Fast Electrons Passing Through Matter'. In: *Selected Papers*. Berlin, Heidelberg: Springer Berlin Heidelberg, 1991 (cit. on p. 78).

[185] J. D. Jackson. *Classical Electrodynamics*. Wiley, 1999 (cit. on pp. 78, 81, 118, 202).

[186] A. M. Smith, M. C. Mancini and S. Nie. 'Second window for in vivo imaging'. In: *Nature Nanotechnology* 4 (2009) (cit. on p. 78).

[187] P. T. K. Chin, M. M. Welling, S. C. J. Meskers et al. 'Optical imaging as an expansion of nuclear medicine: Cerenkov-based luminescence vs fluorescence-based luminescence'. In: *European Journal of Nuclear Medicine and Molecular Imaging* 40.8 (2013) (cit. on pp. 78, 79).

[188] D. L. J. Thorek, A. Ogirala, B. J. Beattie et al. 'Quantitative imaging of disease signatures through radioactive decay signal conversion'. In: *Nature Medicine* 19.10 (2013) (cit. on p. 78).

[189] R. S. Dothager, R. J. Goiffon, E. Jackson et al. 'Cerenkov Radiation Energy Transfer (CRET) Imaging: A Novel Method for Optical Imaging of PET Isotopes in Biological Systems'. In: *PLoS ONE* 5.10 (2010). Ed. by J. G. Gelovani (cit. on p. 78).

[190] F. Liu, L. Xiao, Y. Ye et al. 'Integrated Cherenkov radiation emitter eliminating the electron velocity threshold'. In: *Nature Photonics* 11.5 (2017) (cit. on p. 79).

[191] P. Genevet, D. Wintz, A. Ambrosio et al. 'Controlled steering of Cherenkov surface plasmon wakes with a one-dimensional metamaterial'. In: *Nature Nanotechnology* 10.9 (2015) (cit. on p. 79).

[192] J.-K. So, J.-H. Won, M. A. Sattorov et al. 'Cerenkov radiation in metallic metamaterials'. In: *Applied Physics Letters* 97.15 (2010) (cit. on p. 79).

[193] V. Ginis, J. Danckaert, I. Veretennicoff et al. 'Controlling Cherenkov Radiation with Transformation-Optical Metamaterials'. In: *Physical Review Letters* 113.16 (2014) (cit. on p. 79).

[194] X. Lu, M. A. Shapiro, I. Mastovsky et al. 'Generation of High-Power, Reversed-Cherenkov Wakefield Radiation in a Metamaterial Structure'. In: *Physical Review Letters* 122.1 (2019) (cit. on p. 79).

[195] J. Tao, Q. J. Wang, J. Zhang et al. 'Reverse surface-polariton cherenkov radiation'. In: *Scientific Reports* 6.1 (2016) (cit. on p. 79).

[196] I. Kaminer, Y. T. Katan, H. Buljan et al. 'Efficient plasmonic emission by the quantum Čerenkov effect from hot carriers in graphene'. In: *Nature Communications* 7.1 (2016) (cit. on p. 79).

[197] I. Kaminer, S. E. Kooi, R. Shiloh et al. 'Spectrally and Spatially Resolved Smith-Purcell Radiation in Plasmonic Crystals with Short-Range Disorder'. In: *Physical Review X* 7.1 (2017) (cit. on p. 79).

[198] C. Wu, A. Salandrino, X. Ni et al. 'Electrodynamical Light Trapping Using Whispering-Gallery Resonances in Hyperbolic Cavities'. In: *Physical Review X* 4.2 (2014) (cit. on pp. 79, 83).

[199] L. Ferrari, C. Wu, D. Lepage et al. 'Hyperbolic metamaterials and their applications'. In: *Progress in Quantum Electronics* 40 (2015) (cit. on pp. 79, 83).

[200] P. Bharadwaj and L. Novotny. 'Spectral dependence of single molecule fluorescence enhancement'. In: *Optics Express* 15.21 (2007) (cit. on p. 79).

[201] A. Kinkhabwala, Z. Yu, S. Fan et al. 'Large single-molecule fluorescence enhancements produced by a bowtie nanoantenna'. In: *Nature Photonics* 3.11 (2009) (cit. on p. 81).

[202] G. P. Acuna, F. M. Möller, P. Holzmeister et al. 'Fluorescence Enhancement at Docking Sites of DNA-Directed Self-Assembled Nanoantennas'. In: *Science* 338.6106 (2012) (cit. on p. 81).

[203] A. D. Rakić, A. B. Djurišić, J. M. Elazar et al. 'Optical properties of metallic films for vertical-cavity optoelectronic devices'. In: *Applied Optics* 37.22 (1998) (cit. on pp. 81, 83, 104).

[204] A. Wiener, H. Duan, M. Bosman et al. 'Electron-Energy Loss Study of Nonlocal Effects in Connected Plasmonic Nanoprisms'. In: *ACS Nano* 7.7 (2013) (cit. on p. 81).

[205] F. J. García de Abajo and M. Kociak. 'Probing the Photonic Local Density of States with Electron Energy Loss Spectroscopy'. In: *Physical Review Letters* 100.10 (2008) (cit. on p. 81).

[206] Z. S. Wu, L. X. Guo, K. F. Ren et al. 'Improved algorithm for electromagnetic scattering of plane waves and shaped beams by multilayered spheres'. In: *Applied Optics* 36.21 (1997) (cit. on p. 81).

[207] A. Moroz. 'A recursive transfer-matrix solution for a dipole radiating inside and outside a stratified sphere'. In: *Annals of Physics* 315.2 (2005) (cit. on pp. 81, 200, 204).

[208] G. Mie. 'Beiträge zur Optik trüber Medien, speziell kolloidaler Metallösungen'. In: *Annalen der Physik* 330.3 (1908) (cit. on pp. 83, 89, 202).

[209] M. Wan, P. Gu, W. Liu et al. 'Low threshold spaser based on deep-subwavelength spherical hyperbolic metamaterial cavities'. In: *Applied Physics Letters* 110.3 (2017) (cit. on p. 83).

[210] W. Wu, L. Fan, W. Zang et al. 'Second harmonic generation enhancement from a nonlinear nanocrystal integrated hyperbolic metamaterial cavity'. In: *Optics Express* 25.18 (2017) (cit. on p. 83).

[211] I. A. Starkov and A. S. Starkov. 'Homogenization of the dielectric and magnetic permeability tensors for anisotropic and bianisotropic layered media'. In: *International Journal of Solids and Structures* 160 (2019) (cit. on pp. 83, 209).

[212] S. A. Ramakrishna, J. B. Pendry, M. C. K. Wiltshire et al. 'Imaging the near field'. In: *Journal of Modern Optics* 50.9 (2003) (cit. on p. 83).

[213] C. L. Nehl, N. K. Grady, G. P. Goodrich et al. 'Scattering Spectra of Single Gold Nanoshells'. In: *Nano Letters* 4.12 (2004) (cit. on p. 83).

[214] E. Prodan, C. Radloff, N. J. Halas et al. 'A Hybridization Model for the Plasmon Response of Complex Nanostructures'. In: *Science* 302.5644 (2003) (cit. on pp. 84, 85).

[215] R.-Q. Li, D. Hernángomez-Pérez, F. J. García-Vidal et al. 'Transformation Optics Approach to Plasmon-Exciton Strong Coupling in Nanocavities'. In: *Physical Review Letters* 117.10 (2016) (cit. on p. 87).

[216] A. Cuartero-González and A. I. Fernández-Domínguez. 'Dipolar and quadrupolar excitons coupled to a nanoparticle-on-mirror cavity'. In: *Physical Review B* 101.3 (2020) (cit. on pp. 87, 95).

[217] J. Kennedy and R. Eberhart. 'Particle swarm optimization'. In: *Proceedings of ICNN'95 - International Conference on Neural Networks*. Vol. 4. IEEE (cit. on pp. 87, 206, 207).

[218] Y. Shi and R. Eberhart. 'A modified particle swarm optimizer'. In: *1998 IEEE International Conference on Evolutionary Computation Proceedings. IEEE World Congress on Computational Intelligence (Cat. No.98TH8360)*. IEEE (cit. on pp. 87, 207).

[219] E. Mezura-Montes and C. A. Coello Coello. 'Constraint-handling in nature-inspired numerical optimization: Past, present and future'. In: *Swarm and Evolutionary Computation* 1.4 (2011) (cit. on p. 87).

[220] R. Poli. 'Analysis of the Publications on the Applications of Particle Swarm Optimisation'. In: *Journal of Artificial Evolution and Applications* 2008.1 (2008). Ed. by L. Vanneschi (cit. on p. 87).

[221] S. I. Lepeshov, A. E. Krasnok, P. A. Belov et al. 'Hybrid nanophotonics'. In: *Physics-Uspekhi* 61.11 (2019) (cit. on p. 93).

[222] H. M. Doeleman, C. D. Dieleman, C. Mennes et al. 'Observation of Cooperative Purcell Enhancements in Antenna–Cavity Hybrids'. In: *ACS Nano* 14.9 (2020) (cit. on p. 93).

[223] I. Shlesinger, K. G. Cognée, E. Verhagen et al. 'Integrated Molecular Optomechanics with Hybrid Dielectric–Metallic Resonators'. In: *ACS Photonics* 8.12 (2021) (cit. on p. 93).

[224] M. Pelton. 'Modified spontaneous emission in nanophotonic structures'. In: *Nature Photonics* 9.7 (2015) (cit. on p. 93).

[225] G. M. Akselrod, C. Argyropoulos, T. B. Hoang et al. 'Probing the mechanisms of large Purcell enhancement in plasmonic nanoantennas'. In: *Nature Photonics* 8.11 (2014) (cit. on p. 93).

[226] K. Srinivasan and O. Painter. 'Linear and nonlinear optical spectroscopy of a strongly coupled microdisk–quantum dot system'. In: *Nature* 450.7171 (2007) (cit. on pp. 93, 94).

[227] W. Zhao, S. Wang, B. Liu et al. 'Exciton–Plasmon Coupling and Electromagnetically Induced Transparency in Monolayer Semiconductors Hybridized with Ag Nanoparticles'. In: *Advanced Materials* 28.14 (2016) (cit. on p. 94).

[228] G. Zengin, M. Wersäll, S. Nilsson et al. 'Realizing Strong Light-Matter Interactions between Single-Nanoparticle Plasmons and Molecular Excitons at Ambient Conditions'. In: *Physical Review Letters* 114.15 (2015) (cit. on p. 94).

[229] M. Pelton, S. D. Storm and H. Leng. 'Strong coupling of emitters to single plasmonic nanoparticles: exciton-induced transparency and Rabi splitting'. In: *Nanoscale* 11.31 (2019) (cit. on p. 94).

[230] S. Sun, H. Kim, G. S. Solomon et al. 'A quantum phase switch between a single solid-state spin and a photon'. In: *Nature Nanotechnology* 11.6 (2016) (cit. on pp. 94, 109).

[231] C. Arnold, J. Demory, V. Loo et al. 'Macroscopic rotation of photon polarization induced by a single spin'. In: *Nature Communications* 6.1 (2015) (cit. on p. 94).

[232] L. De Santis, C. Antón, B. Reznychenko et al. 'A solid-state single-photon filter'. In: *Nature Nanotechnology* 12.7 (2017) (cit. on p. 94).

[233] O. S. Ojambati, R. Chikkaraddy, W. D. Deacon et al. 'Quantum electrodynamics at room temperature coupling a single vibrating molecule with a plasmonic nanocavity'. In: *Nature Communications* 10.1 (2019) (cit. on pp. 94, 158).

[234] R. Sáez-Blázquez, Á. Cuartero-González, J. Feist et al. 'Plexcitonic Quantum Light Emission from Nanoparticle-on-Mirror Cavities'. In: *Nano Letters* 22.6 (2022) (cit. on p. 94).

[235] P Törmä and W. L. Barnes. 'Strong coupling between surface plasmon polaritons and emitters: a review'. In: *Reports on Progress in Physics* 78.1 (2015) (cit. on pp. 95, 101, 158, 163).

[236] H. Bethe and J. Schwinger. *Perturbation Theory for Cavities*. N. D. R. C., Contractor's Rpt. D1-117. Cornell University, 1943 (cit. on p. 95).

[237] E. M. Purcell. 'Spontaneous Emission Probabilities at Radio Frequencies'. In: *Physical Review* 69.11-12 (1946) (cit. on p. 95).

[238] A. F. Koenderink. 'On the use of Purcell factors for plasmon antennas'. In: *Optics Letters, Vol. 35, Issue 24, pp. 4208-4210* 35.24 (2010) (cit. on p. 95).

[239] P. Lalanne, W. Yan, K. Vynck et al. 'Light Interaction with Photonic and Plasmonic Resonances'. In: *Laser and Photonics Reviews* 12.5 (2018) (cit. on p. 95).

[240] J.-Y. Li, W. Li, J. Liu et al. 'Room-Temperature Strong Coupling Between a Single Quantum Dot and a Single Plasmonic Nanoparticle'. In: *Nano Letters* 22.12 (2022) (cit. on p. 95).

[241] M. M. Petrić, M. Kremser, M. Barbone et al. 'Tuning the Optical Properties of a MoSe 2 Monolayer Using Nanoscale Plasmonic Antennas'. In: *Nano Letters* 22.2 (2022) (cit. on p. 95).

[242] J. Lambe and S. L. McCarthy. 'Light Emission from Inelastic Electron Tunneling'. In: *Physical Review Letters* 37.14 (1976) (cit. on pp. 96, 97).

[243] A. Martín-Jiménez, K. Lauwaet, Ó. Jover et al. 'Electronic Temperature and Two-Electron Processes in Overbias Plasmonic Emission from Tunnel Junctions'. In: *Nano Letters* 21.16 (2021) (cit. on pp. 96, 98).

[244] H. Qian, S. Li, S.-W. Hsu et al. 'Highly-efficient electrically-driven localized surface plasmon source enabled by resonant inelastic electron tunneling'. In: *Nature Communications* 12.1 (2021) (cit. on p. 96).

[245] Y. Zhu, L. Cui, M. Abbasi et al. 'Tuning Light Emission Crossovers in Atomic-Scale Aluminum Plasmonic Tunnel Junctions'. In: *Nano Letters* 22.20 (2022) (cit. on pp. 96, 98, 102).

[246] M. Buret, A. V. Uskov, J. Dellinger et al. 'Spontaneous Hot-Electron Light Emission from Electron-Fed Optical Antennas'. In: *Nano Letters* 15.9 (2015) (cit. on pp. 96, 98).

[247] C. Ott, S. Götzinger and H. B. Weber. 'Thermal origin of light emission in nonresonant and resonant nanojunctions'. In: *Physical Review Research* 2.4 (2020) (cit. on pp. 96, 98).

[248] P.-J. Peters, F. Xu, K. Kaasbjerg et al. 'Quantum Coherent Multielectron Processes in an Atomic Scale Contact'. In: *Physical Review Letters* 119.6 (2017) (cit. on pp. 96, 98).

[249] E.-D. Fung and L. Venkataraman. 'Too Cool for Blackbody Radiation: Overbias Photon Emission in Ambient STM Due to Multielectron Processes'. In: *Nano Letters* 20.12 (2020) (cit. on pp. 96, 98).

[250] M. Parzefall. 'Optical antennas driven by quantum tunneling'. PhD thesis. ETH Zurich, 2017 (cit. on p. 97).

[251] C. Deeb, J. Toudert and J.-L. Pelouard. 'Electrically driven nanogap antennas and quantum tunneling regime'. In: *Nanophotonics* 12.15 (2023) (cit. on p. 97).

[252] G. Toscano, J. Straubel, A. Kwiatkowski et al. 'Resonance shifts and spill-out effects in self-consistent hydrodynamic nanoplasmonics'. In: *Nature Communications* 6.1 (2015) (cit. on p. 97).

[253] N. A. Mortensen. 'Mesoscopic electrodynamics at metal surfaces'. In: *Nanophotonics* 10.10 (2021) (cit. on p. 97).

[254] U. Muniain, R. Esteban, J. Aizpurua et al. 'Unified Treatment of Light Emission by Inelastic Tunneling: Interaction of Electrons and Photons beyond the Gap'. In: *Physical Review X* 14.2 (2024) (cit. on p. 98).

[255] L. C. Davis. 'Theory of surface-plasmon excitation in metal-insulator-metal tunnel junctions'. In: *Physical Review B* 16.6 (1977) (cit. on p. 98).

[256] D. Hone, B. Mühlschlegel and D. J. Scalapino. 'Theory of light emission from small particle tunnel junctions'. In: *Applied Physics Letters* 33.2 (1978) (cit. on p. 98).

[257] B. N. J. Persson and A. Baratoff. 'Theory of photon emission in electron tunneling to metallic particles'. In: *Physical Review Letters* 68.21 (1992) (cit. on p. 98).

[258] M. Parzefall and L. Novotny. 'Optical antennas driven by quantum tunneling: a key issues review'. In: *Reports on Progress in Physics* 82.11 (2019) (cit. on p. 98).

[259] O. Bitton, S. N. Gupta, L. Houben et al. 'Vacuum Rabi splitting of a dark plasmonic cavity mode revealed by fast electrons'. In: *Nature Communications* 11.1 (2020) (cit. on p. 98).

[260] J. B. Herzog, M. W. Knight, Y. Li et al. 'Dark Plasmons in Hot Spot Generation and Polarization in Interelectrode Nanoscale Junctions'. In: *Nano Letters* 13.3 (2013) (cit. on pp. 100, 110).

[261] A. Arora, M. Koperski, K. Nogajewski et al. 'Excitonic resonances in thin films of WSe 2 : from monolayer to bulk material'. In: *Nanoscale* 7.23 (2015) (cit. on p. 100).

[262] J. Huang, T. B. Hoang and M. H. Mikkelsen. 'Probing the origin of excitonic states in monolayer WSe2'. In: *Scientific Reports 2016 6:1* 6.1 (2016) (cit. on p. 100).

[263] Z. Wu, W. Zhao, J. Jiang et al. 'Defect Activated Photoluminescence in WSe 2 Monolayer'. In: *The Journal of Physical Chemistry C* 121.22 (2017) (cit. on p. 100).

[264] P. Vasa, W. Wang, R. Pomraenke et al. 'Real-time observation of ultrafast Rabi oscillations between excitons and plasmons in metal nanostructures with J-aggregates'. In: *Nature Photonics* 7.2 (2013) (cit. on p. 102).

[265] K. Santhosh, O. Bitton, L. Chuntonov et al. 'Vacuum Rabi splitting in a plasmonic cavity at the single quantum emitter limit'. In: *Nature Communications* 7.1 (2016) (cit. on pp. 102, 158, 165, 172).

[266] H. Chen, Z. Jiang, H. Hu et al. 'Sub-50-ns ultrafast upconversion luminescence of a rare-earth-doped nanoparticle'. In: *Nature Photonics* 16.9 (2022) (cit. on p. 102).

[267] B. Lamprecht, J. R. Krenn, G. Schider et al. 'Surface plasmon propagation in microscale metal stripes'. In: *Applied Physics Letters* 79.1 (2001) (cit. on pp. 104, 111).

[268] J. G. Simmons. 'Generalized Formula for the Electric Tunnel Effect between Similar Electrodes Separated by a Thin Insulating Film'. In: *Journal of Applied Physics* 34.6 (1963) (cit. on p. 106).

[269] R. Sáez-Blázquez, J. Feist, F. J. García-Vidal et al. 'Theory of Energy Transfer in Organic Nanocrystals'. In: *Advanced Optical Materials* 8.23 (2020) (cit. on p. 106).

[270] G. Su, A. Gao, B. Peng et al. 'Observation of in-plane exciton–polaritons in monolayer WSe_2 driven by plasmonic nanofingers'. In: *Nanophotonics* 11.13 (2022) (cit. on p. 107).

[271] C. Jin, J. Kim, K. Wu et al. 'On Optical Dipole Moment and Radiative Recombination Lifetime of Excitons in WSe 2'. In: *Advanced Functional Materials* 27.19 (2017) (cit. on p. 107).

[272] T. Hümmer, F. J. García-Vidal, L. Martín-Moreno et al. 'Weak and strong coupling regimes in plasmonic QED'. In: *Physical Review B* 87.11 (2013) (cit. on p. 109).

[273] C. Cohen-Tannoudji, B. Diu and F. Laloë. *Quantum Mechanics, Volume 2: Angular Momentum, Spin, and Approximation Methods*. Wiley, 2019 (cit. on pp. 112, 214).

[274] H. J. Carmichael, R. J. Brecha, M. G. Raizen et al. 'Subnatural linewidth averaging for coupled atomic and cavity-mode oscillators'. In: *Physical Review A* 40.10 (1989) (cit. on pp. 112, 168, 215).

[275] J. Repp, G. Meyer, S. M. Stojković et al. 'Molecules on Insulating Films: Scanning-Tunneling Microscopy Imaging of Individual Molecular Orbitals'. In: *Physical Review Letters* 94.2 (2005) (cit. on p. 115).

[276] V. Rai, N. Balzer, G. Derenbach et al. 'Hot luminescence from single-molecule chromophores electrically and mechanically self-decoupled by tripodal scaffolds'. In: *Nature Communications 2023 14:1* 14.1 (2023) (cit. on p. 115).

[277] R. Erni, M. D. Rossell, C. Kisielowski et al. 'Atomic-resolution imaging with a sub-50-pm electron probe'. In: *Physical Review Letters* 102.9 (2009) (cit. on p. 118).

[278] S. Morishita, M. Mukai, K. Suenaga et al. 'Atomic Resolution Imaging at an Ultralow Accelerating Voltage by a Monochromatic Transmission Electron Microscope'. In: *Physical Review Letters* 117.15 (2016) (cit. on p. 118).

[279] O. L. Krivanek, T. C. Lovejoy, N. Dellby et al. 'Vibrational spectroscopy in the electron microscope'. In: *Nature* 514.7521 (2014) (cit. on p. 118).

[280] V. Di Giulio, M. Kociak and F. J. G. de Abajo. 'Probing quantum optical excitations with fast electrons'. In: *Optica* 6.12 (2019) (cit. on pp. 118, 119, 138, 161, 163, 165, 182).

[281] A. Crai, A. Demetriadou and O. Hess. 'Electron Beam Interrogation and Control of Ultrafast Plexcitonic Dynamics'. In: *ACS Photonics* 7.2 (2020) (cit. on pp. 118, 172).

[282] G. P. Zouros, G. D. Kolezas, N. A. Mortensen et al. 'Monitoring strong coupling in nonlocal plasmonics with electron spectroscopies'. In: *Physical Review B* 101.8 (2020) (cit. on pp. 118, 172).

[283] B. Barwick, D. J. Flannigan and A. H. Zewail. 'Photon-induced near-field electron microscopy'. In: *Nature* 462.7275 (2009) (cit. on pp. 118, 181, 188, 192).

[284] S. T. Park, M. Lin and A. H. Zewail. 'Photon-induced near-field electron microscopy (PINEM): Theoretical and experimental'. In: *New Journal of Physics* 12 (2010) (cit. on pp. 118, 119, 181, 182).

[285] A. Feist, K. E. Echternkamp, J. Schauss et al. 'Quantum coherent optical phase modulation in an ultrafast transmission electron microscope'. In: *Nature* 521.7551 (2015) (cit. on pp. 118, 137, 181).

[286] J. Breuer and P. Hommelhoff. 'Laser-Based Acceleration of Nonrelativistic Electrons at a Dielectric Structure'. In: *Physical Review Letters* 111.13 (2013) (cit. on p. 118).

[287] K. E. Priebe, C. Rathje, S. V. Yalunin et al. 'Attosecond electron pulse trains and quantum state reconstruction in ultrafast transmission electron microscopy'. In: *Nature Photonics* 11.12 (2017) (cit. on pp. 118, 119, 138, 181).

[288] M. Kozák, J. McNeur, K. J. Leedle et al. 'Optical gating and streaking of free electrons with sub-optical cycle precision'. In: *Nature Communications* 8.1 (2017) (cit. on p. 118).

[289] M. Kozák, N. Schönenberger and P. Hommelhoff. 'Ponderomotive Generation and Detection of Attosecond Free-Electron Pulse Trains'. In: *Physical Review Letters* 120.10 (2018) (cit. on pp. 118, 181).

[290] Y. Morimoto and P. Baum. 'Diffraction and microscopy with attosecond electron pulse trains'. In: *Nature Physics* 14.3 (2018) (cit. on pp. 118, 119, 181).

[291] M. Yannai, R. Dahan, A. Gorlach et al. 'Ultrafast Electron Microscopy of Nanoscale Charge Dynamics in Semiconductors'. In: *ACS Nano* 17.4 (2023) (cit. on p. 118).

[292] D. Nabben, J. Kuttruff, L. Stolz et al. 'Attosecond electron microscopy of sub-cycle optical dynamics'. In: *Nature* 619.7968 (2023) (cit. on p. 118).

[293] J. H. Gaida, H. Lourenço-Martins, M. Sivis et al. 'Attosecond electron microscopy by free-electron homodyne detection'. In: *Nature Photonics* 18.5 (2024) (cit. on pp. 118, 158, 159, 189, 194).

[294] T. Bucher, H. Nahari, H. Herzig Sheinfux et al. 'Coherently amplified ultrafast imaging using a free-electron interferometer'. In: *Nature Photonics* (2024) (cit. on pp. 118, 189, 194).

[295] F. J. García de Abajo, A. Asenjo-Garcia and M. Kociak. 'Multiphoton Absorption and Emission by Interaction of Swift Electrons with Evanescent Light Fields'. In: *Nano Letters* 10.5 (2010) (cit. on pp. 119, 181).

[296] N. Talebi. 'Electron-light interactions beyond the adiabatic approximation: Recoil engineering and spectral interferometry'. In: *Advances in Physics: X* 3.1 (2018) (cit. on pp. 119, 181, 182).

[297] O. Reinhardt and I. Kaminer. 'Theory of Shaping Electron Wavepackets with Light'. In: *ACS Photonics* (2020) (cit. on pp. 119, 138, 181, 182).

[298] V. Di Giulio, O. Kfir, C. Ropers et al. 'Modulation of Cathodoluminescence Emission by Interference with External Light'. In: *ACS Nano* 15.4 (2021) (cit. on pp. 119, 181).

[299] O. Kfir, H. Lourenço-Martins, G. Storeck et al. 'Controlling free electrons with optical whispering-gallery modes'. In: *Nature* 582.7810 (2020) (cit. on pp. 119, 181, 182, 238).

[300] Y. Pan and A. Gover. 'Spontaneous and stimulated emissions of a preformed quantum free-electron wave function'. In: *Physical Review A* 99.5 (2019) (cit. on pp. 119, 182).

[301] O. Kfir. 'Entanglements of Electrons and Cavity Photons in the Strong-Coupling Regime'. In: *Physical Review Letters* 123.10 (2019) (cit. on pp. 119, 182).

[302] J. Lim, S. Kumar, Y. S. Ang et al. 'Quantum Interference between Fundamentally Different Processes Is Enabled by Shaped Input Wavefunctions'. In: *Advanced Science* 10.10 (2023) (cit. on pp. 119, 161, 163, 182).

[303] F. J. García de Abajo and V. Di Giulio. 'Optical Excitations with Electron Beams: Challenges and Opportunities'. In: *ACS Photonics* 8.4 (2021) (cit. on pp. 119, 161, 163, 182).

[304] O. Kfir, V. Di Giulio, F. J. G. de Abajo et al. 'Optical coherence transfer mediated by free electrons'. In: *Science Advances* 7.18 (2021) (cit. on pp. 119, 127, 164, 175, 182).

[305] V. Di Giulio and F. J. García de Abajo. 'Free-electron shaping using quantum light'. In: *Optica* 7.12 (2020) (cit. on pp. 119, 137, 182).

[306] G. Baranes, R. Ruimy, A. Gorlach et al. 'Free electrons can induce entanglement between photons'. In: *npj Quantum Information* 8.1 (2022) (cit. on pp. 119, 182).

[307] F. J. García de Abajo and A. Konečná. 'Optical Modulation of Electron Beams in Free Space'. In: *Physical Review Letters* 126.12 (2021) (cit. on pp. 119, 182).

[308] J.-W. Henke, A. S. Raja, A. Feist et al. 'Integrated photonics enables continuous-beam electron phase modulation'. In: *Nature* 600.7890 (2021) (cit. on pp. 119, 182).

[309] I. Madan, V. Leccese, A. Mazur et al. 'Ultrafast Transverse Modulation of Free Electrons by Interaction with Shaped Optical Fields'. In: *ACS Photonics* 9.10 (2022) (cit. on pp. 119, 182).

[310] Z. Zhao, X. Q. Sun and S. Fan. 'Quantum Entanglement and Modulation Enhancement of Free-Electron-Bound-Electron Interaction'. In: *Physical Review Letters* 126.23 (2021) (cit. on pp. 119, 125, 127, 131, 137, 138, 142, 144, 146, 150, 152, 161, 163–165, 174, 176, 182, 240, 266).

[311] B. Zhang, D. Ran, R. Ianconescu et al. 'Quantum Wave-Particle Duality in Free-Electron–Bound-Electron Interaction'. In: *Physical Review Letters* 126.24 (2021) (cit. on pp. 119, 132, 137, 138, 182).

[312] R. Ruimy, A. Gorlach, C. Mechel et al. 'Toward Atomic-Resolution Quantum Measurements with Coherently Shaped Free Electrons'. In: *Physical Review Letters* 126.23 (2021) (cit. on pp. 119, 127, 131, 132, 137, 152, 155, 161, 163, 164, 174, 176, 182, 266).

[313] D. Rätzel, D. Hartley, O. Schwartz et al. 'Controlling quantum systems with modulated electron beams'. In: *Physical Review Research* 3.2 (2021) (cit. on pp. 119, 142, 146, 182).

[314] Y. Morimoto, P. Hommelhoff and L. B. Madsen. 'Coherent scattering of an optically modulated electron beam by atoms'. In: *Physical Review A* 103.4 (2021) (cit. on pp. 119, 137, 182).

[315] B. Zhang, D. Ran, R. Ianconescu et al. 'Quantum state interrogation using a preshaped free electron wavefunction'. In: *Physical Review Research* 4.3 (2022) (cit. on pp. 119, 132, 137, 140, 152, 182, 269).

[316] D. Ran, B. Zhang, R. Ianconescu et al. 'Coherent Excitation of Bound Electron Quantum State With Quantum Electron Wavepackets'. In: *Frontiers in Physics* 10.July (2022) (cit. on pp. 119, 132, 147, 182).

[317] F. J. García de Abajo, E. J. Dias and V. Di Giulio. 'Complete Excitation of Discrete Quantum Systems by Single Free Electrons'. In: *Physical Review Letters* 129.9 (2022) (cit. on pp. 119, 124, 131, 137, 140, 142, 161, 163, 182, 267).

[318] A. Karnieli, S. Tsesses, R. Yu et al. 'Quantum sensing of strongly coupled light-matter systems using free electrons'. In: *Science Advances* 9.1 (2023) (cit. on pp. 119, 161, 166, 172, 182, 222).

[319] A. Karnieli, S. Tsesses, R. Yu et al. 'Universal and Ultrafast Quantum Computation Based on Free-Electron-Polariton Blockade'. In: *PRX Quantum* 5 (2024) (cit. on pp. 119, 161, 166, 182, 267).

[320] R. Dahan, S. Nehemia, M. Shentcis et al. 'Resonant phase-matching between a light wave and a free-electron wavefunction'. In: *Nature Physics* 16.11 (2020) (cit. on pp. 119, 176, 182).

[321] J. Feist, A. I. Fernández-Domínguez and F. J. García-Vidal. 'Macroscopic QED for quantum nanophotonics: emitter-centered modes as a minimal basis for multiemitter problems'. In: *Nanophotonics* 10.1 (2020) (cit. on pp. 120, 122, 159, 217, 219, 231, 232).

[322] N. Talebi. 'Strong Interaction of Slow Electrons with Near-Field Light Visited from First Principles'. In: *Physical Review Letters* 125 (2020) (cit. on pp. 124, 267).

[323] J. Larson and T. Mavrogordatos. *The Jaynes–Cummings Model and Its Descendants*. 2053-2563. IOP Publishing, 2021 (cit. on p. 126).

[324] C. Gonzalez-Ballestero, J. Feist, E. Moreno et al. 'Harvesting excitons through plasmonic strong coupling'. In: *Physical Review B* 92.12 (2015) (cit. on pp. 127, 245).

[325] N. Talebi and I. Březinová. 'Exchange-mediated mutual correlations and dephasing in free-electrons and light interactions'. In: *New Journal of Physics* 23 (2021) (cit. on p. 127).

[326] S Blanes, F Casas, J. A. Oteo et al. 'A pedagogical approach to the Magnus expansion'. In: *European Journal of Physics* 31.4 (2010) (cit. on pp. 128, 131, 255, 257).

[327] I. I. Rabi. 'Space quantization in a gyrating magnetic field'. In: *Physical Review* 51.8 (1937) (cit. on p. 130).

[328] G. Baranes, S. Even-Haim, R. Ruimy et al. 'Free-electron interactions with photonic GKP states: Universal control and quantum error correction'. In: *Physical Review Research* 5.4 (2023) (cit. on p. 132).

[329] M. O. Scully and M. S. Zubairy. *Quantum optics*. Cambridge: Cambridge University Press, 1997 (cit. on p. 135).

[330] S. V. Yalunin, A. Feist and C. Ropers. 'Tailored high-contrast attosecond electron pulses for coherent excitation and scattering'. In: *Physical Review Research* 3 (2021) (cit. on pp. 137, 138, 150).

[331] F. Chahshouri and N. Talebi. 'Numerical investigation of sequential phase-locked optical gating of free electrons'. In: *Scientific Reports* 13 (2023) (cit. on pp. 137, 138).

[332] N. Talebi, S. Meuret, S. Guo et al. 'Merging transformation optics with electron-driven photon sources'. In: *Nature Communications* 10 (2019) (cit. on p. 137).

[333] M. Taleb, M. Hentschel, K. Rossnagel et al. 'Phase-locked photon–electron interaction without a laser'. In: *Nature Physics* 19 (2023) (cit. on p. 137).

[334] M. Taleb, P. Bittorf, M. Black et al. *Ultrafast phonon-mediated dephasing of color centers in hexagonal boron nitride probed by electron beams*. 2024 (cit. on pp. 137, 189, 194).

[335] D. S. Black, U. Niedermayer, Y. Miao et al. 'Net Acceleration and Direct Measurement of Attosecond Electron Pulses in a Silicon Dielectric Laser Accelerator'. In: *Physical Review Letters* 123 (2019) (cit. on pp. 138, 150).

[336] O. Be'er, A. Gorlach, A. Nage et al. *Free-electron superfluorescence: collective optical dynamics at deep-subwavelength resolution*. 2023 (cit. on p. 143).

[337] M. Abdo, S. Sheng, S. Rolf-Pissarczyk et al. 'Variable Repetition Rate THz Source for Ultrafast Scanning Tunneling Microscopy'. In: *ACS Photonics* 8.3 (2021) (cit. on p. 150).

[338] C. K. Dass, M. A. Khan, G. Clark et al. 'Ultra-Long Lifetimes of Single Quantum Emitters in Monolayer WSe2/hBN Heterostructures'. In: *Advanced Quantum Technologies* 2.5-6 (2019) (cit. on p. 150).

[339] C. Wang, X. Li, H. Xu et al. 'Towards practical quantum computers: transmon qubit with a lifetime approaching 0.5 milliseconds'. In: *npj Quantum Information* 8.1 (2022) (cit. on p. 150).

[340] P. Rungta, V. Bužek, C. M. Caves et al. 'Universal state inversion and concurrence in arbitrary dimensions'. In: *Physical Review A* 64 (2001) (cit. on p. 153).

[341] L. Novotny. 'Strong coupling, energy splitting, and level crossings: A classical perspective'. In: *American Journal of Physics* 78.11 (2010) (cit. on pp. 158, 163).

[342] C. Tserkezis, A. I. Fernández-Domínguez, P. A. D. Gonçalves et al. 'On the applicability of quantum-optical concepts in strong-coupling nanophotonics'. In: *Reports on Progress in Physics* 83.8 (2020) (cit. on p. 158).

[343] D. Sanvitto and S. Kéna-Cohen. 'The road towards polaritonic devices'. In: *Nature Materials* 15.10 (2016) (cit. on pp. 158, 172).

[344] M. Sánchez-Barquilla, A. I. Fernández-Domínguez, J. Feist et al. 'A Theoretical Perspective on Molecular Polaritonics'. In: *ACS Photonics* 9.6 (2022) (cit. on p. 158).

[345] P. Lodahl, S. Mahmoodian and S. Stobbe. 'Interfacing single photons and single quantum dots with photonic nanostructures'. In: *Reviews of Modern Physics* 87.2 (2015) (cit. on p. 158).

[346] A. I. Fernández-Domínguez, S. I. Bozhevolnyi and N. A. Mortensen. 'Plasmon-Enhanced Generation of Nonclassical Light'. In: *ACS Photonics* 5.9 (2018) (cit. on p. 158).

[347] J. J. Baumberg, J. Aizpurua, M. H. Mikkelsen et al. 'Extreme nanophotonics from ultrathin metallic gaps'. In: *Nature Materials* 18.7 (2019) (cit. on p. 158).

[348] N. Rivera and I. Kaminer. 'Light–matter interactions with photonic quasiparticles'. In: *Nature Reviews Physics* 2.10 (2020) (cit. on p. 159).

[349] N. Talebi and C. Lienau. 'Interference between quantum paths in coherent Kapitza–Dirac effect'. In: *New Journal of Physics* 21 (2019) (cit. on p. 181).

[350] S. A. R. Horsley and J. B. Pendry. 'Quantum electrodynamics of time-varying gratings'. In: *Proceedings of the National Academy of Sciences* 120 (2023) (cit. on pp. 186, 190).

[351] S. Mignuzzi, S. Vezzoli, S. A. R. Horsley et al. 'Nanoscale Design of the Local Density of Optical States'. In: *Nano Letters* 19 (2019) (cit. on pp. 187, 192).

[352] S. Molesky, Z. Lin, A. Y. Piggott et al. 'Inverse design in nanophotonics'. In: *Nature Photonics* 12 (2018) (cit. on pp. 187, 192).

[353] I. Flexcompute. *Tidy3D*. 2024 (cit. on pp. 187, 192).

[354] A. C. Ltd. *Lumerical*. 2024 (cit. on pp. 187, 192).

[355] K. Wang, D. Ding and R. Chen. 'A Surrogate Modeling Technique for Electromagnetic Scattering Analysis of 3-D Objects With Varying Shape'. In: *IEEE Antennas and Wireless Propagation Letters* 17 (2018) (cit. on pp. 187, 192).

[356] A. Pietrenko-Dabrowska, S. Koziel and U. Ullah. 'Reduced-cost two-level surrogate antenna modeling using domain confinement and response features'. In: *Scientific Reports* 12 (2022) (cit. on pp. 187, 192).

[357] K. Li, Y. Li, L. Li et al. 'Surrogate modeling of time-domain electromagnetic wave propagation via dynamic mode decomposition and radial basis function'. In: *Journal of Computational Physics* 491 (2023) (cit. on pp. 187, 192).

[358] S. Koziel, A. Pietrenko-Dabrowska and L. Leifsson. 'Antenna optimization using machine learning with reduced-dimensionality surrogates'. In: *Scientific Reports* 14 (2024) (cit. on pp. 187, 192).

[359] COMSOL. *COMSOL Multiphysics*. Version 6.2. 2024 (cit. on pp. 187, 192).

[360] R. Hoyle. *Pattern Formation*. Cambridge University Press, 2006 (cit. on p. 197).

[361] C Ciraci, R. Hill, J. Mock et al. 'Probing the Ultimate Limits of Plasmonic Enhancement'. In: *SCIENCE* 337 (2012) (cit. on p. 247).

[362] A. I. Fernández-Domínguez, A. Wiener, F. J. García-Vidal et al. 'Transformation-Optics Description of Nonlocal Effects in Plasmonic Nanostructures'. In: *Phys. Rev. Lett.* 108 (2012) (cit. on p. 247).

[363] R. Ruppin. 'Optical Properties of a Plasma Sphere'. In: *Phys. Rev. Lett.* 31.24 (1973) (cit. on p. 248).

[364] A. Rosławska, T. Neuman, B. Doppagne et al. 'Mapping Lamb, Stark, and Purcell Effects at a Chromophore-Picocavity Junction with Hyper-Resolved Fluorescence Microscopy'. In: *Physical Review X* 12 (2022) (cit. on p. 252).

Publications

[P1] **J. Abad-Arredondo**, Z. Geng, G. Keijsers et al. 'Spontaneous Symmetry Breaking in Diffraction'. In: *Physical Review Letters* 133 (2024) (cit. on pp. 33, 37).

[P2] **J. Abad-Arredondo**, F. García-Vidal, Q. Zhang et al. 'Fluorescence Triggered by Radioactive β- Decay in Optimized Hyperbolic Cavities'. In: *Physical Review Applied* 14 (2020) (cit. on pp. 34, 77).

[P3] Y. Zhu, J. Yang, **J. Abad-Arredondo** et al. 'Electroluminescence as a Probe of Strong Exciton–Plasmon Coupling in Few-Layer WSe_2'. In: *Nano Letters* 24 (2024) (cit. on pp. 34, 95, 101, 109, 111, 118, 172).

[P4] **J. Abad-Arredondo** and A. I. Fernández-Domínguez. *Quantum state preparation and readout with modulated electrons*. 2024 (cit. on pp. 35, 117, 119, 157, 251).

[P5] **J. Abad-Arredondo** and A. I. Fernández-Domínguez. 'Electron-assisted probing of polaritonic light–matter states'. In: *Nanophotonics* 13 (2024) (cit. on pp. 35, 117, 119, 128, 131, 134, 138, 152, 161, 251, 266).

Further publications not featured in this thesis:

[P6] A. Miguel-Torcal, **J. Abad-Arredondo**, F. J. García-Vidal et al. 'Inverse-designed dielectric cloaks for entanglement generation'. In: *Nanophotonics* 11 (2022) (cit. on pp. 187, 192).

[P7] F. Zhang, P. R. A. Oiticica, **J. Abad-Arredondo** et al. 'Brownian Motion Governs the Plasmonic Enhancement of Colloidal Upconverting Nanoparticles'. In: *Nano Letters* 24 (2024).